Time-Dependent Finite Element Analysis in Restrained Concrete

A study on the effect of analysing the combination of hardening processes and external loading on improving the prediction of the development of design stresses

J. M. Schaper

Master of Science thesis

TU Delft

wagemaker

Time-Dependent Finite Element Analysis in Restrained Concrete

A study on the effect of analysing the combination of hardening processes and external loading on improving the prediction of the development of design stresses

by

J. M. Schaper

to obtain the degree of Master of Science
at the Delft University of Technology,
to be defended publicly on Friday August 25, 2023 at 15:00.

Student number:	5169267	
Project duration:	February 7, 2022 – August 25, 2023	
Thesis committee:	Dr. ir. F. P. van der Meer,	Delft University of Technology, chair
	Prof. dr. ir. M. A. N. Hendriks,	Delft University of Technology
	Dr. ir. B. Šavija,	Delft University of Technology
	Ir. J. W. de Vos,	Wagemaker
	Ir. S. Lambregts,	Wagemaker
Cover:	Underpass Kanaalweg Leiden, image from [1] (modified)	

An electronic version of this thesis is available at http://repository.tudelft.nl/.

TU Delft Delft University of Technology

wagemaker

Preface

This report presents my Master thesis on time-dependent finite element analysis in retrained concrete. This thesis concludes my Master of Science in Civil Engineering at the Technical University of Delft. I consider myself fortunate to have been able to combine my enthusiasm for civil engineering with my interest in the structural mechanics of the hardening process. I am therefore delighted that Wagemaker B.V., an engineering company based in Rosmalen, proposed this research. For the past 1.5 years I have been conducting a study on the effect of analysing the combination of hardening processes and external loading on improving the prediction of the development of design stresses.

First of all, I would like to thank my supervisors at Wagemaker, Jan Willem de Vos and Stef Lambregts, for their input during our meetings and the feedback they provided during my research. I would also like to thank my chair supervisor at TU Delft, Frans van der Meer, for his support during the graduation period. I would also like to thank the other members of the committee, Max Hendriks and Branko Šavija, for their useful suggestions and advice during the progress meetings. I would also like to thank the other Wagemaker staff, in particular Dennis Schoenmakers and Erik de Rooij, for sharing their thoughts and providing new insights during the research.

My gratitude also goes to Ab van den Bos and Pim van der Aa of NLyse Consultants, an engineering consultancy specialising in non-linear finite element analysis, for assisting me with the modelling of the validation experiment at their office in Arnhem and for answering my questions about the modelling of the case study project.

I would also like to thank Anja Klausen from the Norwegian University of Science and Technology for answering questions and providing data from experiments performed in her research that were used in this study.

Finally, I would like to thank my friends and family for their unconditional support and confidence in my abilities. I proudly present this Master's thesis report and hope that you enjoy the reading.

J. M. Schaper
Delft, August 2023

Abstract

Concrete is widely used in civil engineering and despite its long history, accurate prediction of the hardening process, particularly in partially restrained conditions, remains a challenge. During the hardening of partially restrained concrete, residual stresses occur due to restrained deformations caused by factors such as heating/cooling and shrinkage of the concrete. Accurately predicting the development of these residual stresses during restrained hardening is critical for proper design calculations, as cracking must be controlled by reinforcement. However, predicting the development of these design stresses is complex and depends on a number of processes and parameters, including temperature development, development of mechanical properties and the degree of restraint. These stresses also decrease with time due to creep and relaxation, which further complicates predictions, especially when dealing with restrained concrete combined with shrinkage.

In addition, hardening concrete will eventually be subjected to external loads, resulting in additional stresses that may require additional reinforcement. However, when it is difficult to accurately predict the development of design stresses, approximations must be made. These approximations may either take full account of the stresses from both hardening and external loading, or reduce the residual stresses by some factor. Such factors may be based on design codes or rough estimates. Consequently, these approximations can lead to either over- or underestimation of the reinforcement required in the design, mainly due to a lack of understanding of the actual design stresses. Therefore, the research question investigated in this thesis is as follows:

What is the effect of applying time-dependent finite element analysis, including the combination of hardening processes and external loads, on improving the prediction of the development of design stresses for partially restrained concrete?

The research starts with a comprehensive literature review covering the stress development during hardening of restrained concrete, the current calculation methods and models and a validation experiment. The validation experiment, a Temperature-Stress Testing Machine (TSTM) found in literature, is modelled and the analysis results are compared with the experimental results to validate the accuracy of modelling the hardening of partially restrained concrete. A method is developed to accurately predict the hardening of restrained concrete using a combination of transient heat transfer analysis and structural non-linear analysis. This non-linear analysis uses a combination of time and load steps to apply the required degree of restraint. The finite element analysis, using measured thermal and material properties from the literature, shows good agreement with the TSTM experimental results.

In order to verify the accuracy of commonly used material models, the Eurocode and fib Model Code material models within DIANA FEA are compared with the results of the TSTM experiment. However, it was found that these material models have inaccuracies due to the use of large step sizes for the Kelvin chains that define the creep and Young's modulus developments. Therefore, a viscoelastic material model based on the fib Model Code was developed and found to be more accurate. This material model was validated against the TSTM experiment and hand calculations. Although differences were found in the development of design stresses between the experimental results and the prescribed standards, these were mainly due to the difference in autogenous shrinkage and coefficient of thermal expansion.

Using the knowledge gained from the modelling of the TSTM experiment and the validated viscoelastic material model, a case study of the railway underpass in Leiden is performed. The chosen modelling approach is a time-dependent non-linear finite element analysis that includes all construction phases, hardening processes, and external loads within a 3D model of solid 3D elements. The model excludes concrete cracking, reinforcement and prestressing of the deck to limit complexity. This calculation method is expected to provide a more detailed insight into the development of design stresses and ensures high calculation accuracy and completeness compared to other methods. The use of a full 3D model was necessary to accurately model the temperature development in the hardening concrete, which has a significant effect on the design stresses.

The case study analysis performed shows that the residual stresses from hardening at ‘t=0’ are quite close to the original calculation performed using the traditional calculation method, but the design stresses at ‘t=∞’ are much higher. This discrepancy is mainly due to a possibly over-optimistic assumption that residual stresses are reduced by 50% at ‘t=∞’. The actual reduction is only 10%, while the reduction due to creep/relaxation is greater, but this is counteracted by increasing shrinkage. It is therefore recommended that shrinkage is considered in the design process as it was not considered in the original calculation. It was also found that the assumption made in the original calculation that the concrete would crack at 75% of its tensile strength was not conservative. It was therefore recommended to delay the calculation with a cracked section until the full (time-dependent) tensile strength is reached.

The parameter study shows that a higher concrete class significantly increases the design stresses by approximately 40%, potentially requiring more reinforcement. This highlights the importance of specifying a particular concrete class and cement content in the design. The use of a factor to account for increased autogenous shrinkage in CEM III concrete is also recommended, as this also results in higher design stresses of approximately 7.4%. The study also shows that the construction phases have a significant effect on the design stresses. In particular, the use of a pouring strip between the wall and the deck significantly reduces the design stresses by 25% and offers the possibility of reducing the required reinforcement. Other parameters, such as winter and summer temperature conditions, a higher coefficient of thermal expansion and a longer formwork removal time, have a more limited effect (5% maximum) on the design stresses.

While further research is required to fully verify the analysis results from the case study, it is expected that the time-dependent finite element analysis performed can indeed improve the prediction of design stresses, as supported by the validations performed for the TSTM experiment. The integration of time-dependent effects and the consideration of the combination of hardening processes and external loads provide a more comprehensive understanding of stress development than traditional methods. By considering creep, relaxation and shrinkage, the analysis provides a more realistic representation of stress behaviour over time, allowing more accurate and reliable predictions of design stresses in partially restrained concrete. It also allows the determination of the most critical time step for the application of mobile loads. However, it has been found that this type of analysis is very time consuming, with each analysis limited to only one load combination. To overcome this, in practical applications it is recommended that only hardening processes and dead loads are included in the time-dependent finite element analysis. The results of a separate linear analysis, which includes all types of mobile loads and combinations, can then be manually added to limit the number of analyses. As creep reduction does not apply to mobile loads, this alternative approach provides a more practical solution while still benefiting from the application of a more detailed and accurate time-dependent analysis.

Contents

1 Introduction

1.1. Problem definition

Concrete is a widely used material in civil engineering. Although it has been used for many years, the hardening of concrete is still a difficult process to fully predict, especially when it is (partially) restrained by older concrete. As concrete hardens, it expands and contracts due to heating and cooling of the concrete and shrinkage of the concrete. For hardening concrete that is not restrained and can therefore expand and contract freely, this will not cause any stresses. But for (partially) restrained concrete, there are stresses as the concrete is restrained. These are initially compressive stresses as the concrete heats and expands, which are not critical as the concrete can withstand these stresses, but as the concrete contracts due to cooling and shrinkage this will lead to tensile stresses and possibly cracking. The latter is also shown in Figure 1.1.

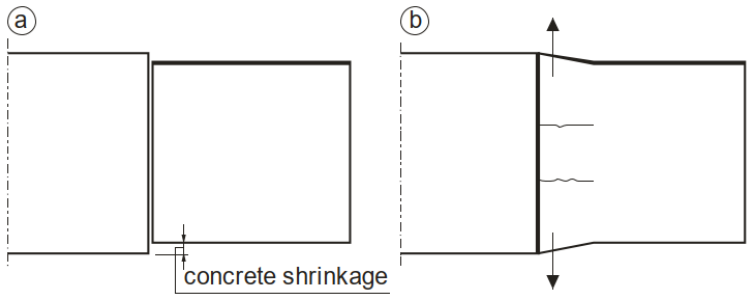

Figure 1.1: New concrete cast against old concrete, where (a) is a fictitious case where the new concrete is free to deform relative to the old concrete, and (b) is restrained deformation and cracking due to restraint, from [2].

The tensile stresses that occur during restrained hardening must be included in the design calculation, as the cracks that may occur must be controlled by reinforcement. However, the development of the residual stresses is very difficult to predict as it depends on various processes and parameters such as temperature development, mechanical property development and the degree of restraint, among others. Over time, these stresses are reduced by creep and relaxation, which adds another layer of complexity, particularly when dealing with restrained concrete combined with shrinkage, making prediction even more difficult.

The hardening concrete will also, after some time, be subjected to external loads which will cause additional stresses in the concrete. This might result in additional reinforcement. If the residual stresses that remain in the hardened concrete cannot be accurately predicted, a rough estimate must be made. This may involve adding the stresses from both hardening and external loads in full, or reducing the residual stresses by a factor. This factor can be based on design codes or rough estimates. This can lead to over- or underestimation of the amount of reinforcement required in the design due to a lack of understanding of the actual design stresses.

This situation, with the combination of partially restrained concrete and external loads, occurs in many projects performed by Wagemaker. In order to better understand this situation, Wagemaker suggested that this study be performed.

1.2. Aim of this research

The aim of this research is to gain a better understanding of the development of design stresses in concrete during the hardening process of partially restrained concrete. If an accurate time-dependent finite element analysis can be performed and validated by experiments that include all the hardening processes involved, the prediction of the development is expected to be improved. The hardening processes include the development of the concrete temperature and the effect of various forms of shrinkage, creep, relaxation and whether cracking occurs. If the prediction of the development of these design stresses can be improved, the critical time step for the application of the governing external/mobile loads can also be determined.

If a time-dependent finite element analysis method and model can be developed that can predict the development of design stresses from the hardening process, including the reduction due to creep and relaxation, this will improve the accuracy of the prediction made in the design. This will allow better assumptions to be made for design calculations, leading to potentially more reliable predictions for the calculation of partially restrained concrete. The main research question is formulated as follows:

What is the effect of applying time-dependent finite element analysis, including the combination of hardening processes and external loads, on improving the prediction of the development of design stresses for partially restrained concrete?

This question is divided into the following sub-questions, which provide a structured way of answering the main research question:

1. How can the hardening process of partially restrained concrete be accurately modelled and predicted using time-dependent finite element analysis?
2. Which type of material model, based on which standard or guideline, is most suitable and accurate for hardening partially restrained concrete?
3. Which specific time-dependent calculation method and model is most beneficial to use for the design of partially restrained concrete?
4. What are the differences in design stresses when comparing the time-dependent method and model with a calculation based on the traditional approach for a specific project?
5. How do different material and model parameters influence the development of design stresses when considering time-dependent finite element analysis?

1.3. Research strategy of this thesis

To answer the research question and sub-questions, the first step is to investigate the modelling of all hardening processes and restrained concrete. The possibility of accurately modelling and predicting stress development using time-dependent finite element analysis is investigated to answer the first sub-question. This is validated by comparing the results of the finite element analysis with data from a selected experiment.

Once the model is validated, the second sub-question is addressed. Different hardening material models, based on different standards and guidelines, are compared with the experimental results. The most suitable and accurate material model is then selected and used in a case study, which is a project calculated using the current traditional calculation approach.

In order to answer the third sub-question and to identify the most appropriate calculation method and model for the case study, the different types of calculation methods and models found in the literature review are compared. Through a thorough consideration of all the methods and models, a possible most appropriate/beneficial calculation method and model can be selected.

Using the chosen method and model, which is a time-dependent finite element analysis, a specific case study is modelled and analysed. A comparison is made between the analysis of this more detailed approach and the original calculation. This is to answer the fourth sub-question and to determine the differences between the design stresses between these two approaches.

To answer the final sub-question, a parameter study is performed in which various material and model parameters are varied. The aim of this study is to determine the influence of these parameter changes on the development of the design stresses. This is to determine whether these parameters have a significant effect on the design of restrained concrete and whether they should be considered in the design process.

By combining all of the research performed and the conclusions drawn from the sub-questions, the main research question can be effectively addressed and supported.

1.4. Research scope

In this thesis the hardening of restraint concrete process and the later added external loads are studied with the following restrictions:

- Only traditional concrete mixtures made with Portland cements, silica fume, fly ash and blast furnace slag cement are studied.
- Only concrete with 'traditional' reinforcing steel B500B and prestressing steel Y1860 are considered.
- For the case study, the same external loads are applied as in the original calculation and calculation model.
- This study will focus on the hardening of concrete until the loading with external loads.
- Cracking is not included in the time-dependent non-linear finite element analysis.
- Reinforcement and prestress was not included in the time-dependent non-linear finite element analysis.

1.5. Outline of this thesis

This thesis starts with the literature review in Chapter 2. The literature presented in this chapter acts as a theoretical background which is used and referred to throughout this thesis. After the literature review, the implementation of the hardening process in the finite element analysis begins. This is first done in Chapter 3 for a model based on the TSTM experiments from the literature in order to validate this model. Different types of material models based on different standards or guidelines are also investigated in this chapter. In Chapter 4, after the most appropriate calculation method and model have been selected, the case study is analysed using time-dependent finite element analysis. In Chapter 5 some of the assumptions and other variables are made to check the influence. These parameters can then be taken into account in the future calculations to give more accurate predictions of the distributed design forces and moments. A discussion of the results is given in Chapter 6. Finally, Chapter 7 concludes this thesis and provided recommendations for further research.

2

Literature review

This chapter presents the main literature found during the literature review. The literature presented is necessary for a better understanding of the study and will be referred to in the rest of the study. The literature review is described according to three subjects. The first is the stress development during the hardening of restrained concrete, which includes all hardening processes, the degree of restraint and the development of mechanical properties. This is followed by a review and overview of current calculation methods and models. The final section selects and describes a validation experiment from the literature. This is used in the next chapter to validate the hardening modelling of partially restrained concrete.

2.1. Stress development during hardening of restrained concrete

During the hardening process of restraint concrete, many processes take place simultaneously. During the chemical hardening process, the concrete gives off heat which causes the concrete to expand and later, when the concrete cools, the concrete will shrink again. This results in temperature induced deformations. In addition to the deformation due to temperature change, the concrete will also experience deformation due to shrinkage and creep. However, as the concrete is (partially) restrained by other concrete, stresses will occur in the concrete which will be partially reduced by creep/relaxation. All of these components, including the temperature development of the concrete, the degree of restraint and the development of the mechanical properties are described in detail in this section.

A large amount of literature is available on all of the individual topics considered. Although a large amount of literature has been studied, for the calculation method, Eurocode and the fib Model Code 2010 have mainly been investigated as these standards are widely used in Europe. CIRIA C766 was also included in the literature review. CIRIA stands for Construction Industry Research and Information Association and is a neutral, independent, non-profit organisation based in the UK. CIRIA C766 focuses on the early thermal cracking of concrete and is a document that has been compiled from a wide range of literature and also reflects the Eurocode. Therefore, in studying these three in particular, not only were the standards examined, but also a wide range of literature.

2.1.1. Development of the concrete temperature

One of the most important parameters in concrete hardening is the temperature development in the concrete. This depends on many different processes and parameters. The hydration process is explained and described first, followed by the adiabatic and semi-adiabatic temperature processes.

The hydration process

When cement and water come into contact, a chemical reaction takes place. Initially, the reaction process is slowed down considerably by the precipitation of the reaction products on the surface of the cement objects. The period in which the reaction proceeds very slowly is called the dormant phase (Figure 2.1). The duration of this process depends on the use of accelerators or retarders [2].

After the dormant stage, the acceleration period begins. During this period, a significant proportion of the available cement reacts rapidly with water. A microstructure is formed as a hydration layer surrounds and contacts the cement particles. The microstructure consists of unhydrated cement particles, hydration products and a partially filled pore system. The acceleration stage is followed by the deceleration stage. In this stage the process is governed by diffusion [2].

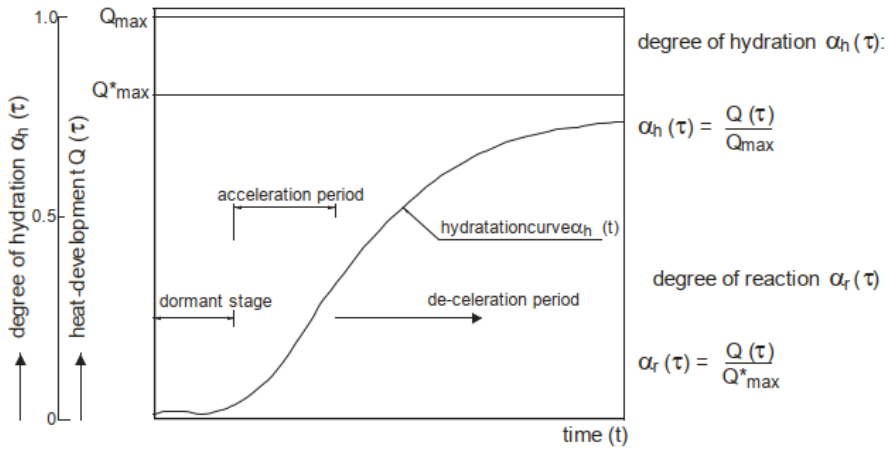

Figure 2.1: Schematic representation of different characteristic stages during hydration, from [2].

An important parameter indicating the ratio of the amount of hydrated cement to the amount of cement available organically is called the degree of hydration ($\alpha_h(t)$). According to Van Breugel et al. [2], the amount of hydrated cement is approximately proportional to the amount of heat released. The degree of hydration can therefore be calculated using Equation 2.1.

$$\alpha_h(t) = \frac{Q(t)}{Q_{max}} \tag{2.1}$$

In which:

$Q(t)$ = the amount of liberated heat at time t $[kJ/kg]$

Q_{max} = the amount of liberated heat at complete hydration of all available content $[kJ/kg]$

The amount of heat liberated depends on the type of cement, for example the Q_{max} of Portland cement is between 350 and 500 kJ/kg cement [2]. Appendix A2 of CIRIA C766 [3] describes a model derived from experiments performed by the Concrete Technology Unit of the University of Dundee. This model describes the heat hydration process and can include fly ash and ground granulated blast furnace slag (ggbs) proportions. Using the equations in this appendix, the heat of hydration can be calculated for each time step. For the influence of the amount of fly ash and ggbs see Figure 2.2.

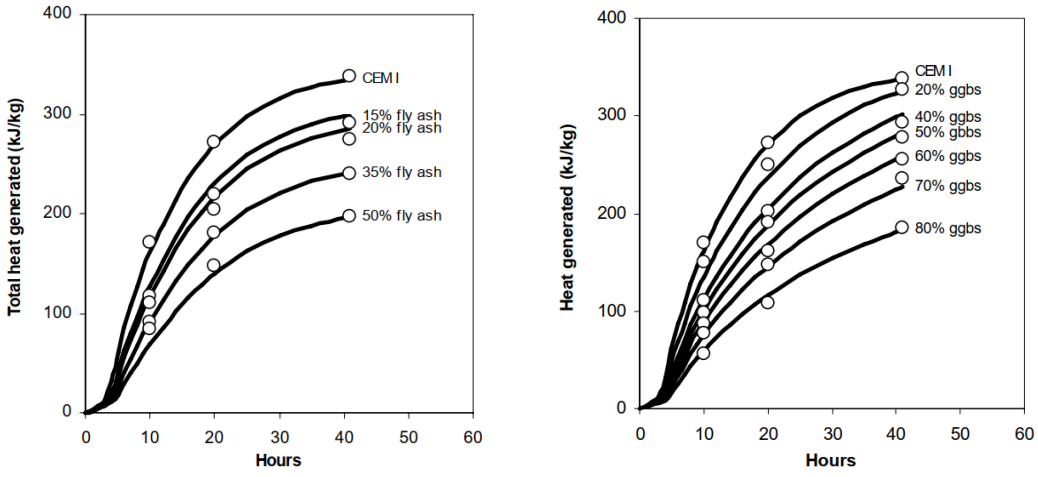

(a) Cement combinations including fly ash (b) Cement combinations including ggbs

Figure 2.2: Compassion between the generated heat for different cement combinations with CEM I, from [3].

The adiabatic temperature process

In the theoretical case where all the heat released during the hardening of the concrete is used for the concrete itself, the reaction process is called an adiabatic process. The temperature in the concrete therefore follows an adiabatic temperature rise and can be calculated using Equation 2.2 [2].

$$\Delta T_a(t) = \frac{\alpha_h(t) \cdot C \cdot Q_{max}}{\rho_c \cdot c_c} \tag{2.2}$$

In which:

C = cement content of the concrete [kg/m^3]

ρ_c = the specific mass of the concrete [kg/m^3]

c_c = the specific heat of the concrete [kJ/kg°C]

The heat capacity ($\rho_c \cdot c_c$) is not a constant during the hardening process. However, it can be assumed to be constant to avoid complications according to Van Breugel et al. [2]. If it is assumed to be constant, there is a linear relationship between the degree of hydration and the adiabatic temperature increase over time, as shown in Figure 2.3.

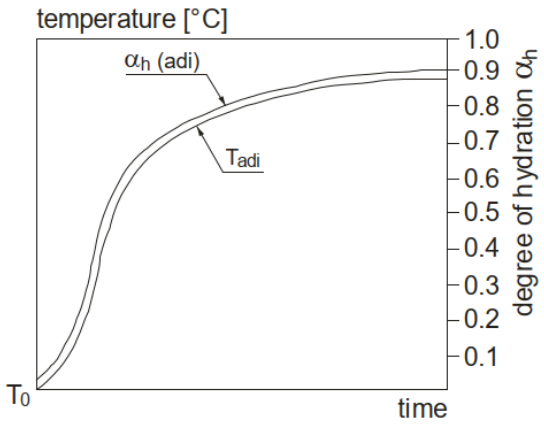

Figure 2.3: Schematic representation of the adiabatic temperature process and the degree of hydration, from [2].

The adiabatic curve (Figure 2.3) is an important input parameter for computer software to calculate the temperature gradient, but the shape of the adiabatic curve depends on the following set of parameters: the chemical composition of the cement, the grain size distribution of the cement, the w/c ratio, the cement content, the temperature of the fresh mix and the availability of accelerators and retarders [2].

The semi-adiabatic hardening process

Under realistic conditions, an adiabatic hardening process is not possible, as heat is transferred to the environment over time. The temperature will decrease over time and the hydration process will slow down. This is called a semi-adiabatic hardening process, see also Figure 2.4 [2].

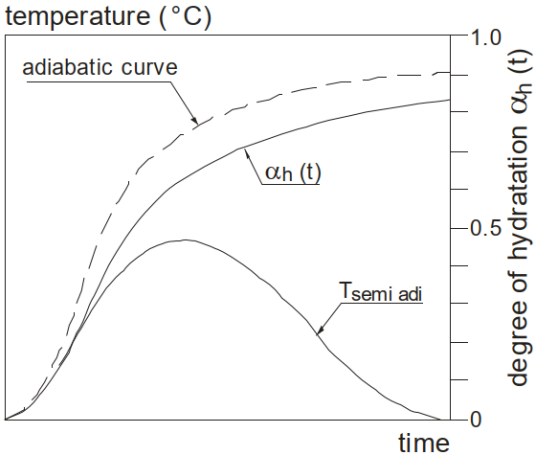

Figure 2.4: Schematic representation of the semi-adiabatic temperature process, the adiabatic curve and the degree of hydration, from [2].

The development of the semi-adiabatic hydration process depends on the temperature at which the process takes place. Conversely, the temperature depends on the amount of heat produced. The mutual dependence between the temperature of the concrete and the degree of hydration means that the calculations of the temperature development and the hardening process must be performed using a step-by-step calculation. This is described in detail in Chapter 7.4 of based on the book “Concrete Structures under Imposed Thermal and Shrinkage Deformations” by Van Breugel, et al. [2] and will not be further explained and described here, as these complex calculations are performed in this study using finite element programs.

2.1.2. Temperature-induced deformations

Changes in the temperature of hardening concrete is associated with a change of volume and/or deformation. The change of concrete strain caused by an increase or decrease in temperature ($\Delta\varepsilon_t(\Delta T(\tau))$) can be calculated using the following equation:

$$\Delta\varepsilon_t(\Delta T(\tau)) = \alpha_c \cdot \Delta T(\tau) \tag{2.3}$$

In which:

α_c = the coefficient of thermal expansion of the concrete

$\Delta T(\tau)$ = the temperature increment at time $t = \tau$, see Figure 2.5

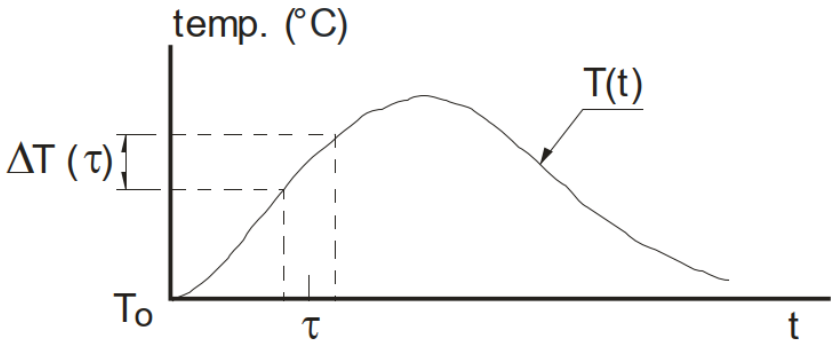

Figure 2.5: Schematic representation of the temperature distribution and incitement, adapted from [2].

The coefficient of thermal expansion depends on the coefficient of expansion of each component of the concrete. As the aggregates make up the largest part of the concrete, the expansion coefficient of this component is dominant. The coefficients of thermal expansion for different types of aggregates can be found, for example, in Table 4.6 of CIRIA C766 [3].

In addition to the aggregates, the cementitious part also plays an important role, especially during the hardening phase. The structure of the matrix of elements changes considerably during the hardening process. In reality, the coefficient of expansion of hardened concrete is therefore a function of the thermal expansion coefficients of the constituents of the mixture. The coefficient of thermal expansion of water is about five times higher than that of concrete, so deformation in the initial phase is dominated by the presence of water. However, as the stiffness of the concrete is still very low, the stresses will also be low. Therefore, according to Van Breugel et al. [2], it seems justified to use a constant value for the coefficient of thermal expansion as it is more practical.

According to EN1992-1-1, Section 3.1.3 (5) [4], in the absence of more precise information, it can be assumed that the coefficient of linear thermal expansion is $10 \cdot 10^{-6}/°C$. This is the same coefficient of thermal expansion given in Section 5.1.10.3 of the fib Model Code 2010 [5] for the structural design of normal weight concrete. However, CIRIA C766 states in Section 4.6 [3] that although this coefficient of thermal expansion is a representative value for a wide range of aggregates, some of the aggregates used in the UK have a $20\text{-}30\%$ higher coefficient of thermal expansion. They therefore recommend that this higher value of $12\text{-}13 \cdot 10^{-6}/°C$ should be used if no data is available. If the aggregates are known, they recommend that the design value should be taken from Table 4.6 of CIRIA C766 [3].

The total temperature induced strain ($\varepsilon_t(t)$) is the combination of the individual strain increments from Equation 2.3. This can be calculated using the following equation:

$$\varepsilon_t(t) = \sum_{i=0}^{i} \Delta\varepsilon_t(\Delta T(\tau_i)) \tag{2.4}$$

2.1.3. Shrinkage

In order to better understand the hardening process, the deformation of the concrete is of great importance in order to obtain information about the stresses that occur during the hardening of the concrete. In addition to temperature induced strains, shrinkage also results in strain deformation. Shrinkage occurs from the moment the concrete is mixed until decades after it has been poured. Shrinkage is defined as the reduction in volume and thus shortening of the concrete without the influence of any load [6] (see Figure 2.6).

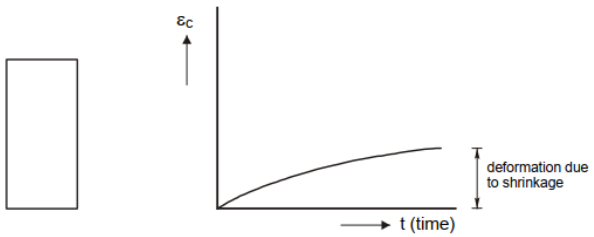

Figure 2.6: Definition of shrinkage, adapted from [6].

In this literature review the following types of shrinkage are investigated and explained: plastic, chemical, autogenous, drying and carbonation shrinkage. The duration and effect of these types of shrinkage are shown in the Table 2.1. In the following paragraphs, each type of shrinkage is explained in more detail and, where applicable, the calculation method is given according to Eurocode (EN1992-1-1), fib Model Code 2010 and CIRIA C766.

Table 2.1: Overview of the different types of shrinkage and period of effect.

Type of shrinkage	Period of effect	Shrinkage effect
Plastic shrinkage	Hours–days	Volume reduction due to evaporation of surface water of freshly poured concrete
Chemical shrinkage	Days–weeks	Internal volume reduction due to ongoing hydrating process of hardening concrete
Autogenous shrinkage	Days–weeks	A decrease in volume due to the available water consumed by the reaction process
Drying shrinkage	Days–years	Volume reduction due to the non-chemically bound water will slowly evaporates into the environment
Carbonation shrinkage	Years–decades	Reduction in volume because an reaction occurs under the present of carbon dioxide in the air

Plastic shrinkage

Plastic shrinkage is caused by the evaporation of water from the surface of freshly poured concrete. In freshly poured concrete, the heavier part of the concrete mix tends to move downwards and the lighter water tends to move upwards. According to Van Breugel et al. [2], this is particularly the case with floor slabs, which often have a thin layer of water on top after pouring. Plastic shrinkage is also increased when the fresh concrete is compacted after pouring. The rate of evaporation depends on ambient conditions such as wind speed, air temperature and concrete temperature.

Evaporation of water, and therefore the effect of plastic shrinkage, can be easily prevented by keeping the concrete wet during the curing process. This can be achieved by adding extra water to the top surface, covering the top surface with a foil layer or applying a curing compound. If water evaporation is prevented, the effect of plastic shrinkage is very small. EN1992-1-1, fib Model Code 2010 and CIRIA C766 do not include calculations for plastic shrinkage. It is therefore not considered in this study as it can be prevented by appropriate measures.

Chemical shrinkage

Chemical shrinkage is defined as the absolute (internal) volume change of cement due to hydration of cementitious materials [7]. The volume of the hydrated cement is less than the sum of the reacting cement and water, causing the concrete to shrink. But according to Van Breugel et al. [2, p. 155]: “Chemical shrinkage manifests itself mainly as capillary pores in the cement paste and hardly as an deformational change of a concrete element. Therefore, negligible or no stresses are generated on a macro-scale.”. EN1992-1-1, fib Model Code 2010 and CIRIA C766 do not cover chemical shrinkage because it hardly results in any external volume change. For this reason, chemical shrinkage will not be taken into account any further in this study.

Autogenous shrinkage

During the hydration process of concrete, the available water in the concrete mix is gradually consumed as a result of the reaction process. This leads to a reduction in volume, particularly at low water/cement ratios. Particularly high-strength concretes may therefore experience large autogenous shrinkage.

According to the Eurocode [4]; autogenous shrinkage is a linear function of concrete strength and can be calculated using the following equations:

$$\varepsilon_{ca}(t) = \beta_{as}(t) \cdot \varepsilon_{ca}(\infty) \tag{2.5}$$

With:

$$\varepsilon_{ca}(\infty) = 2.5(f_{ck} - 10) \cdot 10^{-6} \tag{2.6}$$

$$\beta_{as}(t) = 1 - \exp\left(-0.2t^{0.5}\right) \tag{2.7}$$

In which:

f_{ck} = the characteristic (5%) compressive (cylinder) strength at an age of 28 days in MPa

t = concrete age in days

According to the fib Model Code [5]; the basic shrinkage, which is the same as the autogenous shrinkage, is also dependent on the type of cement. Otherwise it is very closely related to the Eurocode and can be calculated using the following equations:

$$\varepsilon_{cbs}(t) = \varepsilon_{cbs0}(f_{cm}) \cdot \beta_{bs}(t) \tag{2.8}$$

With:

$$\varepsilon_{cbs0}(f_{cm}) = -\alpha_{bs}\left(\frac{0.1 \cdot f_{cm}}{6 + 0.1 \cdot f_{cm}}\right)^{2.5} \cdot 10^{-6} \tag{2.9}$$

$$\beta_{bs}(t) = 1 - \exp\left(-0.2 \cdot \sqrt{t}\right) \tag{2.10}$$

In which:

f_{cm} = the mean compressive (cylinder) strength at an the age of 28 days in MPa

t = concrete age in days

α_{bs} = a coefficient that depends on the type of cement and can be taken from Table 5.1-12 of the fib Model Code 2010 [5]

Although CIRIA C766 also gives an alternative equation in Appendix A4 [3], it recommends and uses the same equation as EN1992-1-1. CIRIA C766 states that the cement type also has an important influence on autogenous shrinkage, but this is not included in this equation or in the equation in the Eurocode. Although CIRIA states that this requires further research, Section A4.4 [3] of CIRIA C766 gives an overview of the studies that have been carried out on the influence of binder type. In particular, silica fume, fly ash and ground granulated blast furnace slag (ggbs) are discussed. CIRIA C766 concludes that, although data are limited, the use of silica fume or ggbs appears to increase the extent of autogenous shrinkage for a given w/b ratio, while the use of fly ash results in a reduction.

An article by T. Lu, Z. Li and H. Huang on the effect of admixtures on the autogenous shrinkage of hardened cement paste concludes: “The measured autogenous shrinkage of BFS cement paste is much bigger than that of Portland cement paste with the same water–binder ratio. The lower Young’s modulus and a larger drop in relative humidity of BFS cement paste are considered as the two major reasons.” [8, p. 12]. BFS stands for blast furnace slag cement and is the cement used in CEM III concrete. So both this literature and CIRIA C766 agree that the autogenous shrinkage of CEM III concrete with BFS is greater than that recommended by the Eurocode and/or the fib Model Code, as they are closely related.

Drying shrinkage

Drying shrinkage occurs in concrete as the water in the non-chemically bound water evaporates into the environment. Water loss starts in the large pores where little shrinkage occurs. Then the water disappears from the smaller capillary pores and later from the gel pores. As a result of this loss of water, the pores shrink, causing the cement stone and therefore the concrete to shrink [9].

The relative humidity, geometry and pore structure all influence the evaporation rate. The pore structure depends on the water-cement ratio, the cement content and the degree of hydration [2]. According to EN1992-1-1 [4]; the drying shrinkage can be calculated with the following equation:

$$\varepsilon_{cd}(t) = \beta_{ds}(t, t_s) \cdot k_h \cdot \varepsilon_{cd,0} \tag{2.11}$$

In which:

$\varepsilon_{cd,0}$ = the nominal unrestricted drying shrinkage according to Table 3.2 or can be calculated with Annex Chapter B.2 both from the EN1992-1-1 [4]

k_h = a coefficient that depends on the notional size h_0, and can be taken from Table 3.3 of the EN1992-1-1 [4]

$\beta_{ds}(t, t_s)$ = $\dfrac{(t - t_s)}{(t - t_s) + 0.04 \cdot \sqrt{h_0^3}}$ (with t in days)
In which t_s is the age of the concrete at the beginning of drying shrinkage

According to the fib Model Code [5]; the drying shrinkage is also dependent on the type of cement. Otherwise it is somewhat related to the Eurocode and can be calculated using the following equations:

$$\varepsilon_{cds}(t, t_s) = \varepsilon_{cds0}(f_{cm}) \cdot \beta_{RH}(RH) \cdot \beta_{ds}(t - t_s) \tag{2.12}$$

In which:

$\varepsilon_{cd,0}$ = the notional drying shrinkage coefficient which can be calculated using Equation 51.80 of the fib Model Code 2010 [5]

R_{RH} = a coefficient that takes into account the effect of ambient relative humidity which can be calculated using Equation 51.81 of the fib Model Code 2010 [5]

$\beta_{ds}(t, t_s)$ = a function describing the time-dependence which can be calculated using Equation 51.82 of the fib Model Code 2010 [5]

The CIRIA C766 uses the same model to calculate the drying shrinkage as the previously described EN1992-1-1. Only the way in which the drying shrinkage has to be combined with the autogenous shrinkage is different, which will be explained later on.

Carbonation shrinkage

When concrete is exposed to an atmosphere containing carbon dioxide, carbonation shrinkage occurs. The carbon dioxide in the atmosphere can react with the hydrated cement in the presence of water. This reaction converts calcium hydroxide crystals to calcium carbonate. Since the volume of calcium carbonate is smaller than the volume of calcium hydroxide, this reaction results in carbonation shrinkage [10]. The process of carbonation shrinkage is very slow and occurs only in the surface layer. The extent is also very small compared to long-term drying shrinkage [11]. As carbonation shrinkage has almost no effect on concrete, it is not mentioned in the Eurocode, fib Model Code and CIRIA and is therefore not considered in this work.

Total shrinkage

Now that all types of shrinkage have been discussed, the total shrinkage can be calculated according to the different standards.

According to EN1992-1-1 Equation 3.8 [4], the total shrinkage ($\varepsilon_{cs}(t)$) is just the sum of the autogenous shrinkage ($\varepsilon_{ca}(t)$) and the drying shrinkage ($\varepsilon_{cd}(t)$). The total shrinkage strain can then be calculated using the following equation:

$$\varepsilon_{cs}(t) = \varepsilon_{cd}(t) + \varepsilon_{ca}(t) \tag{2.13}$$

This is the same equation that can be found in the fib Model Code 2010, Equation 7.1-75 [5], with the exception that the autogenous shrinkage is called basic shrinkage, and therefore the indexes are slightly different.

CIRIA C766 states that: “for the higher strength classes, for which autogenous shrinkage continues beyond 28 days, long-term drying shrinkage measurements will necessarily include a component of autogenous shrinkage” [3, p. 49]. CIRIA therefore recommends that the autogenous shrinkage used

in Equation 2.13 is the value at 28 days or whatever age the drying shrinkage test was started. See also Figure 2.7, which shows that autogenous shrinkage dominates up to 28 days, after which the dry shrinkage is assumed to include the autogenous shrinkage component. So the total shrinkage after 28 days is the autogenous shrinkage of 28 days plus the change in drying shrinkage from 28 days onwards [3].

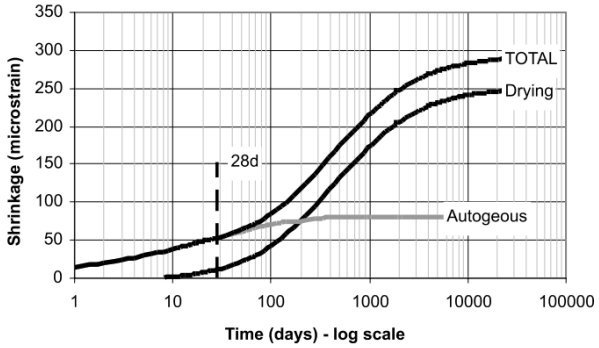

Figure 2.7: Combination of Shrinkage according to the CIRIA C766 [3].

2.1.4. Creep

Creep of concrete is defined as the increase in deformation over time with respect to the direct (elastic) deformation under sustained loading [2], [6] (see Figure 2.8). Creep is caused by the deformation of the gel structure and also by the capillary stress of the chemically non-bonded water.

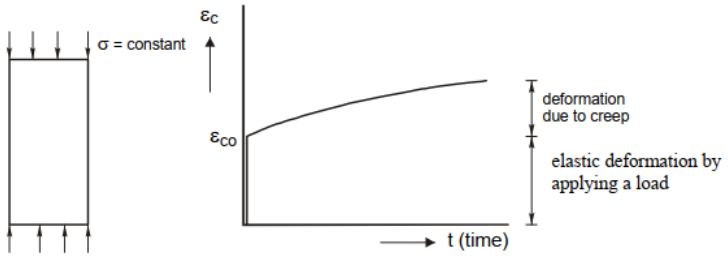

Figure 2.8: Definition of creep, adapted from [6].

According to EN1992-1-1 [4], if the compressive stress is greater than $0.45 f_{ck}(t_0)$ at age t_0, the creep deformation is directly proportional to the elastic deformation. The creep of concrete $\varepsilon_{cc}(t, t_0)$ at time t for a compressive stress σ_c applied at concrete age t_0 can be calculated using the following equation:

$$\varepsilon_{cc}(t, t_0) = \varphi(t, t_0) \cdot \frac{\sigma_c}{E_c} \tag{2.14}$$

In which:

$\varphi(t, t_0)$ = the creep coefficient calculated according to Annex Chapter B.1 from the EN1992-1-1.

E_c = is the Young's modulus, which may be taken as $1.05 E_{cm}$ according to the EN1992-1-1.

Equation 2.14 only applies for a constant compressive stress, which is not possible in most creep calculations. Normally, the stress will gradually increase with time when the construction progresses. For an arbitrary stress development, the principle of superposition according to Boltzmann can be used. This results in a creep deformation for a discrete number of stress increments in the following equation [6]:

$$\varepsilon_{cc}(t, t_i) = \frac{1}{E_c} \sum_{i=0}^{n} \Delta\sigma_i \cdot \varphi(t, t_i) \tag{2.15}$$

This means that the creep deformation at time t must be determined separately for each stress increment $\Delta\sigma_i$. In case of continuously varying stress $\sigma(\tau)$, the previous equation can be adapted to the following equation [6]:

$$\varepsilon_{cc}(t, \tau) = \frac{1}{E_c} \int_0^t \frac{d\sigma(\tau)}{d\tau} \varphi(t, \tau) d\tau \tag{2.16}$$

2.1.5. Simplified method for the calculation of the combination

There are multiple approximation methods available in the literature to simplify the creep equation and to combine the elastic deformation with creep and shrinkage. One is the relatively simple calculation procedure method of Trost. This method assumes a relatively high stress σ_0 initially at t_0, after which relatively small stress increments $\Delta\sigma_i(t_i)$ follow. Due to this assumption the creep equation can be rewritten as follows:

$$\varepsilon_{cc}(t,t_i) = \frac{1}{E_c}\left(\sigma_0 \cdot \varphi(t,t_0) + \sum_{i=1}^{n} \Delta\sigma_i \cdot \varphi(t,t_i)\right) \tag{2.17}$$

Adding the elastic deformation and shrinkage with the previous equation, and using that $\sigma(t) = \sigma_0 + \sum_{i=1}^{n} \Delta\sigma_i$ results to the following equation:

$$\varepsilon_c(t,t_i) = \frac{1}{E_c}\left(\sigma_0[1+\varphi(t,t_0)] + (\sigma(t)-\sigma_0) + \sum_{i=1}^{n} \Delta\sigma_i \cdot \varphi(t,t_i)\right) + \varepsilon_{cs}(t) \tag{2.18}$$

In order to obtain a simple equation, Trost proposed the change in the following equation:

$$\begin{aligned} \varepsilon_c(t,t_0) &= \frac{1}{E_c}[\sigma_0[1+\varphi(t,t_0)] + (\sigma(t)-\sigma_0)\cdot[1+\rho\cdot\varphi(t,t_0)]] + \varepsilon_{cs}(t) \Rightarrow \\ \varepsilon_c(t,t_0) &= \frac{1}{E_c}[\sigma_0[1+\varphi(t,t_0)] + \Delta\sigma(t)\cdot[1+\rho\cdot\varphi(t,t_0)]] + \varepsilon_{cs}(t) \end{aligned} \tag{2.19}$$

Where $\Delta\sigma(t) = (\sigma(t)-\sigma_0)$ and ρ is the 'ageing coefficient' which will generally have a value of 0.8 for normally loaded concrete structures with a creep factor of $1.5 \leq \varphi(\infty,t_i) \leq 4.0$ [6].

2.1.6. Relaxation

Relaxation of concrete is defined as the decreasing of the initially present stresses with time when the deformation of the material is kept constant [6]. See also Figure 2.9.

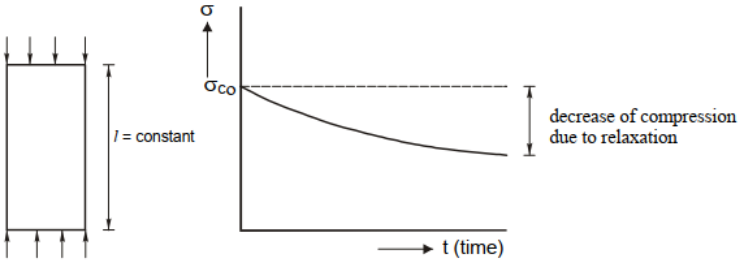

Figure 2.9: Definition of relaxation, adapted from [6].

Relaxation for elastic, shrinkage and creep deformations

The definition of relaxation implies a reduction in stress for a constant deformation. The preceding expression (Equation 2.19) of Trost can be used to derive the equation for relaxation for shrinkage and creep. Assuming $\varepsilon_{c0} = \sigma_0/(E_c \cdot r)$, results in the following equation:

$$\varepsilon_c(t,t_0) - \varepsilon_{c0} = \frac{1}{E_c}[\sigma_0 \cdot \varphi(t,t_0) + \Delta\sigma(t)\cdot[1+\rho\cdot\varphi(t,t_0)]] + \varepsilon_{cs}(t) \tag{2.20}$$

Relaxation occurs when the distortion is kept constant and is therefore $\varepsilon_c(t,t_0) - \varepsilon_{c0} = 0$. This gives the following expression for the change in stress $\Delta\sigma(t)$:

$$\Delta\sigma(t) = \frac{-\sigma_0 \cdot \varphi(t,t_0) - \varepsilon_{cs}(t)\cdot E_c}{1+\rho\cdot\varphi(t,t_0)} \tag{2.21}$$

With the use of $\sigma = E \cdot \varepsilon \cdot r$, were r is the degree of restraint, the following equation can be derived:

$$\sigma(t) = r\cdot(\sigma_0 + \Delta\sigma(t)) = r\cdot\sigma_0\cdot\left[1 - \frac{\varphi(t,t_0) + \varepsilon_{cs}(t)\cdot E_c/\sigma_0}{1+\rho\cdot\varphi(t,t_0)}\right] \tag{2.22}$$

With this equation, the total stress at a given time can be calculated, including elastic deformation, shrinkage, creep and relaxation.

Relaxation for temperature-induced deformations
The stresses for the temperature-induced deformations will also be partially reduce due to relaxation. If Trost approach is used, then the course of the stresses can be approximated by the following equation (assuming $\varepsilon_t = \sigma_0/(E_c \cdot r)$):

$$\sigma_t(t) = E_c \cdot \varepsilon_t(t) \cdot r \cdot \left[1 - \frac{\varphi(t,t_0)}{1 + \rho \cdot \varphi(t,t_0)}\right] \tag{2.23}$$

2.1.7. Relaxation and creep according to the Eurocode

The Dutch National Annex of EN1992-1-1 [12] provides a factor to take into account the combination of creep and relaxation. For elastically calculated force distributions due to settlement of supports and deformations by shrinkage and temperature changes, the stresses may be multiplied by the following factor:

$$k_\phi = \frac{1 - e^{-\varphi(t,t_0)}}{\varphi(t,t_0)} \tag{2.24}$$

Multiplying the stresses with this factor, is an relatively easy and a more conservative approach than the one of Trost.

2.1.8. Degree of restraint

The degree of restraint is a parameter that gives the ratio between the part of the restrained deformation that causes stresses in the cross-section and the total deformation. A degree of restraint of 1.0 means that all deformation is prevented and stresses are induced. A degree of restraint of 0 means that the structure is not restrained and can expand and contract freely. The degree of restraint can be determined in a number of ways. In this thesis the following methods are investigated and described; Eurocode (EN1992-3 Annex L), CIRIA C766 and the finite element method. These will be explained in the following paragraphs.

Eurocode
Annex L of EN1992-3 [13] can be used to determine the degree of restraint relatively quickly. This annex contains a figure (Figure L.1 [13]) of a number of construction types for which the degree of restraint is relevant. This figure can be used in combination with Table L.1 [13] to determine the degree of restraint at various points. Figure L.1.a shows that the degree of restraint between the base/floor and a wall is 0.5 at the joint and between 0 and 0.5 at the top, depending on the L/H ratio. However, according to Appendix A5 of CIRIA C766, the Eurocode degree of restraint includes a creep factor of 0.5 [3]. This means that the actual degree of restraint at the joint is fully restrained (1.0), but with the creep factor.

CIRIA C766
Section 4.8 and Appendix A5 of CIRIA C766 [3] covers the estimation of the degree of restraint. A distinction is made between edge restraint, end restraint and intermittent restraint. These different types of restraint can be calculated in different ways. For edge restraint (in the case of a wall poured on a floor/base), CIRIA proposes an equation to calculate the restraint factor at the joint (R_j) depending on the Young's modulus and the surface area of both the old and the new concrete, see Equation 2.25.

$$R_j = \frac{1}{1 + \frac{A_{new}}{A_{old}} \frac{E_{new}}{E_{old}}} \tag{2.25}$$

When it is not clear whether the whole area (A) provides effective restraint, for example when a wall is cast on the edge of a slab, the ratio A_{new}/A_{old} can be taken as equal to the ratio h_{new}/h_{old}. The ratio between old and new concrete is very variable at early ages, because although the Young's modulus of the old concrete does not change significantly, the new Young's modulus develops rapidly within the first 7 days. See also Figure 2.10 which uses Equation 2.25 and assumes the ratio A_{new}/A_{old} to be 1.0.

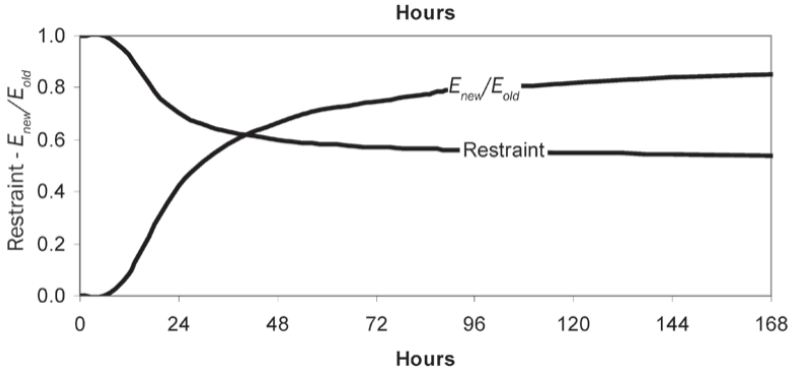

Figure 2.10: The influence on the ratio of E_{new}/E_{old} and the restraint at the joint using Equation 2.25, from [3].

The degree of restraint in Equation 2.25 and Figure 2.10 is around the joint, the CIRIA C766 also gives Equation A5.2 [3] which can be used to calculate the degree of restraint along the height of the wall for a wall cast on a rigid foundation. This equation depends mainly on the L/H ratio. According to CIRIA C766, these restraint factors should be combined with the coefficient $K_c = 0.65$ to account for creep under permanent load. If A_{new}/A_{old} or h_{new}/h_{old} is around 1.0, the degree of restraint including a creep factor is 0.36, which is considerably less than the Eurocode.

Finite element method

Finite element methods (FEM) can also be used to calculate the degree of restraint. This has the advantage that the influence of different parameters on the degree of restraint can be investigated. Another advantage is that all types of structures can be investigated, not just the standard cases described by figures in the Eurocode and CIRIA. According to an article by M. Dijk in Cement [14], when using FEM it is important to assume the stiffness of uncracked concrete. Only then can it be determined what proportion of the restrained deformation will cause stresses in the concrete and therefore cracking [14].

The degree of restraint can be calculated with FEM using the following procedure. First, a temperature load can be applied to the structure, resulting in a deformation due to the linear coefficient of thermal expansion. The resulting normal force can be extracted from the FEM and divided by the total restraint normal force gives the degree of restraint. The total normal force can be calculated as $N = \varepsilon \cdot E \cdot A$. This approach can be used to calculate the degree of restraint at different points.

In the article by M. Dijk [14], a FEM model was created to compare the degree of restraint with, among others, the Eurocode and CIRIA C660. In this article, for the FEM model, taking into account a creep factor of 0.5, a degree of restraint of 0.34 is found. This is close to the value of 0.36 calculated using the CIRIA C766 approach. Both the FEM approach in Cement and that calculated by CIRIA assume that A_{new}/A_{old} or h_{new}/h_{old} is equal to 1.0.

2.1.9. Development of mechanical properties

The development of mechanical properties are important in the hardening phase of concrete. The development of the compressive strength, tensile strength and the Young's modulus is investigated. This is done with the use of both the EN1992-1-1 and the fib Model Code 2010.

Development of the compressive strength

The development of compressive strength can be estimated using equations from EN1992-1-1 Section 3.1.2 (6) [4]. Which states that the mean compressive strength development of concrete depends on the type of cement, temperature and curing conditions. For a mean temperature of $20\,°C$ and hardening according to EN 12390, the mean compressive strength of concrete at different ages $f_{cm}(t)$ can be estimated using the following equations:

$$f_{cm}(t) = \beta_{cc}(t) \cdot f_{cm} \tag{2.26}$$

With:

$$\beta_{cc}(t) = exp\left\{s \cdot \left[1 - \left(\frac{28}{t}\right)^{\frac{1}{2}}\right]\right\} \tag{2.27}$$

In which:

f_{cm} = the mean compressive strength at an age of 28 days
$\beta_{cc}(t)$ = a coefficient which depends on the age of the concrete t
t = the age of the concrete in days
s = a coefficient which depends on the type of cement
$= 0.20$ for cement of strength classes CEM 42,5 R, CEM 52,5 N and CEM 52,5 R
$= 0.25$ for cement of strength classes CEM 32,5 R and CEM 42,5 N
$= 0.38$ for cement of strength classes CEM 32,5 N

The fib Model Code 2010 in Section 5.1.9.1 [5], describes the same equations as used in the Eurocode and shown above, and uses the same coefficients.

Development of the tensile strength
The development of tensile strength is described in the EN1992-1-1, Section 3.1.2 (9) [4]. The Eurocode states that the tensile strength over time is strongly influenced by the curing and drying conditions and the dimensions of the structural members. As a first approximation, the following equations can be used to calculate the mean tensile strength:

$$f_{ctm}(t) = (\beta_{cc}(t))^{\alpha} \cdot f_{ctm} \tag{2.28}$$

In which:

$\beta_{cc}(t)$ = a coefficient which depends on the age of the concrete t calculated with Equation 2.27
α = a parameter equal to 1.0 for $t < 28$ days and $2/3$ for $t \geq 28$ days

To calculate the development for the tensile strength, the fib Model Code 2010 does not give any equations in Section 5.1.9.1 [5]. However, it is stated that; “As a first approximation it may be assumed that for a duration of moist curing $t_s \leq 7$ days and a concrete age $t > 28$ days the development of tensile strength is similar to that of the compressive stress” [5, p. 87]. This can be interpreted to indicate that the same β factor used for compressive stress could also be used for tensile strength development.

Development of the modulus of elasticity
According to the Eurocode EN1992-1-1, Section 3.1.3 (3) [4] the variation of the Young’s modulus with time can be estimated with the following equation:

$$E_{cm}(t) = (f_{cm}(t)/f_{cm})^{0.3} \cdot E_{cm} \tag{2.29}$$

In which:

$f_{cm}(t)$ = the mean compressive strength at an age of t days, calculated with Equation 2.28
f_{cm} = the mean compressive strength at an age of 28 days
E_{cm} = the Young;s modulus at an age of 28 days

The fib Model Code 2010 in Section 5.1.9.3 [5] describes a different equation to that used in the Eurocode, as shown above, and uses the same coefficients.

$$E_{ci}(t) = (\beta_E(t) \cdot E_{ci} \tag{2.30}$$

In which:

$\beta_E(t)$ = $[\beta_{cc}(t)]^{0.5}$ which is a coefficient depending on the age of concrete (t in days)
E_{ci} = the Young’s modulus at an age of 28 days

2.1.10. Influence of cracking on imposed deformation forces

The imposed deformations due to temperature-induced strains and shrinkage strains can cause cracks in the structure. The stiffness of a member is reduced when cracking occurs. The axial forces and moments will therefore decrease in a part of the structure as a result of cracking. To understand this better, the axial force-strain diagram (N-ε) is examined, but the same reasoning applies to the M-κ diagram.

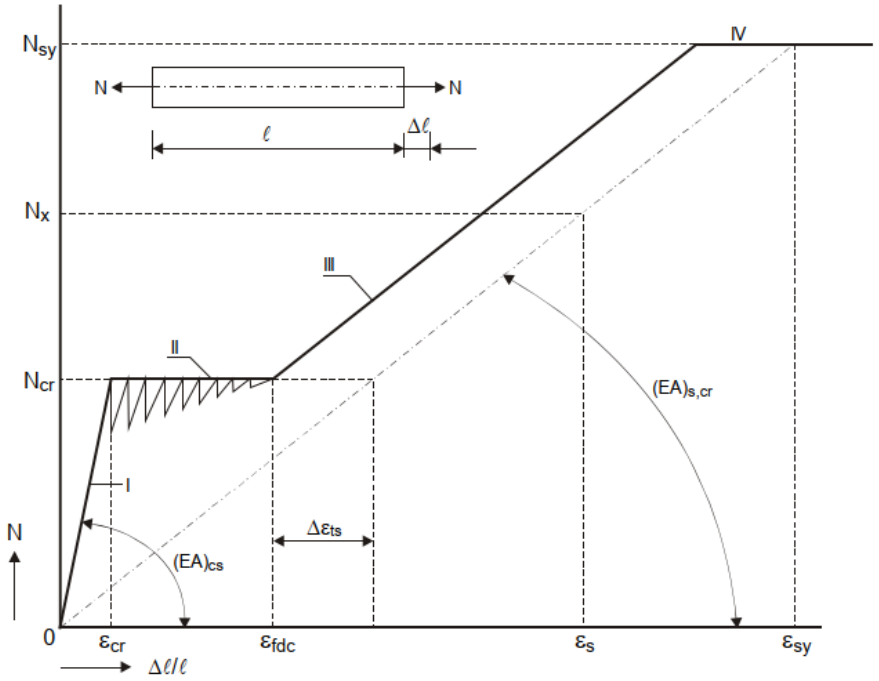

Figure 2.11: Axial force-strain relation of a reinforce concrete tensile member, from [2].

In which the following phases can be distinguished:

I = uncracked phase
II = crack formation phase
III = fully developed crack pattern phase
IV = steel yielding phase

Figure 2.11 shows the force-strain relation for an axially loaded tension member. As the force increases, the stresses and strains in the cross-section increase proportionally. The behaviour is linearly elastic until the cracking force (N_{cr}) is reached and the first crack occurs. Immediately after the formation of a new crack, the stress decreases. As the deformation continues to increase, the stress increases again until the next crack is formed. This results in a typical sawtooth curve in the load-deformation diagram (phase II of Figure 2.11). Cracking continues until the crack pattern is fully developed. Up to this point, there is little increase in force, but a large increase in strain [2].

According to Van Breugel et al. [2], phase II is applicable in practice over a considerable range of imposed deformations. In this phase, the force caused by an imposed deformation ($N_{\Delta\varepsilon} = N_{cr}$) is independent of the magnitude of the imposed strain (which is only true $\varepsilon_{cr} < \Delta\varepsilon < \varepsilon_{fdc}$, where ε_{fdc} is the strain at which the crack pattern is fully developed). So if there is a difference between the assumed strain and the actual strain applied, the resulting force remains the same. However, this is no longer the case when the applied strain is large enough to reach phase III [2].

2.2. Current calculation methods and models

This section will focus on the current calculation methods and models used to calculate/analyse the design stresses for the combination of the hardening process and external loads. To investigate this, a literature review will first be carried out to find the current methods and models proposed in the literature. As these calculation methods and models should be applicable to a case study, specific research is investigated and described, which is validated by carrying out a case study on a project that used hardening of restrained concrete. Two projects will then be investigated and calculated by Wagemaker to find the traditional methods and models used in practice. The first project is a railway underpass on the Kanaalweg in Leiden, where a two-lane road, a cycle path and a footpath pass under a railway line. The second is the widening of the Zeldert viaduct, a 4-span bridge and part of the A1 motorway. An overview is then given of the different calculation methods and models that can be used for the case study in Chapter 4.

2.2.1. Calculation methods and models from literature

Although there is a lot of research on the hardening of (partially) restrained concrete and the occurrence of cracking or not, no representative research was found that included the hardening of restrained concrete over the long term and that included external loads. In particular, none that included a case study to test the theory for a full size structure. Although the fact that it was not found does not mean that no research was conducted, it cannot be included in this thesis to find the calculation method and model of analysis. As mentioned above, research into the hardening of restrained concrete has been conducted for case study projects, and so three of these researches will be discussed briefly. The main focus will be on the calculation method and model used and/or proposed to perform the case study analysis. Also, the conclusion will be briefly mentioned if it was concluded that these calculation methods and models where accurate or not and if it was validated.

Case study in the research of J.R. van Bokhorst's

As part of his Master's thesis [15], J.R. van Bokhorst conducted a case study investigating early cracking in concrete. Specifically, the study investigated how stress relaxation affects the occurrence of early cracking in concrete structures under imposed deformations. The research used a case study of a wall cast on a floor, where a time-dependent finite element analysis approach was used to model the hardening process of the concrete.

The case study included two different models. Firstly, a 2D cross-sectional model was created incorporating thermal boundary conditions to simulate the semi-adiabatic temperature evolution within the wall. Secondly, a separate 2D model was developed using plane stress elements to reflect the stress evolution in the wall over time. The average temperature development from the first model was applied to this second model as a load. However, the research concluded that this approach had certain limitations. In particular, the use of an average temperature function in the model ignored the temperature gradient across the thickness of the section, resulting in reduced accuracy. In addition, this approach did not adequately account for the cooler top surface and its connection to the floor, resulting in large temperature discrepancies between the floor and the wall. Since temperature was applied as a time-dependent load in the analysis, the model could not accurately determine the equivalent maturity age, which affected the prediction of mechanical property development [15].

In summary, while the calculation method and model used in this thesis offers potential for modelling restrained concrete and predicting cracking in partially restrained walls, the inaccuracies introduced by the simplified temperature application limit the overall accuracy and reliability of the results.

Case study in the research of D. Schlicke et al.

The research by D. Schlicke et al. [16] dealt with the structural analysis and crack assessment of confined concrete walls, focusing on a 3D Finite Element Method (FEM) simulation for their case study. The chosen case study was the Møllenberg concrete tunnel project, focusing specifically on the casting of the concrete wall on the floor. In this research, a 3D model was created using solid elements to capture the relevant sections of the wall and floor. The model used symmetry boundary conditions in two directions. The volumetric approach was used because it was found that the associated mechanical system response follows the longitudinal interaction between the hardening wall and the restraining floor slab, as the temperature flow is mainly through the cross-section. To achieve accurate results, the model combined thermal heat analysis and structural analysis, effectively accounting for temperature differences across the height and thickness of the wall. The material model integrated visco-elasticity, with experimental data informing the development of mechanical properties and temperature development.

Ultimately, the research demonstrated how FEM simulations could be used to quantitatively assess restrained stresses and anticipate crack formation. The research not only emphasised the integration of time-discrete material models, but also underlined the importance of a realistic representation of the structure. By carefully interpreting the simulation results, the study effectively evaluated both crack susceptibility and expected crack patterns. The validity of this research and computational approach was demonstrated by its close agreement with field observations [16].

In summery, the calculation method and model employed in this research, which seamlessly merged temperature and structural analysis into a single model using 3D volumetric elements. This research and computational approach has been verified by good agreement with observations on site [16].

Case study in the research of L. Buffo-Lacarriére et al.

An article by L. Buffo-Lacarriére et al. [17] focused on finite element modelling of the concrete hardening process, with the intention of moving from application to prediction of early age cracking in substantial reinforced structures. To validate the proposed model outlined in the research, both a laboratory structure and an in-situ massive structure, a wall of a nuclear power plant, were investigated. The proposed model was based on hydration modelling, followed by a non-linear mechanical representation of the early-stage behaviour of the concrete, including the interplay of creep and damage mechanisms. The case studies were modelled using a 3D model with volumetric 3D elements.

The paper concludes by presenting simulation tools that can assist practitioners in selecting construction methods and concrete compositions to control the risk of cracking. Using the results of a hydration model, the proposed early age mechanical behaviour model analyses the mechanical aspect of any concrete structure subjected to the consequences of hydration (temperature rise, thermal gradients, variation of mechanical properties). The proposed mechanical model, based on the coupling of creep and damage laws, was based on non-linear viscoelastic incremental principles with hydration dependent parameter adjustments. Notably, the research successfully applied this model to validate concrete formulations on actual construction sites and to predict early age cracking within reinforced structures [17].

In summery, the calculation method and model used and prescribed in this article, which incorporates hydration modelling and time-dependent non-linear mechanical analysis within a 3D model using 3D volumetric elements, has demonstrated accuracy in predicting stresses and cracking.

2.2.2. Railway underpass Kanaalweg

ProRail and the municipality of Leiden commissioned the construction of a railway underpass to allow the Leiden-Utrecht railway line to cross the Kanaalweg. The aim of the project was to improve traffic safety and traffic flow. The railway underpass was also a requirement for increasing the frequency of trains between Leiden and Utrecht. The underpass runs parallel to the Rijn-Schie Canal and provides space for a two-lane road, a cycle path and a footpath. In addition to the railway, there will also be a cycle and pedestrian path on the deck. For an overview of the new situation, see Figure 2.12. The project was carried out by the construction company Max Bögel, and the engineering company Wagemaker was contracted to calculate the underpass. Before describing the calculation method and model used in this project, the geometry, phasing of the structure and the assumptions used in the calculation will be discussed, as this is the basis on which the calculation method and model were selected.

Figure 2.12: Overview of the new situation of the Kanaalweg, from [18].

Geometry of the structure

The entire underpass consists of several open sections and one closed section and has a total length of approximately 180 metres. For this project, the focus is on the closed section where the deck is located. The top view of the deck is shown in Figure 2.13. The cross-section and the longitudinal section are shown in Figures 2.14 and 2.15 respectively. All other sections and details can be found in Wagemaker's original calculation [19] and drawing [20]. As this study focuses on hardening stresses due to restrained deformations, the calculation method and model for this structure will focus on the wall, which is monolithically connected between the floor and the deck.

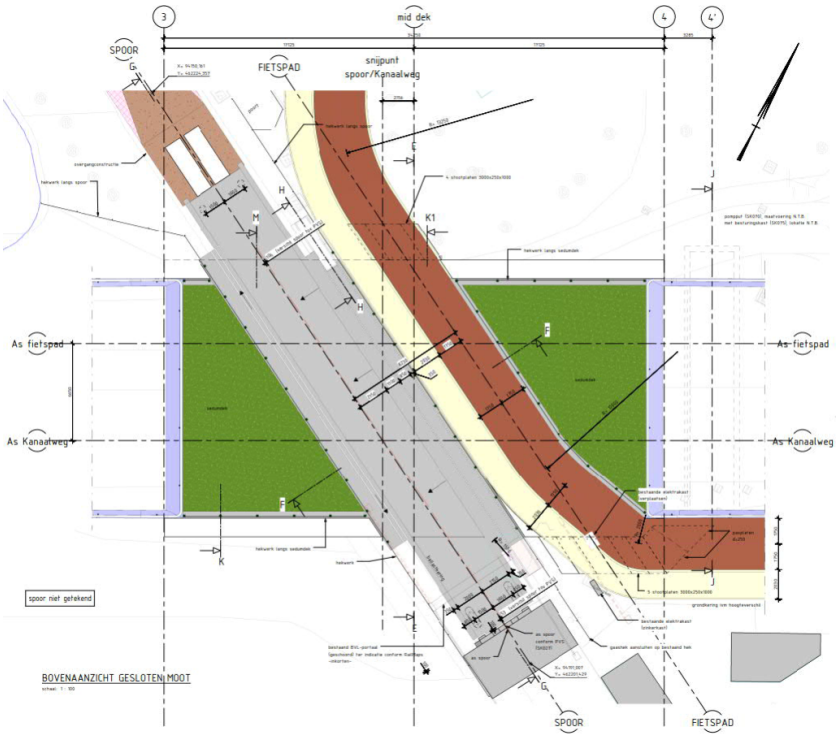

Figure 2.13: Top view of the project Kanaalweg, from [20].

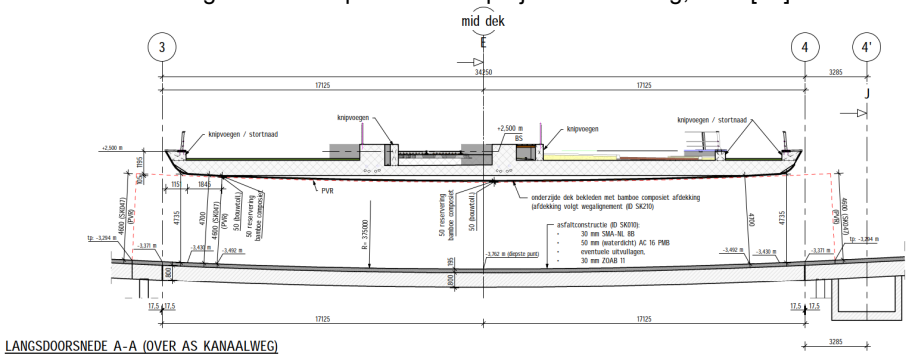

Figure 2.14: Longitudinal section on the axis of the Kanaalweg, from [20].

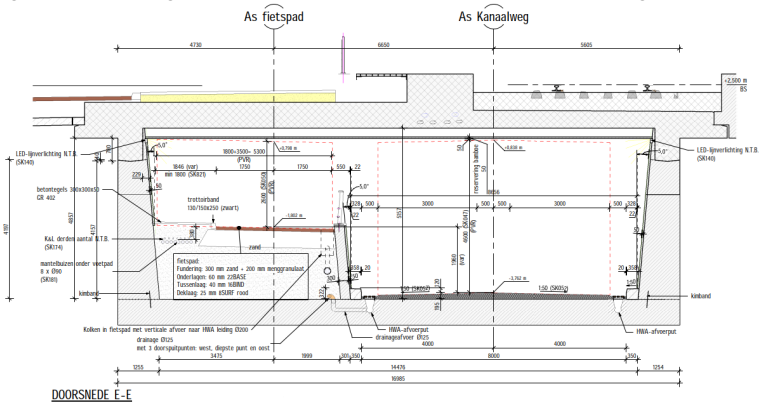

Figure 2.15: Cross-section of the midsection perpendicular to the axis of the Kanaalweg, from [20].

Phasing of the structure
Because the underpass is being constructed under an important railway line, disruption to the trains must be kept to a minimum. Therefore, phasing was important for this project. The construction of the closed section of the underpass consist of the following global phases:

- Construction of the deck at a site close to the final location.
- Sheet piling is installed during the first decommissioning.
- Driving the bridge deck into place and onto the sheet piling during the second decommissioning.
- Excavation of the soil between the sheet piles and under the deck.
- Pouring the floor on top of the soil.
- Pouring the wall between the floor and the deck.
- Removing the connection between the sheet piles and the deck
- Completion and opening of the underpass.

It should be noted that although this phase is used in the construction of the underpass, the original calculation was based on an additional phase with pouring of a pouring strip. So, originally it was assumed that the wall would be poured on the floor and then a pouring strip would be poured between the wall and the deck. This was changed after the calculation was complete, but it was checked that this did not affect the results to change the calculation as this level of detail was not included in the calculation.

Used calculation method and model
The design stresses/forces for this project were calculated only at ‘t=0’ and ‘t=∞’, so it was assumed that by calculating only these two time steps, the governing situation was calculated. This was also based on the assumption that the loads specified in the standards have a positive trend and only need to be satisfied at the end of the service life.

The calculation at ‘t=0’ includes only the temperature induced forces, as no shrinkage has occurred and no external loads are applied. Using assumptions for the amount of cement, the thickness of the wall and the initial and ambient temperatures, an estimate is made for the peak temperature in the wall. This is used to calculate the hardening stress/forces by ‘hand’ using an Excel spreadsheet to calculate the temperature difference and corresponding thermal strain. The thermal strain was found to be at the cracking stage and therefore the concrete was assumed to be cracked. To calculate the design stresses/forces, the cracking normal force (see also Section 2.1.10) was calculated based on assumptions about the time step and mechanical properties at the moment of cracking.

The calculation at ‘t=∞’ includes both the hardening forces and the external loads. However, it is assumed that the temperature stresses/forces are reduced by 50% of those due to creep. The stresses/forces due to external loads were calculated using a linear 3D calculation model using 2D plane shell elements. This model includes all the different loads and load combinations of the structure. Shrinkage was not included in this calculation model as this model was not time dependent, including shrinkage at ‘t=∞’ would have resulted in uniform shrinkage. This would have no significant effect. By adding the resulting hardening/temperature forces to the results of the external loads from the calculation model, the design stress/forces within the wall could be calculated.

To summarise, the method used for this calculation was a combination of a ‘manual’ calculation for the curing phase and a calculation model for the external loads. The model used was a linear 3D calculation model using 2D plane shell elements.

2.2.3. Widening of the Zeldert viaduct

Due to accessibility problems on the main road network in the Utrecht region, the Dutch government had the ambition to upgrade the A1 and A27 to at least 2x4 lanes. This was to counteract the expected increase due to general traffic growth and the development of urban areas in the region. This means that several bridges would have to be widened to accommodate the additional lanes. One of the projects was the Zeldert viaduct. This is a viaduct that forms part of the A1 motorway and is located near the Bunschoten-Spakenburg junction. It consists of two bridge decks, one built in 1963 and widened in 1970, the other completely rebuilt in 1970. Both have four spans of 10, 12, 12 and 10 m respectively. The bridge crosses the Bunschoterstraat, a 2x1 road, and the N199, a 2x2 road. For an overview of the location of the new situation, see Figure 2.16. The overall project of widening the A27/A1 was carried out by a special purpose company, 3Angle B.V., consisting of Fluor, 3i Infrastructure and Heijmans Capital. Wagemaker was contracted to work out the structural design and to calculate the widening of this viaduct. Before describing the calculation method and model used used in this project, the geometry, phasing of the structure and the assumptions used in the calculation will be discussed. This is the basis on which the calculation method and model were selected.

Figure 2.16: Overview of the new situation of the Zeldert viaduct, from [18].

Geometry of the structure

The widening of the Zeldert viaduct consists of the widening of the southern and northern bridges. The top view, longitudial section and the cross-section are shown in Figures 2.17 - 2.19. All other sections and details can be found in Wagemaker's original calculation [21] and drawings [22], [23].

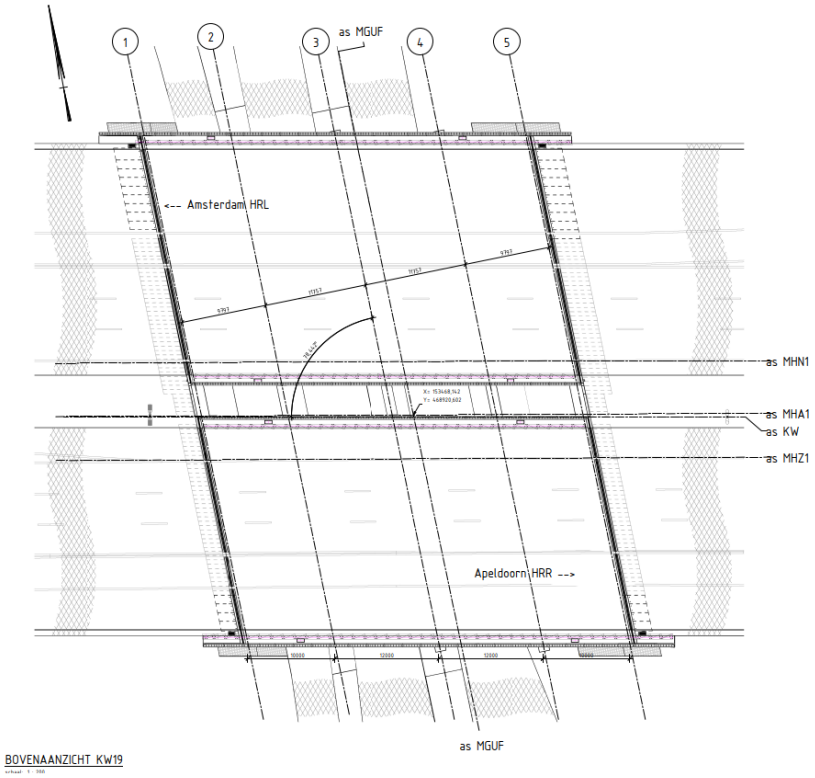

Figure 2.17: Top view of the project viaduct Zeldert, from [22].

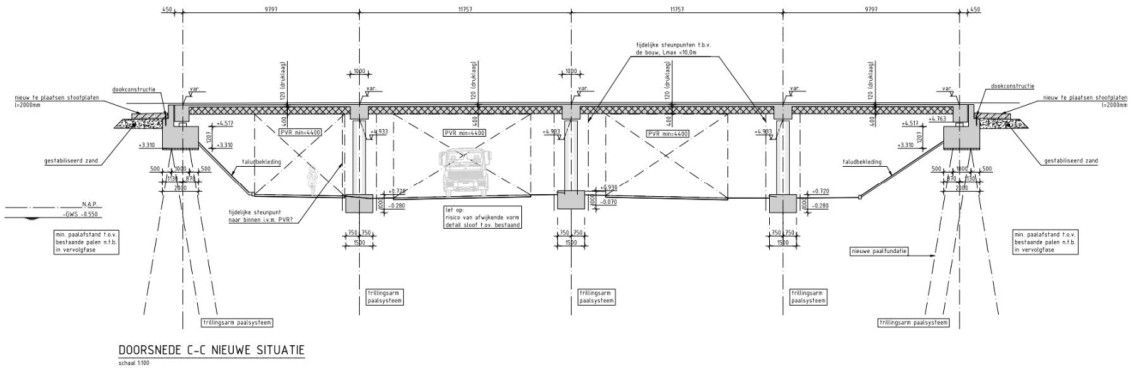

Figure 2.18: Longitudinal section of the Zeldert viaduct perpendicular on the axis of the N-199, from [21].

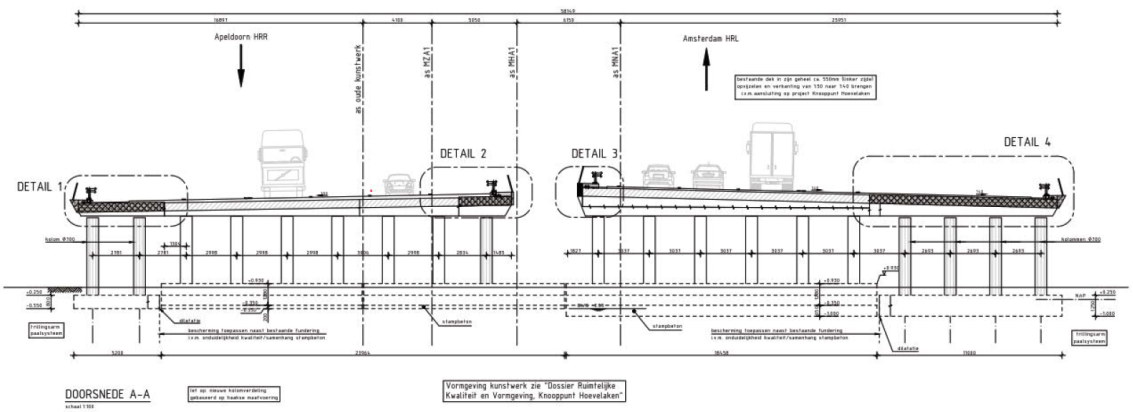

Figure 2.19: Cross-section of the Zeldert viaduct perpendicular on the axis of the A1, from [21].

The south bridge will be widened on both sides, as shown in Figure 2.19. The north bridge will be widened mainly on the outside, the inside will only receive a new edge beam. The three pour strips are all quite similar, so to determine the calculation method and model it was decided to focus on only one of them. This is the outer edge of the southern bridge (Detail 1), shown in Figure 2.20.

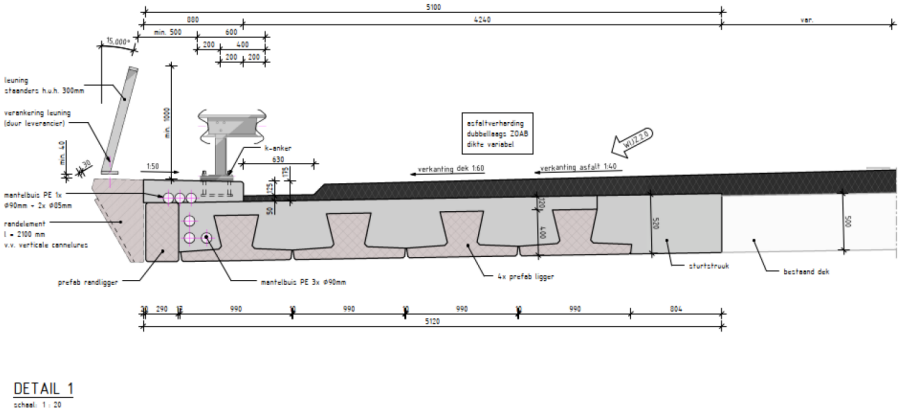

Figure 2.20: Detail 1 of Figure 2.19 of the Zeldert viaduct, from [23].

Phasing of the structure

The construction of the Zeldert viaduct consists of the following global phases:

- Construction of temporary supports for excavation
- Excavation of side embankments and alongside intermediate supports
- Creation of new sections of abutments and intermediate supports
- Place temporary temporary supports for prefabricated beams
- Placing prefabricated beams on temporary support
- Pouring cross girders and spaces between precast girders
- Removal of temporary intermediate supports
- Connect new parts of substructure to existing substructure excluding pouring strips
- Connection of new deck sections to existing ones using poured strips
- Completion of deck construction and groundwork

Used calculation method and model

The design stresses/forces for this project were calculated only at ‘t=0’ and ‘t=∞’, so it was assumed that by calculating only these two time steps, the governing situation was calculated. Where ‘t=0’ is the time just after the hardening of the pouring strip and ‘t=∞’ is at the end of the service life.

For the calculation at ‘t=0’, a hand calculation is made which includes only the temperature induced forces and the autogenous shrinkage, but does not include the drying shrinkage as it is assumed that this has not yet occurred and no external loads are applied. A rough estimation/assumption is made for the temperature difference and hence the thermal strain. It is assumed that cracking will occur and that the concrete is at the crack formation stage. Based on this, the cracking normal force is calculated (see also Section 2.1.10). This has been calculated using assumptions about the time step and mechanical properties at the moment of cracking.

The calculation at 't=∞' includes both the hardening forces and the external loads. However, it is assumed that the cracking force calculated for 't=0' is multiplied by a creep factor based on the Eurocode (Equation 2.24) of 0.632 (assuming a creep factor of 1.0). The stresses/forces due to external loads have been calculated using a linear 3D calculation model with 2D plane elements. Thermal strains and both autogenous and drying shrinkage strains are introduced into the calculation model by applying an equivalent temperature load. Finally, as the strain did not reach the fully developed crack pattern phase, the N_{crack}, reduced by a factor to account for creep, combined with the design moment, was taken as the design loads to calculate the reinforcement. A linear calculation model was used to calculate the development of design stress/forces within the wall.

In summary, the method used for this calculation was a combination of a hand calculation for the hardening phase and a calculation model for the external loads to which the results of the hand calculation were added. The model used was a linear 3D calculation model using 2D plane shell elements.

2.2.4. Overview of possible calculation methods and models

Several methods of calculating the design stresses in a structure have been identified in the literature and in the case projects studied. Both for the hardening stresses due to restrained deformations and for the stresses due to external loads. In this section, an overview and explanation of the different calculation methods is given first. An overview and explanation of the different types of calculation models is then given. These calculation models consist of different types of elements within 2D or 3D models. The information about different calculation methods and calculation models will be used in a Chapter 4 to select the most beneficial calculation method and model to use in the case study.

Different calculation methods

Based on the literature and the case projects studied, three different methods were found to calculate the combination of forces and stresses for the hardening restraint concrete with the external loads added later. The first two are a combination of the separate calculation for the hardening phase with a calculation model for the external load and the third is a combination of both within one calculation model. In practice, due to the complexity of case projects and the number of loads and load cases, the external load will always be calculated in a calculation program. To combine the forces and stresses from the hardening phase with the external loads, three different methods are explained in more detail in this subsection:

- Combination of a 'manual' calculation for the hardening phase with a calculation model for the external loads
- Combination of a calculation model for the hardening phase with a calculation model for the external loads
- A combined calculation model for both the hardening phase and the external loads

The first method is a combination of a 'manual' calculation and a calculation model using calculation software to calculate the external loads and load combinations. This 'manual' calculation is also used in both projects investigated to calculate the expected strain for a given time step using a simple calculation. The calculated strain is then added to the calculation model as a temperature load, or the stress/forces are manually added to the results from the calculation model. The calculation model is traditionally calculated for the expected governing times, namely at the first moment of loading (referred to as 't=0') and at the end of the expected service life (referred to as 't=∞'). For example, 't=0' includes autogenous shrinkage and temperature expansion, and 't=∞' includes dry shrinkage, but everything is multiplied by a reduction factor to account for creep/relaxation. Consequently, the design stresses for the other times are not known, although 't=0' and 't=∞' are the governing situations for external loads, this may not be the case for hardening stresses. Although 'manual' calculation can be very time consuming, it does not normally take into account temperature development, equivalent age and development of mechanical properties. Instead, a simple temperature difference between peak and ambient temperature is assumed/calculated and simply multiplied by a Young's modulus at a given time. Although cooling of the concrete is a gradual process, an important assumption is made in the selection of the specific time for the Young's modulus. The peak temperature is also an important parameter which is quite complicated to calculate manually as it depends on the thermal conductivity, the (time-dependent) thermal boundary conditions, the adiabatic temperature gradient and the amount and composition of the cement. It is also necessary to estimate the degree of restraint, which for standard cases can be derived from a Eurocode table or calculated using CIRIA. For more difficult cases, however, a finite element model is required.

The second method is a combination of two calculation models, where the first model is a time-dependent calculation to calculate the forces and stresses of the hardening restraint concrete. And the second, which is the same as the first, is a calculation model to calculate the forces and stresses from the external loads and load combinations. In this way, different elements or models can be selected for both the time-dependent and external load models. This can save a lot of calculation time. However, it also has a disadvantage: although a time-dependent model is created, only the forces and stresses of a particular time step can be used in the external load model. Using a time-dependent calculation model for the hardening process has the great advantage that the temperature development can be calculated accurately if all time-dependent thermal properties are taken into account. This allows the restrained deformation, consisting of thermal expansion, shrinkage and creep/relaxation, to be accurately analysed, taking into account the development of the mechanical properties. This also allows the governing time step to be found, although it is not trivial that this is the governing time step for the combination with the external load. This is because even the external load is to some extent time-dependent due to prestressing losses, fatigue and the evolution of mechanical properties. Another advantage is that the degree of restraint is automatically included in the calculation model and does not need to be calculated. The disadvantage of this method is that assumptions have to be made when combining the results of the two models. If the results are calculated separately, the forces and stresses from both models must be summed, which means that the deformation, equivalent age and therefore mechanical properties calculated in the hardening model are not included in the external loading model. And if the resulting strain or temperature load from the hardening model is added to the external load model, only a constant value can be applied to the elements instead of the gradient load based on the other model.

The third and final method is a calculation model in which both the time-dependent hardening process and all external loads and load combinations are present. The advantage of this method is that everything is in the same model, so no information is lost between models. The temperature and equivalent age are present in the model so that the correct mechanical properties are modelled when the external loads are added. It is also easier to create one model rather than two separate models, especially if changes are made. The disadvantage is that the model becomes quite complex and the calculation time increases significantly when many loads and load combinations have to be calculated for different time steps. Also, although the dead loads are set to be present from the time of application until the end, the variation load still needs to be applied to the system at a specific time. Therefore, a specific critical time has to be found to test the structure. This is because the computation time will be extreme if all the different variation loads have to be tested at each time step.

Different calculation models

There are different types of computational models where different types of elements are used within a 2D or 3D model. Based on the research of the case studies and DIANA FEA, five different types have been investigated and explained that may be relevant to the modelling of the case studies. These five different types of calculation models are explained in more detail in this subsection:

- 2D plane strain elements within a 2D cross-section model
- 2D plane stress elements within a 2D model
- 2D plate bending elements within a 2D model
- 2D flat shell elements within a 3D model
- 3D solid elements within a 3D model

The first type of calculation model is a 2D cross-section model using regular 2D plane strain elements. This element can be triangular or quadrangular and can have linear interpolation with 3 or 4 nodes, or quadratic interpolation with 6 or 8 nodes. 2D plane strain elements have a 2D plane stress field and also a 2D displacement field. By default, these elements have unit thickness and the strain components perpendicular to the element plane are zero ($\varepsilon_{zz} = 0$). This type of element can only be loaded in the plane of the element. This type of element can be used in combination with a 2D cross-section model, for example, to analyse the cross-section of a long structure where the influence of the sides of the structure and the forces and stresses in the other direction can be neglected. Or it can be used as input to another analysis model to calculate the resulting forces and stresses in the other direction.

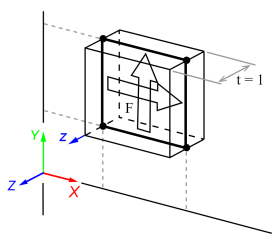

Figure 2.21: Plane strain element characteristics, from [24].

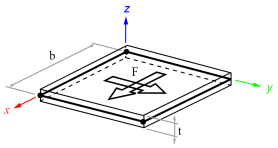

Figure 2.22: Plane stress element characteristics, from [24].

The second type of calculation model is a 2D model using regular 2D plane stress elements. This element has the same linear and quadratic interpolation nodes for the triangular and quadrangular elements and this element also has the same 2D plane stress field and also a 2D displacement field as the previous one. However, this element requires the thickness (t) to be small relative to the dimensions (b) in the plane of the element instead of a unit thickness. Plane stress elements are characterised by the fact that the stress components perpendicular to the plane are zero ($\sigma_{zz} = 0$). This element can only be loaded in the plane of the element. Therefore, this type of element can only be used if there is no bending outside the plane of the structure. This type of element can be used in combination with a 2D model, for example, to analyse walls and other 2D parts that do not experience out-of-plane forces.

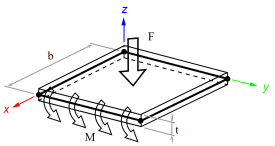

Figure 2.23: Plate bending element characteristics, from [24].

The third type of calculation model is a 2D model using 2D plate bending elements. This element can be triangular or quadrangular and has linear interpolation with 3 or 4 nodes, or quadratic interpolation with 6 or 8 nodes. 2D plate bending elements have a 2D moment-curvature stress field and a 1D displacement field. The thickness (t) should be small relative to the dimensions (b) in the plane of the element. Plate bending elements are characterised by the fact that the direct stress component perpendicular to the plane is zero ($\sigma_{zz} = 0$). The normals of the element plate also remain straight after deformation, but by definition they need not be perpendicular to the element plane. A force load (F) on this element is only possible perpendicular to the element plane, a moment load (M) must act around an axis in the element plane. This type of element can be used in combination with a 2D model to analyse, for example, floors and other 2D parts that do not experience forces in the plane.

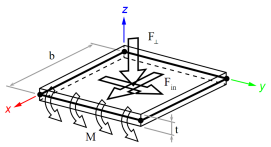

Figure 2.24: Flat shell element characteristics, from [24].

The fourth type of calculation model is a 3D model using regular 2D plane shell elements. These elements are basically a combination of planar tension elements and plate bending elements and have the same number of nodes. Although they can be used in a 3D model, the coordinates of the element must be in a plane. 2D flat shell elements have a 3D stress field and a 3D displacement field. The thickness (t) should be small relative to the dimensions (b) in the plane of the element. The direct stress component perpendicular to the plane is zero ($\sigma_{zz} = 0$) for this type of element. Flat elements are characterised by the fact that the normals of the element plane remain straight after deformation, but by definition they need not be perpendicular to the element plane. Also, the displacement perpendicular to the plane does not vary in the thickness direction. Force loads (F) can act on this element in any direction and moment loads (M) must act in the plane of the element. This type of element combined with a 3D model can be used, for example, to analyse tunnels and other 2D structural elements within a 3D model. There are also 3D curved shell elements that are closely related to this element, which can be used for shell roofs and storage tanks for example, but these will not be discussed further as the elements are not considered relevant to the case study.

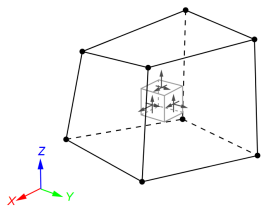

Figure 2.25: Solid element characteristics, from [24].

The fifth and final type of calculation model considered is a 3D model using solid elements. This element can have different solid shapes; a tetrahedron, a pyramid, a wedge and a brick. Linear, quadratic and cubic interpolation schemes can be used, but cubic interpolation will not be discussed further due to its enormous computational time. 3D solid elements have a 3D stress field and a 3D displacement field. Solid elements are general purpose elements and can be loaded arbitrarily in all dimensions. The disadvantage of these elements is that they tend to produce large systems of equations, so they are usually only used when other elements are unsuitable or would produce inaccurate analysis results. This type of element combined with a 3D model can be used, for example, to analyse large structures such as concrete foundations, ground masses and thick walls and floors [24].

2.3. Validation experiment from literature

In this section, an experiment is selected to validate all the hardening processes and the development of the hardening stresses. The experiment is first described, then the experimental results are shown and finally the material properties are given. But first a validation experiment is selected.

The Temperature-Stress Testing Machine (TSTM) experiment was found to be a suitable and reliable experiment for this study, which focused on the hardening and stress development of (partially) restrained concrete. This experiment can measure the stress of (partially) restrained hardening concrete based on a specific temperature history that can be applied. Specifically, the TSTM experiments performed in the research of Anja B. Estensen Klausen, Associate Professor at NTNU University in Trondheim, Norway, are used. The results of her experiments are described in her doctoral thesis [25] and two articles [26] and [27], and provide a good basis for the validation of the hardening processes in the next chapter.

2.3.1. Description of the experiment setup

The TSTM system used in the experiments at the Norwegian University of Science and Technology (NTNU) consists of a dilation rig and a TSTM, see Figure 2.26. Both are connected to a temperature control system that allows an isothermal or realistic temperature gradient to be prescribed for the specimens. While the TSTM system is running, the dilation rig measures the free deformation due to temperature induced deformations and autogenous shrinkage of a sealed specimen. The TSTM experiment is designed to measure the stress evolution of a closed concrete specimen during the hardening phase of the concrete at a selected degree of restraint. The degree of restraint can be varied between 0 (no restraint) and 1.0 (full restraint) [25]. In the following subsections the specific components such as the dilation rig, the TSTM and the temperature control system are explained in more detail.

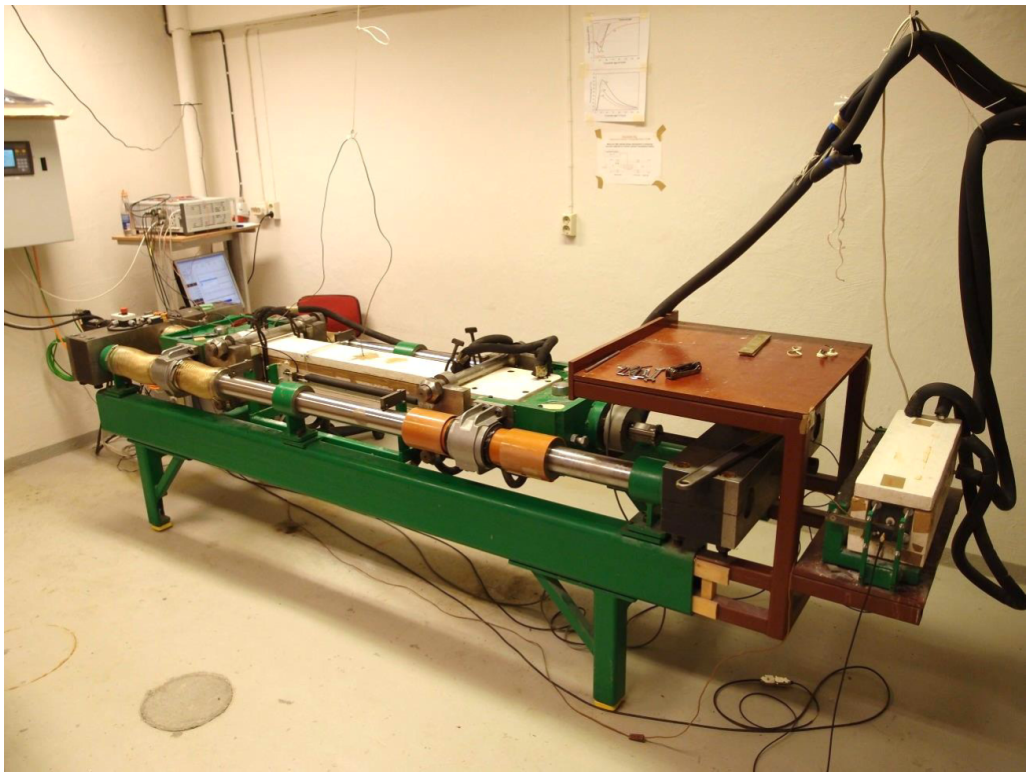

Figure 2.26: The TSTM system at NTNU with the TSTM (left) and the dilation rig (right), from [25].

The dilation rig

According to Klausen's thesis [25], the dilation system used at NTNU consists of a formwork into which a $100{\times}100{\times}460$ mm test piece of concrete is cast. The formwork consists of 5 mm thick copper plates surrounded by 5 mm copper pipes with circulating water connected to a temperature control system. The formwork and copper tubes are covered with insulation, see Figure 2.27. Movable end plates of polystyrene and steel respectively are placed at each short end of the formwork. Before starting the length measurements, the steel support is loosened and moved to allow the end plates, and thus the concrete specimen, to move freely during the test.

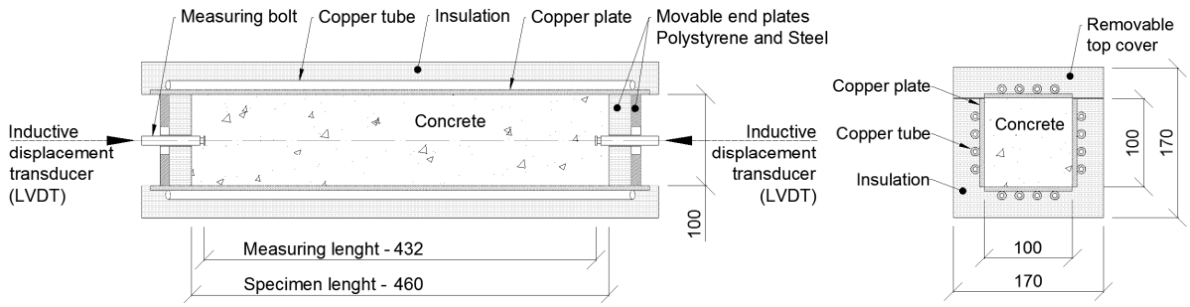

(a) Cross-section (b) Top view

Figure 2.27: Schematic representation of the dilation rig, from [25].

As shown in Figure 2.27, two measuring bolts are poured into the short ends of the concrete test piece. They are embedded in the concrete, have a diameter of 8 mm and are provided with notches to ensure anchorage. A linear variable displacement transducer (LVDT) is mounted on each short end. The two LVDTs measure the change in length of the concrete specimen by measuring the movement of the embedded measuring bolts. In an experiment, the temperature is measured immediately after pouring and the change in length is triggered after about 2 hours, according to Klausen's thesis [25].

The temperature-stress testing machine (TSTM)

The TSTM experiment performed in Klausen's research consists of an outer steel frame on which two movable crossheads and a movable midsection rest. The crossheads and midsection form a formwork into which concrete specimens are poured. The formwork is constructed in the same way as the formwork for the dilation rig and is connected to the same temperature control system. As shown in Figure 2.28, the TSTM specimen has the shape of a 'dog bone'. The dimension of the cross-section in the middle 700 mm, where the length is measured, is $88{\times}100$ mm, where 88 is the width and 100 is the height of the specimen. After the length measured during the experiment, the width of the cross-section increases linearly on both sides to 100 mm at the crossheads. Inside the crossheads the width is further increased to 225 mm to keep the concrete specimen restrained [25].

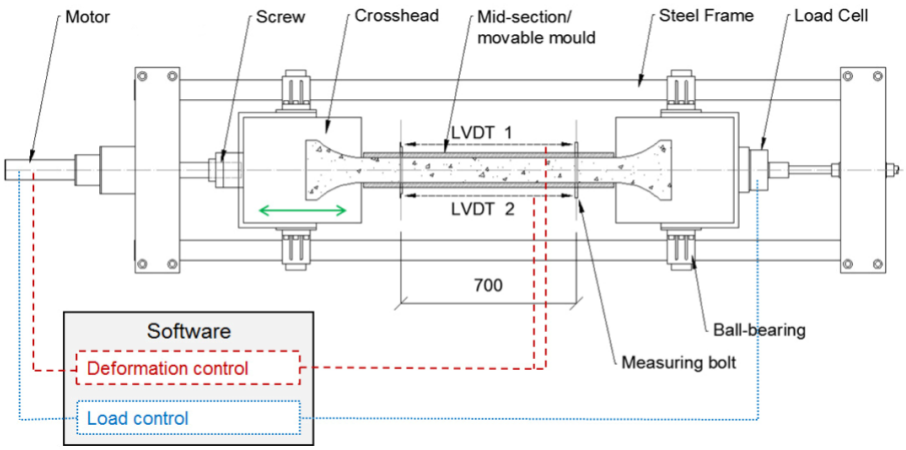

Figure 2.28: Schematic representation of the TSTM experiment, from [25].

Before the concrete specimen is poured, two measuring bolts are installed in the midsection of the TSTM to define the measuring length, see Figure 2.28. The deformation, and therefore the change in length between the pins, is measured by two independent inductive displacement transducers (LVDTs), one on each side of the specimen/mould. When conducting a experiment, the temperature is measured immediately after pouring and the TSTM feedback system is usually started 5-8 hours after mixing [25].

The temperature-control system

Both the dilatation rig and the TSTM are connected to a temperature control system to regulate the temperature of the concrete specimens. Insulated plastic pipes connect this system to the specimens via external copper pipes on the copper formwork panels. Using the Julabo FP45 cooling/heating controller from Klausen's doctoral thesis, an isothermal or realistic temperature profile can be applied to the concrete specimens. It's important to note that due to heat loss to the environment, the programmed temperature does not exactly match the temperature at the core of the concrete specimen in the TSTM

system. To overcome this, the programmed temperature is incrementally increased until it matches the desired temperature within the concrete specimen [25].

The TSTM experiment to be investigated has been conducted under semi-adiabatic conditions so that the concrete specimens are exposed to a realistic temperature history during the tests. This realistic temperature history is based on a model made from the measured adiabatic temperature development of the different types of cement compositions and a hardening wall construction. The wall cross-section on which the realistic temperature history is based is shown in Figure 2.29, where the areas from which the average temperature is selected are shown in grey. The temperature gradients have been calculated in the thesis using the CrackTeSt COIN program for each cement composition for Norwegian summer and winter conditions [25]. This research will only focus on experiments with summer conditions, as these conditions are closer to the average temperature in the Netherlands.

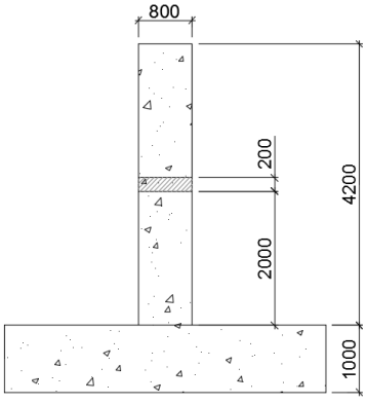

Figure 2.29: Schematic structure used for temperature calculations [mm], from [25].

2.3.2. Experimental results

The main purpose of the verification model is to compare the stress development of models that include all hardening processes with Klausen's experiments. Although many TSTM experiments are performed with different cement compositions in the thesis and articles, it was decided to compare three different cement compositions. The first is a mixture of Portland cement only, the second is a mixture of Portland cement and 33% fly ash, and the last is a mixture of Portland cement and 68% GGBS. The first two are described in the doctoral thesis [25] and the article in Advances in Materials Science and Engineering [26], the last in an article in Structural Concrete [27]. In addition to the comparison of stress development, the development of temperature and tensile stress (as the development of mechanical properties) are also compared. The results of the TSTM experimentals are shown in Figure 2.30. The development of other properties such as Young's modulus and compressive strength can be found in Klausen's publications [25]–[27].

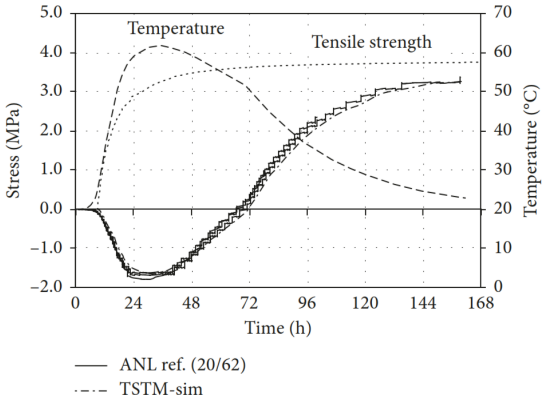

(a) Portland concrete mix

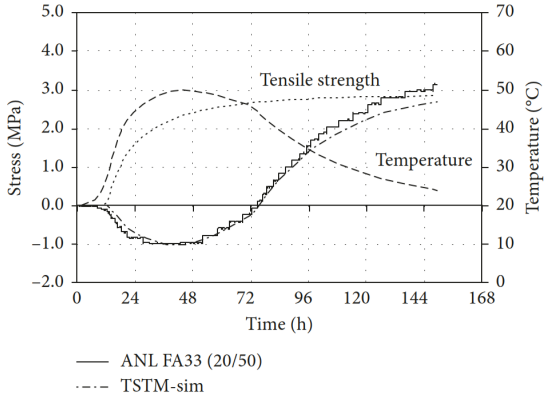

(b) Portland - Fly Ash concrete mix

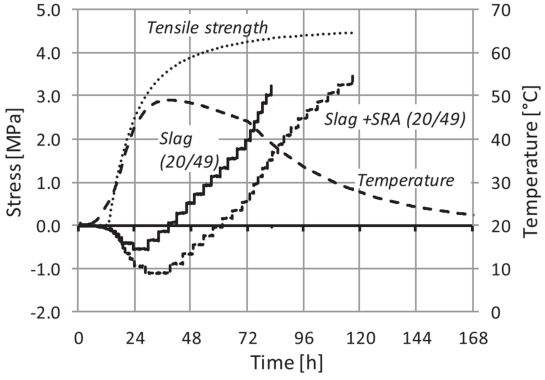

(c) Portland - GGBS concrete mix

Figure 2.30: The temperature, tensile strength and stress development plotted against time for three different cement compositions, subfigure (a) and (b) from [26] and (c) from [27].

2.3.3. Material properties/specifications

Although different types of concrete compositions were tested in Anja Klausen's study, three different types were chosen for this study. These are called 'ANL ref.', 'ANL FA33' and 'Slag' by Klausen, where CEM I, CEM II/B-V and CEM III/B are the specified terms according to Table 1 of EN 197-1 [28]. Therefore, these terms will also be used in this study. CEM I consists mainly of clinker, CEM II/B-V is mainly a combination of clinker and 33% fly ash and CEM III/B is mainly a combination of clinker and 68% ground granulated blast furnace slag. This section describes the specification of the concrete mixes, all material properties, the development of the adiabatic temperature and the mechanical properties. Klausen publications [25]–[27] were used for the material properties/specifications of all three concrete mixes.

Concrete mixture designs and properties

The three specific concrete mixes presented in Klausen's publications [25]–[27] are shown in Table 2.2. As explained earlier, the main difference between the mixes is the cement composition, the first being a Portland cement, the second a Portland fly ash cement and the last a blast furnace cement. All concrete mixes also contain 5% silica fume and all concrete mixes have the same w/c ratio of 0.40.

Table 2.2: Overview of the concrete mixture designs.

	CEM I ('ANL ref.')	CEM II/B-V ('ANL FA33')	CEM III/B ('Slag')
Cement content [kg/m^3]	372.3	355.4	362.4
Fly Ash [kg/m^3]	0	118.3	0
GGBS [kg/m^3]	0	0	246.4
Silica fume [kg/m^3]	18.6	17.6	18.2
Free water [kg/m^3]	163.8	156.2	160.7
Sand 0-8mm [kg/m^3]	1216.3	1216.3	1216.3
Gravel 8-16mm [kg/m^3]	614.1	614.1	614.1
Plasticiser [kg/m^3]	2.05	1.56	2.0
Density [kg/m^3]	2415	2380	2410

Development op mechanical properties

In Klausen's study, the development of mechanical properties is described by a formula for all mechanical properties. This uses the maturation principle for compressive strength, tensile strength and E-modulus and is modelled by the following equation:

$$X(t_e) = X(28) \cdot \left\{ e^{s \cdot \left(1 - \sqrt{\frac{672 - t_0}{t_e - t_0}}\right)} \right\}^n \tag{2.31}$$

Where $X(t_e)$ is the property as a function of time t_e and $X(30)$ is the property at 28 days. s and n are curve fitting parameters determined by Klausen based on different types of experiments and t_0 is the start time of stress development. Table 2.3 contains all the parameters needed to fill in the equation and find the development of the mechanical properties. The properties of CEM I and CEM II/B-V concrete were found in Klausen's thesis [25] and the properties of CEM III/B were provided by Klausen.

Table 2.3: Overview of the parameters from the development of mechanical properties.

	t_0 [hour]	s	n_c	n_t	n_E	f_{c28} [MPa]	f_{t28} [MPa]	E_{28} [GPa]
CEM I	8.8	0.200	1.000	0.484	0.348	80.3	3.86	32.80
CEM II/B-V	12.0	0.356	1.000	0.486	0.252	53.6	3.05	30.50
CEM III/B	13.0	0.347	1.000	0.443	0.377	73.80	4.80	34.00

Thermal properties and the adiabatic temperature development

A constant coefficient of thermal expansion (CTE) was measured and assumed in the Klausen studies. A coefficient of thermal expansion of $9.0 \cdot 10^{-6}$/°C was used for CEM I concrete, $9.2 \cdot 10^{-6}$/°C for CEM II/B-V and $10.1 \cdot 10^{-6}$/°C for CEM III/B. The values for CEM I and CEM II/B-V were obtained from the PhD thesis [25], the values for CEM III/B were obtained on request from Klausen. For thermal conductivity, Klausen assumed a value of 2.2 W/mK for all mixtures. A thermal conductance of 4.4 W/m^2 °C is assumed for 18 mm plywood and 12.6 W/m^2 °C for exposed concrete (assuming a wind speed of 1.5 m/s). For the specific heat, a value of 1.01 kJ/kg°C was used for all mixtures. Both values were obtained from Klausen upon request. The adiabatic temperature development measured by Klausen is shown in Figure 2.31. The development for CEM I and CEM II/B-V was obtained from the doctoral thesis [25], the development for CEM III/B was obtained on request from Klausen.

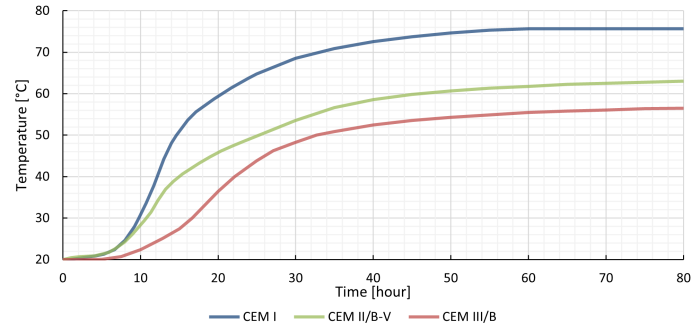

Figure 2.31: The adiabatic temperature development of the three different concrete mixtures.

Shrinkage

The only form of shrinkage that can occur and is considered in Klausen's research is autogenous shrinkage. The reason for this is that the specimen is in a closed, insulated space and therefore no water can evaporate and no drying shrinkage can occur. The development of autogenous shrinkage of CEM I and CEM II/B-V is taken from Klausen's doctoral thesis [25] and the strain for CEM III/B is taken from the article in 'Structural Concrete' by Klausen and Kanstad [27].

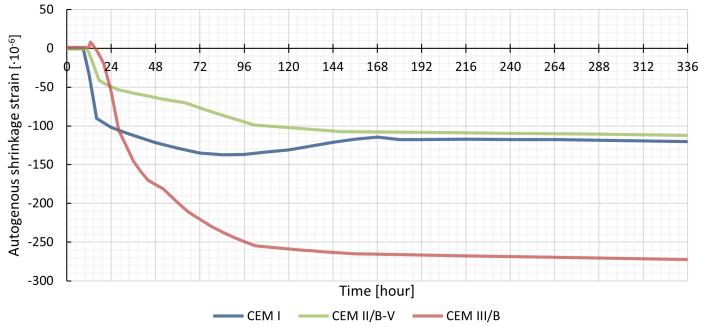

Figure 2.32: The autogenous shrinkage development of the three different concrete mixtures.

The development of the autogenous shrinkage strain of the CEM I concrete is rather unusual because it starts very quickly, but above all because it starts to swell a little after 3 - 4 days. This is not expected, but is used to allow a fair comparison with the experiment.

Creep

The creep strains that occurred in Klausen's experiment can be predicted using the double power law, for which all parameters are determined by testing. Creep at time t can be calculated by multiplying the compliance function of time t for a stress increment induced at time t' by the stress increment at t' for each stress increment. See also Equation 2.32 for the calculation of the creep stress and Equation 2.33 for the compliance function. The corresponding creep parameters for the compliance function are given in Table 2.4. The creep parameters for CEM I and CEM II/B-V were obtained from Klausen's doctoral thesis [25], the development of CEM III/B was obtained upon request from Klausen.

$$\varepsilon_{creep}(t) = \sum_{t'=0}^{t} J(t,t') \cdot d\sigma(t') \tag{2.32}$$

$$J(t,t') = \frac{1}{E_c(t'_{eq})}[1 + \varphi_0 \cdot {t'}_{eq}^{-d} \cdot (t-t')^p] \tag{2.33}$$

Table 2.4: Overview of the creep parameters for the double power law.

	φ_0	d	p
CEM I	0.75	0.20	0.21
CEM II/B-V	0.49	0.22	0.33
CEM III/B	0.58	0.50	0.45

3

Verification model and analysis

This chapter describes the modelling and analysis of the verification model based on the TSTM experiment carried out in the Klausen research [25]–[27], as also explained in Section 2.3. This is done to answer the first two sub-research questions: (1) How can the hardening process of partially restrained concrete be accurately modelled and predicted using time-dependent finite element analysis? and (2) Which type of material model, based on which standard or guideline, is most suitable and accurate for the hardening of partially restrained concrete?

To answer these sub-research questions, two time-dependent finite element models are created. The first model is a semi-adiabatic temperature model, similar to the one created in Klausen's study, which aims to simulate the semi-adiabatic temperature development used in the TSTM experiment. This simulation is based on the theoretical case of a wall poured on a foundation. The objective is to validate the model against the one used in Klausen's research and to investigate the effect of using different thermal properties as defined by standards and/or guidelines compared to those assumed and/or measured in Klausen's research. This information can be used to find the most appropriate and accurate standard and/or guideline to use for the thermal properties in case the specific thermal properties are not available in the case study.

The second section focuses on modelling and analysis of the TSTM experiment itself. The aim is to accurately model all hardening processes and stress development as observed in the experimental results. First, the mechanical parameters measured and assumed by Klausen in her research are used to validate the accuracy of the model against the experiment. This will answer the first sub-research question. Next, a comparison is made between material models based on the different standards and guidelines, with the aim of identifying the material model that best predicts the results of the experiment. This will allow the second sub-research question to be answered, which material model, based on which standard or guideline, is most appropriate and accurate for hardening of partially restrained concrete.

3.1. Semi-adiabatic temperature model and analysis

This section explains the semi-adiabatic temperature model created with DIANA FEA from which the semi-adiabatic/'realistic' temperature development is determined. The temperature development in the centre of the wall of a theoretical case is an important input parameter for the TSTM experiment. This section first explains the modelling approach for the thermal heat calculation model, then the finite element model is described, and after that the phased heat flow analysis is explained in detail. The calculation results and comparison with the experimental results are then described. From this, conclusions can be drawn as to whether the temperature development is modelled correctly/accurately in comparison to the model created in the research by Klausen. In the last subsection, a comparison is made between the thermal properties measured and/or assumed by Klausen and those from the standards/guidelines investigated in this thesis. These were the Eurocode, the fib Model Code and the CIRIA C766. In order to find the most suitable standard/guideline for predicting the thermal properties to be used in the case study in the next chapter.

3.1.1. Modelling approach

The theoretical case of a wall poured on a foundation, see Figure 2.29, is modelled using the finite element program DIANA FEA. The theoretical case is modelled to predict the semi-adiabatic temperature development on the TSTM experiment as a 'realistic' development, as if the specimen were in the middle of the wall. The theoretical case is also described in Section 2.3.1. In order to analyse the semi-adiabatic temperature development, a phased transient heat transfer analysis is performed, which consists of two phases. In the first phase, the foundation is poured and a transient heat transfer analysis is performed for a period of 60 days. After 60 days the concrete temperature is assumed to be stable and the pouring of the wall onto the foundation is simulated. Again using a transient heat transfer analysis. The formwork of the foundation and wall is removed 3 days after pouring.

As the main interest is the temperature in the middle of a long wall, it is sufficient to model only the cross-section of the wall. As the effects of the side boundaries are negligible for the temperature development in the middle cross-section of the wall. This can then be modelled using plane strain elements within a 2D section model. As the wall and foundation are symmetrical along the vertical plane, symmetry is used. As a result, only half of the model is modelled in DIANA FEA. The edges of the foundation and wall exposed to the external environment and the formwork are modelled to apply a time-dependent thermal conductivity or heat transfer coefficient. The initial temperature of the concrete mix for the foundation and wall is 20 °C and the ambient temperature is also 20 °C for the entire duration of the analysis. Both are in accordance with Klausen's thesis [25].

The model described above will be used to analyse the semi-adiabatic temperature development for three different cement compositions described in Section 2.3.3. The 'Power law viscoelasticity and Young hardening' material model is used, although only the heat flow part will be relevant for this analysis. This material model is chosen because it is also used in the TSTM experimental model. This is because all the parameters required for the double power law used in this material model are measured and described in Klausen's research.

3.1.2. Finite element model

This subsection describes the various components that characterise the finite element model created using the DIANA FEA program. These components include the geometry, material properties, boundary conditions, loads and mesh.

Geometry

As chosen in the model approach, only half of the geometry of Figure 2.29 is modelled in DIANA FEA due to symmetry. In the first phase, only the foundation is present, as shown in Figure 3.1a. In the second phase, when the wall is cast, both the foundation and the wall are present, as shown in Figure 3.2a. Both along the edges of the foundation and along the edges of the wall a joint is assigned as a boundary interface. This is set as a flow boundary to model the thermal conductance along the edges.

Material properties

The two concrete material models used for both the foundation and the wall are the 'Power law viscoelasticity and Young hardening' models. All concrete material properties and developments are described in Section 2.3.3. As only a transient heat transfer analysis is performed, only heat flow and maturity effects are included in the material model. For the heat of hydration, the pre-processing method based on element age is selected and the equivalent age calculation is based on Arrhenius.

Two separate materials are created for the foundation and wall boundary surfaces to model formwork removal after 3 days for the foundation and 63 days for the wall (3 days after concreting the wall). Boundary elements are chosen as the heat flow material model, specifying a time-dependent thermal conductance. A heat transfer coefficient of 3.33 W/m^2 °C is assumed for the formwork (18 mm plywood, no wind) and 12.6 W/m^2 °C for a free surface (wind $v = 1.5$ m/s). Both are according to Klausen's doctoral thesis [25].

Boundary conditions

The boundary conditions can be divided into two parts: the thermal boundary conditions and the static boundary conditions. The former consist of an external boundary temperature of 20 °C around the edges of the foundation and the wall (with the exception of the edges of the line of symmetry), and an initial temperature for both the foundation and the wall of 20 °C. For the static boundary conditions,

a horizontal edge constraint is placed on the plane of symmetry, since only half of the model is modelled due to symmetry. A vertical edge constraint is placed at the bottom of the foundation, see also Figure 3.1a and 3.2a.

Loads
As this model is only used to perform a phased transient heat transfer analysis to find the temperature gradient of a small part of the wall, no load is applied to the model.

Mesh
A different mesh size was chosen for the foundation than for the wall because the wall is much thinner. A square of about 200 mm was chosen for the foundation and 80 mm for the wall (shown in Figures 3.1b and 3.2b). Element type CQ16E, a quadrilateral element with 8 nodes, was selected for the foundation and wall. Although quadrilateral elements are selected, linear elements are used for the transient heat transfer analysis. The foundation also required some triangular CT12E elements with 6 nodes around the connection between the foundation and the wall. The boundary elements were modelled using B2HT, straight boundary elements with 2 nodes. More information on element types can be found in Section 2.2.4 or in the DIANA FEA manual [24].

(a) Geometry and boundary conditions (b) Finite element mesh

Figure 3.1: The geometry, boundary conditions and finite element mesh of the semi-adiabatic temperature model for the first phase.

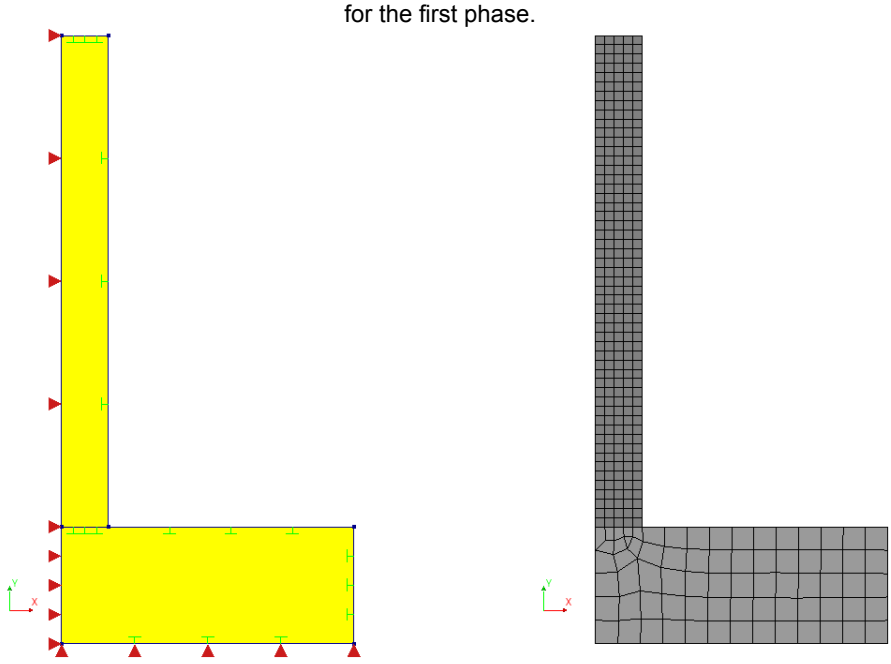

(a) Geometry and boundary conditions (b) Finite element mesh

Figure 3.2: The geometry, boundary conditions and finite element mesh of the semi-adiabatic temperature model for the second phase.

3.1.3. Calculation analysis

The transient heat transfer analysis is divided into two phases, the first being the temperature development within the foundation, which is poured first. The second is the temperature development within the wall, which also transfers heat to the foundation. This is simulated in DIANA FEA in two phases, the first without the wall and wall boundary conditions and the second with all components.

For the first phase, a transient heat transfer analysis is performed, using the initial temperature as initial conditions and selecting a non-linear analysis for the heat of hydration and the calculation of the equivalent age. The time steps used are 0.02083(144x) 0.04166(72x) 0.25(36x) 1.0(18x) 3.0(9x) days,

converted to hours as follows 0.5(144x) 1(72x) 6(36x) 24(18x) 72(9x) hours. Smaller time steps were used initially because this is when the temperature changes the most, and larger time steps were used later. For the non-linear analysis, the default settings for the iteration process were used: a maximum of five iterations, a convergence tolerance of $1 \cdot 10^{-6}$ and the Newton regular method.

For the second phase, the same transient heat transfer analysis is performed as described for the first phase, except that the start time for this analysis is set to 60 days. The other analysis settings are the same, including the time steps used.

Default outputs are used for both transient heat transfer analyses: temperature, heat flux, degrees of reaction and equivalent age. Where only the average temperature at the location shown in Figure 2.29 is of interest.

3.1.4. Calculation results and comparison to experiment model

The results of the finite element model described in Section 3.1.2 and the calculation analysis described in Section 3.1.3 are shown in Figure 3.3. The analysis was performed for the three different concrete mixes CEM I, CEM II/B-V and CEM III/B. The semi-adiabatic temperature development results are plotted above the original graphs taken from the articles by Klausen et al. [26], [27].

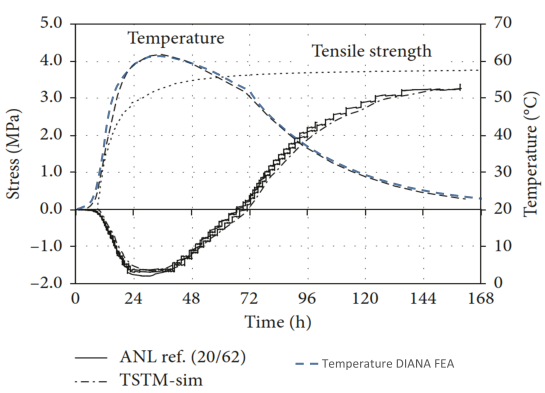

(a) CEM I concrete mix

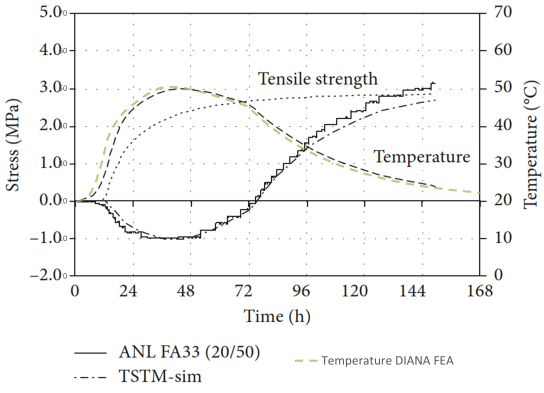

(b) CEM II/B-V concrete mix

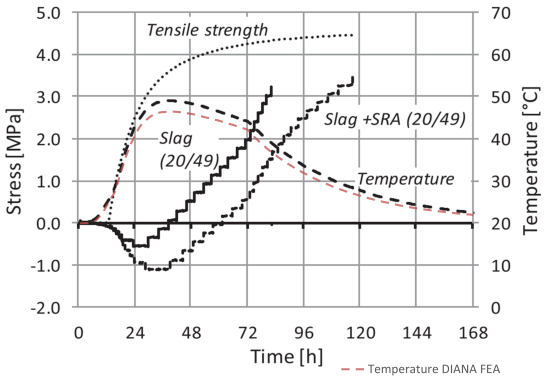

(c) CEM III/B concrete mix

Figure 3.3: The semi-adiabatic temperature development plotted on top of the results by the experiment for three different cement mixtures, subfigure (a) and (b) from [26] and (c) from [27].

As shown in Figure 3.3, the results for CEM I and CEM II/B-V concrete mixes follow the trend relatively well. The maximum average temperature for CEM I is $61.4\,°C$ compared to $61.8\,°C$ reported by Klausen. For CEM II/B-V this is $50.4\,°C$ compared to $49.8\,°C$, so both are very close and about 1% difference. CEM III/B divides a little more, $46.5\,°C$ compared to $49\,°C$. This difference of about 5% is unclear, but could be that one of the input parameters was not correct, e.g. the adiabatic temperature. The CEM III/B concrete is not included in Klausen's thesis [25], so it could also be that the same model or parameters were not used as for the other two concrete mixes. However, as two are very close and one is also reasonably close and follows the correct line, it can be assumed that the model and calculation analysis is working correctly.

3.1.5. Comparison between thermal properties of the experiment model, Eurocode and CIRIA

Many of the heat parameters used in the semi-adiabatic temperature model are taken from Klausen research. Therefore a comparison is made between what standards and guidelines describes and what is used/measured by Klausen. To see whether the predictions of standards and guidelines are close to this particular experiment and thus whether this is useful for the later case studies when the measured thermal properties are not available. This comparison is done for the temperature conditions, the thermal conductance at the surfaces, the thermal conductivity of the concrete and the specific heat and the adiabatic temperature development. All are covered in the CIRIA C766 but in the Eurocode only something about the thermal conductivity of the concrete could be found. Within the the fib Model Code 2010 no specific values could be found for the thermal properties.

Temperature conditions

If no information is available, CIRIA C766 can be used to predict the temperature conditions of the hardening phase. Based on CIRIA, an initial temperature of the cast concrete of 20 °C and an ambient temperature of 15 °C is recommended. Klausen's research uses the same initial concrete temperature as CIRIA, but a different constant ambient temperature of 20 °C, which is 5 °C higher. Appendix A2.5 of CIRIA C766 states that to predict the thermal gradient, the daily temperature variation is required and this can be modelled with a sinusoidal curve.

For the CEM I concrete, the analysis with the ambient temperature of 20 °C was compared with the constant 15 °C from CIRIA C766 and also with a dynamic sinusoidal curve from the Appendix of CIRIA C766. The sinusoidal curve has a mean temperature of 15 °C and an amplitude of 5 °C. It thus varies between 10 °C and 20 °C, based on the highest and lowest average summer temperatures in Norway, which can be found on the Climate Change Knowledge Portal [29]. As the same ambient temperature was assumed for all different cement compositions, only the CEM I concrete model was recalculated, see Figure 3.4 for the semi-adiabatic temperature difference.

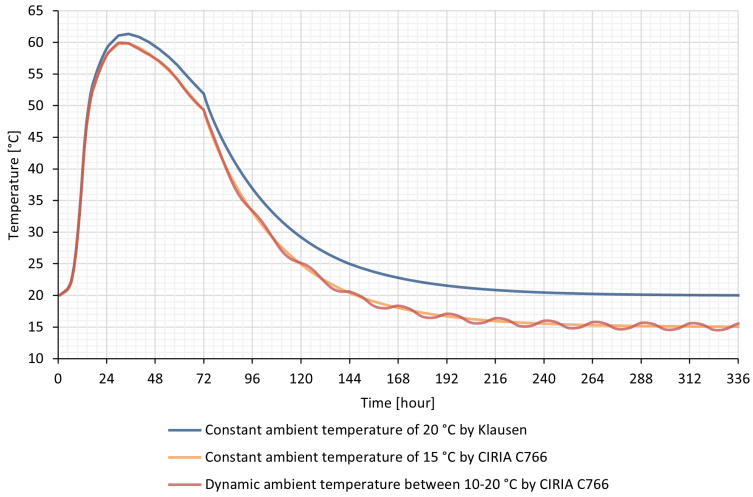

Figure 3.4: Comparison between the experiment and CIRIA C766 for the ambient temperature.

Based on Figure 3.4, it is concluded that when a lower ambient temperature is used, the semi-adiabatic temperature decreases as expected. Although the constant ambient difference is 5 °C lower on the outside, it has much less effect on the average wall temperature within the first 3 days. The average temperature peak of the CIRIA model is about 1.5 °C lower to 59.9 °C instead of 61.4 °C. The fact that the peak temperature is lower is as expected because the concrete is cooled more at lower outside temperatures. Another interesting fact is that using the dynamic ambient temperature has very little effect on the average wall temperature, especially when the formwork is still in place for up to 3 days. After that, a small fluctuation can be seen, but not very significant. The local temperature at the sides of the wall will fluctuate much more, but will not have much influence on the average wall temperature.

Thermal conductance at the surfaces

For the thermal conductance values or heat transfer coefficients of the formwork and exposed concrete in wind, CIRIA C766 recommends different values than those assumed or measured in Klausen's research. For 18 mm plywood formwork without wind, CIRIA recommends, based on Equation A2.25 from Appendix A2 [3], that the thermal conductance is 4.4 W/m^2 °C instead of the 3.33 W/m^2 °C

used by Klausen [25]. For exposed concrete with a wind speed of 1.5 m/s, CIRIA recommends, based on Equation A2.22 from Appendix A2 [3], that the thermal conductance is 11.6 W/m^2 °C instead of 12.6 W/m^2 °C. Using these thermal conductance parameters for the model in DIANA FEA, the semi-adiabatic temperature model is reanalysed for the CEM I concrete, as the same thermal conductance parameters are used for all cement compositions. The results are shown in Figure 3.5.

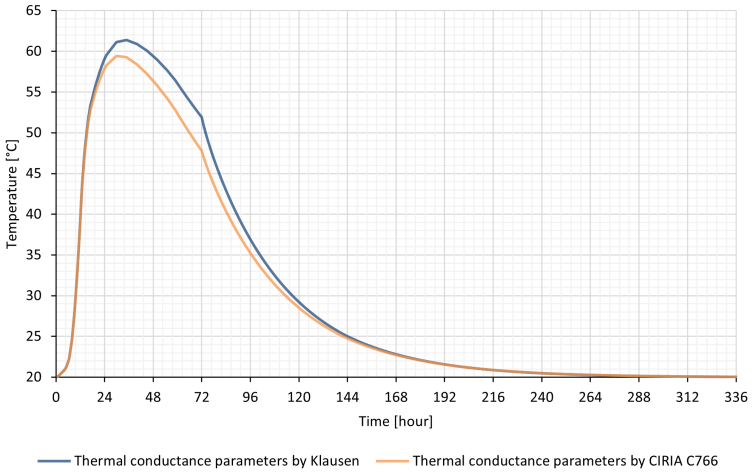

Figure 3.5: Comparison between the experiment and CIRIA C766 for the thermal conductance at the surfaces.

Figure 3.5 shows that the temperature is lower in the first three days as more heat is conducted to the environment. The peak value when using the thermal conductance based on CIRIA C766 is 59.4 °C instead of 61.4 °C, which is about 3.2% lower. After 3 days, when the formwork is removed and the thermal conductance changes, the temperature difference is about 8% lower. Because the thermal conductance is lower after 3 days, the temperature drops more slowly and the difference is smaller.

Thermal conductivity of the concrete

Both CIRIA C766 and EN1992-1-2 recommend different thermal conductivity of the concrete, compared to 2.2 W/mK assumed in Klausen's research for all mixtures. According to Klausen's thesis, all aggregates used in the different mixes consist of a combination of gneiss and granite, which based on Table A2.1 from the CIRIA C766 [3] a thermal conductivity of 1.86 W/m °C for gneiss and 1.91 W/m °C for granite is recommended. The average of these values equals 1.885 W/m °C. Section 3.3.3 of EN1992-1-2 [30] describes a temperature-dependent upper and lower limit for calculating thermal conductivity. The model based on Klausen's thermal conductivity was compared with what is recommended by CIRIA and the two limits of Eurocode. Since the same thermal conductivity is used for all different cement compositions, only the CEM I concrete model was reanalysed, shown in Figure 3.6.

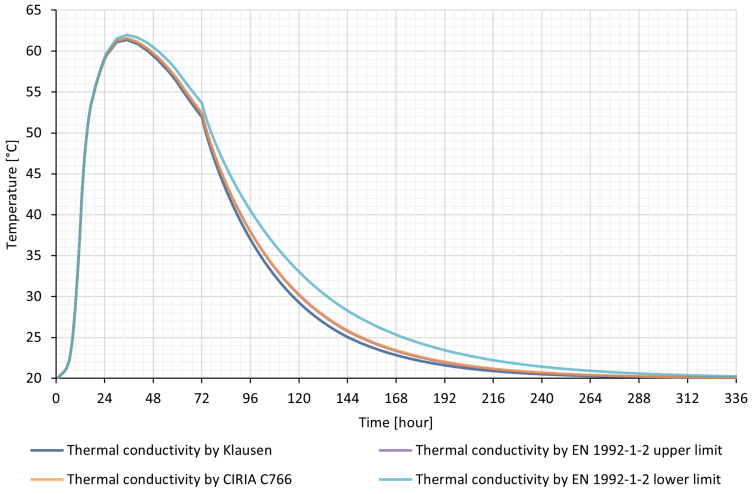

Figure 3.6: Comparison between the experiment, EN1992-1-1 and CIRIA C766 for the thermal conductivity of the concrete.

Although difficult to see in Figure 3.6, the semi-adiabatic temperature development based on the thermal connectivity of CIRIA is approximately equal to the upper limit of the Eurocode, although the value of CIRIA is constant and the Eurocode is temperature dependent. The temperature development is also close to that assumed and used by Klausen. The difference is that the peak of both is only about $0.1\,°C$, so only 0.3%, but over time the difference increases slightly to about 3% for both at 5 days and then the difference decreases again. The temperature development of the Eurocode lower limit deviates slightly more, about $0.7\,°C$ at the peak and about $3.7\,°C$ at 5 days (120 hours).

Specific heat and the adiabatic temperature development

CIRIA C766 can be used to estimate the specific heat and the heat of hydration as a function of the percentage of fly ash and GGBS. This allows the adiabatic temperature gradient to be found, as explained in Section 2.1.1, by applying a combination of Equations 2.1 and 2.2. According to CIRIA C766 Appendix A2.4 [3], the specific heat depends on the cement content and the w/c ratio. Using Figure A2.13 from CIRIA C766, the specific heat for a w/c of 0.4 is approximately $0.978\,kJ/kg\,°C$ for CEM I concrete, $0.970\,kJ/kg\,°C$ for CEM II/B-V concrete and $0.973\,kJ/kg\,°C$ for CEM III/B concrete. The Klausen study uses a value of $1.01\,kJ/kg\,°C$ for all concrete mixes. Figure 3.7 compares the adiabatic and semi-adiabatic temperature development for the three concrete mixtures between the specific heat and adiabatic temperature based on CIRIA and that used by Klausen in the experiment.

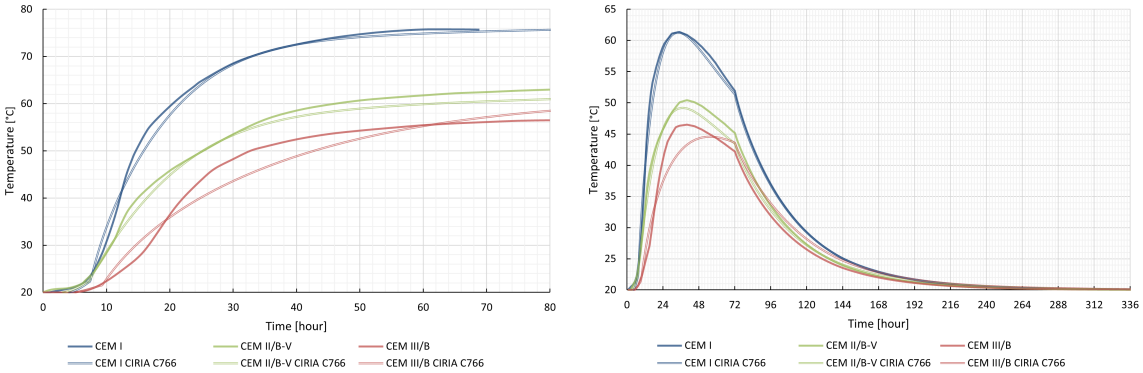

(a) Adiabatic temperature development

(b) Semi-adiabatic temperature development

Figure 3.7: Comparison between the experiment and CIRIA C766 for specific heat and adiabatic temperature development.

Both sub-figures from Figure 3.7 clearly show that CIRIA for CEM I predicts the adiabatic temperature quite well and thus the semi-adiabatic temperature is also very close to that measured and used by Klausen. Both the adiabatic and semi-adiabatic temperature rise of CIRIA based on CEM II/B-V are slightly lower than those of Klausen. The difference in peak temperature for the semi-adiabatic temperature is $49.2\,°C$ instead of $50.4\,°C$, which is about a 2.4% difference. The difference for the CEM III/B is greater because the adiabatic temperature development according to CIRIA is much more gradual and continues to a higher temperature than that measured and used by Klausen. This can also be seen in the semi-adiabatic development, which peaks after 3 days when the formwork is removed, instead of 1.5 days in the adiabatic development measured by Klausen. Although the peak temperature is reached at a different time, the peak temperature is around $44.6\,°C$ instead of $46.5\,°C$, which is only 4.1%. Overall, the CIRIA C766 predicts the specific heat and (semi-)adiabatic temperature quite well.

3.2. TSTM-experiment model and analysis

This section explains the TSTM model created to represent the TSTM experiments described in Section 2.3.1. This model can be used to analyse and predict the stress development of the partially restrained specimen based on a semi-adiabatic/'realistic' temperature development as described and analysed in the previous section. This can then be compared with the experiment performed in the Klausen study. The aim is to accurately model all hardening processes and stress development as found in the experimental results. In this section, the modelling approach for the calculation method and model is first described, then the finite element model is described, and then the calculation analysis is explained in detail. The calculation results and comparison with the experimental results are then described. A refinement of the mesh size and time/load steps is then performed. All this is done to determine if and how the hardening process of partially restrained concrete can be accurately modelled and predicted using time-dependent finite element analysis.

In the following subsections, comparisons are made to determine which material model, based on which standard or guideline, is most suitable to use for the case study analysis in the next chapter. This starts with a comparison for the strain parameters, followed by a comparison between the material models for the mechanical properties. Finally, a new viscoelastic material model is created and compared with the experiment and hand calculations so that it can be used for the case study analysis.

3.2.1. Modelling approach

The TSTM experiment performed in Klausen's research is modelled using the finite element program DIANA FEA. The experiment is explained in full detail in Section 2.3.1 and is shown in Figures 2.26 and 2.28. Only the middle part of the TSTM experiment is modelled, as only from this part, between the measuring bolts embedded in the concrete specimen, the stress development is measured. In order to analyse the stress development of the model, an analysis consisting of a transient heat transfer analysis followed by a structural non-linear analysis is performed.

The concrete specimen from the TSTM is modelled by solid 3D elements using a 3D model. An external temperature development is placed on the outside of the geometry to simulate the semi-adiabatic temperature development from the theoretical case of a wall cast on a foundation. The semi-adiabatic temperature model is explained and implemented in the previous section. This is done by modelling a boundary interface on the long sides with a high conductance or heat transfer coefficient. The initial temperature of the concrete is set at $20\,^{\circ}\text{C}$ and the experiment lasts 3.5-7 days, depending on the concrete mix. Both sides should be restrained in the Y- and Z-directions and one side should also be restrained in the X-direction. The other side is free to expand, but a load is applied to that side. This is used to apply a 50% restraint by increasing or decreasing the load factor. As time steps are taken and the displacement at one end reaches a certain stop value, the load is increased to 50% of the increase in displacement. Time steps are then applied again until a certain displacement is reached and then the load is increased again.

The model described above is used to analyse the stress development and tensile strength for three different cement compositions described in Section 2.3.3. The material model used is 'Power law viscoelasticity and Young hardening'. This material model is chosen because all the creep parameters required for the double power law used in this material model are known from Klausen's research. The model should therefore be close to the experimental results. The analyses in the last sub-section investigate different material models, which will be described later.

3.2.2. Finite Element Model

This subsection describes the various components that characterise the finite element model created using the DIANA FEA program. These components include the geometry, material properties, boundary conditions, loads and mesh.

Geometry

The concrete specimen is modelled in DIANA FEA as a beam with dimensions of $88\times100\times700$ mm. The cross-section is the same as described in Section 2.3.1. The length is the distance between the measuring bolts, as only this section is measured in the experiment. The geometry is shown in Figure 3.8a. For each of the four long sides of the beam a boundary surface is assigned. This is set as a flow boundary to assign an external temperature development. As the end faces are not a boundary in the experiment due to the presence of concrete, no heat can be transferred at this location and therefore no boundary is added there.

Material properties
The material model used for the concrete element is the 'Power law viscoelasticity and Young hardening' model. All concrete material properties and developments are described in Section 2.3.3. For the double power law, an additional parameters was required, which was described in section mentioned, which was the development point. This was set to be around half the calculation period, as advised according to the DIANA FEA [24] manual. For hydration heat, the pre-processing method based on element age and adiabatic heat development is used. For the heat of hydration, the pre-processing method based on element age is selected and the equivalent age calculation is based on Arrhenius.

A flow boundary material is created for the boundary interface. For this material, a extremely-high heat transfer coefficient of $9 \cdot 10^{99}$ W/m^2 °C is used to ensure that the time-dependent prescribed temperature at the boundary can be applied correctly. In reality, thermal conductance is also high because of the copper plates and tubes around the specimen to which heat can be transferred. With this heat transfer coefficient, the maximum difference between the applied temperature on the outside and inside is always less than 0.5 °C, and only 0.1 °C at the temperature peak. This could also be the case in the real experiment.

Boundary conditions
The boundary conditions can be divided into two parts: the thermal boundary conditions and the static boundary conditions. The former consist of an external temperature gradient based on the semi-adiabatic temperature from the DIANA FEA model described in Section 3.1. This is applied to the four boundary faces of the element. The initial temperature is set to 20 °C. For the static boundary conditions, an edge constraint is placed on the left side of the beam in the X-direction. Constraints in the Y- and Z-direction are applied to the node in the middle of the two ends. To limit the possibility of rotation, an additional constraint in the Y-direction is placed on another node on the left side (shown in Figure 3.8a).

Loads
Two loads are applied to the model, an incremental load which provides the degree of restraint and the time-dependent autogenous shrinkage. The incremental load is placed on the right side as a distributed load. A value of 1.0 N/mm^2 is used which is applied by load factors in load steps. This is further explained in the analysis section of the calculation. Autogenous shrinkage is applied as a prescribed time-dependent strain. Although it is normally applied via the material properties, as a combination of time and load steps are applied, it has been chosen to be applied as a time-dependent strain. This is because otherwise DIANA FEA does not see that a load is being applied when time steps are performed and it is not possible to filter on time steps only when the results are shown. Comparisons were made between applying via the material properties and applying as a load, but no difference in results were found.

Mesh
A relatively coarse mesh was chosen, dividing the beam into a total of 24 elements, two in width and height and six in length. This gives the mesh a dimension of $44 \times 50 \times 116.67$ mm see Figure 3.8b. The quadratic solid element type CHX60 has been selected, which is a 20 nodes brick element. The boundary elements are modelled using BQ4HT quadrilateral boundary elements with 4 nodes. More information on element types can be found in Section 2.2.4 or in the DIANA FEA manual [24].

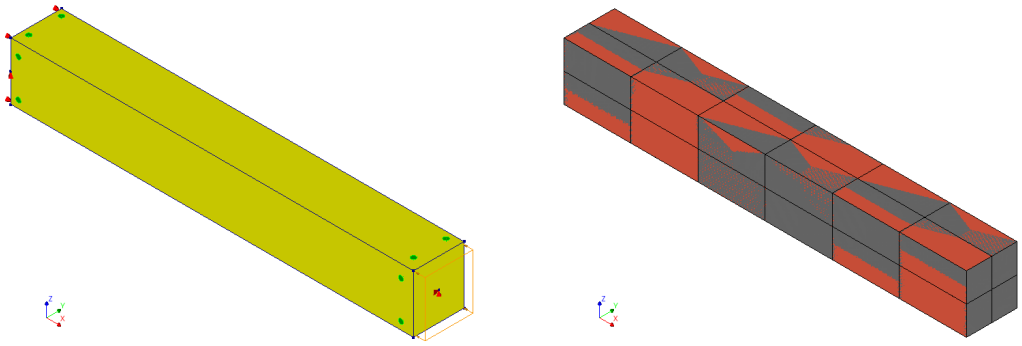

(a) Geometry and boundary conditions (b) Finite element mesh

Figure 3.8: The geometry, boundary conditions and finite element mesh of the TSTM model.

3.2.3. Calculation analysis

A combined analysis is performed, first a transient heat transfer analysis and then a structural non-linear analysis. The transient heat transfer analysis calculates, among other things, the temperature development and equivalent age required for the structural non-linear analysis. The latter analysis is performed with multiple time and load steps to simulate the 50% degree of restraint applied to the experiment.

Transient heat transfer analysis

The transient heat transfer analysis is set up with the initial temperature as the initial condition and a non-linear analysis is selected that includes hydration heat analysis and equivalent age calculation. The same step sizes are used as for the semi-adiabatic temperature model, but only the first 14 days are used. The time steps used are 0.0208(144x) 0.04166(72x) 0.25(32x) days, converted to hours: 0.5(144x) 1(72x) 6(32x) hours. Thus, smaller time steps were used in the beginning because that is when the temperature changes the most, and larger time steps were used later. For the transient heat transfer analysis, up to 15 iterations, a convergence tolerance of $1{\cdot}10^{-6}$ and the regular Newton method were used for the iteration process. The default output is used for the heat transfer analyses, which include: temperature, heat flux, degree of reactions and equivalent age. Of these, only temperature and equivalent age are of most interest.

Structural non-linear analysis

A structural non-linear analysis is performed with many time and load steps to incorporate the degree of restraint of 50%. The time and load step blocks alternate. First, time steps are performed until a specified stop criterion is satisfied, then load steps are performed for the applied load until that specified stop criterion is satisfied, and so on. The stop criterion for the first time block is that the displacement in the right centre node is at least 0.009 mm. When this is satisfied, the load step block is started and the stop criterion is that the displacement in the same node is at most 0.0045 mm. So, in this case, load steps are applied until the right end is reduced to 0.0045 mm, so that the beam is restrained 50%. Once this stop criterion is satisfied, the right end of the element can be increased again 0.009 mm until the displacement is at least 0.0135 mm. The load is then increased until the displacement is reduced to 0.009 mm. These time and load steps are repeated until, after about 1-2 days, the beam begins to contract due to autogenous shrinkage and thermal strain from cooling. When the beam no longer extends by a relative 0.009 mm, a relative decrease of -0.009 mm is used as the stop criterion and the beam is pushed back 0.0045 mm in the other direction in the load step.

Approximately 90 blocks are performed for the analysis, consisting of 45 time blocks and 45 load blocks. The time steps are set to 0.0025 day, which is 3 minutes and 36 seconds. As the load steps depend on the development of the Young's modulus, for the first few blocks the load steps are about 10^{-15}, as the Young's modulus is still close to 0. After that, as the Young's modulus starts to develop, the load steps are between 0.001 and 0.01 until the time is reached where the strain decreases and then negative steps of -0.01 are used. Up to 100 time steps are used between the load blocks, but the load steps are chosen so that about 10-30 steps are needed to reduce the calculation time, but still have enough steps to achieve sufficient accuracy for the stop criterion.

The selected structural non-linear analysis takes into account physically non-linear effects. However, it is important to note that the effect of cracking is excluded from the physically non-linear effect as the elastic material model used for the TSTM experiment does not allow for this possibility.

For the equilibrium iteration, the default Newton-Raphson Regular Method is selected with a maximum of 10 iterations. It is specified that convergence of the solution can only be achieved when both the displacement and force norms are satisfied with a convergence tolerance of $1 \cdot 10^{-2}$.

In addition to the default outputs, an extra output block is added to the analysis. The Young's modulus, tensile strength and creep strain are selected for this output block. These selected outputs, together with the default outputs, should provide all the information necessary to find all the relevant results and to check the results.

3.2.4. Calculation results and comparison to experiment

The results of the finite element model described in Section 3.2.2 and the calculation analysis described in Section 3.2.3 are shown in Figure 3.3. The analysis was performed for three different concrete mixes CEM I, CEM II/B-V and CEM III/B. The semi-adiabatic temperature development, used as input from Klausen's semi-adiabatic temperature model, the tensile strength development and the stress development results are plotted above the original graphs taken from the articles by Klausen et al. [26], [27].

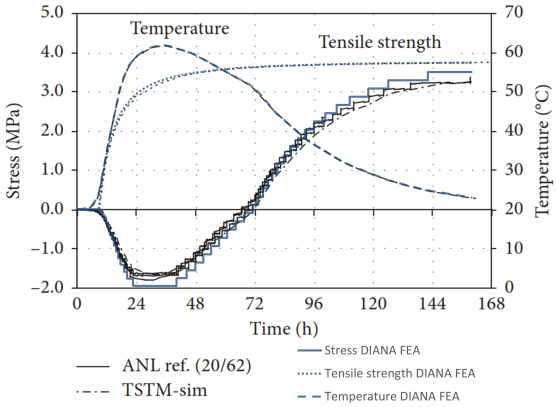

(a) CEM I concrete mix

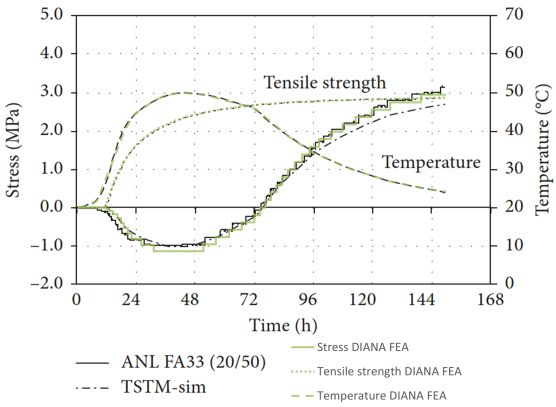

(b) CEM II/B-V concrete mix

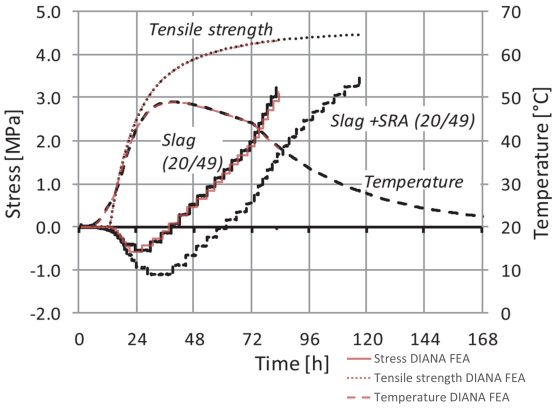

(c) CEM III/B concrete mix

Figure 3.9: The stress, temperature and tensile strength development plotted on top of the results by the experiment for three different cement mixtures, subfigure (a) and (b) from [26] and (c) from [27].

From Figure 3.9 it can be concluded that for all the different cement compositions the stress development is quite close to the experiment. Although the stress is slightly higher or lower in some places, this is as expected and can be explained. For example, the TSTM models assume constant values for the coefficient of thermal expansion, which in reality is time-dependent. Also, the development of material properties is modelled with a start time (t_0), but as the figure shows, the stresses for CEM II/B-V and CEM III/B concrete start earlier than the start time, so the development of material properties is not a perfect fit. So the development of the mechanical properties starts slowly before the start time because otherwise there would be no stresses.

Another point to note is that the force and stress in the TSTM model remain constant between two pushbacks because the pushbacks are applied by adding a load/load step. In the real experiment, an attempt is made to keep the stress constant, but because the experiment is displacement driven and the load is a consequence of the displacement, the force and stress change as the specimen moves. To keep the stress constant, the displacement, and therefore the load, is adjusted between two pushbacks. This can affect the increase in displacement and therefore the time at which the stop criterion is met and pushback should begin. It can also be seen from the figures that by adding a prescribed semi-adiabatic temperature rise around the boundary conditions, the average temperature of the specimen is almost exactly the same. It can also be seen from the graph that the development of the mechanical properties, in particular the development of the tensile strength, is the same as that assumed by Klausen in her study, but this also indicates that the maturity/equivalent age is also correctly implemented in the model.

From the fact that the temperature development, the development of the mechanical properties and also the stress development are all very close to the experiment, it can be concluded that all the hardening processes have been implemented correctly and therefore the experiment could be accurately modelled using a time-dependent finite element analysis. It is also concluded that the ‘Power law viscoelasticity and Young hardening’ material model used was accurate and suitable for this purpose.

3.2.5. Mesh size and time/load steps refinement

To be able to validate that the mesh size and time and load steps are used when using the TSTM model, in this section a comparison is made. First the influence of the mesh size will be analysed, and next the size of the time and load steps are analysed. The displacement increment of 0.009 mm used for the stop criterion is not varied and compared because it is based on the actual displacement increment based on data from the experiment.

Analysing of the mesh size

o check that the correct mesh was used, a comparison was made between the mesh used and specified in the previous sections and a mesh four times larger. As described in Section 3.2.2, a relatively coarse mesh was chosen because there is not much variation within the nodes of the model. However, there is a difference in temperature in the centre compared to the edges, resulting in different equivalent ages and hence different development of Young's modulus and hence stress. These temperature differences are quite small and do not exceed a difference of 0.5 °C. It was therefore assumed that a mesh size of $44 \times 50 \times 116.67$ mm, corresponding to 2 mesh elements in height and width and 6 in length, was sufficient. However, to check this, a comparison was made with a model with four times as many elements in height, width and length. So the model has a mesh size of about $11 \times 12.5 \times 87.5$ mm, as shown in Figure 3.10.

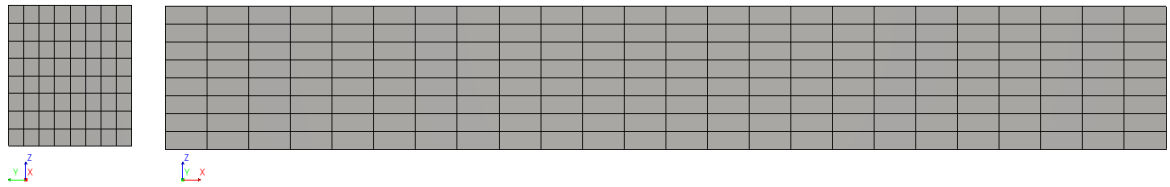

(a) X-direction view (b) Y-direction view

Figure 3.10: The finite element mesh for the mesh refinement analysis (perspective projection).

Based on the refined mesh size shown above, Figure 3.11 shows the result of the mesh refinement analysis and compares the temperature, tensile strength and stress development for the original mesh with the refined mesh size. The results in the figure are averaged from the centre line of the TSTM model.

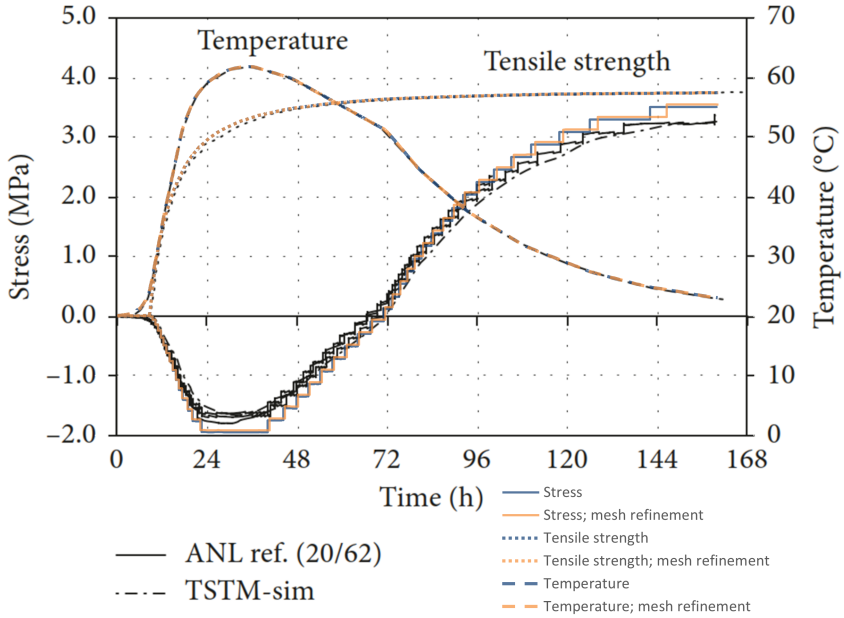

Figure 3.11: Mesh size comparison for the TSTM model.

From Figure 3.11 it is concluded that the four times larger mesh size has no effect on the temperature and tensile strength development. It does have a small effect on stress development, but only after a few days and mostly only at the time the model is pushed back. However, the overall effect is very small and not worth the exponential increase in computation time.

Analysing of the time and load step size

To analyse whether the correct time and load steps were used, a comparison was made between the analysis used and two different analyses in which the time and load steps were four times larger or smaller. As described in Section 3.2.3, the time steps used were about 0.00250 day, which is 3 minutes and 36 seconds. The load steps used were variable, starting very small due to the low Young's modulus of the concrete, but then increasing to about 0.001 and 0.01, and after reaching maximum displacement to -0.01. To check whether these steps are accurate enough, or perhaps unnecessarily small, a comparison was made with four times smaller and larger time and load steps. If the time and/or load steps are too large, the stop criterion is exceeded and the model is more restrained than necessary. Figure 3.12 compares the temperature, tensile strength and stress development for the models with the three different time and load steps. The results in the figure are averaged from the centre line of the TSTM model.

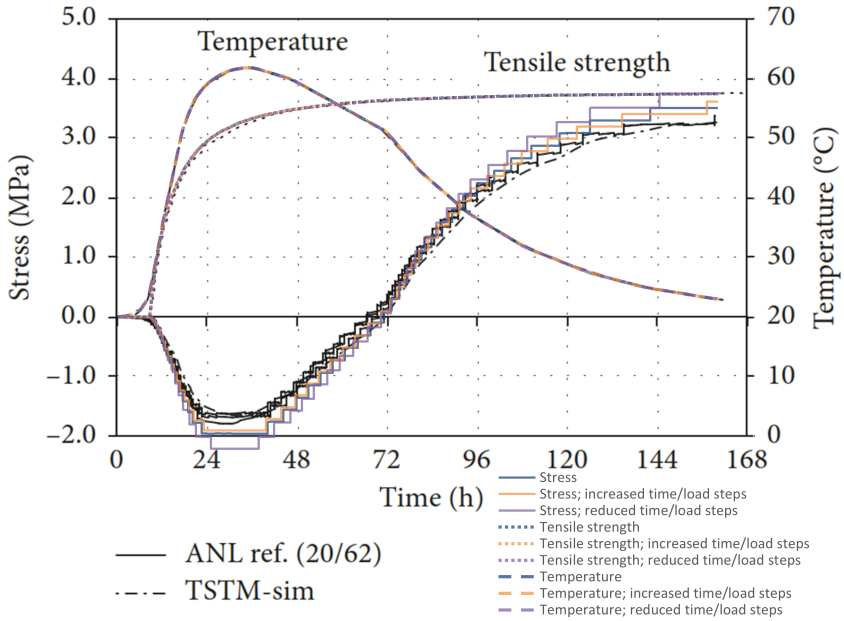

Figure 3.12: Time and load step size comparison for the TSTM model.

From the above figure it is concluded that the time and load steps do not affect the temperature and tensile strength development. However, for the stress development it does, and it can be seen that the larger the time and load steps, the closer the results are to the experiment. In particular, the four times smaller time/load steps deviate by about $0.25 - 0.35$ MPa for both compressive and tensile stresses. The four times larger time/load steps follow the original time/load steps quite well for the first few days, but start to deviate slightly after about 4 days. This appears to be more accurate as it comes closer to the stress development from the experiment, but only by about $0.05 - 0.1$ MPa compared to the original time and load steps. However, this analysis took four times as long to run, about an hour, which is less convenient if several analyses need to be done. Therefore, the original time and stress steps chosen were accurate enough.

3.2.6. Comparison between strain parameters of the experiment, Eurocode, fib and CIRIA

To find the influence of specific strain parameters used in the TSTM model, which is based on all thermal and mechanical properties from the Klausen experiments, a comparison is made between the experiment and what would be chosen in the absence of the experiment based on EN1992-1-1, fib Model Code 2010 and CIRIA C766. This is done first for thermal strain, which is influenced by changing the coefficient of thermal expansion, and then by changing the autogenous shrinkage development.

Coefficient of thermal expansion

The coefficient of thermal expansion (CTE), which dominates the thermal strain for a given temperature development, was measured in the Klausen study for the different concrete compositions. A comparison is made between the experimental CTE and the CTE described in the Eurocode, fib Model Code 2010 and CIRIA C766.

As described earlier in Section 2.1.2, both EN1992-1-1 and the fib Model Code 2010 describe a CTE of $10{\cdot}10^{-6}$/°C, independent of the aggregates used in the concrete mix. CIRIA specifies a specific CTE based on different aggregates, which can be taken from Table 4.6 of CIRIA C766 [3]. For the Klausen study, it is known that a mixture dominated by granite and gneiss aggregates was used, with sand from the same rock. Although gneiss is not included in the table, granite is and has a CTE design value of $10 \cdot 10^{-6}$/°C. If the influence of the unknown CTE of gneiss is neglected for this comparison, and only the CTE of granite is used, all three sources recommend the same CTE of $10 \cdot 10^{-6}$/°C. The same CTE is prescribed regardless of the concrete composition, so a comparison is made between the prescribed CTE value and the CTE based on Klausen's CEM I experiment ($9.0{\cdot}10^{-6}$/°C) CEM I, as this is where the difference is greatest. See Figure 3.13 for the difference in thermal strain and stress development.

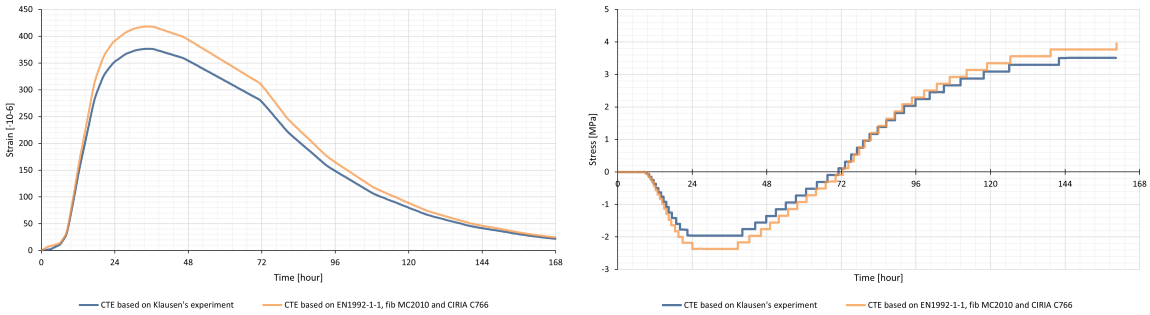

(a) Temperature strain

(b) Stress development

Figure 3.13: Comparison between the experiment model, EN1992-1-1, fib Model Code 2010 and the CIRIA C766 for the coefficient of thermal expansion (CTE).

The figure above shows that the stress development at a higher CTE is more extreme, i.e. both the compressive stress and the tensile stress are higher. This is expected because the thermal strain has increased by 11.1%, causing the specimen to expand and contract more. In order to partially restrain this, more pushback steps are applied, resulting in higher stresses. The maximum compressive stress increases by 21% from -1.96 to -2.37 MPa and the maximum tensile stress increases by 7% from 3.51 to 3.77 MPa. It should be noted that a stress of 3.77 MPa can only be achieved in this model by assuming elasticity, as the beam should actually crack as this stress is higher than the tensile strength.

The CTE of $10{\cdot}10^{-6}$/°C instead of $9{\cdot}10^{-6}$/°C therefore has a influence on the stress development, about 7-21%, although this percentage is not exact as it also has to do with whether an extra pushback step is needed or not. So, especially when using 12-$14{\cdot}10^{-6}$/°C CTE aggregates, the effect of a higher CTE can be very significant.

Autogenous shrinkage

The autogenous shrinkage (AS) development applied to the TSTM model was measured in the dilation rig for the different concrete compositions in the Klausen research. A comparison is made between the AS measured in the dilation rig and that described in the Eurocode, the fib Model Code 2010 and CIRIA C766.

The AS of two different cement compositions were analysed because both the fib Model Code 2010 and CIRIA C766 prescribe different autogenous shrinkage development for them, and also because these are the two most commonly used in the Netherlands.

As explained in Section 2.1.3, AS can be calculated based on EN1992-1-1 and the fib Model Code 2010 using the mean or characteristic cylinder strength. The Klausen study found a mean cubic compressive strength of 80.3 and 75.67 MPa for CEMI and CEM III/B respectively. Both are close to a C60/75 or C60 concrete and therefore have a characteristic cylinder strength of 60 MPa and a mean cylinder strength of 68 Mpa. In addition to the characteristic cylinder strength, the fib Model Code also uses a parameter based on the strength class of the cement used, which in Klausen's experiment was 52.5 N for CEM I and 42.5 N for CEM III/B concrete.

CIRIA C766 recommends the same equation as the Eurocode, but recommends the use of a factor in the design to account for various admixtures in the cement, e.g. silica fume, fly ash and ggbs. Based on this, the CEM I concrete AS should be increased by 50% for the 5% silica fume and the CEM III/B by both 50% for the 5% silica fume and 54.4% for the 68% ggbs. The latter results in an increase of 131.6%. The autogenous shrinkage and the corresponding stress development for CEM I and CEM III/B are shown in Figures 3.14 and 3.15 respectively.

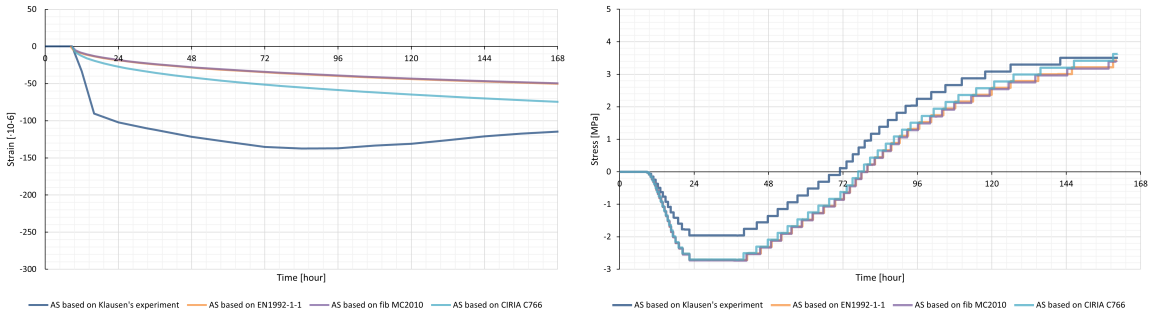

(a) Autogenous shrinkage strain (b) Stress development

Figure 3.14: Comparison between the experiment, EN1992-1-1, fib Model Code 2010 and CIRIA C766 for autogenous shrinkage (AS) development for CEM I concrete composition.

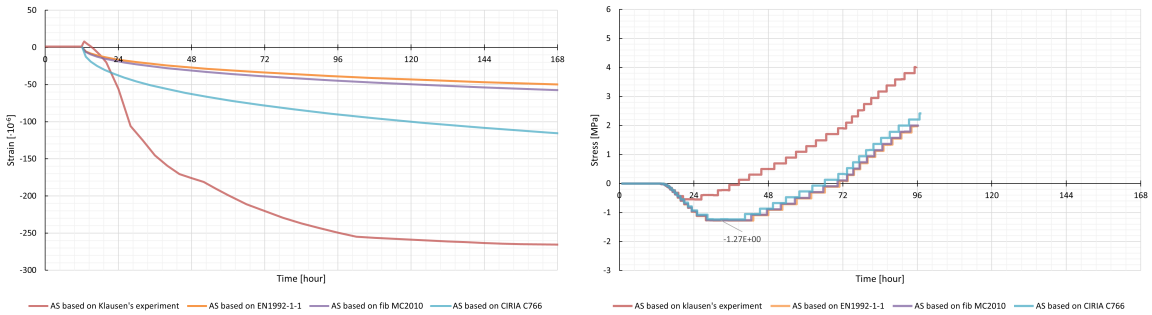

(a) Autogenous shrinkage strain (b) Stress development

Figure 3.15: Comparison between the experiment, EN1992-1-1, fib Model Code 2010 and CIRIA C766 for autogenous shrinkage (AS) development for CEM III/B concrete composition.

Figures 3.14a and 3.15a show that there is a large difference in AS between what is measured within the Klausen dilatation rig and what is prescribed by the standards/guidelines. Although all the AS developments differ significantly, the CIRIA AS, which includes a factor above the Eurocode AS calculation, appears to be in best agreement with the experiment for both cement compositions compared to the Eurocode and the fib Model Code. Both measured AS show a large increase in AS within the first day, whereas the Eurocode and fib Model Code show a very slow increase.

Figure 3.14b, with CEM I concrete, shows that the stress development with the AS based on CIRIA is slightly closer to the experimental model with the measured AS than the Eurocode and the fib Model Code. There is almost no difference between the latter two models. As the AS increases very slowly compared to the measured AS, all the models are more negative in the first few days, after which, as the measured AS from the experiment decreases and the other AS continues to increase, the results of all the analyses become quite close at the end of the analysis.

For the CEM III/B concrete shown in Figure 3.15b, it can also be seen that the stress development of the CIRIA model is slightly closer to the experiment than that of the Eurocode and fib Model Code analyses. Again, there is almost no difference between the latter two models. The reason why all 3 models find a higher negative stress is again mainly because the measured AS in the experiment has a large increase in the first hours when the concrete also experiences large positive thermal stresses and so this is partly compensated by autogenous shrinkage.

In conclusion, all the AS developments analysed underestimate the amount of AS, especially due to the large increase shown in the experiment in the first day(s). In the absence of this large increase, the compressive stress is higher (around 0.7-0.8 MPa) and therefore the development is shifted downwards. Of the three AS studied, the one based on CIRIA was found to be closest to the experiment, but not really close. Therefore, it seems appropriate to consider the different types of shrinkage between the Eurocode/fib Model Code model and CIRIA C766 in the parameter study for the case study analysis.

3.2.7. Comparison between the experiment, Eurocode and fib Model Code

In the analysis of the TSTM model, the 'power law viscoelasticity and Young's hardening' material model was used in combination with all the material properties/developments based on Klausen's research. All these parameters are not available when analysing the case study in the next chapter. Therefore, a comparison is made between the experimental model for the CEM I cement composition and both the Eurocode and the fib Model Code to see which model is more suitable for use in the case study. The same strength class (C60/75 for EN1992-1-1 and C60 for fib Model Code 2010), cement type (52.5N) and autogenous shrinkage are used as explained in the previous section.

For the aggregate type, granite and gneiss were used in the experiment, but as neither is an option based on EN1992-1-1, quartzite is used. For both models, the ambient temperature is chosen to be $20\,°C$, as used in the experiment. For the notional size (h_0), defined as $2A_c/u$, a value close to infinity is chosen ($9 \cdot 10^{10}$ mm), since the specimen is completely closed, u, the perimeter in contact with the atmosphere, will be 0 and thus the notional size goes to infinity. The ambient relative humidity is set to 100% as the specimen is completely sealed and the concrete age at the end of the curing period is set to 0. With these parameters set, the material model calculates the development of the creep factor, the autogenous and the drying shrinkage. The drying shrinkage results to 0 as no drying can take place.

The thermal properties applied are the same as in the original model, since they have little influence, since in this model the temperature development is applied directly to the outside, and a comparison between these parameters is already made in Section 3.1.5 for the semi-adiabatic temperature model.

The results of the analysis and the comparison between the Eurocode and fib Model Code material models are shown in Figure 3.16. Figure 3.16a shows the temperature, tensile strength and stress development and as the Young's modulus development is also an important parameter, and differences can be seen, this is shown in Figure 3.16b.

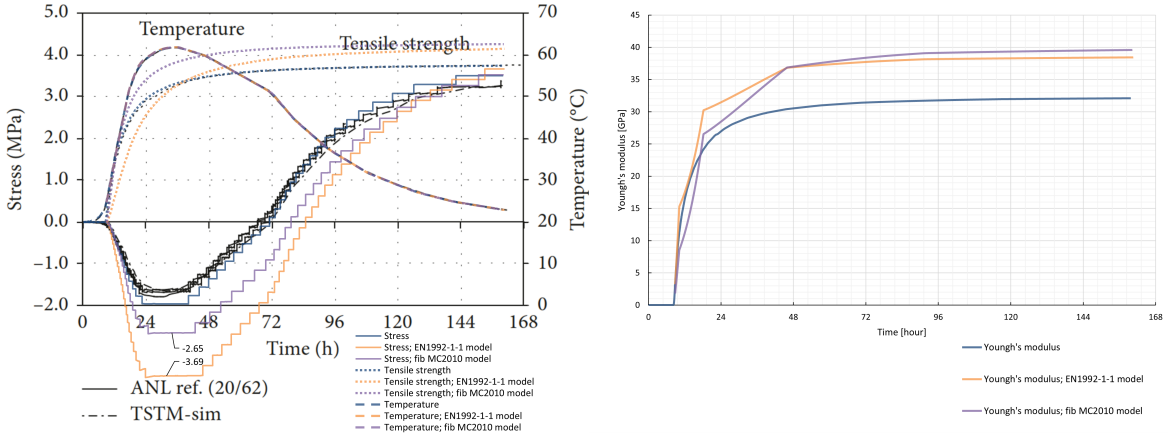

(a) Comparison temperature, tensile strength and stress development

(b) Comparison Young's modulus development

Figure 3.16: Comparison between the experiment, experiment model, EN1992-1-1 model the fib Model Code 2010 for CEM I cement composition.

From Figure 3.16 it can be seen that the temperature development remains the same, which is as expected. The other developments follow the same trend but there are some significant differences. Although the tensile strength development converges to another 28-day tensile strength, the fib Model Code development fits much better. However, this is also due to the way DIANA FEA interprets the fib Model Code, as the fib states that it can be assumed that the tensile strength development is equal to the compressive strength development [5]. While DIANA FEA interprets this as saying that for each time step the corresponding tensile strength should be calculated based on the current compressive strength. This is therefore included in the programmed fib Model Code material model within DIANA FEA. However, the Eurocode uses the same β_{cc} factor for the tensile strength development for the first 28 days as for the compressive strength, which is also an interpretation of what is stated in the fib Model Code. Hence the difference in tensile strength development.

Significant differences can also be seen in the development of Young's modulus and stresses. Both Eurocode and fib Model Code analyses use Kelvin chains for the creep calculation, but the discrete time/maturity steps (0, 0.1, 1, 7, 14, 28 days, etc.) introduce a non-smooth Young's modulus development. While the effect may be limited for long term analysis over several years, it will lead to inaccurate results for a short term calculation of 7 days. The stress development follows a similar trend, but deviates significantly from the experimental results, particularly in the first three days. Although this could be due to the higher Young's modulus, higher CTE and different AS development, it could also be due

to the discrete time/maturity steps used in the models. To ensure this was the case, it was decided to create a new viscoelastic material model based on the fib Model Code, in which more time steps could be implemented, especially in the short term. The fib Model Code was chosen because it gives a slightly better approximation of tensile strength and stress development. As the fib Model Code is completely pre-programmed into the program and cannot be changed, a new material model should be created, which will be explained in the next subsection.

3.2.8. Creating and comparing a new viscoelastic material model

As discussed in the previous subsection, the standard material models used in DIANA FEA showed significant differences from the experimental results, particularly in the first few days. This difference was assumed to be due to the relatively large time/maturity steps used for the creep/Kelvin chains and Young's modulus development. To address this issue, a new viscoelastic material model was created using a Python script provided by NLyse Consultants, an engineering consultancy, which was slightly adapted. This material model, the 'Maxwell/Kelvin chain viscoelasticity' material model, was filled with inputs based on the fib Model Code 2010, which, as mentioned in the previous subsection, showed results closer to experiment than the Eurocode.

Unlike the original material model, which included only five time/maturity steps within the first seven days, the new material model allowed up to 30 maturity steps. The viscoelastic material model included a Kelvin chain/creep function, which was entered into a 30x30 table, as the creep function is both time and maturity dependent. To validate the viscoelastic material model based on the fib Model Code, the analysis results were first compared with the experiment. Then, using a simplified model, the material model was validated against the analytical solution by hand calculations as well as against the default fib Model Code material model within DIANA FEA.

Comparison for the TSTM-model with the experiment

The TSTM analysis is performed using the viscoelastic material model created based on the fib Model Code. In this analysis, the thermal and mechanical properties are the same as those used in the default fib Model Code material model in DIANA FEA. The only differences are the material model itself and the additional steps included during early age. The result of this analysis is shown in Figure 3.17.

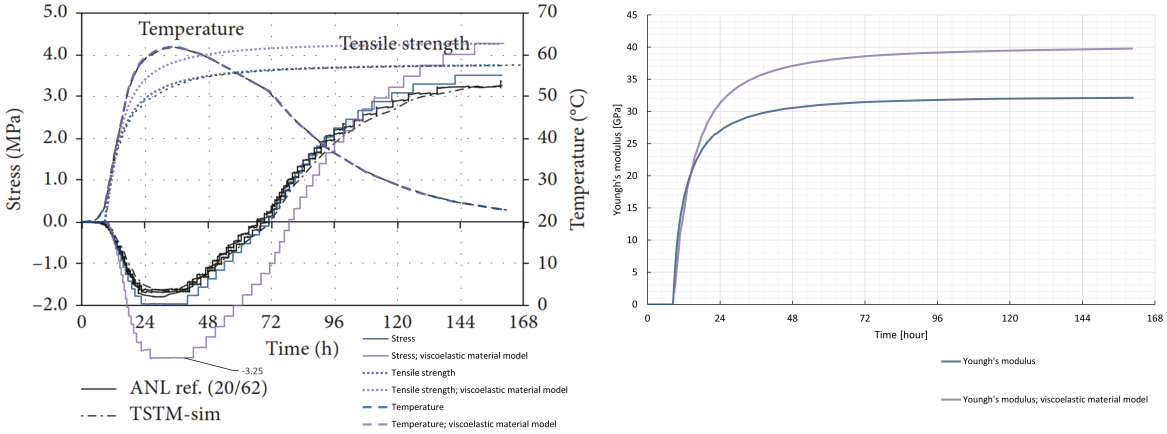

(a) Comparison temperature, tensile strength and stress development

(b) Comparison Young's modulus development

Figure 3.17: Comparison between the experiment, the experimental model and the viscoelastic material model based on the fib Model Code 2010 for CEM I cement composition.

From the results shown in Figure 3.17, it can be seen that the Young's modulus in this analysis is smoother and more consistent with the experiment compared to the original fib Model Code. However, it still tends to approach a higher 28-day modulus.

The stress development for this material model deviates from the experiment even more than the default fib Model Code material model. However, this is partly expected as the previous section showed that the higher predicted coefficient of thermal expansion (CTE) and lower autogenous shrinkage (AS) in the fib Model Code lead to higher compressive stress in the first two days for CEM I cement classes. Specifically, the higher CTE results in an increase in compressive stress of -0.41 MPa, while the AS based on the fib Model Code results in an increase of -0.77 MPa. Combining these effects, the compressive stress is expected to increase by -1.18 MPa. Adding this to the -1.96 MPa from the

original model for the experiment, the expected compressive stress is -3.14 MPa, which is close to the observed -3.25 MPa. This final difference can be attributed to the fact that the 28-day Young's modulus in the fib Model Code is 24% higher (40.73 GPa compared to the measured 32.80 GPa in the experiment), resulting in higher stresses.

To further verify the correctness and accuracy of the Kelvin chain viscoelastic material model based on the fib Model Code, it was decided to perform an additional analysis. A comparison was made between this material model but with the measured material properties based on Klausen's research, the original material model and the experiment. The viscoelastic material model is included with the same CTE and AS taken from the experiment and the 28-day mechanical properties are also corrected. The 28-day modulus was reduced by 24% to give the same 28-day stiffness rather than using the Young's modulus development from the experiment. As the Young's modulus development also affects the Kelvin chains entered for each time/maturity step, it is easier to reduce the total development by the same factor. The 28-day tensile strength of the fib Model Code was reduced by 11.4% to be able to compare the development as well. The results of this analysis using the viscoelastic material model, partially using the experimental properties, are shown in Figure 3.18.

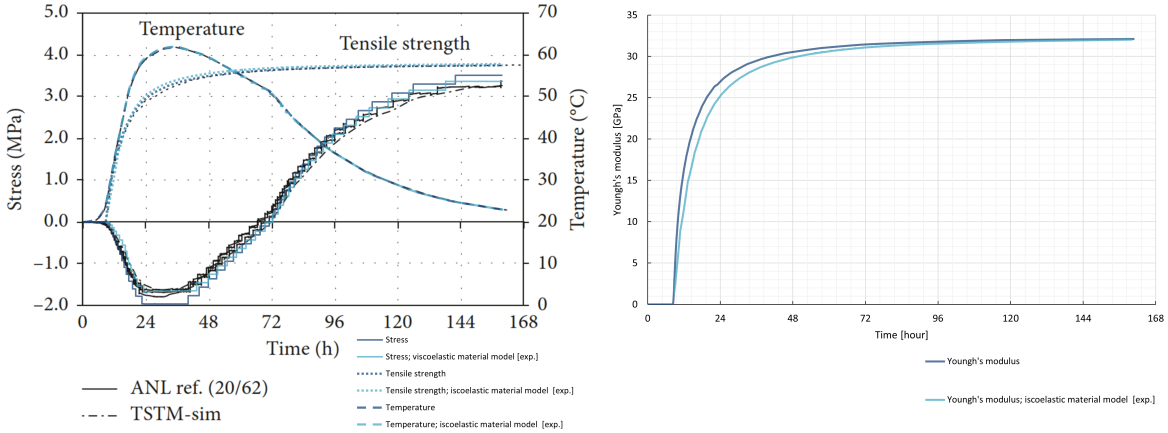

(a) Comparison temperature, tensile strength and stress development

(b) Comparison Young's modulus development

Figure 3.18: Comparison between the experiment, the experimental model and the viscoelastic material model based on the fib Model Code 2010, using the AS, CTE and corrected mechanical properties based on the experiment for CEM I cement composition.

From the above figure it can be seen that for the corrected modified fib Model Code material model the stress development is almost exactly the same as the experiment. Tensile strength and Young's modulus are also quite close as the 28 day results are correct to be the same. It can therefore be concluded that the viscoelastic material model created is accurate. However, the results differ significantly when different CTE, AS and mechanical properties are used. This emphasises the need to performm a parameter study for the case study, particularly for the CTE and AS. It is assumed that the deviations in the mechanical properties are mainly due to the aggregate used in the experiment, which is not specified in the standards. The case study is likely to use more commonly used aggregates, which should result in improved accuracy.

Furthermore, it can be concluded that the viscoelastic material model based on the modified fib Model Code, using Kelvin chains for creep calculations, shows good agreement with the experimental data. This finding suggests that the creep equations from the fib Model Code, implemented in DIANA FEA with Kelvin chain viscoelasticity, can be applied in the case study of the following chapter, even in the absence of experimental creep data.

Comparison for the a simplified analysis with a hand calculation

As significant differences were observed between the viscoelastic material model based on the fib Model Code and the default fib Model Code within DIANA FEA, a comparison is made for simplified scenarios. This comparison also includes a hand calculation to assess the reliability of the results. This is done for two cases, the first is a simplified model, free to deform model, where a constant load is applied at the start and for another analysis at three days. The second case is a load applied for three days as a prescribed displacement which remains in fully restrained. The first case simulates the behaviour of creep, the increase of the deformation with time with respect to the direct deformation under

continuous load, the second case simulates more the relaxation, the decrease of the initial stresses with time while the deformation of the material is kept constant.

In the first case, the same finite element model is used as described in Section 3.2.2, but a different analysis is performed as described in Section 3.2.3. The transient heat transfer analysis is the same and the same time steps are applied, but only one load of 1 MPa is applied either at 0 or 3 days. This simplified model does not include hardening stresses and shrinkage, so the only stress on the specimen is from the applied load. The results of the analysis, specifically the creep strains, are shown in Figure 3.19 for both the default fib Model Code analysis and the viscoelastic material model based on the fib Model Code.

The hand calculation is performed as explained in Section 2.1.4 and Equation 2.14 is used to calculate the creep strain. As the relative humidity is set on 100%, as the TSTM specimen is fully sealed, only the autogenous/basic creep coefficient is calculated using the fib Model Code 2010. The result of the hand calculation is also shown in Figure 3.19.

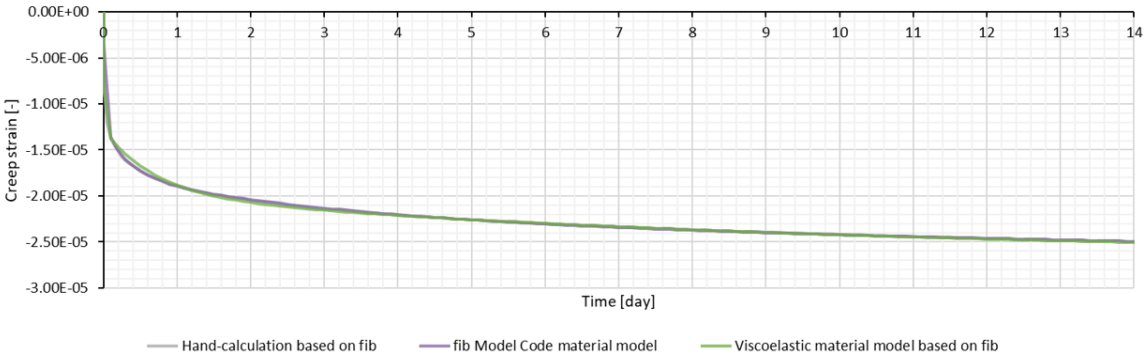

(a) Load applied at $t = 0$ days.

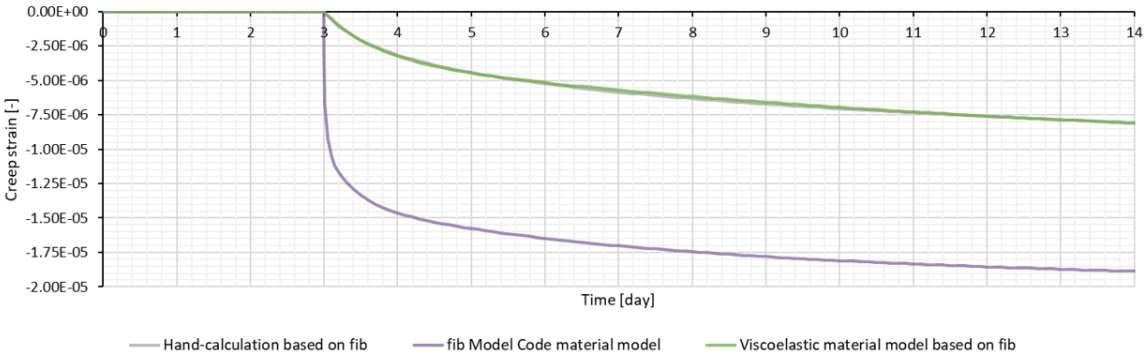

(b) Load applied at $t = 3$ days.

Figure 3.19: Creep strains development for an applied load on two different times for a simplified model.

Although difficult to see, Figure 3.19 shows the same creep development for the viscoelastic material model for the load applied at both times compared to the hand calculation. The default fib Model Code within DIANA FEA only shows the same creep development for the load applied at $t = 0$. For the load applied at $t = 3$ days, the results differ significantly, especially between three and four days. Where the creep strains from the default fib Model Code increase significantly, the creep strains from the hand calculation and the results from the viscoelastic material model increase slowly.

For the second case, the same model and analysis is used as for the previous case, except that both sides are restrained in the X-direction and instead of a load applied at three days, a prescribed displacement is added. The prescribed displacement corresponds to a load of 1 Mpa. This simplified model does not include the hardening stresses and shrinkage, so the only load on the specimen is the prescribed displacement applied. The creep strains are shown in Figure 3.20 and the stress evolution is shown in Figure 3.21 for both the default fib Model Code analysis and the viscoelastic material model based on fib.

The hand calculation for the creep strains is performed using Equation 2.14 as explained in Section 2.1.4. The stress development is calculated as explained in Section 2.1.6 using Equation 2.22 (with $\varepsilon_{cs}(t) = 0$). As the relative humidity is 100% and the TSTM specimen is fully sealed, only the autogenous/basic creep coefficient is calculated using the fib Model Code 2010.

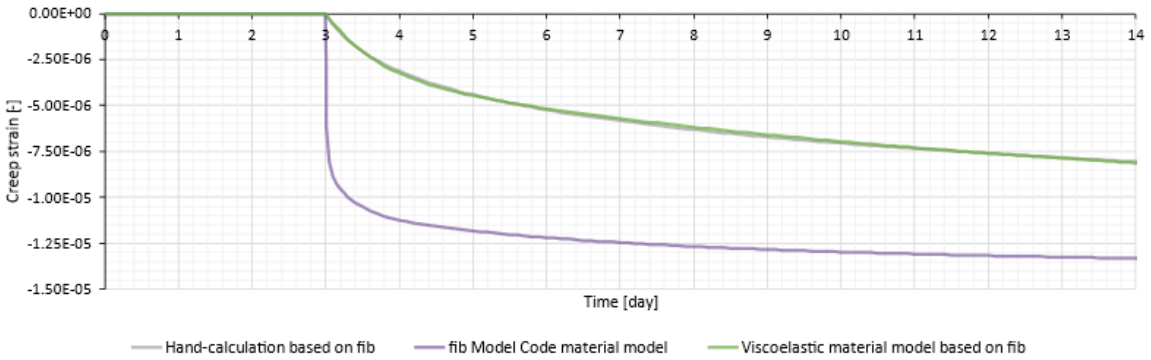

Figure 3.20: Creep strains development for a prescribed displacement applied on 3 days for a simplified model.

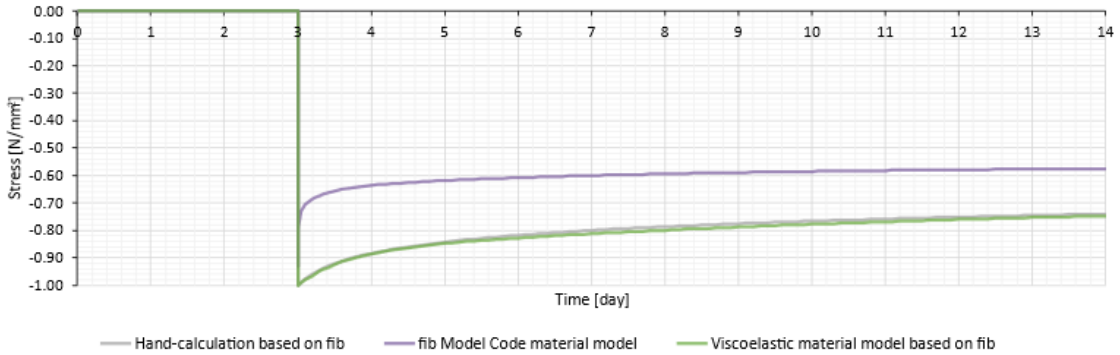

Figure 3.21: Stress development for a prescribed displacement applied on 3 days for a simplified model.

Both Figures 3.20 and 3.21 show, although difficult to see, that the viscoelastic material model follows the same line as that calculated by hand. Both the strains and stresses from the default fib Model Code deviate significantly from the manual calculation. Especially the stress development (Figure 3.21) shows a very unrealistic behaviour, as if in one hour after applying the default stress of 1 MPa the stresses are reduced by $25-30\%$, whereas in the hand calculation it is only about one percent. This is due to the large increase in strain at the same time, which is also not expected from the hand calculation.

In conclusion, from both the 'creep' and 'relaxation' simplified cases, it appears that the viscoelastic material model created using a Phyton script agrees well with the hand calculations. What exactly the problem is within this model is unknown, but is not relevant for the continuation of this research. As it is shown that the viscoelastic material model can be used accurately, it is validated that this material model can be used in the case study.

4

Case study model and analysis

This chapter describes the modelling and analysis of the case study, a project calculated by Wagemaker, based on all the research carried out and described in the previous chapters. The case study is the closed section of the railway underpass at the Kanaalweg in Leiden, previously described in SectionPreliminaryResearchCaseStudy. This is done to answer the third and fourth sub-research questions: (3) Which specific time-dependent calculation method and model is most beneficial to use for the design of partially restrained concrete? and (4) What are the differences in design stresses when comparing the time-dependent method and model with a calculation based on the traditional approach for a specific project?

To answer the third sub-research question, all the different calculation methods and models presented in Section 2.2.4 are compared and considered. The most beneficial calculation method and model is selected on the basis of a decision table when there are several possible options.

Based on the selected calculation method and model, a modelling approach for the case study is developed. This is followed by a description of the material properties/specifications, most of which are taken from the original calculation and the remaining are assumed based on literature. Then, based on the selected method and model, some pre-processing is performed to be able to model the case study. The finite element model, programmed in the finite element program DIANA FEA, is described in the subsequent section. This is then followed by a description of the calculation analysis, also based on the choices made in the modelling approach. Finally, the analysis results and post-processing are described, including several analysis checks to validate the analysis results.

In the final section, based on all the analyses performed, a full comparison is made between the results of the more detailed time-dependent analysis and the traditional approach used in the original calculation. This is done to answer the fourth sub-research question of this research.

4.1. Consideration and selection of calculation method and model

Before the case study can be modelled, some choices and considerations are made for which type of elements and if a 2D or 3D model will be used. In Section 2.2.4 both the different methods to calculate the combination of the hardening stresses with the external loads, and also different types of calculation models are explained. In this section, first a comparison is made between the different calculation methods to decide the most suited method that will be used for the case study. In the subsection after that, based also on the method, a consideration and decision is made between different types of elements and a 2D or 3D model.

4.1.1. Consideration and selection of the calculation method

This subsection describes the consideration and decision which type of calculation method will be used for this particular case study. Below is a brief overview of the three methods, which are explained in more detail earlier in Section 2.2.4.

- Method 1; a combination of a ‘manual’ calculation for the hardening phase with a calculation model for the external loads
- Method 2; a combination of a calculation model for the hardening phase with a calculation model for the external loads
- Method 3; a combined calculation model for both the hardening phase and the external loads

The first method is closely related to the calculation of the case study, where a manual calculation was performed and combined with a 3D calculation model using 2D flat shell elements. The second method is a combination of two calculation models, one where a time-dependent analysis is performed, including all hardening processes, and one where all load combinations from external loads are included. The third method is a calculation model in which both the hardening phase and the external load are combined into one large model that includes time and load steps. To make a decision between the three methods, a decision is made based on; calculation accuracy and completeness, computation complexity and time, engineering time for both pre- and post-processing, and insight into the governing load. These decision points are described and reasoned as not/less beneficial (-), neutral (0) or (more) beneficial (+) compared to the other methods.

Calculation accuracy and completeness
The first method has the lowest accuracy and completeness because it does not take into account time dependence. This means that the development of temperature, equivalent age and mechanical properties cannot be accurately considered and the calculation accuracy, especially for the hardening phase, is low. The second method is slightly more accurate and more complete because the hardening phase is time-dependent and therefore all time-dependent properties can be included. However, as not all results and properties can be transferred to the second external load model, some accuracy and completeness is lost. The third method, with a complete computational model, should have the highest accuracy and completeness because all relevant properties and results are in the same model.

Computational complexity and time
Regardless of the calculation model used, the first method will have the lowest complexity and time because it is not time-dependent and will therefore be beneficial. The second method is in between the first and third because although both a time-dependent calculation and a load calculation are performed, the calculation is separate. This significantly reduces the complexity and time of the calculation. The third method has the highest computational complexity and time, and is therefore less beneficial due to the combination of time and load steps.

Engineering time - pre-processing
The first method requires a lot of engineering judgement and pre-processing to make accurate and difficult scientifically based assumptions, e.g. for the temperature peak. However, because it can be calculated relatively quickly using a standard Excel or other fast calculation, this method is considered neutral. The second and third methods require many more assumptions, such as the ambient and pouring temperatures, time-dependent thermal boundary conditions, specific concrete mix, and so on. This is a lot, but the assumptions are easier to make and justify. For both methods, compared the first method, it is less beneficial to either model two computational models or to model one complex model and explain the assumptions.

Engineering time - post-processing
The fourth decision criterion is the amount of engineering time required for post-processing. For the first and second methods, although the results of the ‘manual’ or hardening phase model have to be combined with the external results, this is not much or a very difficult task. This is therefore considered to be neutrally beneficial. The third method, because both models are combined, there is less post-processing and therefore this method is beneficial.

Insight critical time/governing load
The fifth and final decision criterion is the ability to gain insight into which time step is critical for calculating the governing loads. For the first method, this is less beneficial because the hardening phase is usually only calculated for a specific time step. This can be reduced for other time steps, say ‘$t=\infty$’, to account for creep/relaxation. But there is no insight into when the critical time might occur and at which load. Therefore, conservative assumptions are often made to be on the safe side. The second method is considered to be neutrally beneficial because, when using a time-dependent calculation, the critical time and governing load for the hardening phase can be calculated, but this may not be the total critical time. This may not be the critical time for the external load model because external loads are also time-dependent to some extent. For example, due to fatigue or prestressing losses. So the full insight is still not achieved. The third method is the most insightful, as both analyses are combined, the calculation model can include all time-dependent hardening/external loads to find the critical time step and thus the governing load.

Table 4.1: Decision-making table for the different methods.

	Method 1	Method 2	Method 3
Calculation accuracy and completeness	-	0	+
Computational complexity and time	+	0	-
Engineering time - pre-processing	0	-	-
Engineering time - post-processing	0	0	+
Insight critical time/governing load	-	0	+
Total:	**-**	**-**	**+**

Based on the decision table (Table 4.1), the third method is selected for the case study. This combined calculation model method has some good advantages in terms of computational accuracy and model completeness, and is also the easiest to post-process and gives the most insight into the critical time steps. Although this is the best method based on the decision table, it will be good to consider how the negative aspects of this method could possibly be reduced in the modelling approach. These include computational complexity and time, and pre-processing by modelling the complex model. In the modelling approach, efforts should be made to reduce the number of load combinations or to reduce the complexity, for example. In the following section, the most appropriate computational model for this type of computational method is selected.

4.1.2. Consideration and selection of the calculation model

This subsection describes the consideration and decision of which calculation models to use for this particular case study. Below is a brief overview of the five calculation models, which are explained in more detail earlier in Section 2.2.4.

- 2D plane strain elements within a 2D cross-sectional model
- 2D plane stress elements within a 2D model
- 2D plate bending elements within a 2D model
- 2D flat shell elements within a 3D model
- 3D solid elements within a 3D model

Due to the chosen calculation method, the 2D plane strain elements within a 2D cross-section model, which could have been used to model the hardening phase in one direction, is not possible. This is because they are not suitable to perform the full calculation with the external loads. 2D plate bending elements are also not possible as the main interest for this case study is in the walls, which are dominated by in-plane loading. This is not possible with this type of element. Also the other 2D elements, the 2D plane stress within a 2D model and the 2D flat shell within a 3D model, cannot be used to describe the walls of the case study. This is due to the calculation theory used and according to this theory and the DIANA FEA manual, these elements require the thickness to be thin. In other words, the thickness (t) must be small compared to the dimensions in the plane of the element. This is not the case for the wall in this case study. The thickness of the wall is about $1250\text{-}900$ mm thick and only about 4000 mm high. So the thickness cannot be considered thin compared to the height. The only way to accurately model the structure is to use solid 3D elements.

Solid 3D elements are also the only type of element that can be used to accurately calculate the transient heat transfer analysis. This is because solid 3D elements can calculate the temperature along the thickness and allow all thermal boundary conditions to be described on all surfaces. The main disadvantage of solid 3D elements in combination with the third method is that the computational complexity and time is quite high. This is because many elements must be used to mesh the entire case study to obtain accurate results, and many time steps, phases and loads must be included. In order to reduce the computation time, some assumptions have to be made in the modelling approach.

4.2. Modelling approach

The closed section of the case study, the underpass at the Kanaalweg in Leiden, will be modelled using the finite element program DIANA FEA. As previously specified, this will be done using a combined time-dependent analysis including both the hardening phase and the external loading within a 3D model using 3D solid elements. The case study, as explained in Section 2.2.2, consists of several phases at varying time intervals. While the exact timing is unknown, reasonable assumptions are made based on temporary track suspensions and project visits by Wagemaker. The different phases included in the model and the different time steps are specified below:

- Phase 1, $t = 0$ days; Pouring the deck on support.

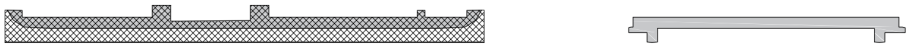

Figure 4.1: Schematic representation of longitudinal and cross-sectional, phase 1.

- Phase 2, $t = 100$ days; Placing the deck onto sheet piles and applying dead loads on deck.

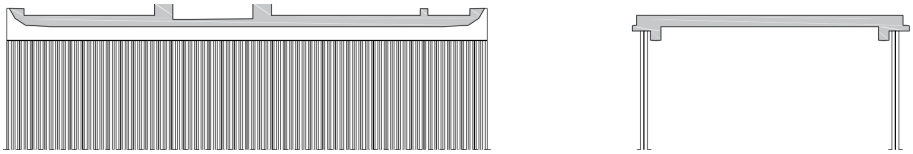

Figure 4.2: Schematic representation of longitudinal and cross-sectional, phase 2.

- Phase 3, $t = 200$ days; Pouring of the floor.

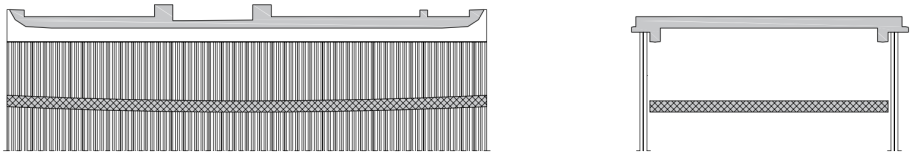

Figure 4.3: Schematic representation of longitudinal and cross-sectional, phase 3.

- Phase 4, $t = 250$ days; Pouring of the walls between the floor and the deck.

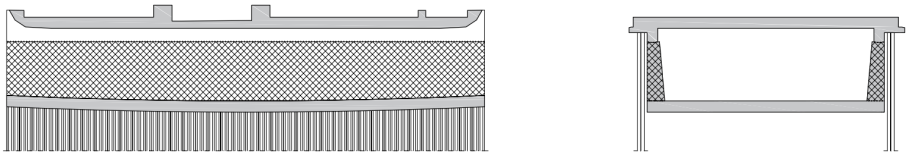

Figure 4.4: Schematic representation of longitudinal and cross-sectional, phase 4.

- Phase 5, $t = 300$ days; Disconnecting the sheet piles and applying dead loads on floor and walls.

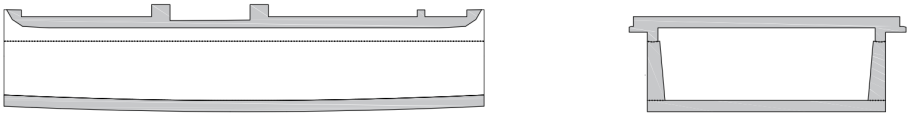

Figure 4.5: Schematic representation of longitudinal and cross-sectional, phase 5.

The model consists of five different phases in order to simulate the actual construction process as closely as possible. It is assumed that there are 100 days between phases 1 and 2, as well as between phases 2 and 3, as opposed to 50 days for the remaining phases. This extension is due to the pre-stressing of the deck after the concrete has hardened before it is placed on the sheet piles[1] between phases 1 and 2, and the extended time required to excavate the underpass and install the floor formwork and reinforcement between phases 2 and 3.

The self-weight of the concrete elements is taken into account immediately after placement. This will result in large deformations for the deck. Therefore, in the first phase, the deck is fully supported in the Z-direction, which is also the case in practice due to the formwork and temporary supports. The dead loads are applied to the deck at the start of the second phase, as the track section is completed during the same track suspension in which the deck is placed. This means that most of the dead load is applied directly on the deck. Dead loads on the floor and walls are assumed to be applied when the connection to the sheet piling is disconnected and the deck is fully supported by the walls.

[1] In the final execution, the choice was made to rest the deck on tubular steel piles. This was checked and recalculated, but no changes were needed because the steel tubular piles were so close together that it closely resembled a line support used for sheet piling. But to make a fair compression on the original calculation, sheet piling was assumed in this case study analysis.

After all the dead loads have been applied to the structure (after phase 5), the critical time step is considered where the mobile load should be added. This is deliberately not done for the deck during the temporary situation as the focus of this study is on the wall and not the deck. Although other options were considered that did not include modelling of the deck, it was finally decided to include it. Mainly because the pre-processing to convert the different loads on the deck to the wall would be very time consuming, and also because the geometry and equivalent age of the deck is important for the degree of restraint of the wall. The mobile loads are therefore added at the critical time step, but at least after the firth phase. The critical time step is obtained from the force/stress development within the wall. It is assumed that the most critical time step is within the first 50 days after sheet pile removal (at 300 days), as creep slowly reduces the residual stresses. It is also assumed that the most governing load combination is expected to occur one day after the sheet piles are connected, as this is likely to occur during a rail suspension. This is conservative because although the mobile load of the train is expected, the mobile loads on the floor and walls are not, as the underpass was not opened to traffic until several months later. However, this is disregarded because some of the dead loads, such as the asphalt in the tunnels, asphalt trucks and other construction vehicles, must be present. Of these, the variable load may be close to the variable load in use.

To reduce the computation time, it was decided to model only half of the underpass. Although the structure of the wall and floor is symmetrical, the deck is not, because the railway does not cross the underpass perpendicularly. However, the influence is expected to be limited. This is concluded from the fact that the displacement in the deck due to dead load and self-weight is almost symmetrical. This means that both walls carry approximately the same weight/load. Wagemaker's calculations showed that the wall on the east side was slightly more critical when calculating the reinforcement for the walls. It was therefore decided to model only this side with its associated forces and to use symmetry supports.

For accurate heat transfer analysis, different thermal boundaries with different heat transfer convection coefficients are used to simulate formwork, soil and free surface convection. Within a phase, a time dependent heat transfer convection coefficient is used to simulate the removal of the formwork after 3 days for the wall and floor. These 3 days are based on a slightly similar case study performed by van Bokhorst [15]. For the deck, 14 days is assumed, as there is no rush to remove the formwork, except for the prestressing of the deck, which may start after 14 days.

The structural analysis will be non-linear, but without the development of concrete cracking. It will include material non-linearity as mechanical properties, creep and shrinkage are time-dependent functions. Some of these are also based on equivalent age/maturity and therefore temperature. No-tension (non-linear) material properties are used for the soil bedding. Geometric non-linearity is also used, although its influence was very limited as the displacements were relatively small.

As a structural non-linear calculation is performed in DIANA FEA, only one load combination can be applied per analysis. Each analysis takes several hours or days, so only one of the more than $10\,000$ load combinations from the original calculation is analysed. Based on the original calculation, the governing loads and combinations are selected to be applied to the model and analysed in the structural non-linear calculation. This is because ultimately only these distributed forces and moments are compared with the original calculations.

The concrete material properties are applied using the viscoelastic material model verified in the previous chapter, which is based on the fib Model Code 2010. In Wagemaker's calculation, a minimum concrete class of C45/55 was specified for the deck and a minimum of C30/37 for the other parts. This is equivalent to C45 and C30 respectively based on the fib Model Code. The original calculation assumes that the concrete deck will not crack due to the prestressing present, but that the walls and floors will crack. This is simulated by reducing the Young's modulus by 50% to make a fair comparison. This is done by reducing the time dependent Young's modulus parameter at a specific time when cracking is expected. This specific time is determined from the crack index, an output of the calculation, which is calculated by dividing the tensile strength by the maximum principal stress. Thus, cracks are expected when the crack index is less than 1.0. For adiabatic temperature development and other thermal properties which are not described in the fib Model Code, the CIRIA C766 is used. The same bedding constants as in the original calculation are used for the sheet piling and soil springs.

The model will and should be discretised using quadratic elements, as this is necessary when combining heat transfer analysis and structural analysis. To ensure deformation compatibility, DIANA FEA automatically solves the heat transfer problem with linear elements and the structural problem with quadratic elements. Consequently, the thermal strain and total strain field are interpolated linearly across elements. The prestressing in the deck is not modelled because it only has a very minor influence on the force action in the wall. Also, all reinforcements are not modelled in the case study model as they do not contribute if no cracking can occur.

4.3. Material properties/specifications

This section specifies the concrete materials used in the case study. The type of concrete and most of the other assumptions are based on the original calculation by Wagemaker. The mechanical properties for the concrete materials will be based on the fib Model Code 2010 and for the thermal properties, which are not specified by the fib Model Code, the CIRIA C766 will be used. In the first subsection, the concrete mixes are specified and then all the mechanical properties and developments are prescribed. Then the thermal properties and adiabatic temperature development are specified and finally shrinkage and creep are specified.

4.3.1. Concrete mixture and properties

For the case study, the specific concrete mixes are unfortunately unknown. However, the specific concrete classes and other calculation assumptions are specified in the original calculation on which the concrete mixes should be designed. For a fair comparison with the original calculation, the same assumptions are made here. The concrete class used for the deck was C45/55 and for both the floor and walls it was C30/37, referred to as C45 and C30 respectively in the fib Model Code. Although the specific concrete mix is unknown, Wagemaker assumes a cement content of 350 kg/m^3 and CEM III concrete for the C30 concrete. Other cement properties were not assumed as they were not required for the calculation. To fairly assume the other mixture parameters, a mixture specification was used from a slightly similar case study performed by van Bokhorst [15]. This mix design was for a C30/37 concrete from concrete manufacturer Mebin B.V. This mixture is a CEM III/B 42.5N concrete with a cement content of 350 kg/m^3 and a w/c factor of 0.45. This mixture with river gravel/sand is assumed for the C30 concrete in this case study. The same properties are assumed for the prestressed deck concrete, but as this is a C45 concrete, a cement content of 450 kg/m^3 is assumed. This is estimated from Table 4.2 of CIRIA C766 [3], where the difference between C30/37 and C45/55 concrete is about 100 kg/m^3 for most cement compositions. A density of 2500 kg/m^3 is assumed for both the reinforced floor and wall, as for the prestressed deck.

4.3.2. Mechanical properties and development

The mechanical properties and their development are important parameters in the calculation analysis. Therefore, they are specified here. The 28-day strengths, 28-day Young's modulus and Poisson's ratio are taken from the fib Model Code 2010 [5]. The mechanical properties for the C30 and C45 concrete used in the case study are given in Table 4.2 below.

Table 4.2: Overview of the (28-day) mechanical properties of the concrete used in the case study.

	f_{ck} [MPa]	$f_{ck,cube}$ [MPa]	f_{cm} [MPa]	f_{ctm} [MPa]	E_{ci} [MPa]	ν
C30 Floor/Wall	30	37	38	2.90	33550.6	0.20
C45 Deck	45	55	53	3.80	37485.5	0.20

Since the case study uses time-dependent finite element analysis for the hardening of the restrained concrete, the development of Young's modulus and tensile strength are important input parameters for the calculation. The development of these mechanical properties is calculated using the fib Model Code 2010, which is also described in Section 2.1.9 and shown in Figure 4.6.

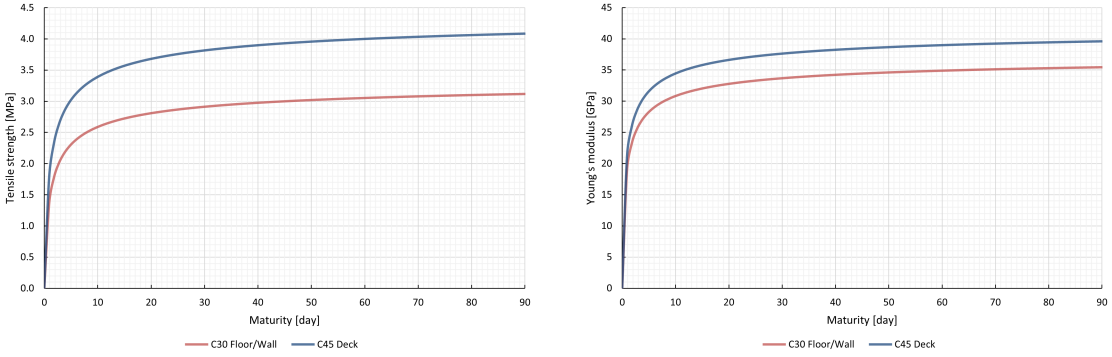

(a) Development tensile strength (b) Development Young's modulus

Figure 4.6: Development of the mechanical properties based on the fib Model Code 2010.

4.3.3. Thermal properties and the adiabatic temperature development

To specify the thermal properties and the adiabatic temperature development in addition to the fib Model Code 2010, CIRIA C766 was also used. For the coefficient of thermal expansion (CTE) $10 \cdot 10^{-6}$/°C is used based on the fib Model Code. CIRIA recommends a 40% higher value of $14 \cdot 10^{-6}$/°C for this specific aggregate used. The original calculation used the CTE specified by the Eurocode, which is the same as the fib Model Code, so to make a fair comparison $10 \cdot 10^{-6}$/°C is used. In the next chapter, the parameter study analyses the CTE from the CIRIA. The following thermal properties have been taken or calculated based on the CIRIA C766:

- Thermal conductivity of concrete: 2.9 W/m °C (taken from Table 4.4 [3])
- Specific heat C30 concrete: 0.987 kJ/kg °C (taken from Figure 4.11 [3])
- Specific heat C45 concrete: 1.048 kJ/kg °C (taken from Figure 4.11 [3])
- Thermal conductance exposed concrete: 23.6 W/m^2 °C (calculated based on Equation A2.22 [3])
- Thermal conductance formwork: 5.3 W/m^2 °C (calculated based on Equation A2.25 [3])
- Thermal conductance sand: 1.3 W/m^2 °C (taken from Table 4.5 [3] (dry sand 25 mm))

To calculate the thermal conductivity for the exposed concrete and formwork, a wind speed of $v = 4.5$ m/s is used. This was calculated by taking the average wind speed between the years 2015-2022 from the KNMI monitoring station in Voorschoten [31], which is closest to the case study project. As the exact dates on which most parts are cast are not known and these dates are not normally available in the calculation, the annual average wind speed is used. The specific thermal conductance of the sand on which the floor is cast is not known, so the thermal conductance of the only type of sand specified in CIRIA C766 is used. Although this is based on 25mm of dry sand, the order of magnitude seems good as it is much lower than exposed concrete and also than 18mm formwork.

The ambient and initial temperatures are the same constant temperatures used in Wagemaker's calculation, 15 °C and 20 °C respectively. A constant temperature was used because it was found in Section 3.1.5 that the influence of a dynamic sinusoidal temperature curve, based on Appendix A2 of CIRIA C766, was very limited on the average temperature in the wall. Figure 4.7 shows the adiabatic temperature development calculated based on what is described in Section 2.1.1 where the heat generation is also based on CIRIA C766.

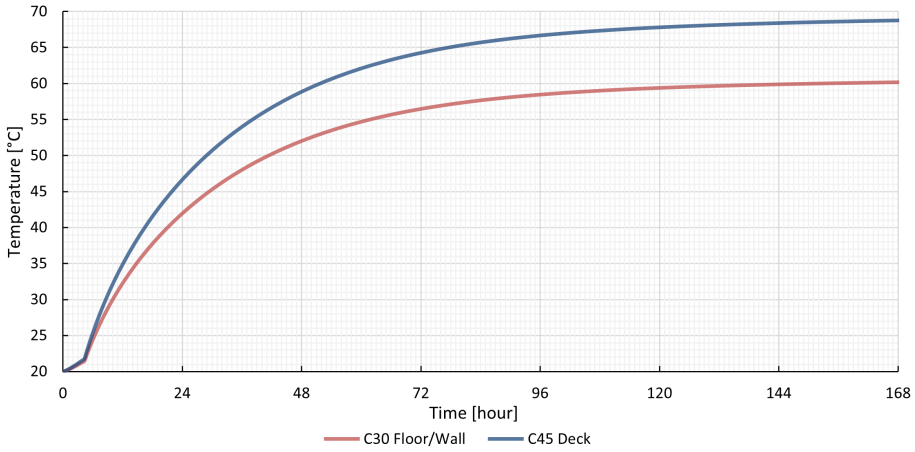

Figure 4.7: The adiabatic temperature development of the C30 and C45 concrete.

The last thermal property to be specified is the time at which the formwork is removed after the concrete has been poured. For this case study, this is not known or specified in the original calculation, so an assumption is made. The assumption is based on the case study research by J.R. van Bokhorst [15], which is slightly similar as it also involves pouring a wall on top of a floor for an underpass. In this study the walls were demoulded after 3 days, so this is also assumed for the removal of the formwork from both the walls and the floor in this case study. A longer formwork removal time is considered in the parameter study in Chapter 5 to determine its influence. The formwork removal time for the deck is assumed to be 14 days. This is based on the fact that it is around this time that the first post-tensioning is applied and the formwork is most likely to be removed.

4.3.4. Shrinkage and creep

Both shrinkage and creep are calculated based on the fib Model Code 2010; this section discusses the input parameters required to calculate the development of both quantities. The shrinkage and creep coefficients consist of two parts, the basic part and the drying part, where the basic part for shrinkage can be interpreted as autogenous shrinkage. To calculate these, in addition to some concrete properties and ambient temperature already specified, the following parameters need to be specified: the notional size, the ambient relative humidity (RH), the concrete age at loading and at the end of the curing period. An overview of these values is given in Table 4.3.

The notional size (h_0) will vary during the different phases due to the presence of for example concrete elements and soil, and thus the perimeter exposed to the atmosphere. Since the main interest is in the wall, where shrinkage will lead to stresses due to restrained concrete, h_0 is calculated based on this phase. Thus, the notional size of the wall is calculated based on the atmosphere exposed perimeter of both sides of the wall, as the soil behind the wall is not filled until the last phase. For the floor, only the floor perimeter between the walls is used as this is where drying can take place. To calculate the notional size of the deck, instead of the area divided by the exposed perimeter, two times the volume divided by the exposed area is used due to the complex geometry. The relative humidity (RH) is based on Wagemaker's calculation to allow a fair comparison. The age of the concrete at loading is assumed to be immediately at '$t_0 = 0$', as stresses may occur due to hardening. The age of the concrete at the end of the curing period (t_s) is assumed to be the same as the time of formwork removal given in the previous section.

Table 4.3: Overview of the properties used in the shrinkage and creep calculation.

	h_0 [mm]	RH [%]	t_0 [day]	t_s [day]
C30 Floor	1691	85	0	3
C30 Wall	1064	85	0	3
C45 Deck	792	75	0	14

Based on the parameters in Table 4.3, the concrete class and the ambient temperature, the shrinkage development and the creep coefficient development can be calculated. This is calculated based on Section 5.1.9.4 of the fib Model Code 2010 [5], which is also briefly explained in Sections 2.1.3 and 2.1.4 of this thesis. As Section 5.1.9.4 assumes an ambient temperature of 20 °C and this case study assumes 15 °C, both creep and shrinkage have been corrected by taking into account Section 5.1.10.7 of the fib Model Code [5]. Figure 4.8 shows the development of the shrinkage strains from the three different concrete elements. The development of the creep function could not be shown in a figure as it is based on both time and maturity. This results in 30 different creep curves as it depends not only on time but also on maturity.

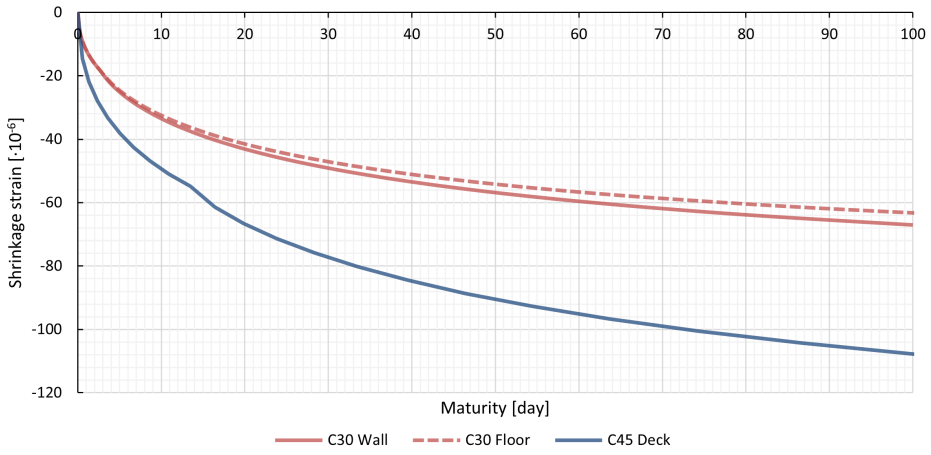

Figure 4.8: Development of the shrinkage strain.

4.4. Pre-processing FEA model

Before the finite element model is modelled and described in the following section, some pre-processing is required. Although this is limited, as mentioned in Section 4.1.1, due to the choice of a 3D model and the use of 3D solid elements, some pre-processing is still required. First, the effective thickness is calculated as the effective area is modelled separately in the case study model. Next, the external loads are determined by taking the governing load combination from the original calculation model. This is to determine all the governing loads to be applied to the case study and to provide a good overview for comparison with the case study. Lastly, the external loads from parts not included in the model are calculated and transferred to what can be applied to the case study model.

4.4.1. Effective thickness

When thick walls are loaded by external forces and cracks occur, only the outer reinforced parts, called the effective area, can take up the loads. This is because if cracks occur in the unreinforced middle section of the wall, the cracks cannot be controlled by the reinforcement on the outside and uncontrolled cracking can occur. As a result, the mid-section will not be able to resist tensile forces and therefore cannot contribute to the force distribution. To determine the effective thickness and thus the effective area of the wall, Figure 7.6-4 from the fib Model Code 2010 [5] is used, which is shown in Figure 4.9. From this figure, situation (c) will be relevant for the wall of this case study, both for the right and left side of the wall.

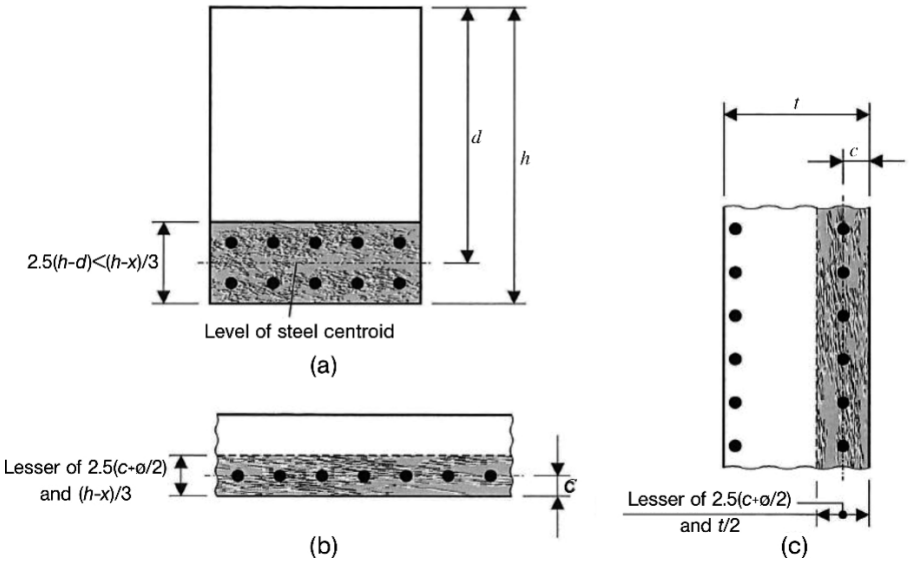

Figure 4.9: Calculation of the effective thickness and area based on the fib Model Code 2010, taken from [5].

Using the equation from Figure 4.9c, the effective thickness (t_{eff}) for the wall can be calculated. The concrete cover (c) used in the case study is 70 mm, but because the horizontal reinforcement will be in the second layer and a 25 mm reinforcement bar is used in the first layer, the total concrete cover on the horizontal reinforcement is 95 mm. Based on the original calculation, a ⌀25 mm reinforcement bar was used and the total thickness (t) of the wall is variable, but between 1250 and 900 mm. This results in an effective thickness for the left and right sides of the wall of 268.75 mm, which is always less than $t/2$ and therefore independent of the variable thickness of the wall. To simplify post-processing, the wall can be divided into three parts, the left outer part, the inside part and the right outer part.

4.4.2. Determination of external loads

Before the modelling of the case study model can begin, it is necessary to determine which governing external loads must be applied to the model. As the analysis is non-linear, only one load case can be analysed per analysis. It was therefore decided to model only the governing load/load combination from the original calculation model. In the original calculation model, hundreds of loads and thousands of load combinations were calculated and it was found that the highest design moments occur on the groundside of the wall.

The original calculation calculated the reinforcement for two different load combinations, one with the highest design force and associated design moment and one with the highest design force and associated design moment. However, the former was found to be governing, so this particular load combination and its associated load and load factors were selected to be applied to the case study model. This governing load combination consisted of 20 load groups, but to limit the number of load groups some were combined if they had the same load factor and were applied at the same time and place. Tables 4.4 and 4.5 gives an overview of the applied loads, load factors and the distributed forces and moments.

Table 4.4: Overview of the distributed forces found in the original calculation model per load group.

Orig. load nr.	Load group description	Load factor	n_{xx} [kN/m]	n_{yy} [kN/m]	n_{xy} [kN/m]
1, 8	Dead weight	1.00	46.98	-329.91	-32.06
2, 3, 4	Dead Load Deck	1.00	52.75	-78.49	-32.78
9, 18, 26	Dead Load Floor/Wall	1.00	30.08	-9.39	2.88
22, 23, 24	Mobile Load Deck	0.80	1.58	-10.02	-10.10
137	Mobile Train Load Deck	1.21	170.36	-79.65	-101.62
15	Mobile Load Train Breaking Deck	0.97	-4.60	1.34	-21.99
13	Mobile Load Traffic Breaking Deck	0.80	-0.33	0.17	-0.51
303, 322	Mobile Load Traffic Floor	0.80	52.10	28.25	-27.55
67	Dowel Force Load Wall	0.88	6.49	0.41	-1.71
10	Summer Temperature	0.29	24.54	5.28	-15.31
6, 7	Prestress Load Deck	0.90	-42.80	-4.90	-33.49
			337.16	**-476.92**	**-274.24**

Table 4.5: Overview of the distributed moment found in the original calculation model per load group.

Orig. load nr.	Load group description	Load factor	m_{xx} [kNm/m]	m_{yy} [kNm/m]	m_{xy} [kNm/m]
1, 8	Dead weight	1.00	-103.29	-515.94	-2.85
2, 3, 4	Dead Load Deck	1.00	-23.85	-110.22	-4.81
9, 18, 26	Dead Load Floor/Wall	1.00	8.04	43.29	-0.75
22, 23, 24	Mobile Distributed Load Deck	0.80	-2.78	-15.43	1.26
137	Mobile Train Load Deck	1.21	-26.50	-100.03	-13.66
15	Mobile Train Breaking Load Deck	0.97	-2.66	-14.97	0.38
13	Mobile Traffic Breaking Load Deck	0.80	-0.16	-0.82	-0.25
303, 322	Mobile Traffic Load Floor	0.80	8.74	39.58	-11.12
67	Dowel Force Load Wall	0.88	0.22	2.30	0.29
10	Summer Temperature	0.29	-75.66	-26.20	-1.51
6, 7	Prestress Load Deck	0.90	-0.05	-13.34	-37.66
			-217.94	**-711.80**	**-70.68**

In order to be able to compare the distributed design forces and moments with the result from the case study model later in this chapter, this is first calculated for this specific governing load combination. Using the results of the distributed forces in Table 4.4 and the distributed moments in Table 4.5, the distributed design forces and moments can be calculated. In the original calculation, this is calculated by the SCIA Engineer calculation program, which states that it is based on the Eurocode [32]. Therefore, the same method will be used here, but also for the case study.

Since $n_{yy} < n_{xx}$ and $n_{yy} < -|n_{xy}|$, the distributed design force in the horizontal direction (n_{xD}) can be calculated with $n_{xD} = n_{xx} + n_{xy}^2/|n_{yy}|$, which is equal to 494.9 kN/m. For the positive horizontal distributed moment, since $m_{yy} < |m_{xx}|$ and $n_{yy} < |n_{xy}|$, the design moment in the X-direction (m_{xD+}) can be calculated as $m_{xD+} = -m_{xx} + |m_{xy}|$, which is equal to 288.6 kNm/m. The positive horizontal distributed design moment is the moment on the groundside of the wall, there is no need to calculate the negative horizontal design moment as this is not the governing load combination for that side.

As explained previously in Section 2.2.2, to calculate the distributed design force at 't=∞', 50% of the calculated hardening forces calculated for 't=0' is added to the distributed design force in the horizontal direction. This is approximately 500 kN/m, so the reinforcement is calculated with a total horizontal distributed design force of 994.9 kN/m. This can be used in the final section to compare the original calculation with the non-linear case study performed.

4.4.3. Transferring of external loads

In order to reduce the calculation time, it was decided in the modelling approach to deviate from the original calculation model and to exclude the rail impact plate and the impact plates for the cycle and footpath. This is because there is no interest in the stresses and forces within the impact plates. In addition, the deck is made up of several edge and retaining walls, but these have cut joints introduced so that they are not structurally involved in the distribution of forces. These should therefore not be entered as geometry but as loads in the calculation model. In this section, the loads from the impact plates are calculated to be added as loads in the case study.

Rail impact plate

To determine the additional load required to compensate for the absence of the rail impact plate in the case study model, a separate linear DIANA FEA model was created. This model contains the full geometry of the rail impact plate taken from the original 3D Revit file and the associated loads were placed on this model, such as self-weight, dead loads, mobile train loads and train braking loads. However, without going into detail, as will be done in the case study itself, the main assumptions are explained.

Firstly, the model will include two circular piles, modelled as lines with geometry, together with a spring X/Y support with varying stiffness along the length to simulate different soil types. At the bottom of the lines there is a point spring in the Z-direction. All stiffnesses and material properties are taken from the original calculation. In addition, a high stiffness Z-direction spring line support was placed between the impact plate and where the deck would be located. The distributed support forces from this line support could then be applied as loads to the case study model. Figure 4.10 shows the geometry, loads, boundary conditions and finite element mesh of the impact plate.

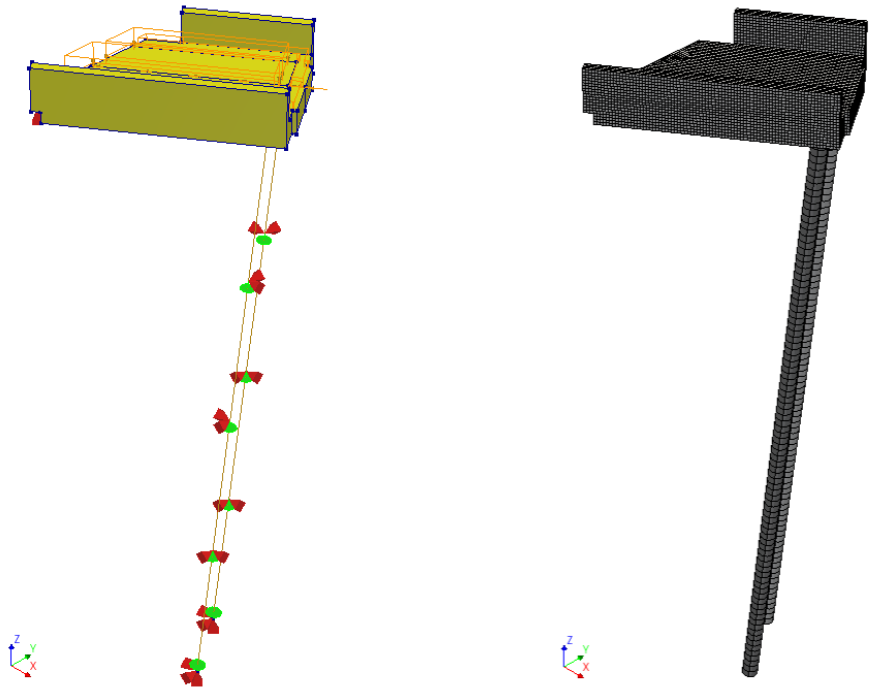

(a) Geometry, loads and boundary conditions (b) Finite element mesh

Figure 4.10: The geometry, loads, boundary conditions and finite element mesh of the rail impact plate.

The linear DIANA FEA model of the rail impact plate is used to analyse the nodal reaction forces on the line support between the impact plate and where the deck should be. This is done for three load cases, the first of which is for the dead loads, which includes the self-weight and the ballast bed. This is taken together because both are applied to the deck at around the same time. The second load case is the mobile train loads and the third is the mobile train breaking load. The results of the analysis using the linear DIANA FEA analysis are shown in Figure 4.11. Using the nodal reaction forces, it is straightforward to calculate a distributed line force which can be used in the case study to apply the forces from the rail impact plate to the deck.

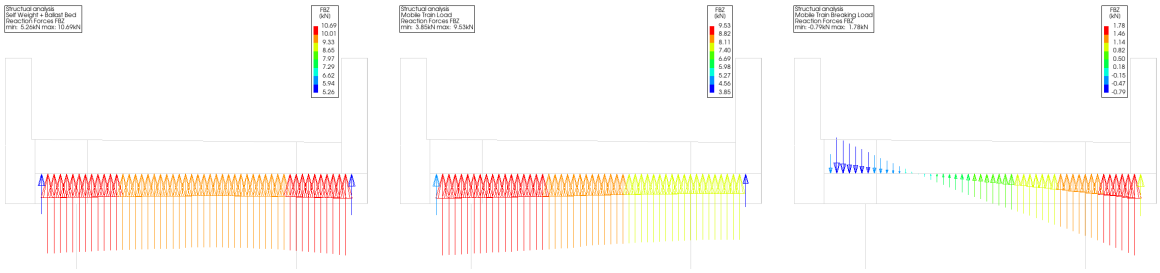

(a) Self weight + ballast bed (b) Mobile train loads (c) Mobile train breaking load

Figure 4.11: Nodal reaction forces along the deck connection for three different load cases.

Bicycle and footpath impact plates

To calculate the load to be applied to the case study model in the next section, a hand calculation is made because of its simple geometry. Although the impact plates are at an angle, they can be approximated by a straight plate with the following dimensions: 3000 mm long, 1000 mm wide and 250 mm thick. This corresponds to 3.00 m^2 and 0.75 m^3 per plate, and also per metre on the deck. It is assumed that 50% is loaded on the deck and 50% on the soil, which is a conservative assumption. Below the loads are calculated for the dead load (which is 3.22 kN/m^2 (conform original calculation)) and the mobile distributed load (which is 5.00 kN/m^2 (conform original calculation)).

$$q_{Self-weight} = 0.5 \cdot (0.75 \cdot 2500 \cdot 9.81) = 9.20 \text{ kN/m}$$

$$q_{Dead\ Load} = 0.5 \cdot (3.00 \cdot 3.22) = 4.83 \text{ kN/m}$$

$$q_{Mobile\ distributed\ load} = 0.5 \cdot (3.00 \cdot 5.00) = 7.50 \text{ kN/m}$$

The calculated loads are used as input to replace the need to model the impact plates in the case study model. Both the self-weight and the dead weight should be applied as a dead loads to the deck, as the impact plates are placed when the deck is already on the sheet piles.

Edge and retaining wall elements

The deck consists of a number of edge and retaining wall elements that are poured at a later stage, when the deck is already in it's final position. These wall elements contain cut joints to ensure that they do not contribute structurally to the force analysis. They are therefore not included in the case study model, but their self-weight does need to be included in the analysis as a dead load. Figure 4.12 shows the cross-section of the deck with the edge and retraining walls, which will be applied as loads, marked in red.

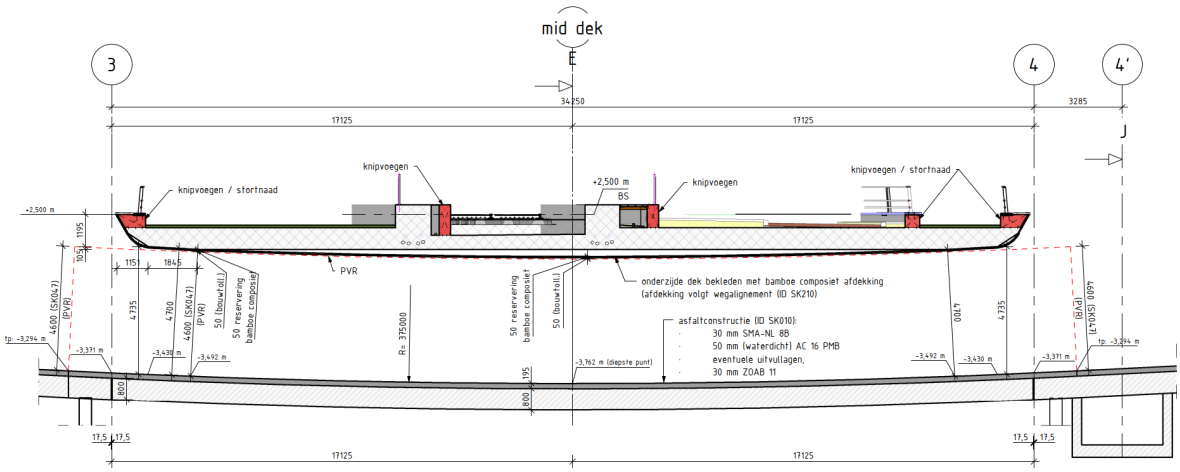

Figure 4.12: Cross-section of the deck perpendicular on the axis of the road of the Kanaalweg.

4.5. Finite element model

This section describes the various components that characterise the finite element model created using the DIANA FEA program. These components include the geometry, material properties, boundary conditions, loads and mesh.

4.5.1. Geometry

As chosen in the modelling approach, only the south side of the railway underpass is modelled in DIANA FEA due to its assumed symmetry. In the first two phases, only the deck is present. In the third phase the floor is added and in the fourth the wall, so that in the fourth and fifth phases all elements are present. The concrete geometry was imported directly from the original Revit 3D model, although some changes were made; for example, the deck contained many edge and boundary elements that did not contribute structurally due to cutting joints, so these were removed. See Figures 4.14 - 4.18 for the geometry present at each phase.

When analysing the results of the model, it was found that when the wall was added, including its self-weight, the weight of the wall pulled the deck down. This increased the support force through the sheet piling and resulted in high tensile stresses in the wall at the first time step. This is not to be expected as the self-weight should be transferred to the floor. To overcome this, a rigid connection was modelled between the deck and the wall and the fourth phase was split into two subphases. In the first, only a small time step is applied with the connection off, so that all the self-weight is added to the floor. Then, in the second sub-phase, the connection is switched on for the remainder of the analysis, allowing the deck to provide a restraint.

Boundary interface connections are applied to all exposed surfaces which differ between phases in order to properly model the thermal properties. The specific thermal properties for boundary conditions are discussed later in the boundary conditions section.

In order to simplify the post-processing of the analysis results of the wall, the wall is divided into three parts, two effective areas (roadside and groundside) and the inside part in between. Due to the mesh size chosen, this resulted in only one element being created within the thickness of the effective area, so it was decided to divide each effective area into two parts, forcing two mesh elements along the thickness for the entire effective area. This results in the geometry of the wall consisting of five elements, which does not affect the results.

Three composite surfaces were added in the wall to allow the distributed forces and moments of the wall to be easily post-processed. Two of the composed surfaces are located in the centre of the two effective areas, exactly on the line between the two parts of the effective areas. The composed surfaces have the same thickness as the full effective thickness and therefore cover the entire effective area. The last one is in the inside part of the wall and has the thickness to cover the complete wall. Figure 4.13 shows the geometry of the wall with the composed surfaces shown in red.

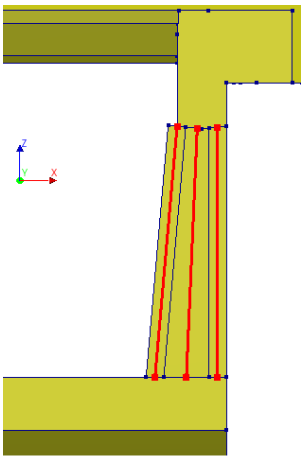

Figure 4.13: Geometry wall and composed surfaces.

4.5.2. Material properties

To model the concrete parts, three different concrete materials were created, one for the deck, floor and wall. The concrete material model used for all of them is the 'Maxwell/Kelvin chain viscoelasticity' model, from which Kelvin chains are selected for creep and the input parameters are based on the fib Model Code 2010. All material properties and development inputs are described in Section 4.3.2.

Five heat flow boundary interface material models are created, to model the different convection parameters of the surfaces, three of which are time-dependent to model the change in convection heat transfer from the formwork to the exposed concrete after the formwork is removed. The other two prescribe constant exposed concrete or soil convection. The convection factors used are specified in Section 4.3.2.

For both the sheet piles and the soil bedding, a no-tension spring material model is created with spring constants based on the original calculation. For the sheet piles, assuming 10 mm thick sheet piles, a normal stiffness modulus (global Z-direction) of $8500 \cdot 10^3$ kN/m^3, a shear stiffness of $10 \cdot 10^3$ kN/m^3 in the global X-direction and $1 \cdot 10^3$ kN/m^3 in the global Y-direction is assumed. A normal stiffness modulus (global Z-direction) of 5000 kN/m^3 is assumed for the soil bedding and 500 kN/m^3 is assumed for the shear stiffness in both global X- and Y-direction.

4.5.3. Boundary conditions

The applied boundary conditions can be divided into two parts: the static boundary conditions and the thermal boundary conditions. The static boundary conditions depend on the phase, e.g. in the first phase the deck is supported by a full Z-direction support when poured and in the second phase the deck is placed on a sheet piling support. This is a line support in the X-, Y- and Z-direction combined with the sheet pile spring material model described in the previous section. These sheet piles are then removed in the final phase and the loads are transferred to the wall/floor. The floor is supported by face support in the global X-, Y- and Z-direction in combination with the soil spring material model. Symmetry supports are applied to both the deck and the floor by applying the global Y-direction support to the face along the assumed symmetry line. This keeps the symmetry plane vertical but allows it to move in the global X- and Z-direction.

Thermal boundary interfaces are applied to all exposed surfaces to properly model the heat convection. As a distinction is made between exposed concrete, formwork and sand, and time-dependent combinations of these, different thermal boundary conditions are created. Some of these are switched on and off during different phases, details of which can be found in Figures 4.14 - 4.18. An external temperature of $15\,^{\circ}$C is applied to all these thermal boundary conditions to simulate the ambient temperature. An initial temperature of $20\,^{\circ}$C is applied to all concrete elements to simulate the pour temperature.

4.5.4. Loads

In the modelling approach, it was decided to model only the governing load groups/combination based on the original calculation model. As each non-linear analysis can only include one load combination, the analysis of multiple load groups/combinations will take excessive time. Section 4.4.2 provides an overview and explanation of this governing load combination and the applied load groups. For each load that contributed to the governing load combination, the same load is applied as in the original calculation. The loads on the impact plates from the original calculation have been converted to a distributed line load in Section 4.4.3 and added to the appropriate load group.

As the prestressing of the deck has not been included, as was decided in the modelling approach, the prestressing loads have also not been applied in the model. The prestressing is excluded because the influence of the prestressing in the deck is small for the force distribution within the wall, but significantly increases the complexity of the model. During modelling it was found that a gradient temperature load could not be applied as a load with load factor. Therefore, the distributed forces and moments (shown in Table 4.4 and 4.5 respectively) for both load groups are manually added to the final results of the case study model. Table 4.6 provides an overview of the load groups, load factors and the phase/time at which the load groups are applied.

To describe varying loads along certain axes/lengths, some loads are applied using a function. For example, the water load varies along the height/Z-direction and the load from the impact plate to the deck varies along the length/Y-direction. Therefore, a function is used to accurately model these varying loads.

Table 4.6: Overview of load groups with associated load factor and phase/time of application.

Load nr.	Load group description	Load factor	Applied from phase
1	Self weight	1.00	1
2	Dead Load Deck	1.00	2
3	Dead Load Floor/Wall	1.00	5 ($t = 300$)
4	Mobile Load Deck	0.80	5 ($t > 301$)
5	Mobile Train Load Deck	1.21	5 ($t > 301$)
6	Mobile Load Train Breaking Deck	0.97	5 ($t > 301$)
7	Mobile Load Traffic Breaking Deck	0.80	5 ($t > 301$)
8	Mobile Load Floor	0.80	5 ($t > 301$)
9	Dowel Force Load Wall	0.88	5 ($t > 301$)
10	Summer Temperature Deck/Floor/Wall	0.29	Not applied
11	Prestress Deck	0.63	Not applied

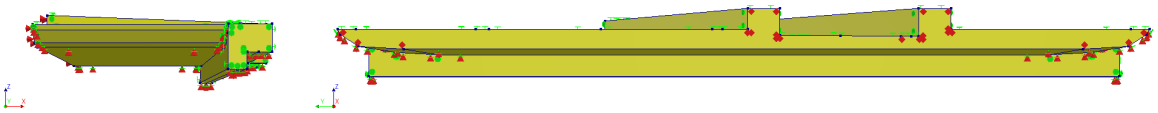

(a) Y-direction view (b) X-direction view

Figure 4.14: The geometry and boundary conditions for phase 1 of the analysis (perspective projection).

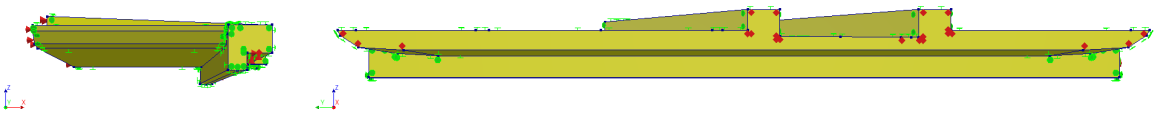

(a) Y-direction view (b) X-direction view

Figure 4.15: The geometry and boundary conditions for phase 2 of the analysis (perspective projection).

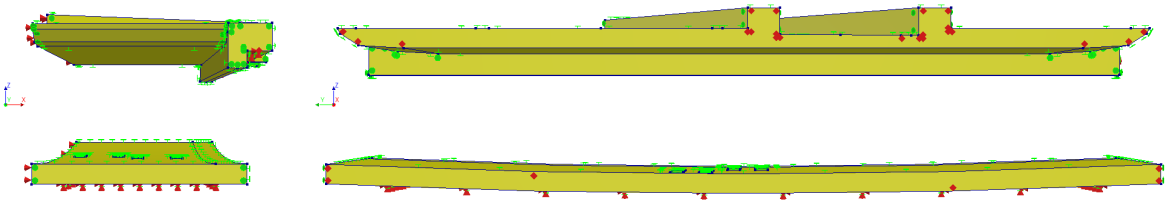

(a) Y-direction view (b) X-direction view

Figure 4.16: The geometry and boundary conditions for phase 3 of the analysis (perspective projection).

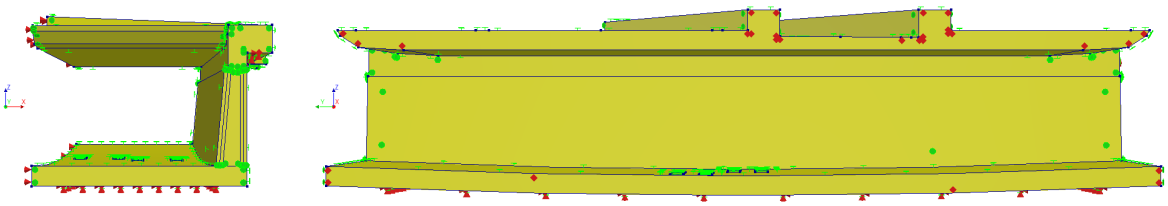

(a) Y-direction view (b) X-direction view

Figure 4.17: The geometry and boundary conditions for phase 4 of the analysis (perspective projection).

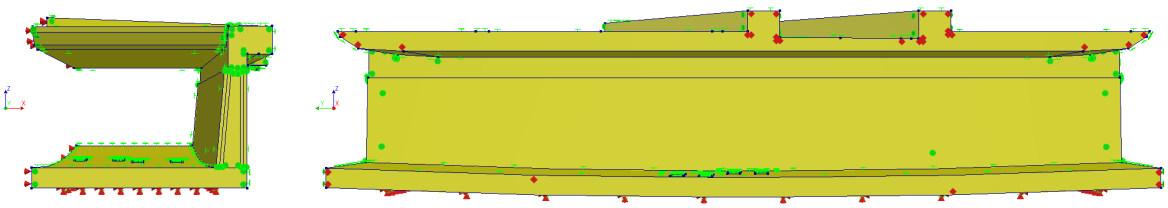

(a) Y-direction view (b) X-direction view

Figure 4.18: The geometry and boundary conditions for phase 5 of the analysis (perspective projection).

4.5.5. Mesh

As described in the modelling approach, the concrete geometry is descretised using solid 3D elements within a 3D model, which were previously explained in Section 2.2.4. Special types of quadrilateral elements are used for the (thermal) boundaries and composite surfaces. The model is discretised using quadrilateral elements as this is necessary for the combination of thermal and structural analysis. To ensure deformation compatibility, DIANA FEA automatically solves the heat transfer problem with linear elements and the structural problem with quadratic elements. As a result, the thermal and total strain fields are linearly interpolated across elements.

An element size of 268.75 mm is selected for the wall, which is the same as the effective thickness calculated in Section 4.4.1. Although this appeared to be quite good along the height and width of the wall, it resulted in only one element in the thickness of the effective area. To increase this, the effective area was split into two parts so that when a mesh was generated, two elements were created along the effective thickness.

A twice as large element size of 537.5 mm is used for the deck and floor. This is because the main interest of this analysis is the wall and the floor and deck are only used to transfer the external loads and support the wall. To avoid many triangular elements around the wall and the deck/floor connections, the vertical faces of the deck and floor adjacent to the wall have been given the same mesh size as the wall. This can be seen in Figure 4.19.

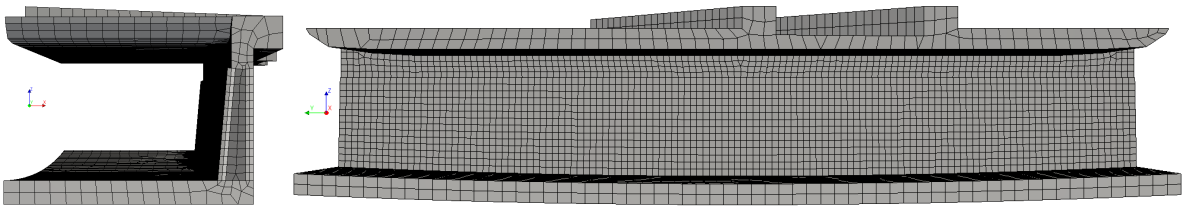

(a) Y-direction view (b) X-direction view

Figure 4.19: The finite element mesh for the analysis (perspective projection).

4.6. Calculation analysis

A staged analysis is created, which consists of a number of phases in which first a transient heat transfer analysis is performed followed by a structural non-linear analysis. The transient heat transfer analysis calculates, among other things, the temperature development and equivalent age required for the structural non-linear analysis. The latter is performed first with a start step, then with several time steps, and in the final phase a load step is applied to include the mobile loads. In this section the different phases are discussed first, then the transient heat transfer analysis and finally the structural non-linear analysis.

4.6.1. Analysis phases

The analysis consists of five general phases, but as explained in Section 4.5.1, the connection between the deck and the wall requires an additional phase. This consists of only a short time step to avoid the self-weight of the wall going directly to the deck. An overview of which geometry shapes, supports and connections are present in each phase is shown in Figure 4.20. For the geometry shapes this is quite straightforward and follows the modelling approach. For the geometry supports, it can be seen that the formwork supports are only present in the first phase, and then the sheet piling is present until the last phase. The other supports are straightforward. The geometry connections are a little more complex. The 'Deck Boundary Sheet Piles Spring' and the 'Floor Boundary Soil Spring' are present when the corresponding support sets are present, in order to assign the correct spring material model to the supports. The deck connection is present from the 'Wall Casting 2/2' phase until the end.

Most of the thermal boundaries are present if the corresponding geometry shape is present, except for the temporary thermal boundaries between the deck and the wall and between the floor and the wall. These are removed when the wall is present. In the case of the combination between the formwork and the exposed convection boundary connections, a material model was applied where the convection changes at the time of formwork removal, eliminating the need to apply three additional phases.

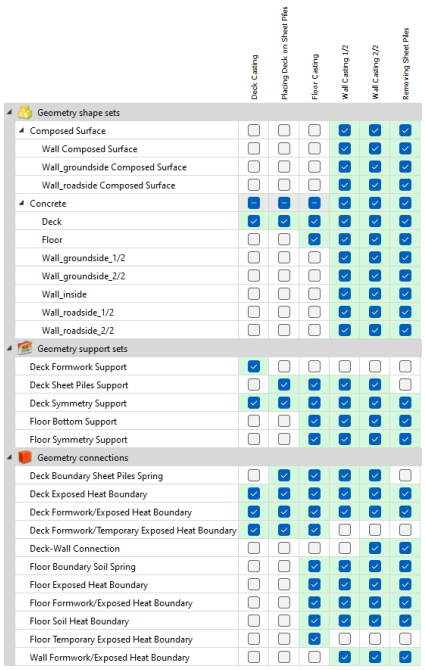

Figure 4.20: Overview of which geometry shapes, supports and connections are present in each calculation phase.

4.6.2. Transient heat transfer analysis

Before a non-linear analysis can be performed at each time step, a transient heat transfer analysis is first performed. This is because the non-linear analysis requires the temperature and equivalent age/maturity to calculate the development of mechanical properties and temperature strain. The same type of transient heat transfer analysis is set for all phases, with different start times and time step sizes. An overview of the different start time/day and time step sizes used for each phase is shown in Table 4.7. The transient heat transfer analysis is set up with the poured concrete temperature as the initial condition, which is $20\,^{\circ}$C. A non-linear analysis with hydration heat analysis and calculation of the equivalent age is chosen, using an initial degree of reaction of 0.01 and an initial equivalent age of 0.001 day respectively. For the transient heat transfer analysis, up to a maximum of 10 iterations, a convergence tolerance of $1 \cdot 10^{-6}$ and the regular Newton method were used for the iteration process. Default outputs are used for the heat transfer analyses, which include: temperature, heat flux, degree of reaction and equivalent age. Of these, only temperature and equivalent age are of interest.

Table 4.7: Overview of the start time and time step sizes for each phase.

Phase nr./ name	Start day	Time step sizes [day]
1; Deck Casting	0	0.001 0.249 0.250(27x) 0.50(14x) 1.0(7x) 2.0(8x) 7.0(9x)
2; Deck on Sheet Piles	100	0.001 0.249 0.250(3x) 0.50(2x) 1.0(7x) 2.0(7x) 7.0(11x)
3; Floor Casting	200	0.001 0.249 0.250(27x) 0.50(14x) 1.0(7x) 2.0(4x) 7.0(3x)
4; Wall Casting (1/2)	250	0.001
4; Wall Casting (2/2)	250.001	0.124 0.125(55x) 0.25(28x) 0.5(14x) 1.0(8x) 3.5(6x)
5; Removing Sheet Piles	300	0.001 0.124 0.125(7x) 0.25(4x) 0.5(8x) 1.0(9x) 3.5(10x)

4.6.3. Structural non-linear analysis

At each phase, the transient heat transfer analysis is followed by a structural non-linear analysis to calculate all strains, stresses and forces. Each structural non-linear analysis starts with a start step and is followed by multiple time steps. In the start steps, the previously applied load is reapplied to the newly poured concretes and in some phases an additional (external) load is applied, as shown in Table 4.6. This is particularly the case for phases 1, 2 and 5 ($t = 300$ days). In the last phase, the mobile loads are added at the governing time step for the stresses/forces within the wall. This occurs at the earliest after 301 days, as described in the modelling approach, and it is assumed that this critical time point occurs at the latest at 350 days. From a first analysis, the force/stress development could be determined, and from this development, the exact time at which the forces/stresses in the wall are critical can be determined, to which the mobile load can be added in a second analysis.

The time steps applied are the same as those used in the transient heat analysis and are shown in Table 4.7. The full load factor of 1.0 is used for the start steps at the beginning of each phase and for the load step for the mobile load, as elastic material properties are used there is no need to apply this in small load steps.

The structural non-linear analysis takes into account various non-linear effects, including both physically non-linear effects and geometrically non-linear effects. However, it is important to note that the effect of cracking is excluded from the physically non-linear effect and therefore from the analysis as described in the modelling approach. The effect of cracking is taken into account by first determining the cracking point, for both the wall and the floor, where the tensile stress is higher than the tensile strength and therefore cracking is most likely to occur. In a second analysis, the Young's modulus is reduced by 50% to account for the lower Young's modulus in the cracked concrete.

For the equilibrium iteration during the non-linear analysis, the default Newton-Raphson Regular Method is selected with a maximum of 10 iterations. It is specified that convergence of the solution can only be achieved when both the displacement and force norms are satisfied. A convergence tolerance of $1 \cdot 10^{-4}$ is selected for both.

In addition to the default outputs, an extra output block is added to the analysis. For this output block, Young's modulus and tensile strength are selected for all phases. For the phases after the wall is added, the crack index, creep strain and distributed design moments are also included as outputs. These selected outputs, together with the default outputs, should provide all the information necessary to find all the relevant results and to check the results.

4.7. Analysis results and post-processing

This section presents the results of the analyses performed and the various post-processing steps. The first subsection focuses on the results of the 'uncracked' analysis. These results are then subjected to post-processing to find the time step at which cracking is most likely to occur in the structure. This specific time step is used as input for the subsequent 'cracked' analysis. In the second subsection, a second analysis is performed in which the reduced stiffness due to cracking is simulated by reducing the Young's modulus of the structure at the assumed moment of cracking. This analysis is used to investigate the critical time step for the application of mobile loads, which will be applied in the third and final analysis. The results of the final analysis are post-processed to obtain the final results. This involves calculating the horizontal distributed design force and the positive distributed moment.

In the final subsection, the analysis results are validated by performing various checks to ensure the accuracy and reliability of the results obtained. These checks include comparing the displacements and forces in the wall with the original calculations. Analyses are also performed to check the influence of creep, shrinkage and long-term results. Additionally, a mesh and time step refinement is performed to validate the validity and reliability of the results.

4.7.1. Analysis results and post-processing 'uncracked' analysis

This subsection provides an overview of the analyses performed based on the finite element model described in Section 4.5 and the calculation analysis described in Section 4.6. The primary purpose of this first 'uncracked' non-linear analysis was to determine the time step at which cracking is most likely to occur. The analysis took about 10-12 hours to complete and resulted in a data set of about 38 GB, containing relevant output results for each time step. Convergence was achieved after one to a maximum of three iterations for both transient heat transfer and structural non-linear analysis.

To determine at which time step cracking is most likely to occur, the crack index is used as explained in the modelling approach (Section 4.2). The crack index is calculated in the program by dividing the tensile strength by the maximum principal stress for each node. If the crack index is equal to or less than 1.0, it indicates a high probability of cracking and therefore a cracked section. This principle is consistent with what is presented in the fib Model Code 2010, which states: "Where the maximum tensile stress in the concrete calculated on the basis of an uncracked section under the characteristic combination of loads exceeds f_{ctm}, the cracked state should be assumed." [5, p. 280].

The results of the crack index analysis for three different time steps during the fourth phase are shown in Figures 4.21 and 4.22. The first subfigure shows the crack index within the middle cross-sections of the wall, while the second subfigure shows it for the entire model. The legend used in the figures is divided into three ranges: 0 - 0.769, 0.769 - 1.0 and 1.0 - 1.429. These ranges correspond to different probabilities of cracking. The first range indicates a 95% or higher chance of the cracking of the structure, the second range between 0.769 and 1.0 indicates a 95% to 50% chance of cracking, and the last between 1.0 and 1.429 indicates a 50% to 5% chance of cracking. The values of 0.769 $(1/1.3)$ and 1.429 $(1/0.7)$ are calculated based on the fib Model Code, which specifies that the characteristic value of tensile strength at the 0.95 quantile ($f_{\text{ctk,0.95}}$) is equal to $1.3 \cdot f_{\text{ctm}}$, and the characteristic value at the 0.05 quantile ($f_{\text{ctk,0.05}}$) is equal to $0.7 \cdot f_{\text{ctm}}$.

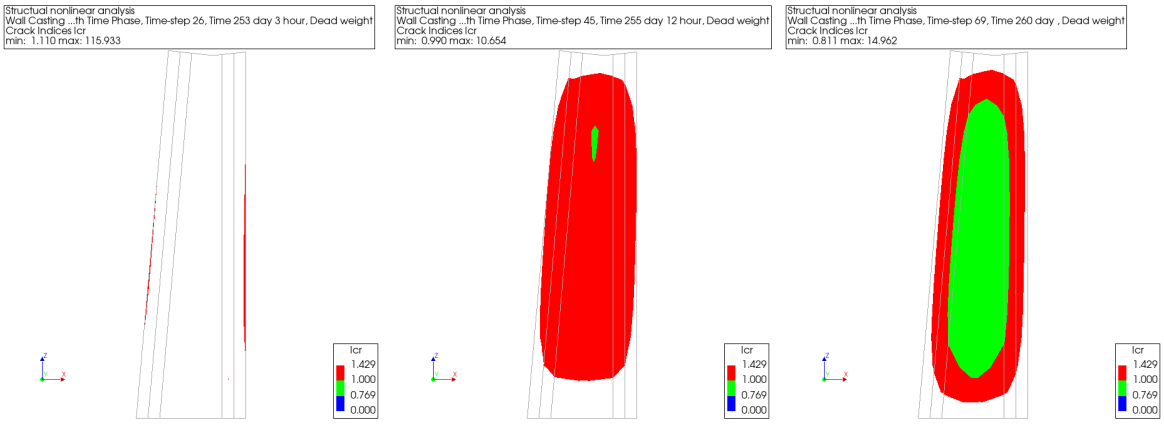

(a) Result at 253 days and 3 hours (b) Result at 255 days and 12 hours (c) Result at 260 days

Figure 4.21: The crack index analysis result shown for the middle wall cross-section for three different time steps.

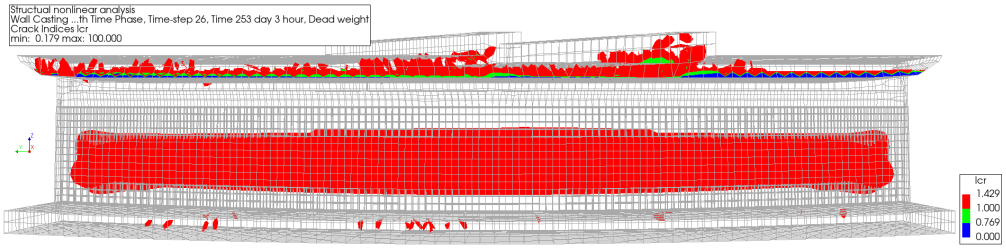

(a) Result at 253 days and 3 hours

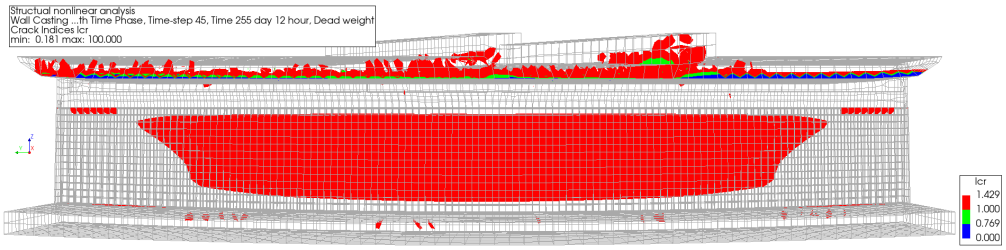

(b) Result at 255 days and 12 hours

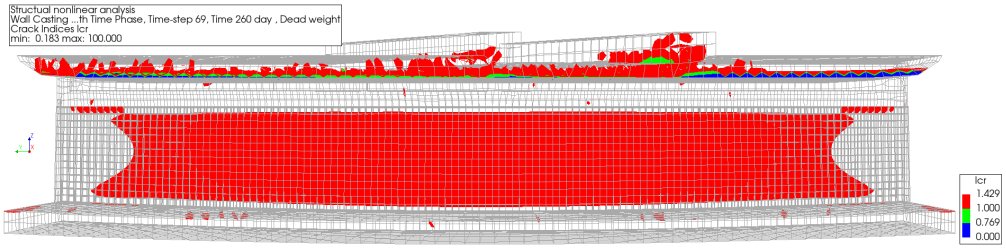

(c) Result at 260 days

Figure 4.22: The crack index analysis result shown for the full structure for three different time steps.

Figures 4.21a and 4.22a show the crack index at 253 days and 3 hours, which corresponds to the time step immediately after removal of the formwork after three days. Both figures show a 5% or higher probability of cracking in the wall at this time step. The area showing a 5% or higher probability of cracking gradually increases until 255 days and 12 hours when a crack index of 1.0 is first reached. This is shown in Figures 4.21b and 4.22b. From this time step forward, there is a 50% or higher probability that the wall will crack as the tensile strength becomes lower than the maximum principal stress locally. According to the fib Model Code 2010, a cracked section should then be assumed. At 260 days, as shown in Figures 4.21c and 4.22c, the minimum crack index of 0.811 is reached for this phase, giving a probability of about 90.0% that the wall will crack. It is therefore very likely that the wall will eventually crack, and as explained, the most probable time for this to happen is around 255 days and 12 hours.

Before performing the second analysis, it is necessary to determine the maturity/equivalent age (EQA) in order to reduce the Young's modulus appropriately at a specific maturity age. Unfortunately, it has been found that the current version of DIANA FEA does not allow the Young's modulus to be modified at a specific time step during the analysis, nor does it allow the material model to be changed during the analysis without losing the loading history. Therefore, the creep function was changed to allow for the reduction in Young's modulus at a specific maturity step. This will result in some inaccuracy as the maturity age is not the same across the cross-section of the wall, resulting in a non-uniform stiffness reduction. Figure 4.23, shows the variation of maturity/equivalent age within the middle cross-section, which varies between 5.07 and 11.55 days. By comparing this with Figure 4.21b, it can be approximated that crack initiation can occur at a maturity/equivalent age (EQA) of approximately 9.12 to 9.93 days (highlighted in the yellow range). Therefore, in the following 'cracked' analysis described in the next subsection, the Young's modulus is reduced from a maturity age of 9.1 days to simulate the expected cracking.

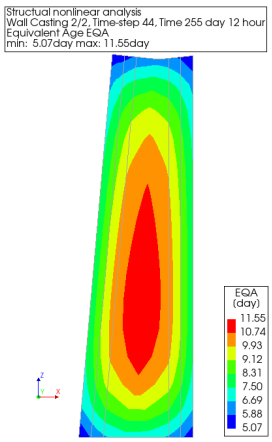

Figure 4.23: Maturity age at expected cracking wall.

In addition to the fact that the wall is expected to crack, Figure 4.22 also shows that the deck is very likely to crack as large areas have a 95% or higher chance of cracking. However, the Young's modulus of the deck is not reduced as the actual deck is prestressed and therefore less likely to crack. This is not taken into account in the model, as explained in the modelling approach, but the Young's modulus is not reduced in the original calculation either. Figure 4.22 also shows that there is a small possibility of cracking in the floor in some very small areas during the pouring of the wall phase. However, it is not certain that cracking will occur as it does not reach a crack index of 1.0. It is far more likely that cracking will occur when the sheet piles are removed and the self-weight and dead loads are transferred from the deck to the wall and subsequently to the floor. Both the time step before ($t = 300.0$ days) and after ($t = 300.001$ days) removal of the sheet piles are shown in Figure 4.24. In this figure it can be seen that in the fifth phase some areas of the floor have a crack index equal to or less than 1.0. There are even some places below 0.769, which means that there is a 95% or higher chance of cracking. Therefore, for the next analysis at this time step, the Young's modulus of the floor is also reduced to 50%. The time step of 300.001 days corresponds to an EQA or maturity age of between $80.04 - 86.61$ days, as shown in Figure 4.25, which shows the middle cross-section at this time step. To ensure that the entire floor experiences the reduced stiffness at this particular time step, the Young's modulus is reduced at a maturity age of 80.0 days.

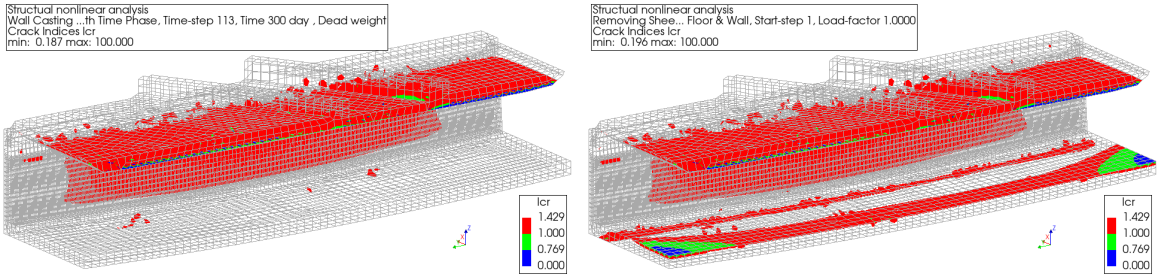

(a) Result at 300.0 days (phase 4). (b) Result at 300.001 days (phase 5).

Figure 4.24: The crack index analysis result shown for the full structure for two different time steps, before and after removal of the sheet piles (perspective projection).

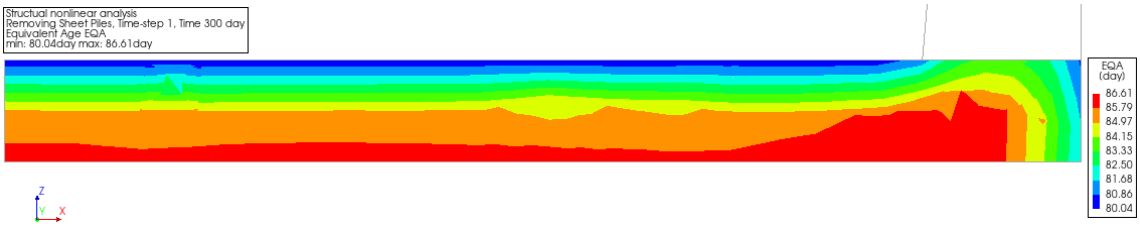

Figure 4.25: Maturity age at expected cracking floor ($t = 300.001$ days)

Figure 4.26 shows the development of the reduced Young's modulus for both the wall and the floor. This information is used as input for the next analysis described in the next subsection. The inputs shown in the figure are limited to 100 days for the wall and 150 days for the floor, representing a period of 50 days after removal of the formwork.

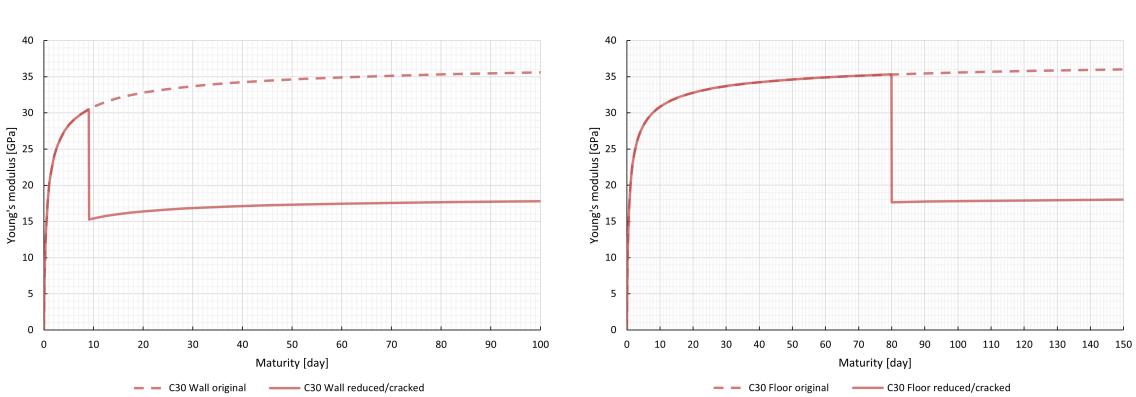

(a) Development Young's modulus wall (b) Development Young's modulus floor

Figure 4.26: Comparison between the normal and the reduced/corrected development of the Young's modulus.

4.7.2. Analysis results and post-processing ‘cracked’ analysis

An overview of the second analysis is given in this subsection. The second analysis is performed using the same finite element model and calculation as the previous analysis. With the exception that this ‘cracked’ analysis simulates the cracking of the wall and floor by reducing the Young’s modulus at a specific time step, as explained in the previous subsection. The purpose of this analysis is to examine the development of the results after 301 days in order to determine the critical time for the application of mobile loads. This information is required to perform the third and final analysis in the next section.

Similar to the previous analysis, this analysis required around 10-12 hours to complete, resulting in a dataset of around 38 GB of relevant output results for each time step. Convergence was achieved after one to a maximum of three iterations for both the transient heat transfer and structural non-linear analyses.

Firstly, Figure 4.27 shows the results of the Young’s modulus development in the wall. The Young’s modulus of the middle cross-section is shown at three different time steps. The first time step, at 254 days, represents the moment when a maturity age of 9.10 days is first reached, resulting in the start of Young’s modulus reduction as described in the input and shown in Figure 4.26a. The second time step, at 255 days and 12 hours, is chosen because, based on the previous subsection, cracking is expected to occur around this time step. Consequently, the Young’s modulus should be reduced at this time step, particularly in the area where the first crack is expected. The final time step is taken at 260 days, which shows a reduction in Young’s modulus over almost the entire cross-section.

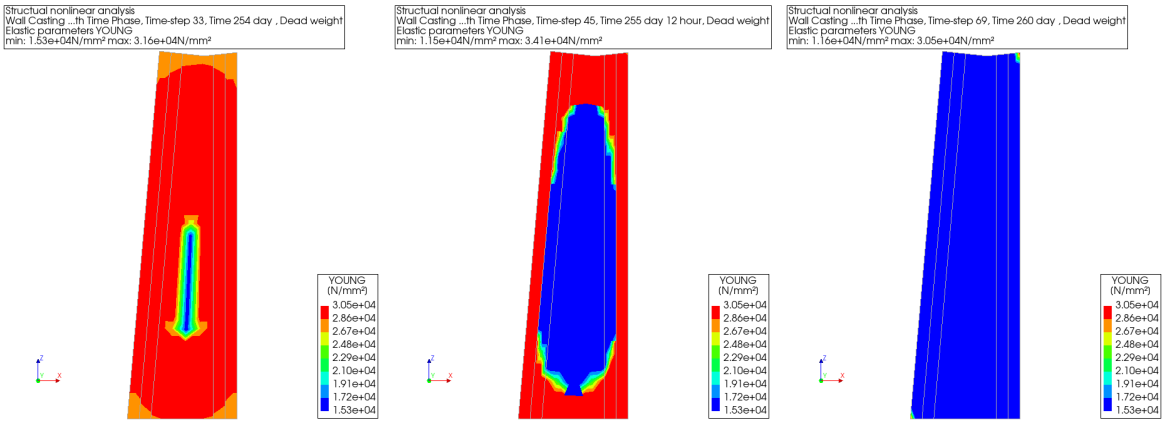

(a) Result at 254 days (b) Result at 255 days and 12 hours (c) Result at 260 days

Figure 4.27: The Young’s modulus result shown for the middle wall cross-section for three different time steps.

As expected, when using maturity instead of time to specify the reduction in Young’s modulus, a non-uniform reduction in Young’s modulus is observed, as shown in the figure above. To check whether there are any significant changes before and around the time of cracking between the first and second analyses, the horizontal stress developments within the effective areas of the wall are compared in Figure 4.28. In addition, the development of the tensile strengths is shown. The selected nodes are taken along the wall thickness in the middle of the wall approximately 1000 mm from the top (where the crack index first falls below 1.0).

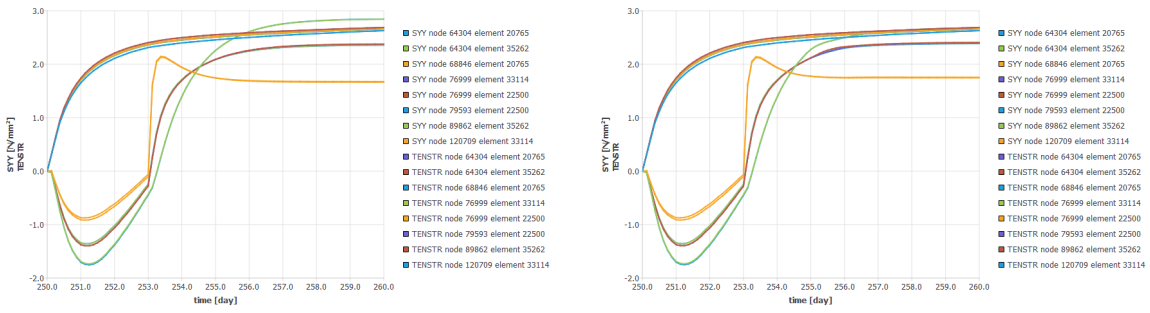

(a) Analysis results from the first ‘uncracked’ analysis (b) Analysis results from the second ‘cracked’ analysis

Figure 4.28: Comparison between the horizontal stress development and tensile strength development between the two analyses taken from the selected nodes along the thickness.

From Figure 4.28 it can be seen that the stress developments are quite similar between the two analyses, at least up to the expected moment of cracking (at 255 days and 12 hours). After that, some minor changes can be seen, especially in the green/blue line representing the nodes within the inside part of the wall. This is expected due to the lower Young's modulus in the next steps, resulting in less stress increase due to temperature and shrinkage strain increase. However, since the developments are quite similar up to the assumed moment cracking, it can be concluded that the results are valid and that the non-uniform stiffness reduction has only a small influence. As the reduced Young's modulus is implemented with sufficient accuracy, the governing time step can be found with this analysis. It should be noted that although the tensile stress (which is almost equal to the maximum principal stress due to the horizontal dominance) no longer exceeds the tensile strength, this is purely coincidental. This is because the concrete stress cannot be limited to the tensile strength when considering the elastic properties of the material.

In preparation for the third analysis, the critical time step for applying the mobile loads should be determined. This is done by checking the development of the horizontally distributed normal forces (n_{xx}) within the effective thickness of the walls and the positively distributed design moments (m_{xD+}) across the entire wall. These developments are shown in Figures 4.29a and 4.29b respectively. It should be noted that ideally Figure 4.29a should show the distributed design forces; however, this specific output cannot be selected for this type of analysis in DIANA FEA. Nevertheless, the influence of the distributed shear force (n_{xy}), which is relatively small (about -7 kN/m compared to about 500 kN/m), is negligible and does not change noticeably. The elements selected for the figures are located approximately 650 mm above the bottom of the wall and approximately 1900 mm in the negative Y-direction from the centre of the wall. This region corresponds to the region where the governing design forces and moments were initially found in the original calculation model. Consequently, it is likely that this region will also be governing in the case study model, particularly when the mobile loads are included.

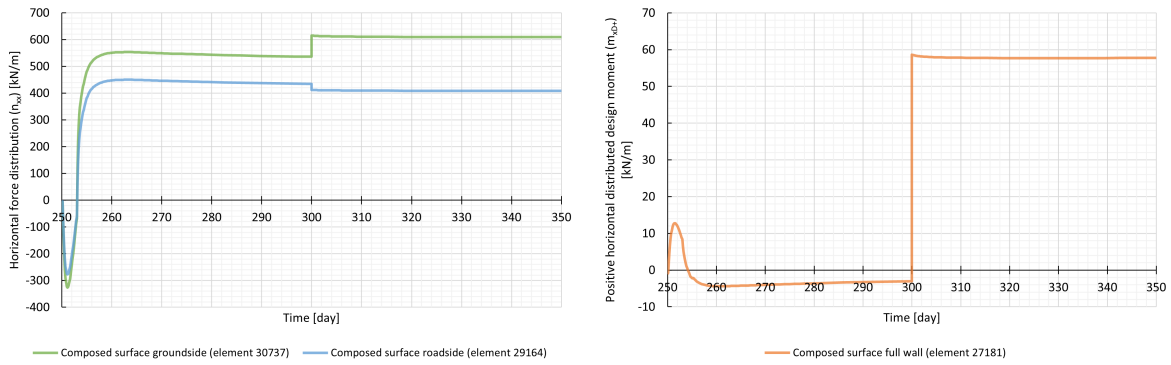

(a) Horizontal distributed forces (n_{xx}) developments (b) Positive distributed design moment (m_{xD+}) development

Figure 4.29: Analysis results from the wall to find the governing time step to apply the mobile loads.

The figures above show the development from 250 days (pouring of the wall) to 350 days, where the influence of the removal of the sheet piling and the application of dead loads to the wall and floor can also be seen at 300 days. Removal of the sheet piling and application of the dead loads resulted in an increase in the distributed normal forces from 536.0 to 615.1 kN/m for the effective area on the roadside and a decrease from 434.4 to 412.0 kN/m for the groundside. The reason that one side decreases as the other increases is because the design moment in the full wall increases from -3.03 to 58.61 kNm/m. Note that a negative design moment does not appear in the calculation definition used in this study, but is mentioned and shown in the figure for completeness. Although difficult to see, it can be observed that the distributed forces and moments decrease slightly after 300.001 days. Specifically, the distributed forces decrease to 411.2 kN/m and 613.6 kN/m respectively at 301 days, which according to the modelling approach is the first day on which the mobile load can be expected. Thereafter, the forces continue to gradually decrease to 408.8 kN/m and 609.7 kN/m respectively. The positive distributed design moment follows a similar trend, decreasing to 58.31 kNm/m at 301 days and 57.75 kNm/m at 350 days. Based on the values described and the figures, it can be concluded that the forces and moments are gradually decreasing. Therefore, 301 days is considered to be the most critical time step and it is at this time step that the mobile loads are applied in the analysis in the next subsection.

4.7.3. Analysis results and post-processing 'cracked' analysis including ML

This subsection presents the analysis results and post-processing of the third and final analysis, which includes the application of mobile loads at the governing time step, as discussed in the previous subsection, at 301 days. This analysis is performed using the same finite element model and calculation as the previous analysis and therefore also assumes a 'cracked' wall section at 255 days and 12 hours by reducing the Young's modulus by 50%.

To apply the mobile loads at 301 days, the time steps listed in Table 4.7 were adjusted by removing the time steps beyond 301 days. Consequently, the following time steps were used in the fifth phase: 0.001, 0.124 and 0.125(7x) days. The analysis with these adjusted time steps took a slightly shorter time of about 8 hours and generated a data set of about 34 GB. Convergence was achieved within one to a maximum of three iterations. In this subsection, the results for the distributed forces are presented and post-processed first, followed by the results for the distributed moments.

Results distributed forces and post-processing

The analysis results of the distributed forces are shown in Figures 4.30, 4.31 and 4.32. These correspond to the distributed horizontal normal forces (n_{xx}), the distributed vertical normal forces (n_{yy}) and the distributed shear forces (n_{xy}) respectively. The figures are taken from the two composite surfaces within the effective areas and each figure also shows the elements from which the averages are calculated. The selected elements in the figures are located approximately 650 mm above the bottom of the wall and approximately 1900 mm in the negative Y-direction from the center of the wall. This specific region corresponds to the location where the governing design forces and moments were initially found in the original calculation model and from which the governing load combination is taken. By selecting the results from the elements in this region, a fair comparison can be made with the original model.

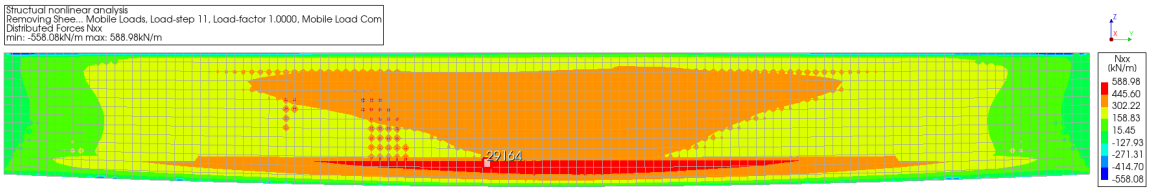

(a) Composed surface in the effective area at the roadside of the wall.

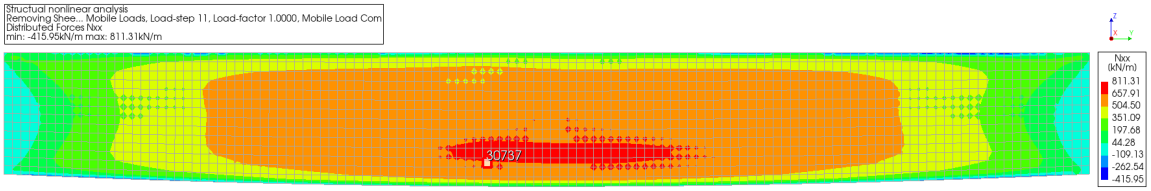

(b) Composed surface in the effective area at the groundside of the wall.

Figure 4.30: Horizontal distributed forces (n_{xx}) at 301 days (after applying the mobile loads).

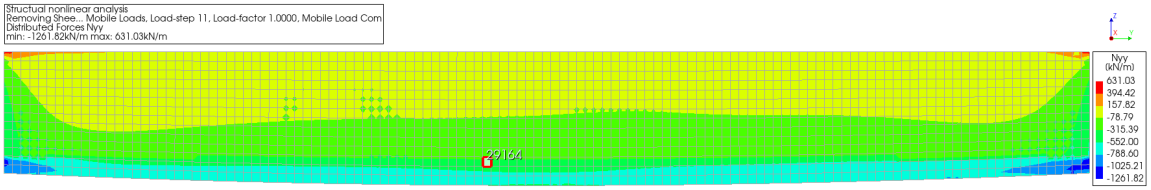

(a) Composed surface in the effective area at the roadside of the wall.

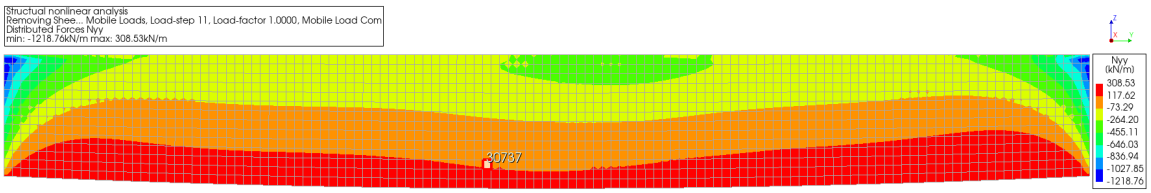

(b) Composed surface in the effective area at the groundside of the wall.

Figure 4.31: Vertical distributed forces (n_{yy}) at 301 days (after applying the mobile loads).

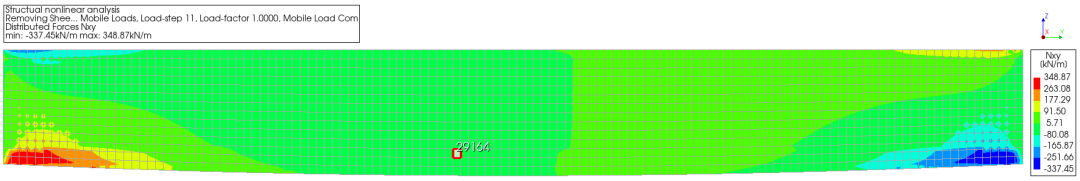

(a) Composed surface in the effective area at the roadside of the wall.

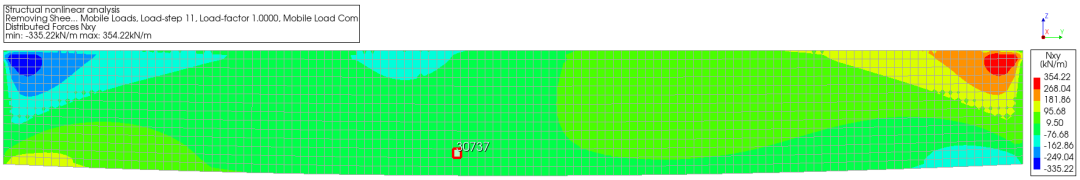

(b) Composed surface in the effective area at the groundside of the wall.

Figure 4.32: Distributed shear forces (n_{xy}) at 301 days (after applying the mobile loads).

The analysis results in Figures 4.30 - 4.32 show the distributed forces from the composed surfaces within the effective areas. Taking the average of the nodes within in elements 29164 and 30737 gives a horizontal distributed force of 436.40 kN/m and 669.34 kN/m for the roadside and groundside respectively. The vertically distributed normal forces are -367.65 kN/m and 111.28 kN/m and the distributed shear forces are -40.78 kN/m and -26.59 kN/m respectively. These distributed forces are only the results taken from the effective areas of the wall. Although this is correct for the internal forces due to temperature, shrinkage and creep, it is not the case for the external loads. The external loads are now distributed across the entire thickness of the wall, but since only the outside is reinforced and can therefore be controlled for cracking, this is where the loads should be transferred. Unfortunately, it was found that the combination of different areas could not be incorporated into a single analysis using DIANA FEA.

An approach was considered which involved reducing the Young's modulus of the internal area between the effective sections to approximately 1% after cracking. However, this adjustment in the stiffness of the wall resulted in a significant change in the structural behaviour. More specifically, it resulted in a 50% change in the distributed forces within the wall. Therefore, it was decided not to implement this approach and to just do a slightly larger post-processing. This post-processing was performed by extracting the increase in distributed forces at the start/load steps from the composed surface of the entire wall and subtracting this value from the increase in distributed forces within the two effective composed surfaces. The resulting increase, denoted Δn, was calculated for both the distributed normal forces and the distributed shear forces as shown in Table 4.8. This step was performed for three specific time points: 250 days, representing the application of the self-weight of the wall; 300 days, representing the application of the external loads from the deck; and 301 days, representing the application of the mobile loads.

Table 4.8: Distributed forces increase in the inside of the wall.

	Δn_{xx} [kN/m]	Δn_{yy} [kN/m]	Δn_{xy} [kN/m]
Increase at t=250 (self-weight)	-9.844	-50.474	0.044
Increase at t=300 (loads from deck)	46.057	-251.750	-13.080
Increase at t=301 (mobile loads)	105.428	-43.079	-80.153
Total increase from external loads	**141.64**	**-345.30**	**-93.19**

Table 4.8 shows the total load increase for the external loads applied to the wall that are not applied to the effective areas. These values do not include the effect of creep/shrinkage, although this should be included for the loads applied at 250 and 300 days. An approximate hand calculation showed that the effect of creep/relaxation on the distributed design forces was minimal. Using the approximate Equation 2.21, without considering the effect of shrinkage, the reduction in forces was estimated. For the self-weight load applied at 250 days, with a $\varphi(t = 51, t_0 = 0) = 1.95$, a reduction of 76.1% was calculated at 301 days. Similarly, for the external loads from the deck applied to the wall at 300 days, with a $\varphi(t = 51, t_0 = 50) = 0.165$, a reduction of 11.9% was calculated at 301 days. Consequently, there is a slight decrease in Δn_{xx}, which primarily governs the horizontal distributed design force, from 141.64 kN/m to 141.54 kN/m. It is important to note that this hand calculation does not take into account the degree of restraint or the influence of shrinkage, which makes it less accurate. Nevertheless, the results suggest that the effect of creep/relaxation is almost negligible for this particular load increase and is therefore not considered.

In addition to the load increase explained above, the two load cases not included in the DIANA FEA case study model must also be added to the analysis results. These are the variable summer temperature and the prestressing load in the deck, the corresponding horizontal distributed forces are shown in Table 4.4. The total distributed loads are calculated and shown in Table 4.9.

Table 4.9: Overview and summation of the total distributed forces.

	n_{xx} [kN/m]	n_{yy} [kN/m]	n_{xy} [kN/m]
DIANA FEA result	1105.75	-256.02	-67.37
External loads increase	141.64	-345.30	-93.19
Excluded load cases	-18.26	0.38	-48.80
Total distributed force	**1229.67**	**-600.94**	**-209.36**

From the total distributed forces shown above, the horizontal distributed design force can be calculated. Since $n_{yy} < n_{xx}$ and $n_{yy} < -|n_{xy}|$ the design force can be calculated using $n_{xD} = n_{xx} + (n_{xy})^2/n_{yy}$. This gives a horizontal distributed design force of 1302.1 kN/m.

Results distributed moments and post-processing

Unlike for the distributed forces, it was possible to show the distributed design moments for the distributed moments. Figure 4.33 shows the positive distributed design moment obtained from the composed surface located throughout the entire wall. The figure also shows the element selected to calculate the average value, which is the same location as previously mentioned for the distributed forces. Only the positive distributed design moment is shown, as this is the only relevant output considering that the applied governing load case in this analysis was only governing the groundside, and therefore only the positive side is considered. If the roadside is of interest, a different load case should be applied as explained in Section 4.4.2.

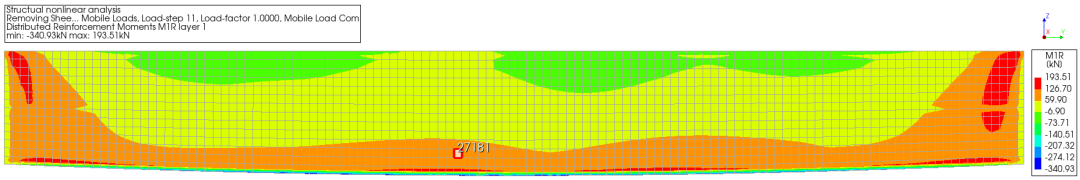

Figure 4.33: Positive distributed design moment (m_{xD+}) in the full wall, taken from middle composed surface at 301 days (after applying the mobile loads).

The analysis results in the figure above show the positive distributed design moment from the composed surface within the full wall. When taken the average from the nodes within element 27181, the positive distributed design moment is 83.64 kNm/m. The positive face is the groundside of the wall. Unlike as for the distributed forces, the distributed moments are taken for the full wall instead of only the effective areas, because the influence of the internal forces on the moments is quite small, and therefore no post-processing is required for the external load increments. Post-processing is required to be able to include the two load cases that were not included in the DIANA FEA case study model. These are the variable summer temperature and the prestressing load in the deck, the corresponding distributed moments are shown in Table 4.5. This is added to the DIANA FEA results in Table 4.10, which shows the distributed moments instead of the distributed design force, so that they can be added together. Because of the different positive moment definitions between SCIA Engineer, where the original calculation was made, and DIANA FEA, a minus is added to the analysis results, which does not affect the design moment calculated later.

Table 4.10: Overview and summation of the total distributed moments.

	m_{xx} [kNm/m]	m_{yy} [kNm/m]	m_{xy} [kNm/m]
DIANA FEA result	(-)69.65	(-)322.18	(-)13.99
Excluded load cases	-75.70	-39.55	-39.16
Total distributed moment	**-145.35**	**-361.73**	**-53.15**

Based on the total distributed moments shown above, the positive horizontal distributed design moment can be calculated. Since $m_{yy} < m_{xx}$ and $m_{yy} < -|m_{xy}|$, the positive design moment can be calculated using $m_{xD+} = -m_{xx} + |m_{xy}|$. This gives a positive distributed design moment of 198.5 kNm/m.

4.7.4. Analysis checks

This subsection focuses on performing several checks to validate the results obtained from the finite element analysis. The validation process involves comparing the case study results with the original calculation model and performing additional analyses. The following checks are performed:

- Displacement comparison and symmetry check
- External force comparison verification check
- Creep and shrinkage influence check
- Influence of a long-term analysis check
- Mesh refinement check
- Step size refinement check

These checks ensure the reliability and validity of the finite element results by comparing them with the original model and performing additional analyses to verify key aspects of the analysis.

Displacement comparison and symmetry check

To validate the displacements obtained from the finite element analysis performed in Section 4.7.3, a comparison is made with the original calculations. This comparison helps to assess the similarity between the two sets of analyses, which indicates the accuracy of the model. In addition, the symmetry assumption made in the modelling approach is checked and validated.

Figure 4.34 shows the displacement results in the Z-direction obtained from the analysis performed in Section 4.7.3. The figure shows the displacements at the start of each phase (start step) and the load step at the fifth phase when the mobile load is applied.

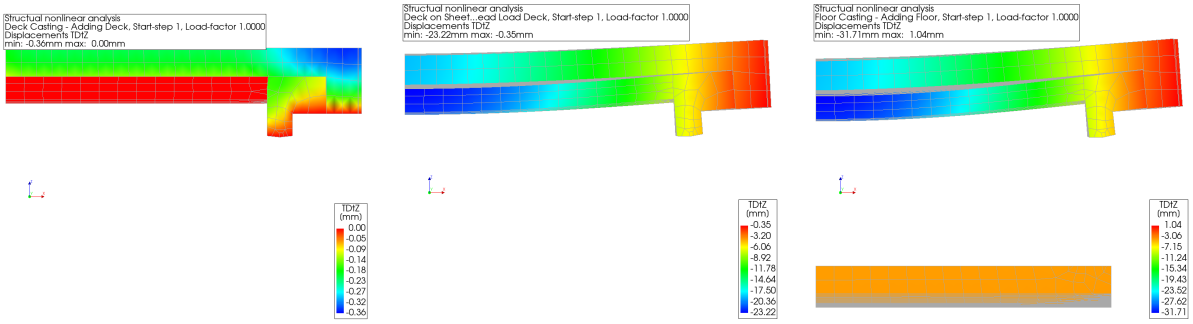

(a) Phase 1; $t = 0$ days

(b) Phase 2; $t = 100$ days

(c) Phase 3; $t = 200$ days

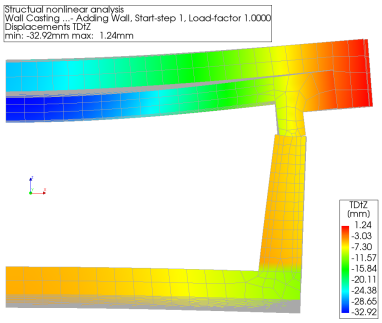

(d) Phase 4; $t = 250$ days

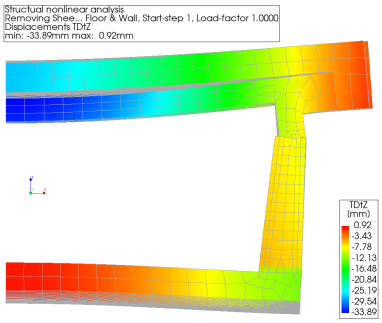

(e) Phase 5; $t = 300$ days

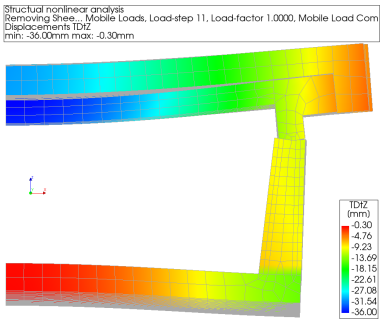

(f) Phase 5; $t = 301$ days

Figure 4.34: Displacement in Z-direction for the case study model at 6 different times (deformation scale = 25).

From Figure 4.34 it can be seen that the total displacement reaches 36.00 mm. It can also be seen that the symmetry plane on both the floor and the deck moves vertically while remaining vertical, indicating that the boundary conditions are correctly modelled. Figure 4.34a shows that the deck cannot move downwards due to the support of the formwork which is removed at 100 days as shown in Figure 4.34b. The removal of the sheet piles and the application of dead loads to the wall and floor can be seen between Figures 4.34d and 4.34e. Figure 4.34f shows the effect of applying the mobile loads.

To compare the results with the original calculation model, the specific governing load combination was calculated in the original SCIA Engineer model. In this calculation model, the prestressing load and the summer temperature load groups were removed in order to run exactly the same governing load combination as applied in the case study model. The displacement results in the global Z-direction are shown in Figure 4.35.

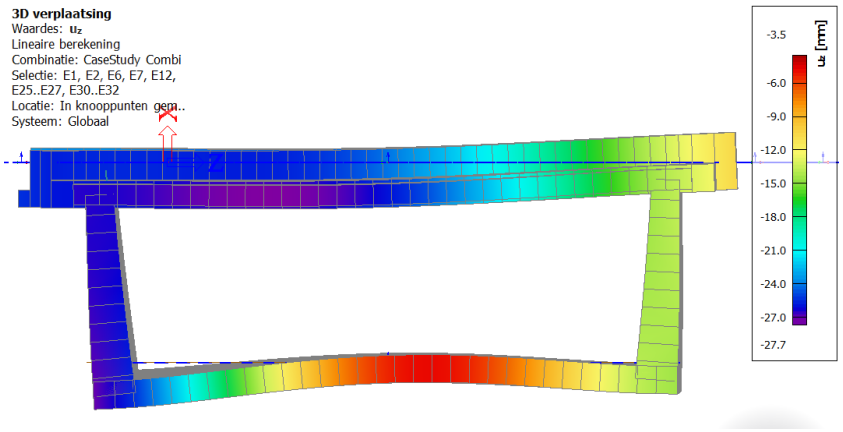

Figure 4.35: Displacement in Z-direction for the original calculation model within SCIA Engineer.

Figure 4.35, shows that the total displacement in the original calculation model is -27.70 mm, located at the bottom of the deck, slightly to the left of the centre of the deck. When analysing the right side of the deck, a displacement of -26.3 mm was found. Comparing these results with the case study model, the displacement of -36.00 mm is significantly higher. However, this difference can be explained by the fact that the original model does not take into account the pouring/loading phases or the effect of creep on the displacement.

In order to make a fair comparison with the original calculation model, a simplified analysis was performed using only a linear static analysis with the geometry of the last phase. The results are shown in Figure 4.36a. In addition, to investigate the effect of symmetry on displacement, an extra model was created that included the full geometry and all loads on both sides. The same linear analysis was performed on this model and the displacement in the Z-direction is shown in Figure 4.36b.

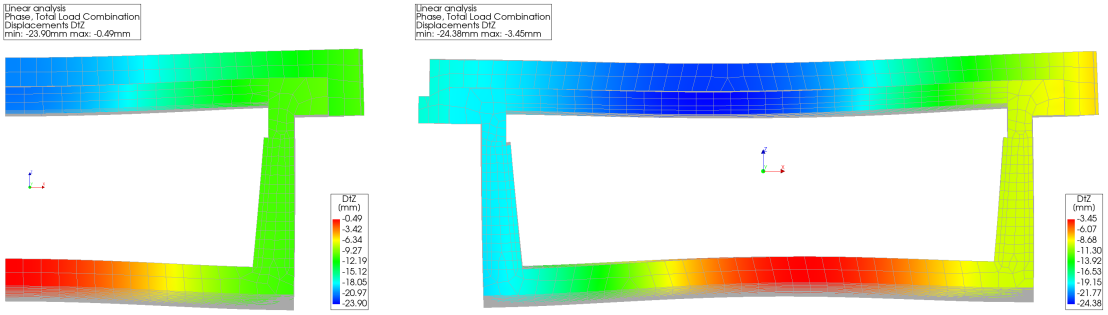

(a) Linear symmetry model (b) Linear full model

Figure 4.36: Displacement in Z-direction for the two different linear case study models (deformation scale = 25).

The maximum displacement in the Z-direction for the linear model using symmetry, shown in Figure 4.36a, is -23.9 mm. This is close to the displacement of -26.7 mm found in the original calculation model. This slight difference is probably due to the use of 3D elements in the case study model compared to the 2D elements in the original model. The 3D elements allow for a more accurate modelling of the geometry which, for example, influences the amount of self-weight. This can be seen in Figure 4.35, where the geometry overlaps at the connections between the walls and the deck/floor, resulting in additional self-weight compared to the 2D elements. As self-weight is a significant contributor to displacements, this discrepancy is likely to be the reason for the small difference.

Comparing the subfigures in Figure 4.36 it can be seen that the results between the linear symmetry model and the full model are quite close. The structure using symmetry has a maximum displacement in the Z-direction of -23.90 mm, while the full structure has a maximum displacement of -24.38 mm. Focusing only on the right part of the structure, a maximum displacement of -24.13 mm is found, which is only 0.23 mm more than the symmetry model. The differences on the floor are slightly larger, around 3.0 mm, because the symmetry model does not take into account the large load from the floor for the cycle path in the underpass on the left. Overall, however, both models show similar behaviour, concluding that the symmetry approach was a valid approximation.

External force comparison verification check
The external forces calculated in the case study are compared with the forces obtained from the original calculation model to ensure consistency and accuracy. First, the external forces from the analysis in Section 4.7.3 are compared and post-processed. Table 4.11 shows the increase in distributed forces and moments within the composed surface after the external loads are applied. The distributed forces and moments from the excluded external load cases are added to allow a fair comparison with the original calculation model. As the increases are taken at the start/load steps, the influence of internal forces/moments due to temperature and shrinkage and the influence of creep are not included. Note that for the moments in the table, a (-) is added due to the different positive definitions between the case study model in DIANA FEA and the original calculation in SCIA Engineer.

Table 4.11: Overview and summation of the total external distributed forces and moments.

	n_{xx} [kN/m]	n_{yy} [kN/m]	n_{xy} [kN/m]	m_{xx} [kN/m]	m_{yy} [kN/m]	m_{xy} [kN/m]
Increase at t=250 (self-weight)	-17.00	-87.42	0.06	-(-)1.20	-(-)6.36	-(-)0.04
Increase at t=300 (loads from deck)	102.76	-325.42	-21.56	(-)59.94	(-)301.11	(-)1.70
Increase at t=301 (mobile loads)	186.30	-52.42	-134.72	(-)14.45	(-)53.72	(-)10.89
Excluded external load cases	-18.26	0.38	-48.80	-75.70	-39.55	-39.16
Total distributed force/moment	**253.80**	**-464.89**	**-205.11**	**-148.89**	**-388.01**	**-51.70**

The results shown in the table above are compared with the original calculation in Table 4.12. As significant differences were found, the linear model, discussed in the previous section, was also post-processed to compare with both the case study and the original calculation. The analysis results of this linear model, which does not consist of multiple time steps or phases, were added to the excluded external load cases. The results of this are also shown in Table 4.12 together with the case study results and the original calculation. The distributed forces and moments of the original calculation were previously described in Section 4.4.2.

Table 4.12: Distributed forces and moments of the wall from three different analyses.

	n_{xx} [kN/m]	n_{yy} [kN/m]	n_{xy} [kN/m]	n_{xD} [kN/m]
Case study model (phased/non-linear)	253.80	-464.89	-205.11	**344.3**
Linear case study model	334.29	-455.37	-222.32	**452.8**
Original calculation model	337.16	-476.92	-274.24	**494.9**
	m_{xx} [kN/m]	m_{yy} [kN/m]	m_{xy} [kN/m]	m_{xD+} [kN/m]
Case study model (phased/non-linear)	-148.89	-388.01	-51.70	**200.6**
Linear case study model	-194.93	-590.21	-60.16	**255.1**
Original calculation model	-217.94	-711.80	-70.68	**288.6**

From the results of the analysis performed in Table 4.12 it can be seen that the results from the case study model are quite a bit lower than both the linear analysis and the original calculation model. Although it is not surprising that phasing has an influence, it was not expected to be around $21 - 24\%$ when comparing the phased/non-linear with the linear model. When comparing the linear case study model with the original calculation model it can be seen that the results are quite similar despite the different type of elements used (3D compared to 2D in the original calculation) and a slightly different geometry. This suggests that all external loads applied to both case study models are correctly applied and the differences between the phased case study model and the original calculation model are only due to the application of phasing. This appears to result in a different force distribution, resulting in a lower horizontal distributed design force and a positive distributed design moment.

Creep and shrinkage influence check

Two additional analyses were performed to determine the influence of both creep and shrinkage on the force development. These analyses were performed because it was found in the case study model that the distributed forces did not decrease as much as expected due to creep and relaxation. The same model used in Section 4.7.3 was reanalysed but with slight variations.

In the first analysis, to find the influence of shrinkage, shrinkage was excluded from the current material model by simply deselecting it. In the second analysis, the effect of creep was investigated by replacing the current material model with an alternative material model that did not include creep effects. This alternative material model used a linear approach without creep and included the same material properties as the original model, except for the reduced Young's modulus development. This was because, when a reduced Young's modulus development was used in the first attempt, the stresses decreased as the Young's modulus decreased. This result was unexpected as it did not occur in the other analyses. Consequently, the full Young's modulus development was used, which should not affect the results as Figure 4.28 shows that the reduced Young's modulus had no significant effect on the stress development up to 300 days. At least not for the horizontal distributed force within the effective areas which is of interest. Therefore, Figure 4.37 shows the horizontal distributed force development from the analysis without creep and shrinkage by taking the combined average of elements 30737 and 29164 in the effective areas up to 300 days.

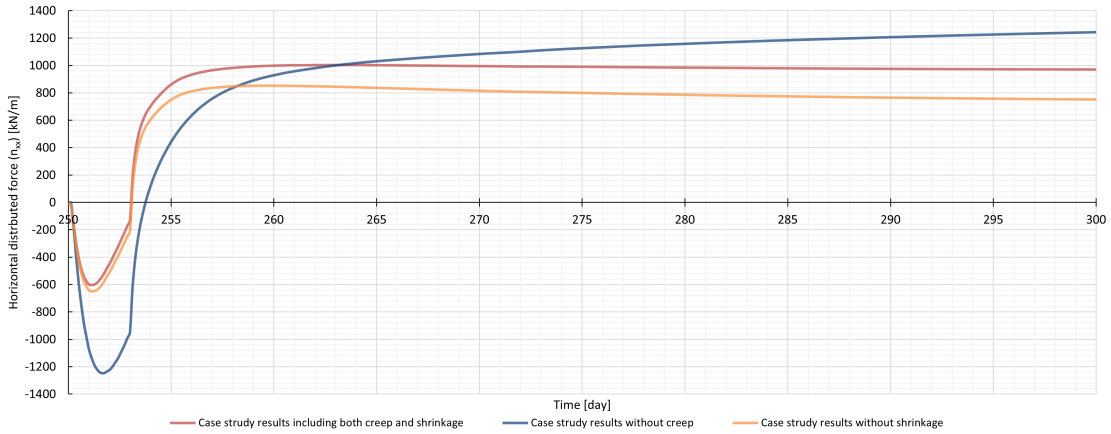

Figure 4.37: Horizontal distributed forces development for the analysis without creep and shrinkage and the analysis performed in Section 4.7.3 (combined average of element 30737 and 29164 in the effective areas).

Based on Figure 4.37, which compares the analysis result without creep with the case study result, it is clear that creep has a significant effect. The analysis without creep shows that both the negative and positive horizontal distributed forces were significantly higher. At 300 days, the horizontal distributed force, almost equal to the design distributed force at this phase, calculated by averaging the nodes within the elements within the two effective areas, was 1242.2 kN/m compared to 970.5 kN/m when creep is included. Thus, the internal forces due to hardening in the case study analysis are reduced by 28.0% in 50 days due to creep. The distributed force development without creep shows a continuous increase after the first few days, instead of a very slight decrease in the analysis with creep.

The results of the analysis without shrinkage, shown in Figure 4.37, show a more significant reduction in horizontal distributed forces compared to the analysis including shrinkage. At 300 days, the total horizontal distributed force, calculated by averaging the nodes of the elements within the two effective areas, was 751.5 kN/m compared to 970.4 kN/m when shrinkage is included. Therefore, including shrinkage in the analysis resulted in a 22.7% higher result for the case study model. It can also be seen that, as expected, the distributed force decreases more without shrinkage than including shrinkage.

Overall, it can be concluded that the effects of shrinkage and creep partially cancel each other out. While the distributed forces gradually decrease due to creep and relaxation, they remain relatively stable due to the continuation of the increasing shrinkage strain. These additional analyses provided further insight into the individual components of creep and shrinkage and validated the correctness of both creep and shrinkage implemented in the case study model.

Influence of a long-term analysis check

The modelling approach assumed that the most critical period for the wall would be between 1 and 50 days after removal of the sheet piles ($t = 301$ and $t = 350$ days in the analysis). As it was found in Section 4.7.2 that the distributed forces and moments slowly decrease after 301 days, this was considered to be the critical time step and no analyses were performed for a longer period. However, in order to provide an additional comparison with the original calculation performed at 't=∞', an attempt was made to extend the analysis of the case study model for a longer duration. An analysis was performed for 665 days, with simulations performed up to one year after removal of the sheet piles instead of the initial 50 days (as described and performed in Section 4.7.2).

Due to limitations in the current material model in DIANA FEA, only a maximum of 30 time/maturity steps could be selected for the creep/Young's modulus input. This limitation affects the accuracy of the extended analysis, as specifying a longer time period for creep and Young's modulus requires fewer time/maturity steps in the crucial first two weeks after the wall is cast. In the case study model with 100 days of maturity/time steps specified for the wall, 16 of these time/maturity steps were within the first 14 time/maturity days. However, for the extended analysis (415 days) only 9 time/maturity steps were used. This may result in a slight reduction in accuracy, but it is expected to be sufficient to analyse the development of distributed forces between 350 and 665 days of the analysis.

The same analysis was performed as described in section 4.7.2, except that the material input was specified up to 665 days instead of 350 days, and the time step sizes were extended to include the 665 days. The following time step sizes were used instead of those specified in Table 4.7: '0.001 0.124 0.125(7x) 0.25(4x) 0.5(8x) 1.0(9x) 3.5(10x) 7(13x) 14(16x)' days. The same reduced Young's modulus development was used as found in Section 4.7.1 and therefore the same time sep of cracking is assumed.

As only 18 additional steps were added, the additional calculation time was only about 2 hours. The main output, the horizontal distributed forces within the effective areas, is shown in Figure 4.38. This figure also includes the distributed forces obtained from the calculation performed in Section 4.7.2. The distributed forces shown in the figure represent the combined average distributed forces from the two effective areas within elements 30737 and 29164.

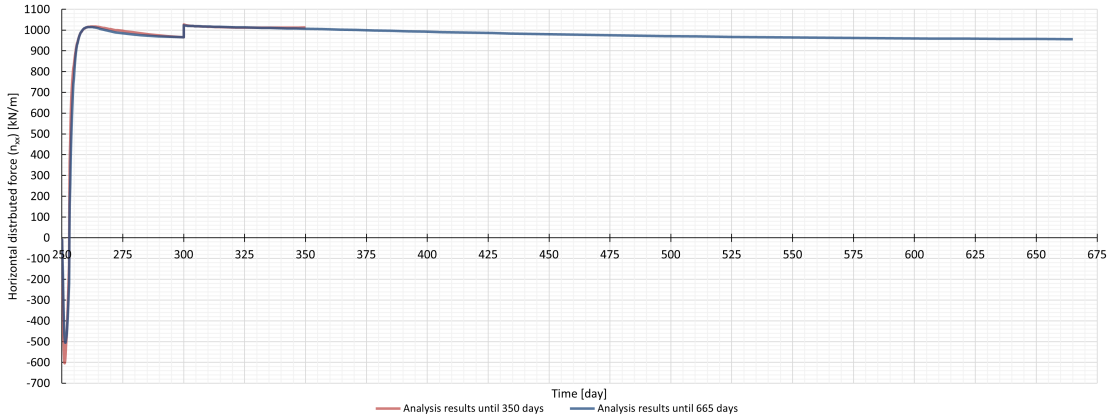

Figure 4.38: Horizontal distributed forces development for the extended analysis and the analysis performed in Section 4.7.2 (combined average of element 30737 and 29164 in the effective areas).

Figure 4.38 shows small differences in the analysis results for the first few days, but they are quite close for most of the time to the end of the 350 day analysis. The initial difference is, as expected, due to the reduced number of time/maturity steps resulting in less accuracy in the Young's modulus development.

The extended analyses for long-term predictions show a decrease in the distributed forces that continues after 350 days, mainly due to a larger creep/relaxation decrease compared to shrinkage induced increases. After 500 days no changes are seen in the figure, but analysis of the results of each time step shows that the distributed force continues to decrease up to 665 days. At 300 days the horizontal distributed force is 1023.0 kN/m which decreases to 956.6 kN/m at 665 days, a decrease of 6.5% within one year. Of this, only 0.25% is reduced in the last 50 days. Therefore, although this analysis only covers one year after removal of the sheet piles, it can be concluded that no significant further reduction in creep/relaxation can be expected in the long term.

By performing the same post-processing as in Section 4.7.3, it was found that the horizontal distributed design force is 1240.9 kN/m, and the positive horizontal distributed design moment is 198.4 kNm/m. These values are only slightly lower than those obtained in Section 4.7.3.

Mesh refinement check

A mesh refinement study was performed to assess the accuracy of the results. Refinement of the mesh increases the number of elements, resulting in a more accurate representation of the structural behaviour. To perform a mesh refinement, the same model as described in Section 4.7.3 was used, but with a refined mesh. For the first attempt, the mesh size was reduced by 50%, resulting in a mesh size of 268.75 mm for the deck and floor and 134.375 mm for the wall. The effective areas were divided into 4 sections per side to create 4 elements along the effective thickness. When generating the mesh, between 3 and 5 elements were created inside the wall, resulting in a total of between 11 and 13 elements in the wall thickness. The total number of elements used for the wall, including composed surfaces and boundary elements, was $121\,275$. The deck used $71\,984$ elements and the floor $49\,498$. Unfortunately, when this model was calculated it was found that the computer used did not have enough memory to solve the system of equations for the $242\,757$ elements. Although substructuring and different types of solvers were used to reduce the memory requirement, it was found that this was not possible with this computer.

In order to still be able to perform a mesh refinement check, a second model was created in which the mesh size for the deck and floor was halved, but the mesh size for the wall was not halved but reduced by a third. This reduction of approximately 33.3% resulted in a mesh size for the wall from 268.75 mm to 179.167 mm. The effective areas were divided into three sections instead of two per side to force the mesh generator to create three elements along the effective thickness. Between two and four elements were created inside the wall, giving a total of between 8 and 10 elements in the thickness. This results in between 17 and 21 nodes along the thickness of the wall due to the quadratic elements used. A total of $56\,335$ elements were used for the wall, including the composed surfaces and boundary elements. For the deck, $60\,353$ elements were used and for the floor, $37\,402$ elements were used. For these $154\,090$ elements it was found possible to analyse the structure. The mesh of the concrete parts is shown in Figure 4.39, without the composed surfaces and thermal boundary elements. The original mesh is shown in Figure 4.19 and used $48\,426$ elements. So in total the mesh refinement uses more than 3 times as many elements as the original model.

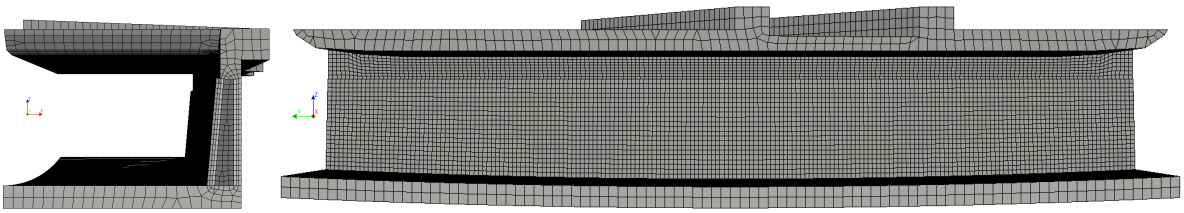

(a) Y-direction view (b) X-direction view

Figure 4.39: The Finite Element Mesh for the analysis (perspective projection).

Although the analyses could be performed, it was found that the analysis took an extremely long time to run. It was expected to take significantly longer than previous analyses, but unfortunately it took so long that it was decided not to complete the analysis. The first three phases, which normally take about an hour, took about 8 hours, which was doable. However, from the fourth phase onwards, the computation time increased even more, most likely because it was right at the limit of the computer. After another 6 days of running it had only reached step 82 of 112 steps of the structural non-linear analysis in phase 4; 'Wall Casting (2/2)'. This meant that it would have taken approximately 4 more days of running to complete the fourth and fifth phases. Unfortunately, there was no time left to complete this full analysis. The uncompleted analysis resulted in a dataset of around 120 GB of relevant output results for each time step.

Despite the fact that the analysis was stopped after 300 days for the transient analysis and 263 days and 6 hours for the structural non-linear analyses, it is still possible to compare the results up to this time step. The results from the original case study model are checked against the mesh refinement model by comparing the peak temperature in the wall, the temperature development in the wall and the total displacement at the final step.

Firstly, the peak temperatures, which are the maximum temperatures reached during the analysis, are compared in Figures 4.40a and 4.40b, which shows the middle cross-section at the maximum temperature time step at 252 days. The temperature developments of the nodes where the highest peak temperature was found are compared and shown in Figure 4.40c. The temperature development is shown up to 275 days because after that both are rounded to 15.0 °C and no changes can be seen.

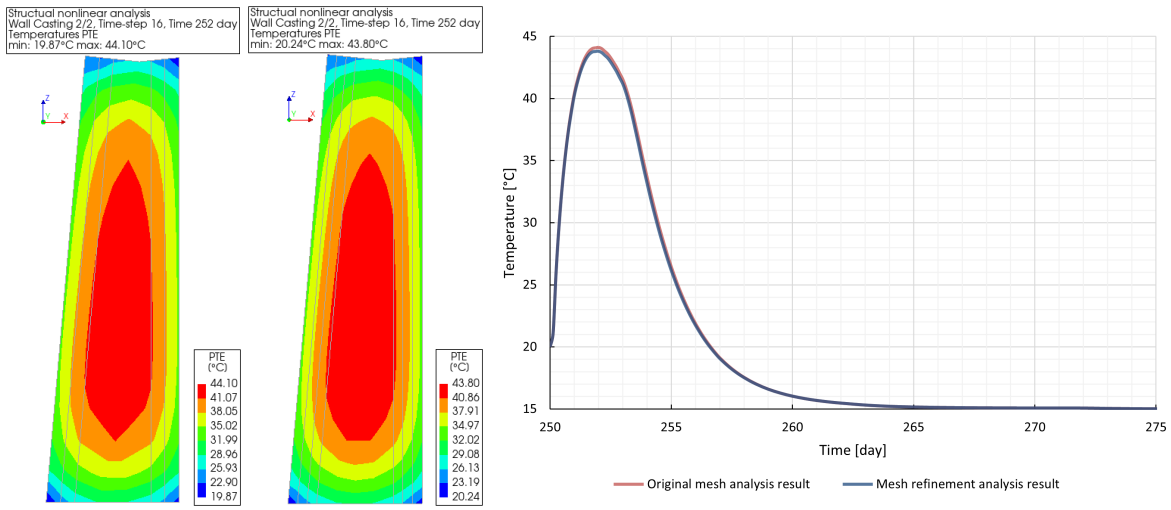

(a) Original mesh (b) Mesh refinement (c) Comparison of temperature development from the nodes with the highest temperature peak

Figure 4.40: Temperature analysis results comparison between the original and the refined mesh.

The figure above shows that the results of the mesh refinement analysis and the original mesh analysis are very close. The maximum temperature at the peak step on 252 days is 44.10 °C for the original mesh size and 43.80 °C for the refined mesh size. This is a difference of only 0.68%. The same difference was found for the maturity/equivalent age, which was 4.52 days instead of 4.55 days at this time step. As the maturity/equivalent age is very close, this also means that the development of the mechanical properties will be almost the same.

Another comparison is made between the mesh refinement analysis and the original mesh size, which is the displacement in the Z-direction of the structure. Figure 4.41a shows the displacement in the Z-direction at the last step of the non-linear analysis of the mesh refinement analyses, which was at 263 days and 6 hours. This is compared with the same time step from the case study model with the original mesh, shown in Figure 4.41b.

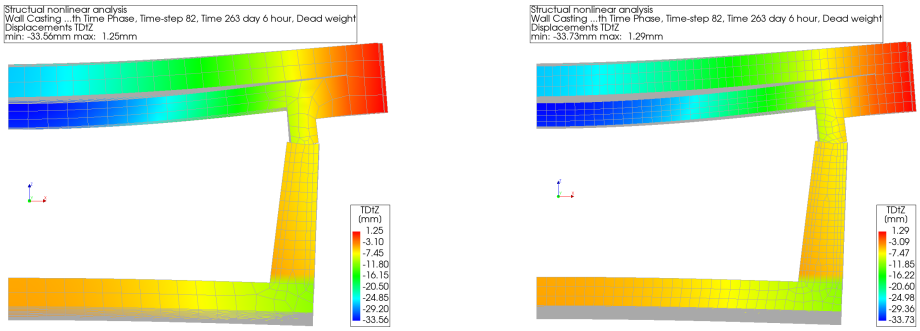

(a) Original mesh (b) Mesh refinement

Figure 4.41: Displacement in Z-direction for the two different mesh size models (deformation scale = 25).

Figure 4.41 shows that the displacements in the Z-direction are very similar. The maximum negative displacement in the Z-direction is -33.73 mm for the mesh refinement compared to -33.56 mm, which is only a 0.51% difference. The difference in the maximum positive Z-direction is only 0.01 mm. So both are very close, showing that the refined mesh does not have that much influence.

The development of the distributed forces were also compared between the analysis with the refined mesh and the analysis with the original mesh size. Although this could only be done for all the steps, very similar results were found. It can therefore be concluded that no significant changes (greater than 1%) were found, at least up to 263 days and 6 hours, but most probably for the full analysis. This indicates that the original mesh size in the case study was sufficiently small.

Step size refinement check

A step refinement analysis is performed to check the accuracy of the results. By refining the time step increment the time dependent behaviour of the structure can be captured more accurately. The same analysis as in Section 4.7.3 is performed but with time steps that are 50% as small. This results in about twice as many time steps 551 instead of 278. The new time step sizes are shown in Table 4.13 and can be compared with Table 4.7 for the first four phases and with '0.001, 0.124 and 0.125(7x)' for the fifth phase. The last phase has been adjusted in Section 4.7.3 to apply the mobile loads at 301 days instead of 350 days.

Table 4.13: Overview of the time step sizes for each phase in the time step refinement

Phase nr./ name	Time step sizes [day]
1; Deck Casting	0.0010 0.1240 0.1250(55x) 0.250(28x) 0.50(14x) 1.0(16x) 3.50(18x)
2; Deck on Sheet Piles	0.0010 0.1240 0.1250(7x) 0.250(4x) 0.50(14x) 1.0(14x) 3.50(22x)
3; Floor Casting	0.0010 0.1240 0.1250(55x) 0.250(28x) 0.50(14x) 1.0(8x) 3.50(6x)
4; Wall Casting (1/2)	0.0010
4; Wall Casting (2/2)	0.0615 0.0625(111x) 0.125(56x) 0.25(28x) 0.5(16x) 1.75(12x)
5; Removing Sheet Piles	0.0010 0.0615 0.0625(15x)

The analysis with these refined time steps took about 15 hours to complete and generated a data set of about 67 GB. Both are almost twice as much, which was to be expected due to the twice as many time steps. Convergence was achieved within one to a maximum of three iterations. The results of the original case study model are checked against the results of the time step refinement model by comparing four things. First, both the peak temperature in the wall and the temperature development in the wall are compared. Second, both the total displacement and the horizontal distributed forces and moments in the final step are compared.

First, the peak temperature between the two different mesh sizes is compared in Figure 4.42a and 4.42b, which shows the middle cross-section at the maximum temperature time step at 252 days. The temperature development of the nodes where the highest peak temperature was found is compared and shown in Figure 4.40c. The temperature development is shown up to 275 days because after that both are rounded to 15.0 °C and no changes can be seen.

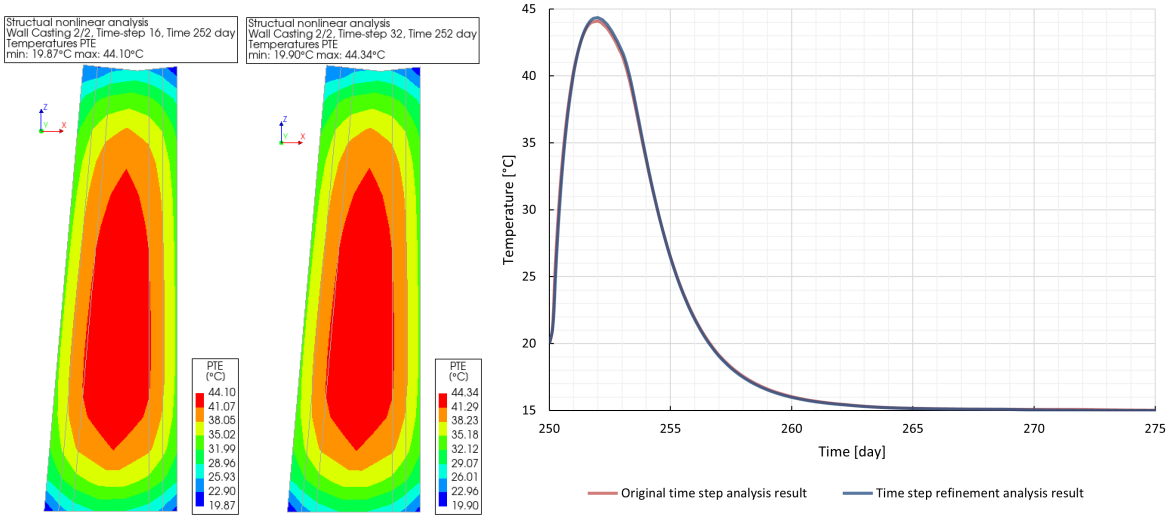

(a) Original time steps (b) Time step refinement (c) Comparison of temperature development from the nodes with the highest temperature peak

Figure 4.42: Temperature analysis results comparison between the original and the refined time steps.

The figure above shows that the influence of the time step refinement on the temperature is very limited. The maximum temperature at the peak step on 252 days is 44.10 °C for the original step size and 44.34 °C for the refined step size. This is an increase of only 0.54%. Surprisingly, when comparing the maturity/equivalent age, a slight decrease was found which was 4.46 days instead of 4.55 days at this particular time step. This is a difference of 1.87%, but when comparing Young's modulus only a difference of 0.2% was found. So although the equivalent age is slightly different, the development of the mechanical properties will be almost the same.

Another check performed is the displacement in the z-direction of the structure at the final steps of both analyses, which was at 301 days including the mobile loads. This is shown in Figure 4.43.

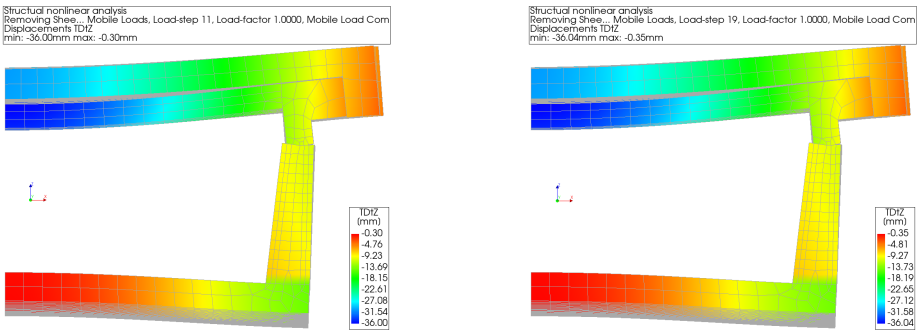

(a) Original step sizes (b) Step size refinement

Figure 4.43: Displacement in Z-direction for the two different step size models (deformation scale = 25).

Figure 4.41 shows that the displacements in the Z-direction are very similar. The maximum negative displacement in the Z-direction is -36.03 mm for the step refinement compared to -35.99 mm, a difference of only 0.11%. The difference in the maximum positive Z-direction is slightly larger, but still only 0.05 mm. So both are very close, showing that the refined step size does not have that much influence. As a final check, the distributed forces and moments are compared with the case study model using the original step sizes. Although all the distributed forces have been compared, the one that dominates the design moment calculation, the horizontal distributed force, is shown in Figure 4.44. The positive horizontal design moment is shown in Figure 4.45.

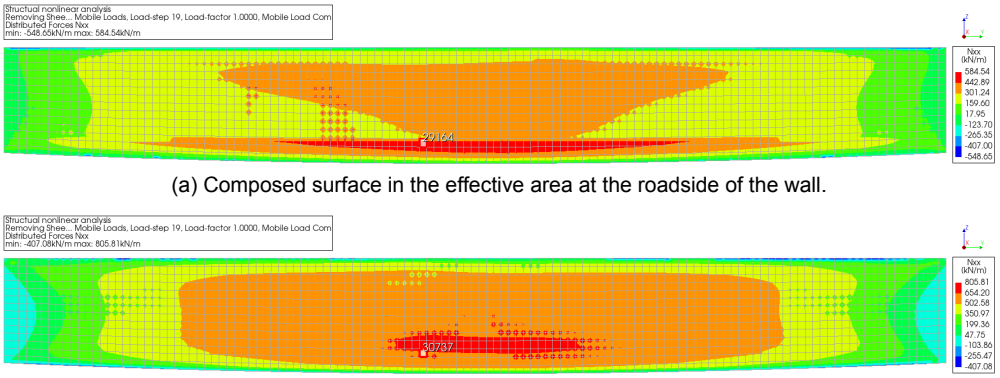

(a) Composed surface in the effective area at the roadside of the wall.

(b) Composed surface in the effective area at the groundside of the wall.

Figure 4.44: Horizontal distributed forces (n_{xx}) at 301 days (after applying the mobile loads) for the time step refinement analysis.

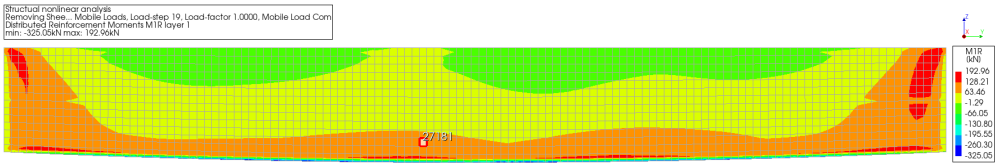

Figure 4.45: Positive distributed design moment (m_{xD+}) in the full wall, taken from middle composed surface at 301 days (after applying the mobile loads) for the time step refinement analysis.

Comparing Figure 4.44 from the time step refinement with Figure 4.30 which shows the case study results, it can be seen that the results are very close. A maximum horizontal distributed force of 584.54 and 805.81 kN/m was found with the time step size refinement compared to 588.98 and 811.31 kN/m with the original step size for the roadside and groundside respectively. This is 0.75% and 0.68% lower respectively. For the positive horizontal distributed design moment shown in Figure 4.45, which can be compared with Figure 4.33, a maximum design moment of 192.96 kNm/m was found instead of 193.51 kNm/m. Witch is only 0.29% lower. It can therefore be concluded that no significant changes were found, indicating that the original time step size in the case study was sufficiently small.

4.8. Final results and comparison

The analyses in this chapter have, as far as possible, used the same assumptions as in the original calculation in order to make a fair comparison. Where in the next chapter some of these assumptions are varied to determine their influence, this section compares the case study with the original calculation.

The main difference between the case study and the original calculation is in the calculation approach, where the time-dependent approach calculates the design stresses at each time step, whereas the original calculation only calculates them for two time steps. These are at 't=0', where only the thermal hardening forces are considered, and at 't=∞', where 50% of the thermal hardening forces and the external loads are considered. No steps are calculated in between, as it is assumed that there is a positive trend in the load specified in the Eurocode to incorporate the heavier loads expected in the future, and therefore only 't=∞' is calculated. However, as this trend is not specified, the full mobile load is applied to the case study model at the most critical time step (which was found to be 301 days, 51 days after pouring the wall), but an additional long term analysis was performed to see the influence of applying the mobile load at a later time step. The results of these analyses are shown in Table 4.14 together with the results of the original calculation.

Table 4.14: Comparison of the results found in the case study analyses with the original calculation.

	Without external load				With external and mobile loads			
	't=0'		t=300 days		t=301 days		't=∞'	
	n_{xD} [kN/m]	m_{xD+} [kNm/m]	n_{xD} [kN/m]	m_{xD+} [kNm/m]	n_{xD} [kN/m]	m_{xD+} [kNm/m]	n_{xD} [kN/m]	m_{xD+} [kNm/m]
Original calculation	1005	0	N/A	N/A	N/A	N/A	995	289
Case study analysis	1003[1]	0[1]	971	0	1302	199	1241[2]	198[2]

[1] = Results at 263 days, this is the time when all temperature induced forces/moments have occurred.

[2] = Results at 665 days, which was the maximum time for the long-term analysis, but it was found to be a good assumption for 't=∞'

From the table above it can be seen that the results prior to the application of external and mobile loading are very similar. However, it should be noted that the case study results include the effect of creep. Excluding creep, the distributed design force at 300 days reaches a significantly higher distributed force of approximately 1242 kN/m. When comparing the results including external and mobile loads, both the 301-day value and the prediction for 't=∞' (derived from analysis up to 665 days) are significantly higher than those of the original calculation. Although the external load contribution is about $30-31\%$ lower for both the distributed design force and moment due to phasing and improved geometry with 3D elements, this isn't the case for the restrained hardening forces, which are significantly higher. This is because the original calculation assumed a 50% reduction in hardening forces, which was not shown in the long-term analysis of the case study. In fact, the reduction is only 3.2% between 't=0' (at 262 days in the analysis) and 300 days, and 6.5% between 300 and 665 days for the distributed force. Together this is only about 10% compared to the 50% assumed in the original calculation. This is because, as the shrinkage strain continues to increase, it counteracts the creep/relaxation reduction, and because a creep reduction of 28.0% (971 instead of 1242 kN/m) was already found in the first 50 days.

The higher restrained concrete in the case study analysis without creep compared to the original calculation can be explained by two things. First, the original calculation, based on the book "Concrete Structures under Imposed Thermal and Shrinkage Deformations" by Van Breugel, et al. [2], assumes concrete cracking after 3 days at 70% strength development and at 75% of the average tensile strength. This corresponds to 1.58 MPa instead of the average tensile strength of 2.56 MPa found at the expected time of cracking in the case study analysis. Although the initial notion of cracking at 75% tensile strength appeared conservative, it proved to be non-conservative in the context of the distributed force development, as a higher tensile strength resulted in a higher distributed force.

Secondly, the original calculation excludes shrinkage at both 't=0' and 't=∞'. As in the calculation at 't=0', shrinkage would not have developed yet, and even if shrinkage for the first 50 days had been included in the hand calculation, it would not have increased the distributed force. As the temperature strain combined with the shrinkage strain is still in the crack formation phase, and therefore results in the same N_{crack}/distributed force (see Section 2.1.10). Including shrinkage in the calculation model for 't=∞' would have no significant effect either, as the shrinkage at 't=∞' is almost equal between the elements, resulting in almost uniform shrinkage. However, this contradicts the results of the case study where a 22.7% lower (751 instead of 971 kN/m) distributed force was found in the analysis without shrinkage, and thus the variation in shrinkage between the elements does result in an increasing distributed force.

In addition to increasing the distributed force, shrinkage also has a significant effect on force development. Where the original calculation assumed a 50% reduction due to creep/relaxation, this is overestimated due to shrinkage as the increasing shrinkage strain counteracts the reduction in creep/relaxation strain.

5

Parameter study

In the case study analyses, the same assumptions as in the original calculation model are used as far as possible to maintain a fair comparison between the two different methods and approaches of calculating the combination of restrained hardening stresses with external loads. This chapter answers the fifth sub-research question, which was: How do different material and model parameters influence the development of design stresses when considering time-dependent finite element analysis?

To answer this question, some of the assumptions made during the case study for the material and model parameters are varied to check their influence. So that when further calculations are made, these influences are known and can be taken into account. The parameter study is performed for the following parameters:

- Summer and winter temperature conditions
- Different coefficient of thermal expansion
- Different autogenous shrinkage development
- Higher concrete class
- Different formwork removal time
- Different geometry/phasing with pouring strip

For the first three parameters, a comparison is made between the assumptions made in the case study and the original calculation and what is recommended in CIRIA C766 for thermal properties. This is because CIRIA recommends different initial and ambient temperatures for winter and summer conditions, a different coefficient of thermal expansion than the Eurocode and also a different autogenous shrinkage. By performing the parameter study, the influence of these can be found. The influence of a higher concrete class is then investigated, as the original calculation specifies a minimum of C30/37, which means that (due to the high environmental class) a higher concrete class can be used in the construction. This will result in higher material properties but also higher adiabatic temperature development due to the increase in cement. Next, a higher formwork removal time is investigated and finally the original geometry/phasing in the original calculation, which included a pouring strip between the wall and the deck, is investigated.

Unless otherwise stated, the same material properties/specifications, finite element model and calculation analysis are used as were used for the case study in the previous chapter. The analyses and post-processing are also performed in the same way as described for the case study in Section 4.7. Thus, first an ‘uncracked’ analysis is performed with the full Young’s modulus development to find the most likely moment when cracking (where the crack index reaches 1.0) could occur. Next, an analysis is performed using the reduced Young’s modulus from the moment of expected cracking and the critical moment for mobile loads is determined. Finally, an analysis including the mobile loads is performed and the results are post-processed.

5.1. Summer and winter temperature conditions

To determine the influence of winter and summer temperature conditions on the design stresses, a parameter study is performed. In the case study, an initial and ambient temperature of $15\,°C$ and $20\,°C$ was used, which is also recommended as the default temperature in CIRIA C766. However, for concrete poured in winter conditions, the recommended initial and ambient temperatures are $15\,°C$ and $10\,°C$, and for concrete poured in summer conditions, $25\,°C$ and $20\,°C$ respectively.

From the first 'uncracked' analysis it was found that the crack index exceeded 1.0 at 256 days for the winter conditions analysis and at 255 days and 3 hours for the summer conditions analysis. This is later and earlier respectively than the 255 days and 12 hours found in the case study. Through post-processing it was found that the corresponding maturity/equivalent age for these times was 7.75 days for the winter conditions and 10.85 days for the summer conditions. This is, as expected, lower and higher respectively than the maturity/equivalent age found in the case study model of 9.10 days due to the temperature difference. The peak mid-section temperatures of both analyses and the temperature history of both analyses and the case study model can be seen in Figure 5.1.

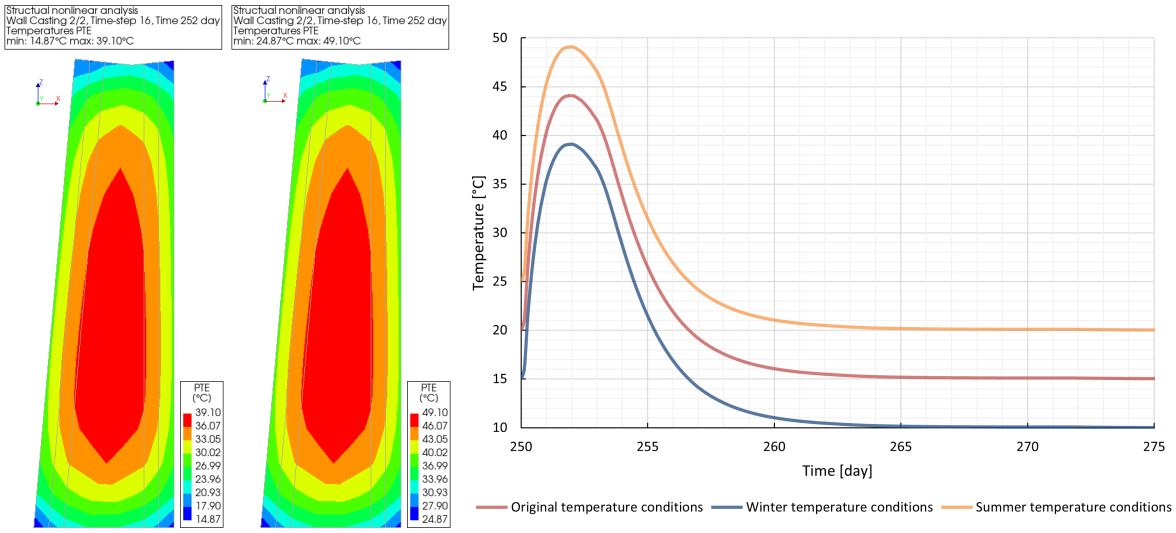

(a) Winter conditions (b) Summer conditions (c) Temperature developments from the nodes with the highest temperature

Figure 5.1: Cross-section of the peak temperature results (at 252 days) and comparison between the winter, summer and original temperature developments.

The peak temperature reaches $39.10\,°C$ for the winter conditions shown in Figure 5.1a and $49.10\,°C$ for the winter conditions shown in Figure 5.1b. These peak temperatures are exactly $5\,°C$ lower and higher than the $44.10\,°C$ found in the original case study analysis. The temperature development shown in Figure 5.1c is very similar, but also shifted by $5\,°C$.

The horizontal distributed force, which is almost the same as the horizontal distributed design force up to 300 days, within the effective areas of the wall from both analyses and the original case study analysis is shown and compared in Figure 4.38. The distributed forces shown in the figure represent the combined average distributed forces from the two effective areas within elements 29164 and 30737.

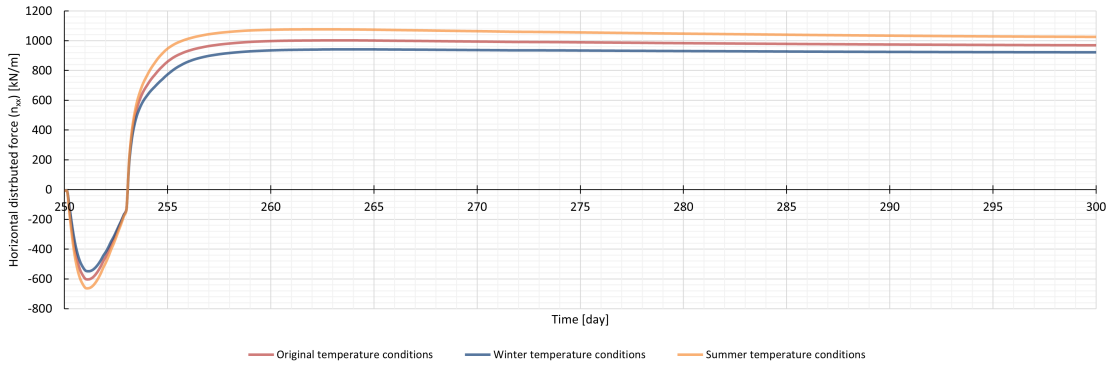

Figure 5.2: Horizontal distributed forces development for the different winter and summer conditions analysis and the analysis performed in Section 4.7.3 (combined average of element 29164 and 30737 in the effective areas).

Figure 5.2 shows that there are some differences between the horizontal force developments, but are eventually reasonable close. The differences can be explained by the difference in Young's modulus development, shrinkage and creep. Because all are effected by temperature or indirect by the maturity/equivalent age.

The results of the final step of the analysis at 301 days (including the mobile loads) are shown in Figures 5.3 and 5.4. Where the first shows the horizontal distributed force (n_{xx}) and the second shows the horizontal distributed design moment (m_{xD+}). Only the left side of the wall is shown because the element from which the results are subtracted is on that side, as shown in the figure.

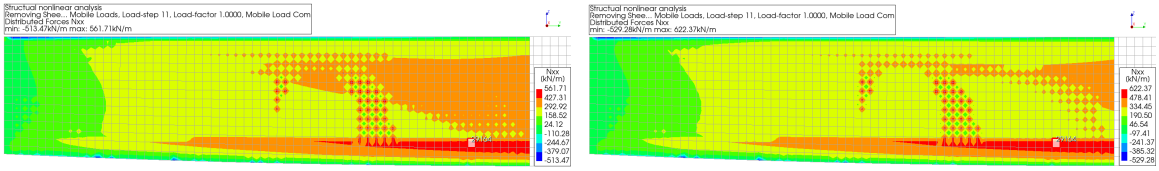

(a) Winter temperature conditions at the roadside (b) Summer temperature conditions at the roadside

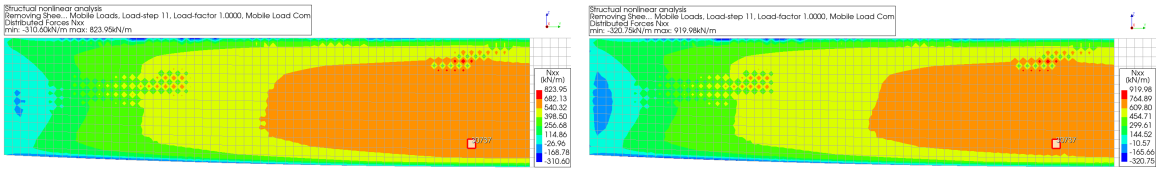

(c) Winter temperature conditions at the groundside (d) Summer temperature conditions at the groundside

Figure 5.3: Horizontal distributed forces (n_{xx}) in the effective areas at 301 days (after application of mobile loads) from the winter and summer temperature conditions analysis.

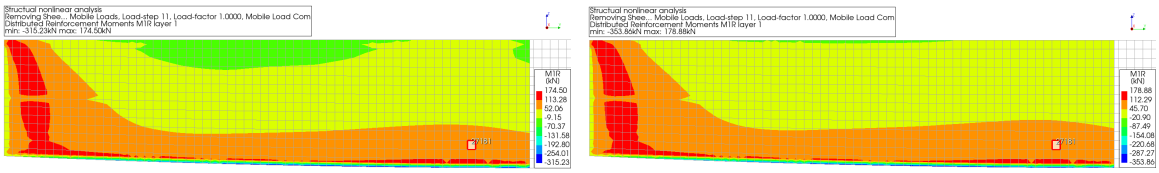

(a) Winter temperature conditions in the full wall (b) Summer temperature conditions in the full wall

Figure 5.4: Positive horizontal distributed design moment (m_{xD+}) in the full wall, taken from the middle composed surface at 301 days (after application of mobile loads) from the winter and summer temperature conditions analysis.

The subfigures of Figures 5.3 and 5.4 can be compared with each other and with Figures 4.30 and 4.33 respectively, which show the result of the original case study model with original temperature conditions. Using the results of the analyses and the same post-processing as performed in Section 4.7.3, the design forces and moments can be calculated including the external loads in the inside section of the wall and the excluded load groups. This is shown and compared in Table 5.1.

Table 5.1: Comparison of the distributed design forces and moments from the winter and summer temperature analysis with the results of the case study.

	Without external loads $t = 300$ days		With external and mobile loads $t = 301$ days	
	n_{xD} [kN/m]	m_{xD+} [kNm/m]	n_{xD} [kN/m]	m_{xD+} [kNm/m]
Case study analysis	971	0	1302	199
Winter temperature conditions	923 (−4.9%)	0 (0%)	1252 (−3.8%)	199 (0%)
Summer temperature conditions	1026 (+5.7%)	0 (0%)	1359 (+4.4%)	199 (0%)

Based on the results shown in the table above, the different temperature conditions have an effect on the distributed design forces but no effect on the design moments. The difference is found (almost entirely) in the hardening phase without external loads, as shown in Figure 5.2. The influence of the winter conditions on the final distributed force is only slightly smaller (−3.8%) than that of the summer conditions (+4.4%). The differences in the distributed force are mainly due to the higher equivalent/maturity age, which results in a higher Young's modulus development. It can be concluded that when the casting season is unknown or known to be summer, it is definitely recommended to include these temperature conditions to better predict the results.

5.2. Different coefficient of thermal expansion

A parameter study is performed to determine the influence of using the coefficient of thermal expansion (CTE) based on CIRIA C766 on the design stresses. Both the Eurocode and the fib Model Code 2010 prescribe a CTE of $10{\cdot}10^{-6}$ without taking into account the type of aggregate used in the concrete mix. CIRIA makes a distinction and recommends a CTE of $14 \cdot 10^{-6}$ for the quartzite aggregates used in this case study. So in this parameter study a comparison is made between the original CTE used in the case study and the higher CTE.

From the first 'uncracked' analysis it was found that the crack index exceeded 1.0 at 253 days and 3 hours, which is just one time step after the formwork was removed. In the case study, although the 5% characteristic value was reached at this time step (crack index of 1.429), it did not reach 1.0 until 255 days and 12 hours. The crack index result is shown in Figure 5.5, which shows both the middle cross-section of the wall and the side view of the entire structure modelled.

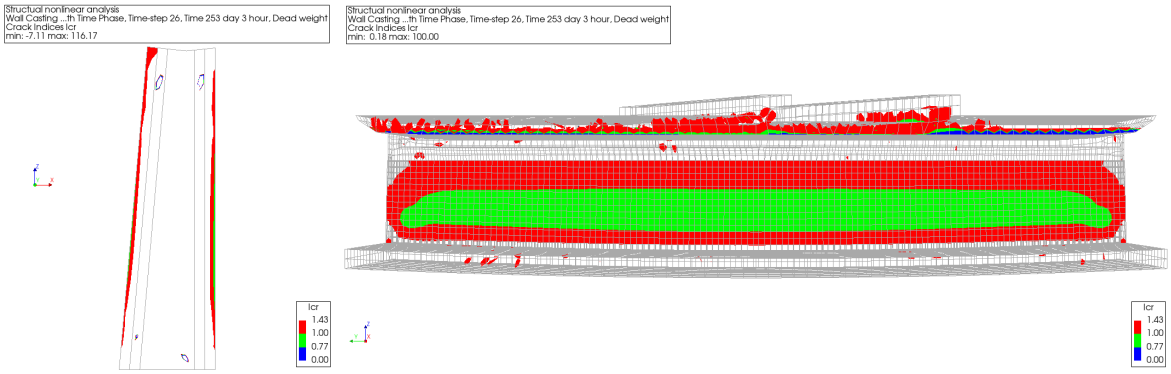

(a) Middle wall cross-section (b) Full structure view (perspective projection)

Figure 5.5: The crack index analysis result shown at 253 days and 3 hours.

Figure 5.5 shows that a change of 50% or more will cause cracking to occur at around 253 days and 3 hours and that this will start from the outside rather than the inside as in the case study shown in Figures 4.21 and 4.22. This is due to the rapid increase in temperature strain due to the higher CTE as the formwork is removed, which immediately results in a stress that exceeds the tensile strength when using the higher CTE based on the fib Model Code. This does not occur in the case study analysis using the CTE based on the Eurocode/fib Model Code.

Through post-processing it was found that the corresponding maturity/equivalent age for the 253 days and 3 hours was 6.00 days compared to the maturity/equivalent age found in the case study model of 9.10 days. As expected, no changes in peak temperature and temperature development were found between the higher CTE analysis and the original case study model.

The horizontal distributed force, which is almost equal to the horizontal distributed design force up to 300 days, within the effective areas from the wall of both the higher CTE analysis and the original case study analysis is shown and compared in Figure 5.6. The distributed forces shown in the figure represent the combined average distributed forces from the two effective areas within elements 29164 and 30737. In addition to the distributed forces from the final analysis using the reduced Young's modulus development, the result from the analysis using the full Young's modulus development is also shown in the figure as it was found that there was a large difference between them for this analysis.

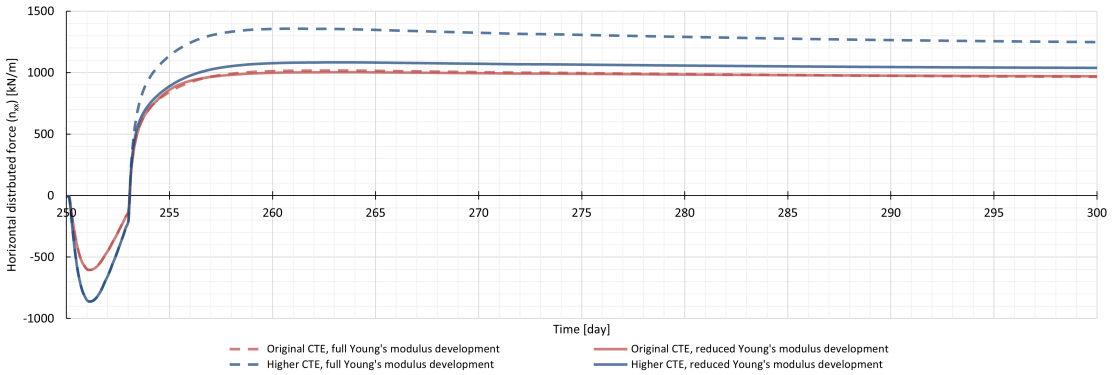

Figure 5.6: Horizontal distributed forces development for the higher CTE analysis and the analysis performed in Section 4.7.3 (combined average of element 29164 and 30737 in the effective areas).

In Figure 5.6 it can be seen that there are significant differences between the 'uncracked' analyses using the full Young's modulus, but that the differences in the reduced Young's modulus analyses are much closer. Comparing the distributed forces at 263 days, it was found that although the CTE increased by 40%, resulting in a 31% increase in distributed force, this is only 6.4% in the reduced Young's modulus analysis. This is most likely due to the fact that because the Young's modulus is reduced much earlier, there is less stress/distributed force increase due to the cooling of the concrete. Where in the original case study there is (almost) no change between the full and reduced Young's modulus developments, as most of the stress/distributed force has already taken place at 255 days and 12 hours.

The analyses results of the final step of the analysis at 301 days (including the mobile loads) are shown in Figures 5.7 and 5.8. The former shows the horizontal distributed force (n_{xx}) and the latter the horizontal distributed design moment (m_{xD+}).

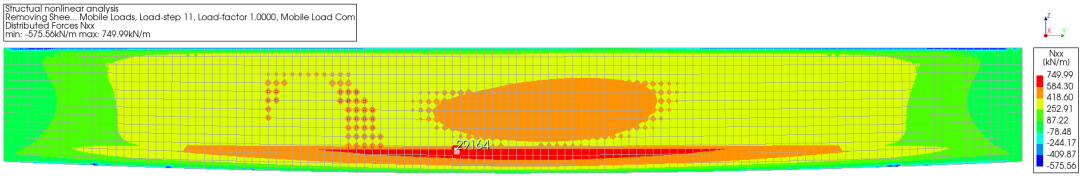

(a) Composed surface in the effective area at the roadside

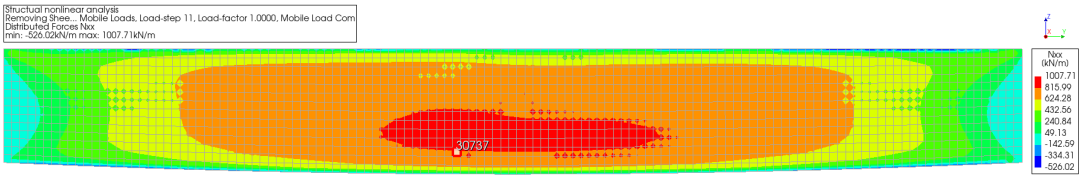

(b) Composed surface in the effective area at the groundside

Figure 5.7: Horizontal distributed forces (n_{xx}) in the effective areas at 301 days (after application of mobile loads) from the higher CTE analysis.

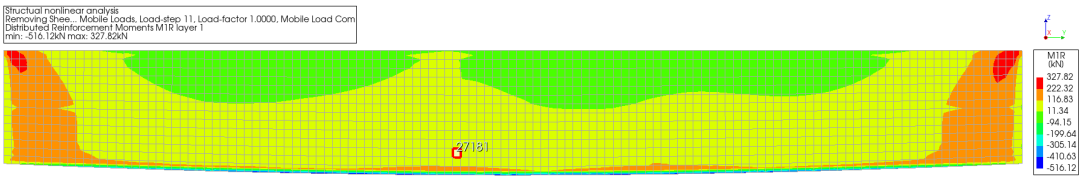

Figure 5.8: Positive horizontal distributed design moment (m_{xD+}) in the full wall, taken from the middle composed surface at 301 days (after application of mobile loads) from the higher CTE analysis.

Figures 5.7 and 5.8 can be compared to Figure 4.30 for the distributed force (n_{xx}) and Figure 4.33 for the distributed design moment (m_{xD+}) where the case study results are shown. Using the results of the analyses and the same post-processing as performed in Section 4.7.3, the design forces and moments can be calculated including the external loads in the inside section of the wall and the excluded load groups. This is shown and compared in Table 5.2.

Table 5.2: Comparison of the distributed design forces and moments from the higher CTE analysis with the results of the case study.

	Without external loads $t = 300$ days		With external and mobile loads $t = 301$ days	
	n_{xD} [kN/m]	m_{xD+} [kNm/m]	n_{xD} [kN/m]	m_{xD+} [kNm/m]
Case study analysis	971	0	1302	199
Higher CTE based on CIRIA	1038 (+7.0%)	0 (0%)	1371 (+5.3%)	199 (0%)

Based on the results shown in the table above, the higher CTE has an effect on the distributed design forces but not on the design moments. The difference is caused in the hardening phase as shown in Figure 5.6. At 300 days the distributed design force is 7.0% higher than with the original CTE, which is much less than that found in the 'uncracked' analysis. The influence of the higher CTE on the final distributed design force is less ($+5.3\%$) as no changes in force increase were observed. It can therefore be concluded that, in the absence of more detailed information on the CTE of the specific concrete mix used in a project, it would be more conservative to use the higher recommended CTE based on CIRIA C766, but that the effect of the higher CTE is less than expected.

5.3. Different autogenous shrinkage development

In order to determine the influence of a higher autogenous shrinkage (AS) development based on CIRIA C766 on the design stresses, a parameter study is performed. Where both the Eurocode and the fib Model Code 2010 prescribe AS independent of cement composition, CIRIA C766 describes an additional factor to account for different binder types, as also explained in Section 2.1.3. CIRIA C766 states that the cement type also has an important influence on the AS, but this is not included in the Eurocode equation (which is closely related to the equations from the fib Model Code).

Therefore, a factor is applied to the previously calculated AS (in Section 4.3.2) for the different concrete elements to include the influence of the binder. The factor used is 1.544, as CIRIA recommends an increase of 8% for each 10% of ggbs (which was 68%). The shrinkage development (including autogenous and drying shrinkage) is shown in Figure 5.9, which shows the original AS and the AS based on CIRIA C766.

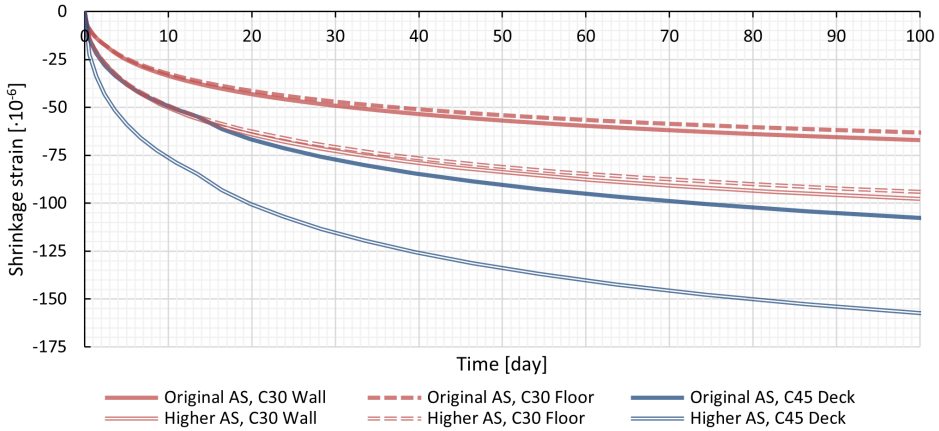

Figure 5.9: Shrinkage strain development comparison with and without the factors applied on the autogenous shrinkage (AS) based on the CIRIA C766.

From the first 'uncracked' analysis, it was found that the crack index exceeded 1.0 at 255 days and 6 hours, only 6 hours earlier than in the case study. This is due to the fact that there is more (autogenous) shrinkage, resulting in more stress and therefore tensile strength is reached earlier. Through post-processing it was found that the corresponding equivalent/maturity time was 8.85 days, compared to the equivalent/maturity age found in the case study model of 9.10 days. As expected, no changes were found in the peak mid-section temperatures and temperature history between the differential shrinkage analysis and the case study model.

The horizontal distributed force, which is almost equal to the horizontal distributed design force up to 300 days, within the effective areas from the wall of the analysis and the original case study analysis is shown and compared in Figure 5.10. The distributed forces shown in the figure represent the combined average distributed forces from the two effective areas within elements 29164 and 30737. No changes could be seen between the distributed forces from the final analysis using the reduced Young's modulus development and the analysis using the full Young's modulus development, so they are not included in the figure.

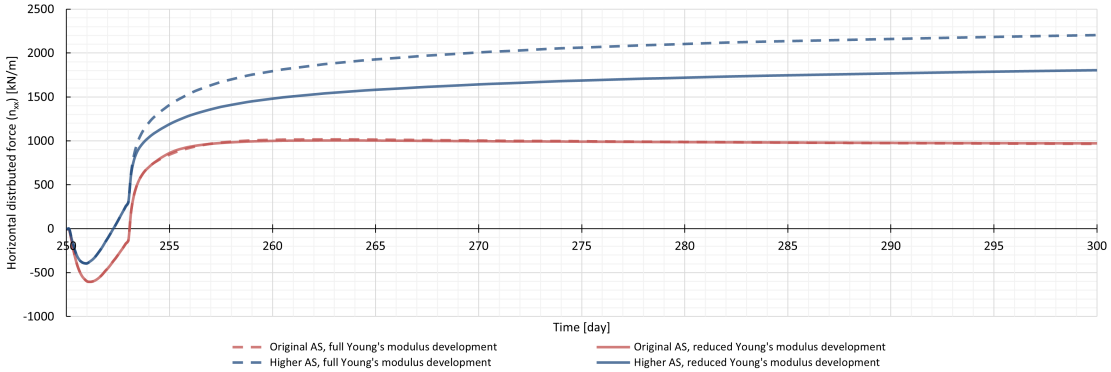

Figure 5.10: Horizontal distributed forces development for the higher AS analysis and the analysis performed in Section 4.7.3 (combined average of element 29164 and 30737 in the effective areas).

Figure 5.10 shows that the developments are quite close until about 3 days. Then the analysis with the higher AS increases more than with the original AS. This is as expected, as the shrinkage strain increases more with the higher AS, resulting in a higher distributed force within the wall.

The analysis results of the final step of the analysis at 301 days (including the mobile loads) are shown in Figures 5.11 and 5.12. The former shows the horizontal distributed force (n_{xx}) and the latter the horizontal distributed design moment (m_{xD+}).

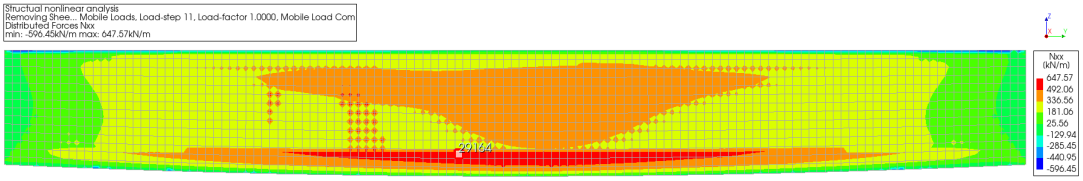

(a) Composed surface in the effective area at the roadside

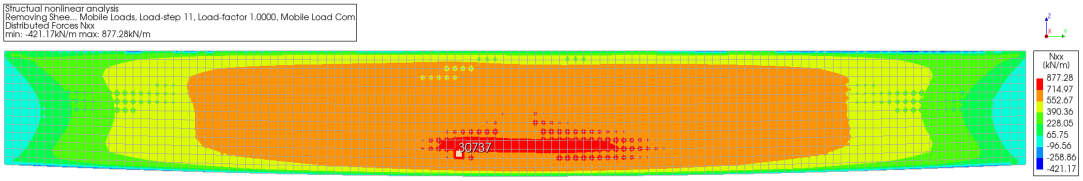

(b) Composed surface in the effective area at the groundside

Figure 5.11: Horizontal distributed forces (n_{xx}) in the effective areas at 301 days (after application of mobile loads) from the higher AS analysis.

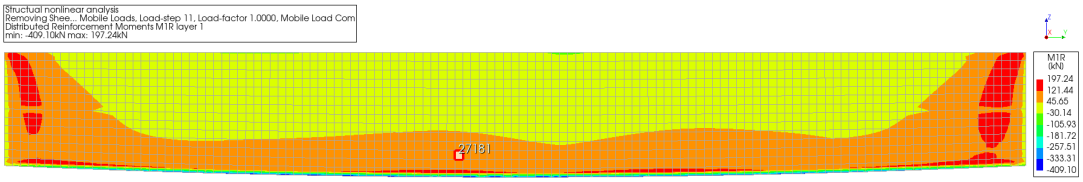

Figure 5.12: Positive horizontal distributed design moment (m_{xD+}) in the full wall, taken from the middle composed surface at 301 days (after application of mobile loads) from the higher AS analysis.

Figures 5.11 and 5.12 can be compared to Figure 4.30 for the distributed force (n_{xx}) and Figure 4.33 for the distributed design moment (m_{xD+}) where the case study results are shown. Using the results of the analyses and the same post-processing as performed in Section 4.7.3, the design forces and moments can be calculated including the external loads in the inside section of the wall and the excluded load groups. This is shown and compared in Table 5.3.

Table 5.3: Comparison of the distributed design forces and moments from the higher AS analysis with the results of the case study.

	Without external loads $t = 300$ days		With external and mobile loads $t = 301$ days	
	n_{xD} [kN/m]	m_{xD+} [kNm/m]	n_{xD} [kN/m]	m_{xD+} [kNm/m]
Case study analysis	971	0	1302	199
Higher AS based on CIRIA	1071 (+10.3%)	0 (0%)	1399 (+7.4%)	198 (−0.3%)

As shown in the table above, the higher shrinkage resulted in a $+10.3\%$ higher distributed design force at 300 days and a 7.4% higher final result. The higher AS also affected the distributed design moment at 301 days, which was -0.3% lower. However, this is only because the distributed design moment at 300 days was more negative (-4 instead of -3 kNm/m) than in the original calculation, as the increase of 202 kNm/m remained the same. It can therefore be concluded that shrinkage development, and AS in particular, has a significant influence on the results. Therefore, to accurately predict the distributed design forces, it is advisable to test the concrete mix, as the factor based on CIRIA C766 is only an approximation based on limited experimentation. Especially as it was found in Section 3.2.6 that even the higher AS, based on CIRIA, still underestimates the shrinkage strain for the experiment investigated. However, for design purposes it would be more conservative to use the higher recommended AS based on CIRIA C766 as it at least includes a factor for the influence of the binder.

5.4. Higher concrete class

A parameter study is performed to determine the influence of a higher concrete class, C45, for the wall and floor on the design stresses. Since the original calculation specified a minimum concrete class of C30/37 (C30), there is a real possibility that a higher concrete class with more cement will be used in the construction to meet the high environmental class. To incorporate the higher concrete class into the model, the same developments for mechanical properties and adiabatic temperature are used as already specified in Section 4.3.2 for the C45 deck. Shrinkage and creep are also recalculated using the higher concrete class parameters.

From the first 'uncracked' analysis it was found that the crack index exceeded 1.0 at 256 days and 6 hours, 18 hours after the 255 days and 12 hours found in the case study with the original C30 concrete. Post-processing found that the corresponding maturity/equivalent age at this time was 10.15 days compared to 9.10 days found in the case study analysis. The peak temperature at the middle cross-section and the temperature development of the performed analysis and the case study analysis are shown in Figure 5.13.

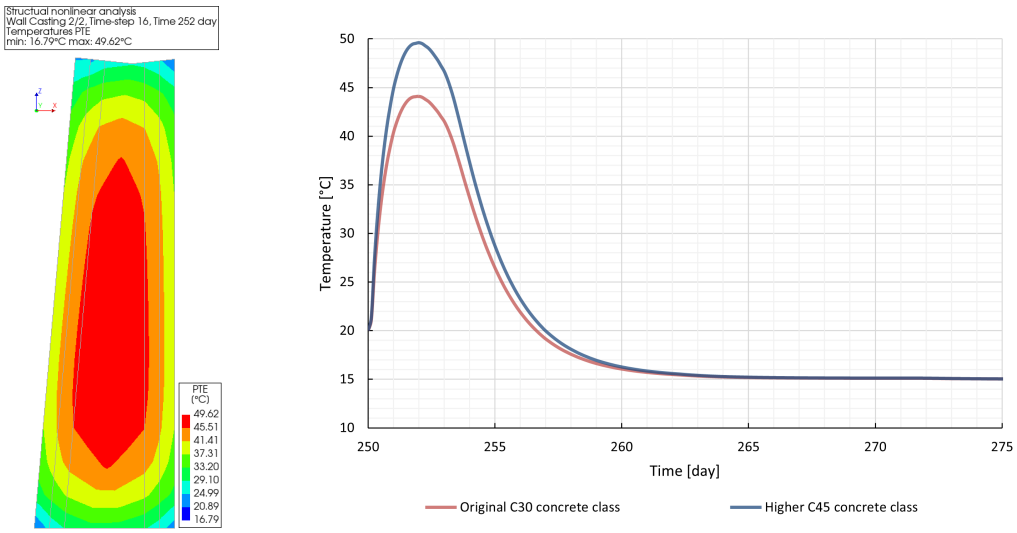

(a) Peak temperature (b) Temperature developments from the nodes with the highest temperature

Figure 5.13: Cross-section of the peak temperature result (at 252 days) and comparison between the higher C45 and the original C30 concrete class temperature developments.

The peak temperature for the analysis using the C45 concrete class is 49.62 °C as shown in Figure 5.13, which is a temperature increase of 29.62 °C. This is 22.9% higher than the 24.10 °C from the case study analysis. This is due to the higher adiabatic temperature development from the higher cement content.

The horizontal distributed force, which is almost equal to the horizontal distributed design force up to 300 days, within the effective areas from the wall of the analysis and the original case study analysis is shown and compared in Figure 5.14. The distributed forces shown in the figure represent the combined average distributed forces from the two effective areas within elements 29164 and 30737.

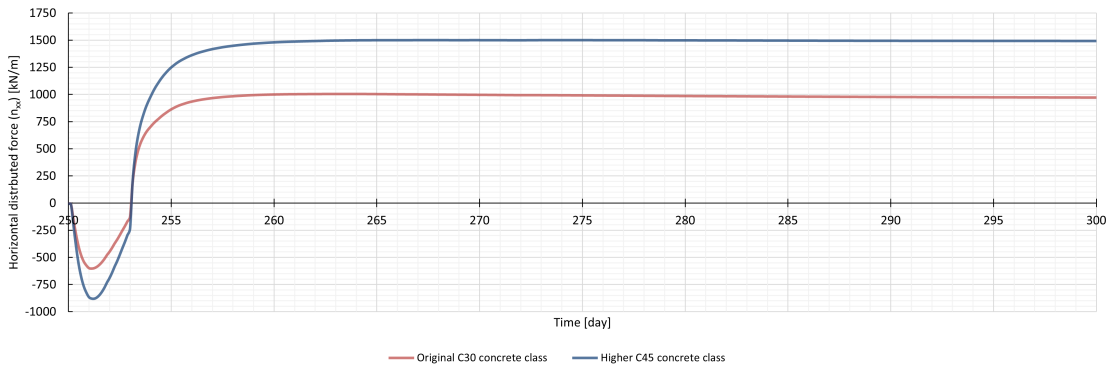

Figure 5.14: Horizontal distributed forces development for the higher concrete class analysis and the analysis performed in Section 4.7.3 (combined average of element 29164 and 30737 in the effective areas).

In Figure 5.14 it can be seen that there are very significant differences between the analysis with different concrete classes. This is to be expected as both the temperature and shrinkage strains are higher. This, combined with the higher Young's modulus, results in a higher stress and therefore distributed force in the effective areas.

The analysis results of the final step of the analysis at 301 days (including the mobile loads) are shown in Figures 5.15 and 5.16. The former shows the horizontal distributed force (n_{xx}) and the latter shows the horizontal distributed design moment (m_{xD+}).

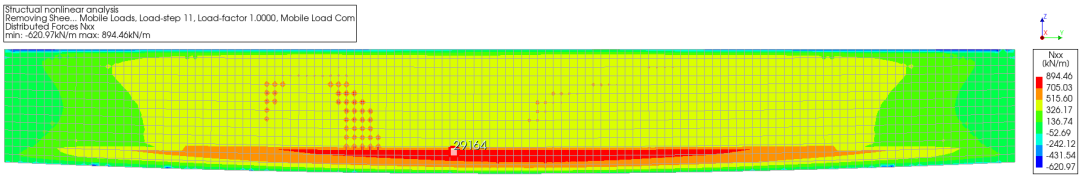

(a) Composed surface in the effective area at the roadside

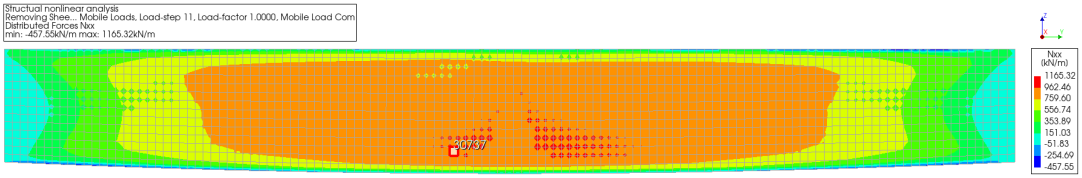

(b) Composed surface in the effective area at the groundside

Figure 5.15: Horizontal distributed forces (n_{xx}) in the effective areas at 301 days (after application of mobile loads) from the higher concrete class analysis.

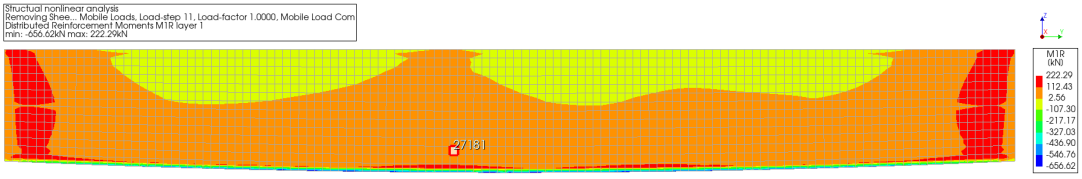

Figure 5.16: Positive horizontal distributed design moment (m_{xD+}) in the full wall, taken from the middle composed surface at 301 days (after application of mobile loads) from the higher concrete class analysis.

Figures 5.15 and 5.16 can be compared to Figure 4.30 for the distributed force (n_{xx}) and Figure 4.33 for the distributed design moment (m_{xD+}) where the case study results are shown. Using the results of the analyses and the same post-processing as performed in Section 4.7.3, the design forces and moments can be calculated including the external loads in the inside section of the wall and the excluded load groups. This is shown and compared in Table 5.4.

Table 5.4: Comparison of the distributed design forces and moments from the higher concrete class analysis with the results of the case study.

	Without external loads $t = 300$ days		With external and mobile loads $t = 301$ days	
	n_{xD} [kN/m]	m_{xD+} [kNm/m]	n_{xD} [kN/m]	m_{xD+} [kNm/m]
Case study analysis	971	0	1302	199
Higher concrete class (C45)	1493 (+53.9%)	0 (0%)	1825 (+40.1%)	198 (−0.4%)

From the results shown in the table above, it is clear that the higher concrete class for the wall and floor has a significant effect on the distributed forces. This is around $+53.9\%$ at 300 days (as also shown in Figure 5.14) and 40.1% for the final result. The higher Young's modulus of the higher concrete class had only a small (1 kN/m) effect on the distributed design force increment. Where the design moment in the original case study of 202 kNm/m increased from -3 to 199 kNm/m, this was 205 kNm/m for the higher concrete class. This only resulted in a slight decrease of 0.8 kNm/m (-0.4%) for the design moment because the positive design force at 300 days was -7 kNm/m (which was negative, resulting in a 0 in the table). It can therefore be concluded that information on the concrete class and/or cement content of the specific concrete mix used in a project is very important to know or to specify in the calculation in order to accurately predict the distributed design forces. As it was found that the influence of this is very significant.

5.5. Different formwork removal time

To determine the influence of a longer formwork removal time on the design stresses, a parameter study is performed. Whereas in the case study it is assumed that the formwork will be removed relatively quickly, after 3 days for the wall and floor, here it is decided to analyse the effect of removing the formwork after 14 days. The removal of the formwork after 14 days affects the input to the model, particularly for the convection coefficient development, but also for the drying shrinkage development.

From the first 'uncracked' analysis, it was found that the crack index exceeded 1.0 at 259 days and 12 hours, which is within the 14 days of the formwork being present. This is four days later than the 255 days and 12 hours found in the case study. Post-processing showed that the corresponding maturity/equivalent age at this time was 13.9 days, which is also later than the 9.1 days found in the case study analysis. The peak temperature in the middle cross-section and the temperature development of the performed analysis and the case study analysis can be seen in Figure 5.17.

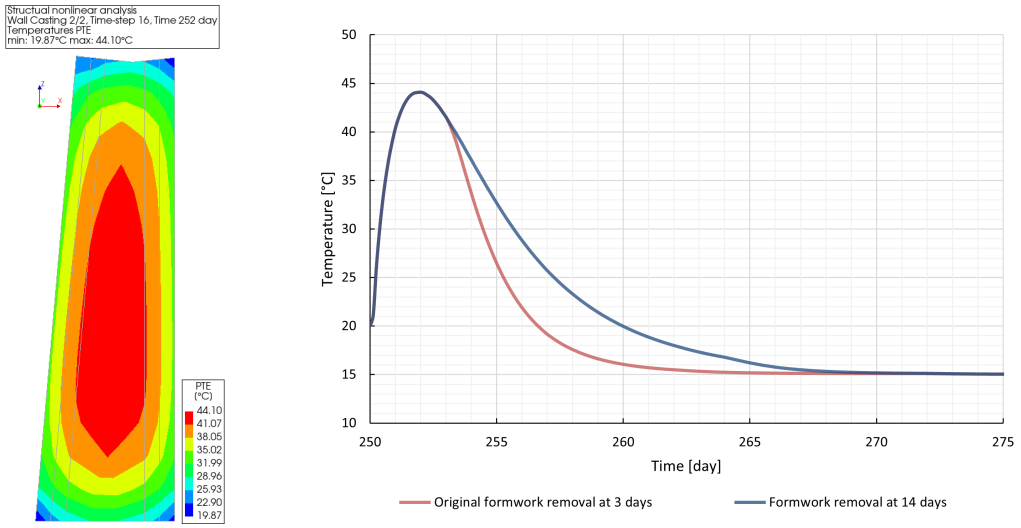

(a) Peak temperature (b) Temperature developments from the nodes with the highest temperature

Figure 5.17: Cross-section of the peak temperature result (at 252 days) and comparison between the formwork removal time of 3 and 14 days temperature developments.

The peak temperature for the 14 day formwork removal analysis is $44.10\,°C$ as shown in Figure 5.17, which is the same as found in the case study analysis. This is as expected as there are no changes in the input until three days. This can also be seen in the temperature development which shows that there are differences only after three days. These differences are due to the formwork remaining in place for 14 days, resulting in lower thermal conductance and therefore slower temperature reduction.

The horizontal distributed force, which is almost equal to the horizontal distributed design force up to 300 days, within the effective areas from the wall of the analysis and the original case study analysis is shown and compared in Figure 5.18. The distributed forces shown in the figure represent the combined average distributed forces from the two effective areas within elements 29164 and 30737. In addition to the distributed forces from the final analysis using the reduced Young's modulus development, the result from the analysis using the full Young's modulus development is also shown in the figure as it was found that there was a large difference between them for this analysis.

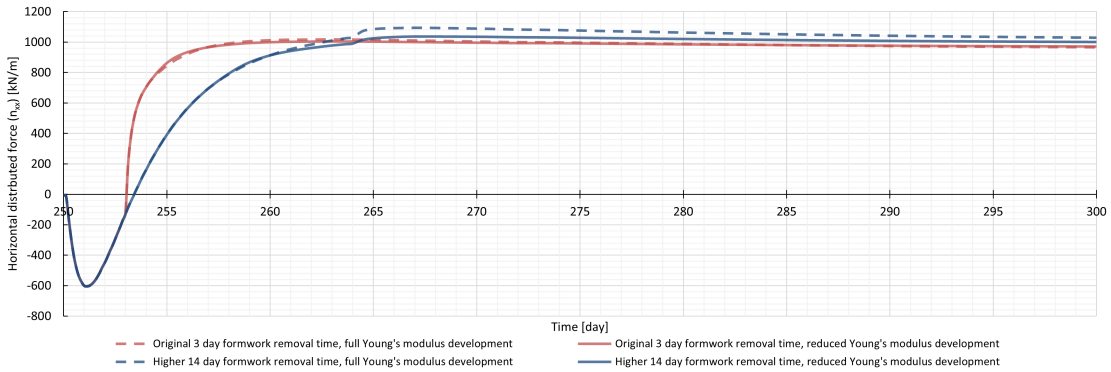

Figure 5.18: Horizontal distributed forces development for the different formwork removal time analysis and the analysis performed in Section 4.7.3 (combined average of element 29164 and 30737 in the effective areas).

Figure 5.18 shows that although the developments are the same up to three days, there are significant differences after that. While the distributed force continues to increase gradually when the formwork is removed after 14 days, the force increases rapidly when the formwork is removed after 3 days. This is due to the much faster cooling of the concrete as the temperature difference between the concrete and the ambient temperature is much greater. At 300 days, the 14 day formwork removal time is only slightly higher than the original 3 day results. This is most likely because as the temperature decreases more gradually, the force increase will eventually be greater as the Young's modulus develops, resulting in a higher distributed force.

The analysis results of the final step of the analysis at 301 days (including the mobile loads) are shown in Figures 5.19 and 5.20. The former shows the horizontal distributed force (n_{xx}) and the latter shows the horizontal distributed design moment (m_{xD+}).

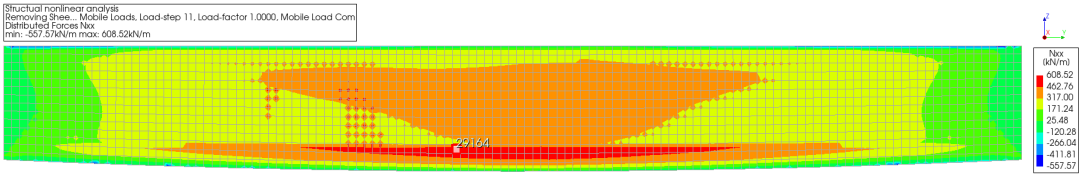

(a) Composed surface in the effective area at the roadside

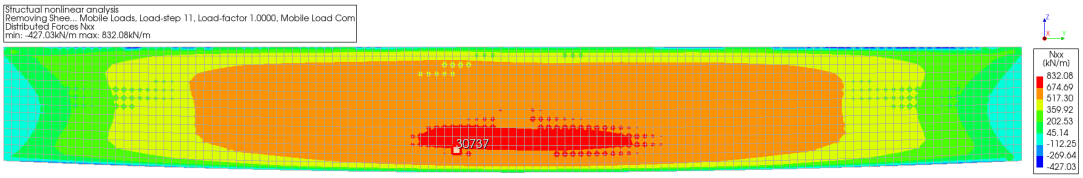

(b) Composed surface in the effective area at the groundside

Figure 5.19: Horizontal distributed forces (n_{xx}) in the effective areas at 301 days (after application of mobile loads) from the higher formwork removal time analysis.

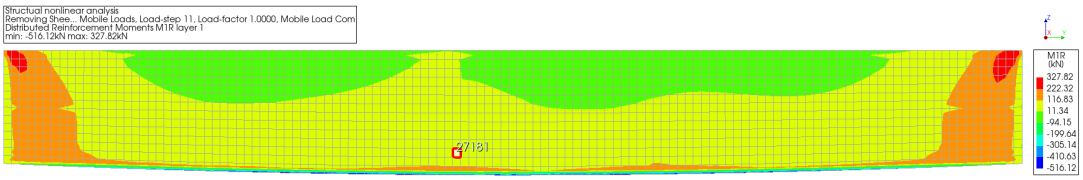

Figure 5.20: Positive horizontal distributed design moment (m_{xD+}) in the full wall, taken from the middle composed surface at 301 days (after application of mobile loads) from the higher formwork removal time analysis.

Figures 5.19 and 5.20 can be compared to Figure 4.30 for the distributed force (n_{xx}) and Figure 4.33 for the distributed design moment (m_{xD+}) where the case study results are shown. Using the results of the analyses and the same post-processing as performed in Section 4.7.3, the design forces and moments can be calculated including the external loads in the inside section of the wall and the excluded load groups. This is shown and compared in Table 5.5.

Table 5.5: Comparison of the distributed design forces and moments from the higher formwork removal time analysis with the results of the case study.

	Without external loads $t = 300$ days		With external and mobile loads $t = 301$ days	
	n_{xD} [kN/m]	m_{xD+} [kNm/m]	n_{xD} [kN/m]	m_{xD+} [kNm/m]
Case study analysis	971	0	1302	199
14 day formwork removal time	1000 (+3.1%)	0 (0%)	1326 (+1.8%)	198 (−0.2%)

Based on the results shown in the table above, the later removal of the formwork results in slightly higher distributed forces at 300 days of about $+3.1\%$, as shown in Figure 5.18. The influence of 14 days removal time on the final distributed design force is slightly less ($+1.8\%$), as no (significant) changes in force increase were observed. A very slight decrease of 0.3 kNm/m (-0.2%) was found for the design moment, which is a result of a slightly lower positive design force at 300 days (which was negative, resulting in a 0 in the table). It can therefore be concluded that extending the formwork time results in a later cracking time, but slightly increases the distributed forces in the wall.

5.6. Different geometry/phasing with pouring strip

A parameter study is performed to determine the influence of a different geometry using a pouring strip on the development of design stresses. In the original calculation of the case project, it was initially assumed that the wall would consist of a wall poured on the floor and a strip poured between the wall and the deck.This was eventually changed to pouring the entire wall in one pour, presumably to save construction time. This change did not result in any different results to the original calculation as this level of detail was not included in the calculation. The influence of this change is therefore investigated in this parameter study. The geometry of the new model, where the original wall is split into two parts, the wall connecting to the floor and a pouring strip between the wall and the deck, is shown in Figure 5.21.

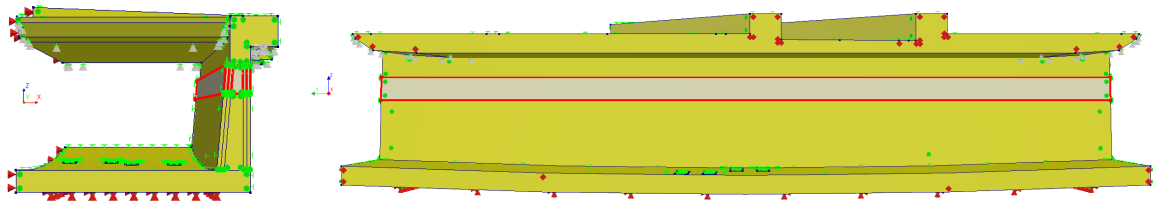

(a) Y-direction view (b) X-direction view

Figure 5.21: The geometry and boundary conditions for model with different geometry including a pouring strip (highlighted) (perspective projection).

To include the pouring of the pouring strip, an additional phase is added to the analysis after the wall is poured and before the sheet piles are removed. The total time is also increased as it is assumed that the strip is added 50 days after the wall is cast and 50 days before the sheet piles are removed and the external loads are added. This changes the total analysis time before the sheet piles are removed from 300 days to 350 days. The same material model with mechanical and thermal properties is used for the pouring strip as was used and described for the wall.

From the first 'uncracked' analysis, it was found that although the wall was poured first, the pouring strip cracked first. This occurred at 305 days and 3 hours (5 days and 3 hours after pouring). The wall did not exceed 1.0 until 350 days, when external loads were applied and the sheet piles were disconnected. Post-processing showed that the corresponding maturity/equivalent age for the pouring strip was 7.10 days and for the wall it was 79.8 days. The peak temperature in the middle cross-section inside the wall was quite close to the peak temperature of the original case study analysis, $44.05\,°C$ compared to $44.10\,°C$. The same development for the mechanical properties was observed as the maturity/equivalent age development within most of the parts was quite similar.

The horizontal distributed force, which is almost equal to the design horizontal distributed force up to 350 days for the different geometry analysis and 300 days for the original geometry analysis, within the effective areas of the wall from the analysis and the original case study analysis is shown and compared in Figure 5.22. The distributed forces shown in the figure represent the combined average distributed forces from the two effective areas within elements 23216 and 24486. These elements are in exactly the same location as elements 29164 and 30737 in the mesh of the case study analysis.

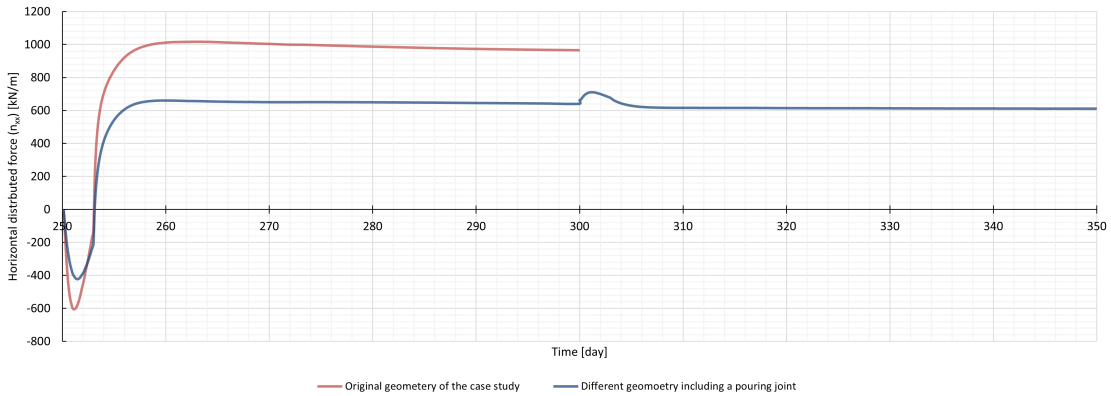

Figure 5.22: Horizontal distributed forces development for the different geometry and phases analysis and the analysis performed in Section 4.7.3 (combined average of element 23216 and 24486 or 29164 and 30737 in the effective areas).

Figure 5.22 shows significant differences between the two analyses. Both the early age compressive and tensile stresses are much lower, i.e. less extreme. When comparing the results before the sheet piles are removed and the deck is resting on the wall/pouring strip, there is a decrease of 37% for the different geometry analysis. This is most likely due to the lower degree of restraint as the wall is not connected to the deck, allowing the top to expand and contract freely during the first 50 days. Note that only the results in the wall, at the same location, are compared, so the results for the pouring strip are not included.

The analysis results of the final step of the analysis at 301 days (including the mobile loads) are shown in Figures 5.23 and 5.24. The former shows the horizontal distributed force (n_{xx}) and the latter shows the horizontal distributed design moment (m_{xD+}).

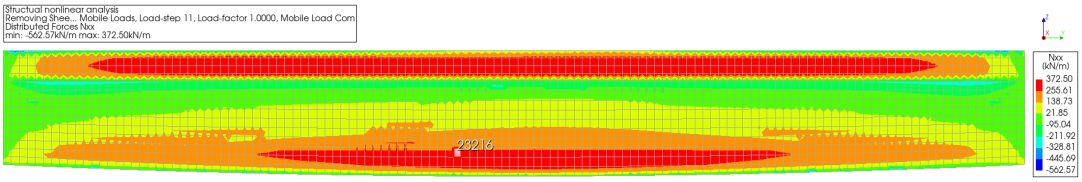

(a) Composed surface in the effective area at the roadside

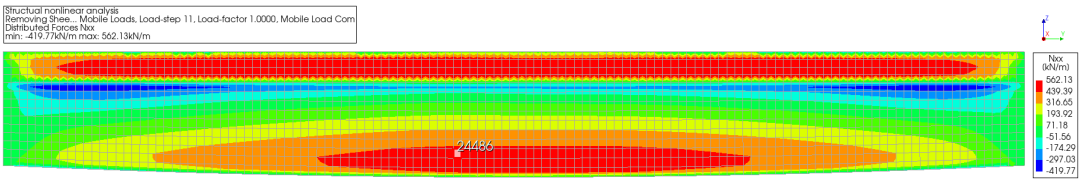

(b) Composed surface in the effective area at the groundside

Figure 5.23: Horizontal distributed forces (n_{xx}) in the effective areas at 301 days (after application of mobile loads) from the different geometry and phases analysis.

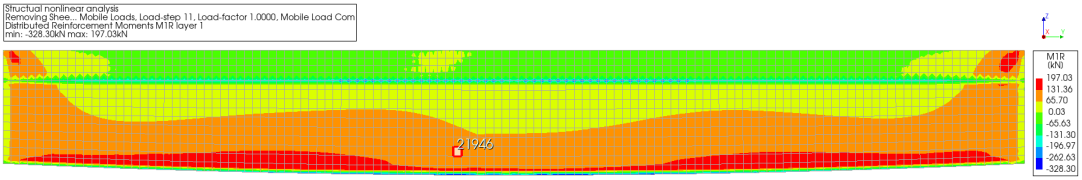

Figure 5.24: Positive horizontal distributed design moment (m_{xD+}) in the full wall, taken from the middle composed surface at 301 days (after application of mobile loads) from the different geometry and phases analysis.

Figures 5.23 and 5.24 can be compared to Figure 4.30 for the distributed force (n_{xx}) and Figure 4.33 for the distributed design moment (m_{xD+}) where the case study results are shown. Using the results of the analyses and the same post-processing as performed in Section 4.7.3, the design forces and moments can be calculated including the external loads in the inside section of the wall and the excluded load groups. This is shown and compared in Table 5.5.

Table 5.6: Comparison of the distributed design forces and moments from the different geometry and phases analysis with the results of the case study.

	Without external loads $t = 300/350$ days		With external and mobile loads $t = 301/351$ days	
	n_{xD} [kN/m]	m_{xD+} [kNm/m]	n_{xD} [kN/m]	m_{xD+} [kNm/m]
Case study analysis	971	0	1302	199
Different geometry and phases	$613\ (-36.9\%)$	$0\ (0\%)$	$979\ (-24.8\%)$	$204\ (+2.9\%)$

Based on the results shown in the table above, the different geometry including a pouring strip results in significantly lower results at 300/350 days of about -36.9%, as also shown in Figure 5.22. The influence of the different geometry on the final distributed design force is slightly less (-24.8%), as no (significant) changes in force increase were observed. A very slight increase of $+2.9\%$ was found for the design moment, which is a result of a slightly lower positive design force at 300 days (which was negative, resulting in a 0 in the table). It can therefore be concluded that the inclusion of a different phase, which includes a pouring strip, can have a significant effect on the results for the wall, as the distributed forces, at least for the wall, are reduced by almost 25%.

6

Discussion

This research starts with a comprehensive literature review covering four main topics: stress development during hardening of restrained concrete, preliminary research on the case project, modelling with DIANA FEA, and an overview and possible calculation methods. The focus of the literature review is mainly on the book “Concrete Structures under Imposed Thermal and Shrinkage Deformations” by Van Breugel, et al. [2], the Eurocode [4], the fib Model Code 2010 [5] and CIRIA C766 [3]. Although this approach may disregard other potentially more accurate and recent literature, it ensures reliability by limiting the study to these sources, which contain a wide range of validated literature and can therefore be used or prescribed for the calculation of civil projects.

Following the literature review, an extensive study is performed to model a Temperature-Stress Testing Machine (TSTM) experiment using time-dependent finite element analysis. The results of the experiments performed by Klausen in her doctoral research are compared with the DIANA FEA model to validate the results of the partially restrained hardening analysis using a DIANA FEA model. The results show that the created TSTM model accurately simulates the experiments for three different concrete mixes/cement compositions when the material properties from the experiment are used. However, it should be noted that these results do not necessarily apply to all possible concrete mixes. However, as all input parameters were known or specified, it is reasonable to assume that the model created could accurately simulate other scenarios if all input parameters were known.

Next, the default material models within DIANA FEA based on the Eurocode and the fib model code were compared to the same experiment. These models were found to be less accurately defined within DIANA FEA, mainly due to the use of large step sizes for the Kelvin chains that define Young’s modulus and creep. As a result, a viscoelastic material model based on the fib Model Code is created and found to be more accurate. This created material model is validated by hand calculations and comparison with the experiment. It is observed that the model deviates from the experiment when using the mechanical properties based on the fib Model Code. However, when using the corrected Young’s modulus, autogenous shrinkage and coefficient of thermal expansion based on the experiment, an almost exact match is found. This shows the significant differences that can occur between experimental results and those prescribed by the standards, affecting the overall accuracy of the results. Consequently, a parameter study is performed for the case study to further investigate these influences.

As far as possible, the same assumptions were made for the case study as were made for the original calculation. However, certain aspects were unknown or unspecified and assumptions had to be made. For example, the time intervals between different phases were assumed based on temporary track closures and project visits by Wagemaker. Similarly, assumptions were made for the concrete mix design, including water to cement (w/c) ratio, cement content and composition, based on a similar project found in the literature. Although these assumptions may be reasonable, they may result in differences. In addition, most of the thermal properties such as thermal conductivity, thermal conductance, specific heat and adiabatic temperature development were unknown. Nevertheless, Section 3.1.5 suggests that the influence of these parameters is expected to be minimal, with a maximum difference of 4.1% between the parameters used in Klausen’s research and those recommended in CIRIA C766. It is therefore expected that the case study will be able to predict the results reasonably accurately even without precise knowledge of these parameters.

Although a time-dependent, non-linear and phased calculation is performed, including transient heat transfer analysis and structural non-linear analysis, one important non-linearity is not considered. This is the simulation of cracking as a viscoelastic material model is chosen which does not include non-linear material developments and therefore reinforcement is also not modelled. This decision was made in the model approach to reduce the complexity of the analysis and because it would not be possible to accurately simulate cracking with the required element size reduction for the whole structure. As a result, the stress levels in the model can exceed the tensile strength, which would normally not be possible as this would result in cracking and a (temporary) constant concrete stress as the reinforcement is expected to absorb the further increase. To compensate for this, an engineering approach is used to reduce the Young's modulus when the principal stress equals or exceeds the tensile strength of the concrete. This approach is not an exact simulation, but provides an approximation for comparison with the case study. The influence of this approach is unknown and could influence the results.

Implementing the reduction in Young's modulus at the expected cracking time was difficult to incorporate into the analysis. As Young's modulus is embedded in the viscoelastic material properties, it had to be reduced based on maturity/equivalent age. Since different parts of the wall do not have the same maturity/equivalent age at the time of expected cracking, a non-uniform reduction in stiffness occurs. However, as explained in Section 4.7.2, this non-uniformity did not result in significant changes in the distributed force for the case study model. Therefore, the influence of this non-uniform reduction is also expected to be limited in the parameter study.

In the model approach, it was chosen not to include prestressing elements and/or loads in the deck to minimise complexity, given its limited influence on the wall. It was also found that it was not possible to include a gradient temperature load/strain as a load in the modelling of the structure. Therefore, the distributed forces and moments from the governing location in the original computational model were added to the case study results. As the forces and moments from the excluded load groups are not the same for each element, it was difficult to find the governing element. However, by checking different elements, it was highly likely that the dominant element was eventually selected. Furthermore, as only one dominant load combination from the original calculation model was used in the case study analysis, it cannot be guaranteed that this is also the governing load combination for the combination with hardening stresses. However, as this load combination was found to be governing at the same location, the probability is high.

Lastly, when performing the long-term analysis for the case study to predict the results at 't=∞', only an analysis up to 665 days (one year after removal of the sheet piles) could be performed. Attempts to perform a longer analysis, such as three years, resulted in unreliable results for the first 50 days after the wall was poured. This is due to the limitations of DIANA FEA, which only allows 30 maturity/time steps. This results in insufficient steps during the first few days after casting when using a proper distribution over time, leading to inaccurate results. However, the analysis of 665 days shows a slowdown in the reduction of the distributed forces, with the reduction percentages gradually decreasing to only -0.25% in the last 50 days of the analysis. Although it can be assumed that the distributed forces will continue to decrease beyond this period, the negative trend indicates that the effect would not be significant.

7

Conclusion and recommendations

This thesis focuses on the following research question; *What is the effect of applying time-dependent finite element analysis, including the combination of hardening processes and external loads, on improving the prediction of the development of design stresses for partially restrained concrete?*

While further research is required to fully verify the analysis results from the case study, it is expected that the time-dependent finite element analysis performed can indeed improve the prediction of design stresses, as supported by the validations performed for the TSTM experiment. The integration of time-dependent effects and the consideration of the combination of hardening processes and external loads provide a more comprehensive understanding of stress evolution than traditional methods. By taking into account creep, relaxation and shrinkage, the analysis provides a more realistic representation of stress behaviour over time, allowing more accurate and reliable predictions of design stresses in partially restrained concrete. It also allows the determination of the most critical time step for the application of mobile loads.

The case study research showed that the assumption that 50% of the hardening forces are reduced when the governing external loads are applied was overly optimistic. This was mainly because the original calculation did not take into account shrinkage, which counteracted the reduction in creep/relaxation, resulting in a reduction of only 10% after one year. This is because the shrinkage strain continues to increase, counteracting the reduction in creep/relaxation. It was also found that the assumption in the original calculation that the concrete would crack at 75% of its tensile strength was not conservative. It is therefore recommended that shrinkage is considered during the design process and that cracking is not assumed to occur at 75%, but at the time-dependent tensile strength.

Furthermore, the case study also found that the external loads applied to the model resulted in approximately $30-31\%$ lower design stresses due to the implementation of phased loading and more accurate modelling calculations. However, this type of analysis was found to be very time consuming, with each analysis limited to only one load combination. To overcome this, in practical applications it is recommended that only hardening processes and dead loads are included in the time-dependent finite element analysis. The results of a separate linear analysis, which includes all types of mobile loads and combinations, can then be manually added to limit the number of analyses. As creep reduction does not apply to mobile loads, this alternative approach provides a more practical solution while still benefiting from the application of a more detailed and accurate time-dependent analysis.

The parameter study showed that a change to a higher concrete class (C45 instead of C30) resulted in a significant 40.1% increase in design stresses. As the original calculation only specified a minimum concrete class, there's a real possibility that a higher concrete class with more cement will be used in the construction to meet the high environmental class. The increased cement content would increase the concrete class and affect both the peak temperature and tensile strength at cracking. It is therefore recommended that the concrete class and the corresponding cement content are strictly known or specified for the design.

Furthermore, the parameter study showed that the use of an increased autogenous shrinkage, by using a factor from CIRIA C766 to account for the binder type ggbs, resulted in an increase in the distributed design forces of approximately 7.3%. It is therefore recommended that a higher autogenous shrinkage be considered when using CEM III concrete if no shrinkage data is available from testing. This is because it is widely accepted in the literature that both the Eurocode and the fib Model Code do not accurately predict autogenous shrinkage for high admixture cements, which was also concluded from the tests considered in the TSTM experiment.

Based on the other parameters it is also concluded that the influence of winter and summer temperature conditions (-3.8% and $+4.4\%$), a higher coefficient of thermal expansion (5.3%) and an extended formwork removal time ($+1.8\%$) has a somewhat limited effect. Although the best possible assumptions should be made to accurately predict the results, any incorrect assumptions regarding these parameters would have a limited effect. The different geometry by using a pouring strip between the wall and the deck was found to significantly reduce (-24.8%) the design stresses, at least in the wall. This highlighted the influence of phasing and that the use of a pouring strip could significantly optimise and possibly reduce the reinforcement within the wall.

In summary, this research highlights the effectiveness of applying time-dependent finite element analysis in improving the prediction of design stress development for partially restrained concrete elements. The findings provide valuable insights for more detailed and accurate modelling, consideration of relevant parameters and accurate analysis of design stresses, contributing to more optimised and reliable structural design solutions.

Although this thesis has been quite extensive, there are still areas for improvement and further research. Below are some recommendations for future work;

- The current research only includes one case study. It is recommended to expand the research by conducting additional case studies to determine if the same conclusions apply in different cases.
- It is also recommended that further research be undertaken to investigate non-linear material properties and the modelling and simulation of cracking.
- Further research and testing could be performed on the development of mechanical properties and (autogenous) shrinkage. This would allow for even more accurate prediction and simulation of stress development, thereby improving the reliability of the analysis.

By addressing these aspects in future research, a more comprehensive understanding of the subject can be achieved, leading to improved design and analysis methods.

Bibliography

[1] *Onderdoorgang Kanaalweg Leiden*, Accessed: 12-07-2023. [Online]. Available: https://ipvdelft.nl/portfolio-item/onderdoorgang-kanaalweg-leiden.

[2] K. van Breugel, C. R. Braam, C. van der Veen, and J. C. Walraven, *Concrete Structures under Imposed Thermal and Shrinkage Deformations*. TU Delft - Concrete Structures - Capita Selecta, 2016.

[3] P. B. Bamforth, "Control of cracking caused by restrained deformation in concrete (CIRIA C766)," CIRIA, London, UK, Tech. Rep. CIRIA C660, RP722, 2019.

[4] "NEN-EN 1992-1-1+C2, Eurocode 2: Design of concrete structures - part 1-1: General rules and rules for buildings," Nederlands Normalisatie-instituut, Postbus 5059, 2600 GB Delft, Tech. Rep., 2011.

[5] Walraven, Bigaj-van Vliet, Balazs, *et al.*, *Model Code 2010 - First complete draft*. International Federation for Structual Concrete (fib), 2010, vol. 1, ISBN: 978-2-88394-095-6. DOI: https://doi.org/10.35789/fib.BULL.0055.

[6] J. C. Walraven and C. R. Braam, *CIE3150/4160 Prestressed concrete*. TU Delft - Faculty of Civil Engineering and Geosciences, 2018.

[7] T. Zhang, P. Gao, R. Luo, Y. Guo, J. Wei, and Q. Yu, "Measurement of chemical shrinkage of cement paste: Comparison study of ASTM C 1608 and an improved method," *Construction and Building Materials*, vol. 48, pp. 662–669, 2013, ISSN: 0950-0618. DOI: https://doi.org/10.1016/j.conbuildmat.2013.07.086.

[8] T. Lu, Z. Li, and H. Huang, "Effect of Supplementary Materials on the Autogenous Shrinkage of Cement Paste," *Materials*, vol. 13, no. 15, 2020, ISSN: 1996-1944. DOI: https://doi.org/10.3390/ma13153367. [Online]. Available: https://www.mdpi.com/1996-1944/13/15/3367.

[9] E. Vermeulen, "Nieuwe inzichten autogene krimp," *Betoniek Standaard*, vol. 17/06, Apr. 2021.

[10] A. Neville, *Properties of concrete*. Essex, England: Longman Group Limited, 1995, vol. (4th edition).

[11] J. Feij, "Shrinkage reducing agent in concrete," M.S. thesis, TU Delft Civil Engineering and Geosciences, Delft, The Netherlands, Mar. 2020. [Online]. Available: http://resolver.tudelft.nl/uuid:b0921d17-503f-495f-99bc-96f4f19b95df.

[12] "National Annex to NEN-EN 1992-1-1+C2 Eurocode 2: Design of concrete structures - Part 1-1: General rules and rules for buildings," Nederlands Normalisatie-instituut, Tech. Rep., 2020.

[13] "NEN-EN 1992-3:2006, Eurocode 2: Design of concrete structures - Part 3: Liquid retaining and containment structures," Nederlands Normalisatie-instituut, Postbus 5059, 2600 GB Delft, Tech. Rep., 2011.

[14] M. Dijk, "Verhinderingsgraad," *Cement*, vol. 7, pp. 58–65, 2021.

[15] J. R. van Bokhorst, "Early-age cracking of concrete," M.S. thesis, TU Delft Civil Engineering and Geosciences, Delft, The Netherlands, Apr. 2020. [Online]. Available: http://resolver.tudelft.nl/uuid:5f782dca-8f58-4204-9241-1177e3f261f4.

[16] D. Schlicke, N. Tue, A. Klausen, T. Kanstad, and Ø. Bjøntegaard, "Structural Analysis and Crack Assessment of Restrained Concrete Walls - 3D FEM-Simulation and Crack Assessment," Jun. 2014.

[17] L. Lacarrière, A. Sellier, A. Turatsinze, and G. Escadeillas, "Finite element modelling of hardening concrete: Application to the prediction of early age cracking for massive reinforced structures," *Materials and Structures - MATER STRUCT*, vol. 44, Dec. 2011. DOI: 10.1617/s11527-011-9740-y.

[18] *Google Maps*. [Online]. Available: https://www.google.com/maps.

[19] H. J. de Rooij, “DO/UO Spooronderdoorgang Kanaalweg te Leiden - DO/UO Berekening gesloten moot,” Wagemaker, Tech. Rep. W15216-RAP-02-V1.0, 2016.

[20] L. den Elzen and J. van den Tillaart, “Spooronderdoorgang Kanaalweg te Leiden - Doorsneden tekening,” Wagemaker, Tech. Rep. SKL-1.1-DO-WM-TEK-0002, 2016.

[21] D. Schoenmakers, “Berekeningsnotitie DO KW19 bovenbouw - Viaduct Zeldert,” Wagemaker, Tech. Rep. 3ANGLE-BER-11-5186, 2017.

[22] M. van der Linden, “KW19 - Viaduct Zeldert - Overzicht tekening,” Wagemaker, Tech. Rep. 3ANGLE-TEK-11-5384, 2017.

[23] ——, “KW19 - Viaduct Zeldert - Dekconstructie tekening,” Wagemaker, Tech. Rep. 3ANGLE-TEK-11-5385, 2017.

[24] D. Ferreira and J. Manie, Eds., *Diana finite element analysis - diana documentation - release 10.6*, DIANA FEA BV, 2022. [Online]. Available: https://manuals.dianafea.com/d106/Diana.html.

[25] A. E. Klausen, “Early age crack assessment of concrete structures,” Ph.D. dissertation, Norwegian University of Science and Technology (NTNU), Trondheim, Norway, 2016, ISBN: 978-82-326-1851-4. [Online]. Available: http://hdl.handle.net/11250/2430293.

[26] A. E. Klausen, T. Kanstad, and Ø. Bjøntegaard, “Hardening Concrete Exposed to Realistic Curing Temperature Regimes and Restraint Conditions: Advanced Testing and Design Methodology,” *Advances in Materials Science and Engineering*, vol. 2019, 9071034, 2019. DOI: https://doi.org/10.1155/2019/9071034.

[27] A. E. Klausen and T. Kanstad, “The effect of shrinkage reducing admixtures on drying shrinkage, autogenous deformation, and early age stress development of concrete,” *Structural Concrete*, vol. 22, no. S1, E596–E606, 2021. DOI: https://doi.org/10.1002/suco.201900583.

[28] “NEN-EN 197-1:2011, Cement - Part 1: Composition, specifications and conformity criteria for common cements,” Nederlands Normalisatie-instituut, Postbus 5059, 2600 GB Delft, Tech. Rep., 2011.

[29] *Climate Change Knowlegde Portal*, Accessed: 10-12-2022. [Online]. Available: https://climateknowledgeportal.worldbank.org/country/norway/climate-data-historical.

[30] “NEN-EN 1992-1-2+C1, Eurocode 2: Design of concrete structures – Part 1-2: General rules – Structural fire design,” Nederlands Normalisatie-instituut, Postbus 5059, 2600 GB Delft, Tech. Rep., 2011.

[31] *KNMI Daily weather data in the Netherlands*, Accessed: 27-03-2023. [Online]. Available: https://www.knmi.nl/nederland-nu/klimatologie/daggegevens.

[32] *SCIA Engineer Design internal forces*, Accessed: 03-04-2023. [Online]. Available: https://help.scia.net/22.0/en/results/displaying_results/design_internal_forces.htm.